



Technische Universität München
Fakultät für Chemie

Synthesis of supported and freestanding graphene: fundamental understanding of the reaction thermodynamics and kinetics on Cu

Paul Maurice Leidinger

Vollständiger Abdruck der von der Fakultät für Chemie der Technischen Universität München zur Erlangung des akademischen Grades eines

Doktors der Naturwissenschaften (Dr. rer. nat.)

genehmigten Dissertation.

Vorsitzender: Prof. Dr. Hubert A. Gasteiger

Prüfende der Dissertation:

1. Prof. Dr. Sebastian Günther
2. Prof. Dr. Joost Winterlin
3. Prof. Dr. Barbara Lechner

Die Dissertation wurde am 02.03.2022 bei der Technischen Universität München eingereicht und durch die Fakultät für Chemie am 25.04.2022 angenommen.

Eidesstattliche Erklärung

Ich erkläre an Eides statt, dass ich die bei der Fakultät für Chemie der TUM zur Promotionsprüfung vorgelegte Arbeit mit dem Titel: „Synthesis of supported and freestanding graphene: fundamental understanding of the reaction thermodynamics and kinetics on Cu“ in der Fakultät für Chemie in dem Zeitraum von Februar 2017 bis Februar 2022 unter Anleitung und Betreuung durch Prof. Sebastian Günther ohne sonstige Hilfe erstellt und bei der Abfassung nur die gemäß § 6 Abs. 6 und 7 Satz 2 angegebenen Hilfsmittel benutzt habe.

(Ort, Datum, Unterschrift)

Abstract

The systematic examination of 2D material growth processes requires the development of new analysis methodologies, which are acquired using graphene as model material. The goal of this work is the experimental identification of the relevant reaction parameters for the chemical vapor deposition (CVD) of methane on copper towards graphene and the subsequent determination of fundamental material properties.

The thermodynamic equilibrium of the graphene formation reaction is identified by exposing pre-grown graphene flakes to varying reaction conditions. The flakes' size evolution and shape change were used to identify the transition between graphene growth and decay. These indicators enable a precise determination of the thermodynamic equilibrium constant K_{eq} in dependence of the temperature T , leading to a reaction enthalpy of $\Delta_R H^\circ = 91.8 \pm 2.4 \text{ kJ mol}^{-1}$ and reaction entropy $\Delta_R S^\circ = 108.0 \pm 1.8 \text{ J mol}^{-1} \text{ K}^{-1}$.

Using the thermodynamic equilibrium as an anchoring point, it is possible to systematically analyze the kinetics of the graphene formation reaction. Experimental results were shown to coincide with the predictions from a graphene growth model assuming pre-equilibrated surface C_{ad} species. The predictions of the graphene flake evolution can be correctly applied to a large number of reported growth velocities from literature studies. Deduced from the experimental results, the C_{ad} surface concentration during reaction conditions can be estimated to a value of $10^{-10} - 10^{-8} \text{ ML}$. Using this understood parameter regime as a reference, it is possible to identify new growth conditions, in which the provided methane limits the growth rate of graphene flakes. With the precise knowledge of the graphene thermodynamic equilibrium and its offset regarding graphene on graphite, a certain parameter space with selective multilayer graphene growth is identified and also experimentally verified.

The nucleation process defines the density and growth starting time of the graphene flakes. Tracking the parameter-dependent nucleation density allows to identify heterogeneous nucleation as the main formation pathway in the used growth regime. A special nucleation behavior is observed far away from K_{eq} and at elevated pressures above $\approx 100 \text{ mbar}$.

Impurities present during growth, such as oxygen, silicon or secondary carbon sources influence the graphene quality, multilayer nucleation and potential decay during CVD treatment. The appearance and impact of these impurities is explored and specific ways are described to suppress their influence on the reaction outcome.

After synthesis, the post-growth modification and transfer from the growth substrate are crucial when using graphene for certain applications. Based on established transfer mechanisms, new recipes are developed, specifically tailored for the fabrication of ultrathin, pressurized, vacuum-compatible cells.

Zusammenfassung

Die systematische Untersuchung des Wachstumsprozesses von 2D-Materialien erfordert die Entwicklung neuer Analyse-Methodiken, welche anhand von Graphen erarbeitet werden. Ziel dieser Arbeit ist die experimentelle Identifikation der relevanten Wachstumsparameter für die chemische Gasphasenabscheidung (CVD) von Methan auf Kupfer zu Graphen und die darauf aufbauende Ermittlung grundlegender Materialeigenschaften.

Die Position des thermodynamischen Gleichgewichts der Graphenabscheidung (K_{eq}) wird ermittelt, indem vorgewachsene Grapheninseln variierenden Reaktionsbedingungen ausgesetzt werden. Die Größenentwicklung und Inselform werden dabei genutzt, um den Übergang von Graphenwachstum zu -zerfall zu identifizieren. Diese Indikatoren erlauben die genaue Bestimmung der Gleichgewichtskonstante K_{eq} in Abhängigkeit von der Temperatur T , was die Berechnung der Reaktionsenthalpie $\Delta_R H^\circ = 91.8 \pm 2.4 \text{ kJ mol}^{-1}$ und -entropie $\Delta_R S^\circ = 108.0 \pm 1.8 \text{ J mol}^{-1} \text{ K}^{-1}$ erlaubt.

Mit dem thermodynamischen Gleichgewicht als Ankerpunkt ist eine systematische Studie der CVD-Reaktionskinetik möglich. Die experimentellen Ergebnisse stimmen mit den Vorhersagen eines Wachstumsmodells überein, welches ein vorgelagertes Gleichgewicht der Methan-Zersetzungsreaktion bis zum adsorbierten Kohlenstoff C_{ad} annimmt. Das Modell wird erfolgreich auf experimentelle Literaturdaten aus diesem Wachstumsbereich angewandt. Abgeleitet von diesen Ergebnissen lässt sich die Kohlenstoffatombedeckung unter Reaktionsbedingungen auf $10^{-10} - 10^{-8} \text{ ML}$ abschätzen. Ausgehend von diesem, dem Modell folgenden, Wachstumsbereich werden Bedingungen identifiziert, bei denen der Methan-Eintrag das Inselwachstum als limitierender Schritt bestimmt.

Die Nukleation der Graphenkristalle bestimmt die Inseldichte und den Startzeitpunkt des Wachstumsprozesses auf der Unterlage. Systematische Untersuchungen der Parameterabhängigkeit der Nukleation führen zu dem Schluss, dass in dem untersuchten Wachstumsbereich heterogene Nukleation vorliegt. Das identifizierte Reaktionsgleichgewicht der Graphenabscheidungsreaktion auf Cu ist gegenüber dem der Graphitbildung verschoben. Damit lassen sich Reaktionsbedingungen für selektives Multilagenwachstum voraussagen, welche auch experimentell nachgewiesen werden.

Das Vorkommen und die Auswirkung von Verunreinigungen durch Sauerstoff, Silizium und sekundäre Kohlenstoffquellen wird untersucht und spezielle Reaktionswege werden erarbeitet, die deren Einfluss auf das experimentelle Ergebnis unterdrücken.

Nach der Graphensynthese sind weitere Behandlungsschritte für das Ablösen des Graphenfilms von der Wachstumsunterlage wichtig, um die Nutzung in einem breiten Anwendungsfeld zu ermöglichen. Dazu werden Verfahren entwickelt, die auf bekannten Transferprotokollen aufbauen und diese erweitern, mit dem Ziel der Erzeugung freitragender Graphenmembranen zur Abdeckung von vakuumkompatiblen Hochdruckzellen.

Contents

1	Introduction	9
2	Introduction to graphene.....	12
2.1	Properties of graphene.....	12
2.2	Properties of copper	13
2.3	General introduction to crystal nucleation and growth	15
2.4	Energetics of graphene on copper	19
3	Synthesis of graphene by chemical vapor deposition of methane on copper	25
3.1	Reactor-Setup	25
3.2	Graphene growth recipes	34
3.3	Characterisation techniques of graphene.....	36
3.4	Analysis and modification of grown graphene samples.....	49
4	Thermodynamics of the graphene formation reaction	57
4.1	Graphene decay in the reactive gas atmosphere of $CH_4 + H_2$	57
4.2	Determination of the thermodynamic equilibrium constant K_{eq}	60
5	Growth kinetics	74
5.1	Modelling of graphene growth on copper.....	74
5.2	Presentation of the current graphene growth model.....	76
5.3	Verification of the time independency of $v(t) = dr/dt$	80
5.4	Graphene growth at conditions leading to equal Q_{exp} -values	82
5.5	Fitting the unknown reaction parameters $\Delta_{dec}S^\circ$ and E_{det} to experimental data.	83
5.6	Experimental exploration of the decay term in the kinetic model	90
5.7	Evaluation of the literature graphene growth coincidence with the proposed growth model.....	92
5.8	Growth velocities observed at deficient gas phase supply.....	98
6	Understanding and controlling the nucleation of graphene flakes.....	108
6.1	Distinguishing between homogeneous and heterogeneous nucleation.....	116
6.2	Graphene nucleation dependence on the temperature and Q_{exp}	118
6.3	Evaluation of several performed experiments regarding their nucleation behavior.....	120
6.4	Nucleation conditions at high pressures.....	123
6.5	CVD synthesis strategies with control of the flake nucleation.....	125
7	Selective growth of multilayer graphene flakes.....	128
7.1	Experimental verification of simultaneous growth and decay of graphene with different layer numbers	129
7.2	Approaches to receive large areas of multilayer graphene	131

8	Etching of graphene by oxygen	142
8.1	Graphene decay experiments reported in literature	142
8.2	Influence of oxygen impurities in the CVD-atmosphere.....	149
9	Contaminations influencing the CVD growth of graphene and the character- istics of grown graphene samples.....	153
9.1	Silicon contaminations	153
9.2	Carbon contaminations.....	173
10	Graphene transfer methods	184
10.1	Enhanced treatment steps required for the transfer of graphene layers	186
10.2	Formation of artificial stacks of multiple graphene membranes	190
10.3	Combination of patterned materials with a continuous graphene layer.....	193
10.4	Selective transfer of ideal sample areas to single hole apertures.....	199
11	Summary and Conclusions.....	202
12	Appendix.....	206
12.1	Calibration of the XPS signal ratio C/Cu for SLG.....	206
12.2	Derivation of the correlation between the carbon coverage and the configura- tional entropy S_{config}	215
12.3	Correlation between the oxygen sticking and the etching rate of a hexagonal hole	219
12.4	Estimation of the Area of Capture from the limiting growth velocity and the adsorbed methane	221
13	List of Experiments.....	223

1. Introduction

A large number of chemical compounds has been found that can be assigned to the group of 2D-materials. Starting with the discovery of graphene in 2004,¹ the field has since been extended by a large number of newly detected compounds,² several more candidates are predicted and await their experimental verification.^{3,4} Additionally, the formation of van der Waals heterostructures composed by stacked 2D materials creates an almost endless amount of possible ultrathin structures with customized properties, such as topological insulators, semiconductors, insulators, semimetals or metals.⁵ Several scientific milestones regarding 2D-materials and especially graphene have been achieved in recent years,⁶ paving the way for this broad research field, combining the specialized knowledge of, among others, chemists, physicists, biologists and material scientists.

This quick development of a new material category also required the simultaneous adaptation of synthesis, characterization and treatment techniques. While the first scotch-tape synthesis method led to the proof of existence and subsequently to the awarding of the Nobel-prize, the proposed synthesis routes since then span from the wet-chemical reduction of graphene oxide sheets^{7,8} over the decomposition of SiC,⁹ the epitaxial growth on metals in UHV setups^{10,11,12} to the decomposition of carbon precursors on metal surfaces by chemical vapor deposition (CVD).¹³ While successful graphene growth has been shown on several metal surfaces,^{14,15} special attention is turned to the CVD growth of graphene on copper surfaces using methane as a precursor molecule, as a large fraction of the current scientific research is performed on this system. Due to the low solubility of carbon in Cu,¹⁶ graphene formation with high precision and an approximately self-limiting growth after a continuous graphene layer formation is possible.^{17,18} The synthesis by CVD in relative proximity to thermodynamic equilibrium allows the formation of high-quality graphene¹⁹ with large domain sizes^{20,21,22,23} in ideal hexagonal shape²⁴ combined with high reaction rates^{25,26,27,28} and the omitted need for an ultra-high vacuum reactor setup, allowing the scaling to industrial production rates.^{29,30} The control over the substrate Cu foil in the meantime also allows the *in situ* recrystallization to a single-crystalline substrate foil.^{31,32}

The traditional characterization techniques for surface structures are mainly UHV-based, particularly surface sensitive methods, such as X-ray photoelectron spectroscopy (XPS), Low energy electron diffraction and microscopy (LEED/LEEM) or scanning tunneling microscopy (STM). The appearance of surface-like 2D materials, stable at common laboratory air conditions, has profited strongly from these techniques. But through the enormous growth of this research area, non-destructive methods with higher throughput, lower costs and easier availability were needed and developed. The standard characterization methods for assessment of graphene samples have shown to be Raman spec-

troscopy,^{33,34} Scanning electron microscopy,^{35,36} optical microscopy,³⁷ and conductivity measurements,^{38,39} as they offer fast insight into the characteristics of grown samples. Nevertheless, the results from these measurement techniques often depend on several sample parameters simultaneously, which must be considered in the analysis. In this way, the Raman spectrum of a graphene layer is for example highly dependent on the sample substrate,^{40,41,16} layer number,³³ interlayer rotation,^{42,43,44} defect density,^{45,46,47} tensile strain,⁴⁸ electronic doping,⁴⁹ intercalating species,⁵⁰ laser wavelength,⁴⁷ edge structure^{51,52} and sample age.⁵³

Simultaneously with the knowledge about graphene, the number of possible applications is growing continuously. These can roughly be divided into applications using the electronic properties of graphene and the ones exploiting its mechanical properties. In the first category, bandgap-engineered bilayer electronic switching devices,⁵⁴ ultracapacitors,⁵⁵ ultrafast photodetectors,⁵⁶ superconductive devices⁵⁷ and light-emitting diodes (LED)⁵⁸ can be named exemplarily. Setups included in the latter group are for example leak-tight gas cells,^{59,19,60} semipermeable membranes (e.g. for water desalination,^{61,62} proton conductivity,⁶³ gas separation,⁶⁴ battery electrodes,^{65,66} corrosion protection⁶⁷ or conservation of organic cells⁶⁸).

For all these applications, a high degree of control over the graphene growth process is required, but equally important is the post-growth modification of the synthesized graphene sheets. The correct transfer mechanism after the growth process allows the combination of graphene with arbitrary materials⁶⁹ and the formation of lateral heterostructures⁷⁰ and large freestanding membranes.^{71,72} A large number of treatments have been proposed to achieve this transfer while retaining graphene quality and purity, but also several subsequent cleaning procedures have been described in literature.^{73,74}

The main focus of this thesis lies in the understanding and control of the graphene growth mechanism by decomposition of methane on copper and the subsequent transfer to create freestanding graphene membranes.

A short summary of the properties and energetics of graphene is given in section 2. In chapter 3 a thorough description of the used reactor setup and reactants is presented to allow the correct interpretation of all experimental results. In chapter 4, the thermodynamic equilibrium conditions for graphene formation by methane decomposition on copper are determined. Based on the knowledge of the thermodynamic equilibrium position, it becomes possible to establish a detailed growth model in chapter 5, which is capable to correctly predict the graphene growth rates over a large parameter space of the CVD process. Using this correctly described parameter space as an anchoring point, it is possible to determine the limitations of the model and expand it thereupon, which is exemplarily done regarding the methane partial pressure in section 5.8. Using these findings allows to correctly estimate the growth rates of most literature references. Chapter 6 focusses on the nucleation of graphene islands. Several relevant parameters are identified

as key points in order to control the amount of formed graphene flakes and the time of nuclei formation. The precise pinpointing of growth and decay processes results in the identification of a new, intermediate growth regime regarding the formation of multilayer graphene samples, which is experimentally explored in chapter 7. The specific influence and parameter dependence of oxygen impurities on graphene growth are discussed in chapter 8, silicon and carbon based impurities are analyzed in chapter 9. Lastly, the *ex situ* transfer of the synthesized graphene films to create freestanding graphene membranes is the topic of chapter 10.

2. Introduction to graphene

2.1. Properties of graphene

Graphene consists of a 2-dimensional lattice of sp^2 -hybridized carbon atoms in a hexagonal honeycomb structure with two atoms per unit cell, as illustrated in Fig. 1. Each atom is connected to three neighbors by σ -bonds with a bond length of 1.42 \AA , while the remaining valence electron forms a delocalized π -orbital, leading to the completely filled valence band. Due to a special electron dispersion relation in single layer graphene the

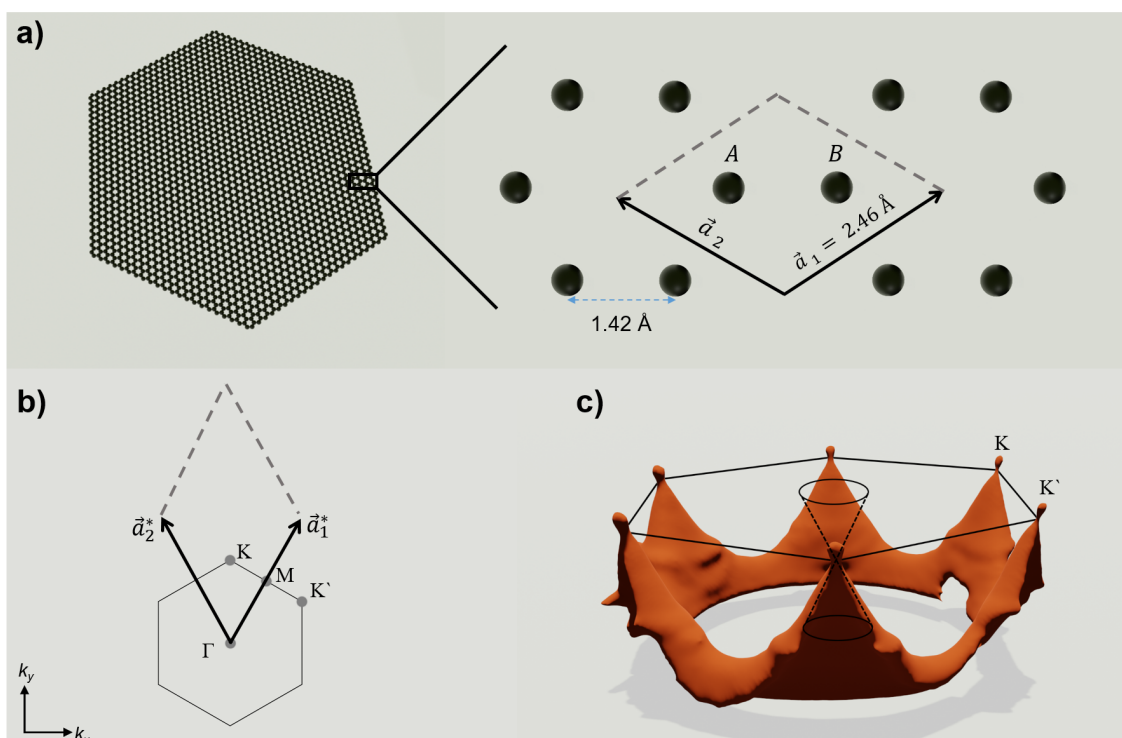


Figure 1 : Graphene in real and reciprocal space. a) Real space representation of carbon atoms forming a graphene flake. The magnification shows the unit cell of graphene. b) Reciprocal space representation of the first Brillouin zone with marked reciprocal space vectors and high symmetry points. c) Electronic structure of graphene in reciprocal space as measured by angular resolved photoelectron spectroscopy (ARPES, stylized 3D model, unpublished), including the (marked) Dirac cone with a linear electronic dispersion around the K and K'-points.

full valence band and empty conduction band meet at the Fermi level at a vanishing density of states and without band gap, which constitutes the semi-metallic characteristics of the material. Around the K- and K'-points in reciprocal space (see Fig. 1b-c) the band structure shows a linear dispersion, referred to as Dirac cone, around which the electrons behave like massless Dirac fermions.⁷⁵ As for bilayer graphene, a double cone electronic structure forms⁷⁶ with or without a band gap depending on the interlayer rotation⁵⁴ and

the gate voltage.^{77,78}

The electronic structure leads to a high carrier mobility,³⁹ zero-field conductivity⁷⁹ and even superconductivity (found in rotated bilayer graphene).⁵⁷ The high thermal conductivity of about $5 \times 10^3 \text{ W mK}^{-1}$ is even larger than that of diamond.⁸⁰

Following the two carbon atoms in the unit cell of graphene, there are six possible phonon branches, shown in Fig. 2. These are categorized as acoustic (A) or optical (O), in-(i) or out-of-plane (o) and longitudinal (L) or transverse (T). The strong σ -bonds in the

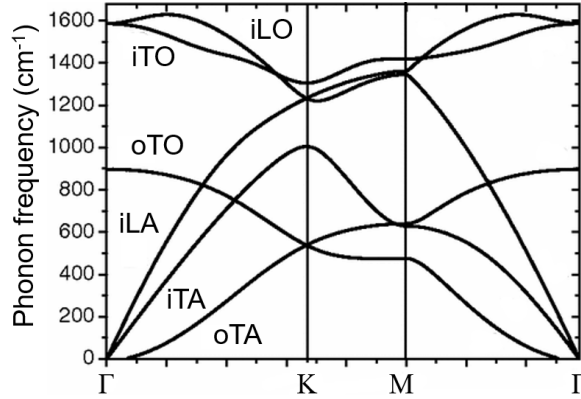


Figure 2 : Reduced representation of the phonon dispersion of graphene along high-symmetry lines. Graphene has six phonon branches, including three optical (O) and three acoustical (A) phonons. Adapted from reference⁸¹. Copyright 2008 American Physical Society.

graphene layer lead to a Young's modulus of 1 terapascal and intrinsic strength of 130 gigapascals.⁸² This impressive material strength enables the fabrication of freestanding graphene membranes suspended over extended apertures^{71,72} and exposed to high physical strains.^{82,83,84} The combination of this property with the fact that pristine graphene is impermeable to all gases⁸⁵ and shows a high adhesion to substrate surfaces through van der Waals-interactions⁸⁶ allows the production of gas-tight atmospheric pressure cells compatible with ultra-high vacuum setups.^{87,59,60} With an atomically thin separating membrane, it is possible to use surface-sensitive analytical techniques on samples under environmental conditions.⁵⁹ The electron transmission can be calculated using the known values of the three-dimensional equivalents,⁸⁸ while the optical transmission is defined by the fine structure constant α .⁸⁹

2.2. Properties of copper

Graphene is grown on a copper substrate, a transition metal with the atomic number $Z = 29$, an atomic mass of $m_{Cu} = 63.5 u$ and a face-centered cubic (fcc) crystal structure. The surface during reaction is mostly Cu(111)-textured. Fig. 3 displays the geometry of

a Cu(111) surface. Four high symmetry surface adsorption sites exist for this surface: the adsorption directly on the metal atom (top), between two atoms (bridge) or in the cavity between three Cu atoms. If in the second atomic layer this site is occupied by a Cu atom it is referred to as hcp-type, if it is occupied in the third row as fcc-type hollow adsorption site. The atomic distance on the Cu(111)-surface is of $a_{Cu} = 2.56 \text{ \AA}$, leading to a unit cell size of $A_{Cu} = (2.56 \text{ \AA})^2 * \sin(120^\circ) = 5.66 \text{ \AA}^2$ and an atomic density of $N_{Cu} = 1.77 \times 10^{19} m^{-2}$. The interlayer distance between Cu layers is 2.09 \AA .

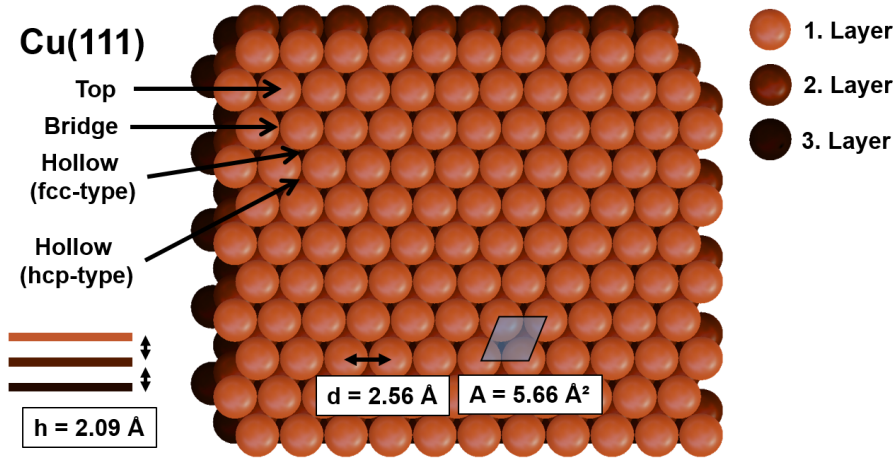


Figure 3 : Sketch of the Cu(111) surface and the two lower atomic layers stacked in the ABC-type of the fcc crystal structure. Possible adsorption sites are marked with arrows, the atomic distance and unit cell of the Cu(111) surface are marked in the figure.

Copper has the electron configuration $[Ar]3d^{10}4s^1$. The completely filled d-band lies energetically below the Fermi level. The density of states (DOS) at the Fermi level is therefore comparatively low,^{90,91,92} which reduces the electronic interaction between copper and possible adsorbates.⁹³

2.2.1. Interaction between Cu and graphene

At room temperature, the lattice mismatch between Cu(111) and graphene is approximately 4%. This value is even larger at growth conditions of $1045 \text{ }^\circ\text{C}$, as Cu expands by 1-2% over the temperature increase by $1000 \text{ }^\circ\text{C}$.⁹⁴ The thermal expansion coefficient of freestanding graphene is significantly lower and may in a certain temperature range even be negative.^{95,96,97} At room temperature, graphene islands aligned with the Cu(111) substrate (0° rotation angle) show a moiré pattern with $\approx 6 \text{ nm}$ length,⁹⁸ corresponding to approximately 25 graphene unit cell lengths. During cooling of the sample after the growth experiment, the thermal contraction of the Cu substrate induces strain in the graphene layer. This strain might be released by two mechanisms. The graphene-covered

Cu tends to form parallel facets, which increase the effective Cu surface, as sketched in Fig. 4.¹⁹ The graphene can adapt according to the facet structure, reducing the acting strain in this direction. Graphene exposed to high compressive strain can form wrinkles in the graphene layer to reduce the acting strain (right image in Fig. 4).^{99,100} Even though both Cu and graphene have hexagonal structure, the wrinkles often appear in perpendicular direction to the Cu facets.¹⁰¹

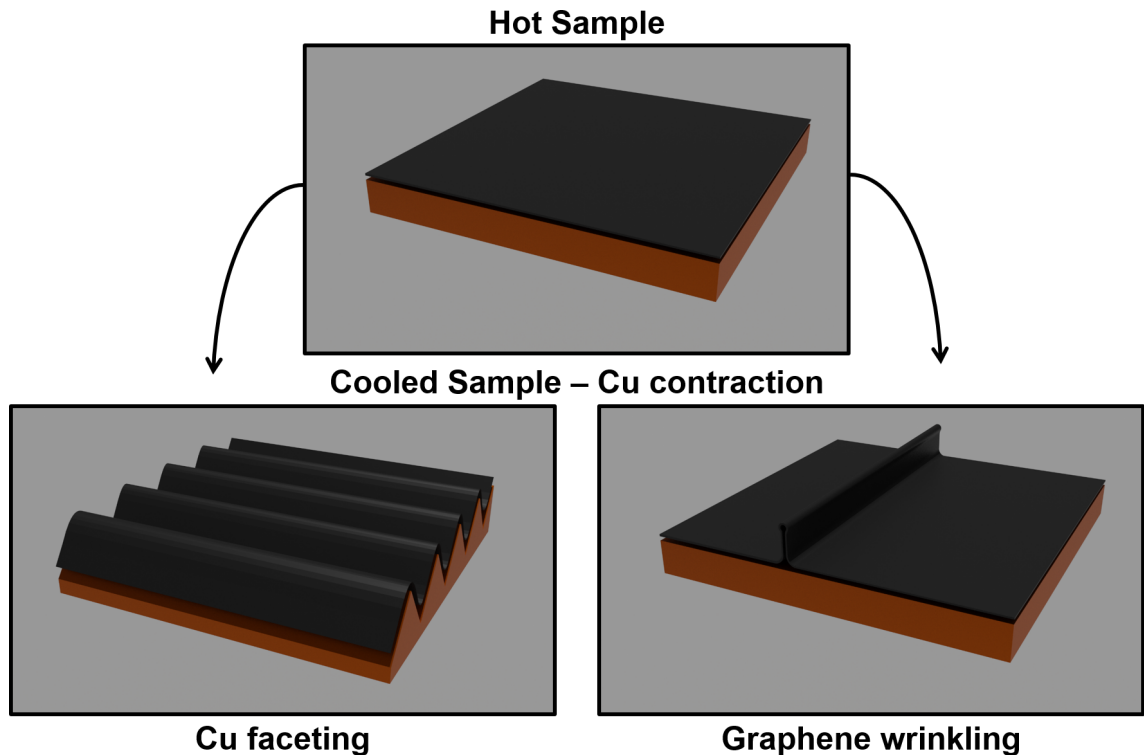


Figure 4 : Sketches of a graphene layer grown on Cu in the hot synthesis condition and the modifications appearing after cooling of the sample to room temperature. Due to the much lower thermal expansion coefficient of graphene compared to Cu, the contracting Cu forms facets to increase its surface area. In a second possible relaxation, the graphene layer folds and forms wrinkles to compensate for the Cu contraction. Both processes appear simultaneously in graphene on Cu.

2.3. General introduction to crystal nucleation and growth

2.3.1. Crystal nucleation

The classical formation of new 3-dimensional crystals from solution starts with the agglomeration of several individual crystal components in the crystal geometry. This crystal seed consisting of few atoms has a very high surface-to-volume ratio and is at first thermodynamically unstable.¹⁰² In the case of CVD growth of graphene, 2-dim crystals are grown from a gas phase reaction, in our case by methane decomposition over Cu. Although the growth process does not take place from a fluid but rather on a heterogeneous

catalyst (the Cu foil) the same growth concept can be applied. Its scaling relation is slightly different with respect to the formation of 3-dim crystals due to the 2-dim nature of the graphene islands (so-called flakes).

Only if the initial crystal nucleus reaches a certain size defined by the free energy Δg , the exergonic growth sets in. The free energy Δg indicates the difference between the free energy of the precursor molecule and the mean free energy of the atoms in the nucleus. This latter value is defined by two quantities:

- The atoms in the crystal bulk have saturated bonds/coordination and are more stable than the precursor pendant. The bulk free energy Δg_{Bulk} is negative and scales with r_{Nuc}^2 for 2D-materials, as shown in Fig. 5.
- The atoms on the crystal rim have unsaturated bonds and are unstable compared to the precursor. The free energy of the rim atoms Δg_{Rim} is positive and scales as the crystal circumference with r_{Nuc}^1 .

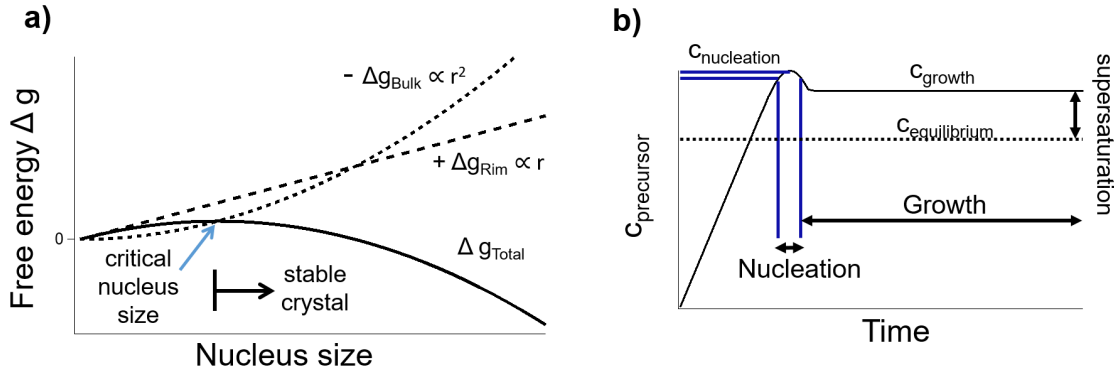


Figure 5 : a) Free energy Δg of a 2D seed as a function of the seed size. Δg is composed of the stabilizing effect from the bulk atoms, scaling with r^2 and the destabilizing effect of the rim atoms, scaling with r . At a certain critical nucleus size the bulk effect prevails and the total free energy Δg decreases with nucleus size. b) Precursor concentration $c_{precursor}$ as a function of time for an experiment with constant precursor addition to the sample. $c_{precursor}$ increases linearly, until reaching a certain supersaturation required for the formation of stable nuclei, $c_{nucleation}$. The formed nuclei reduce the precursor concentration until a steady-state situation is reached, labeled c_{growth} .

The sum of Δg_{Bulk} and Δg_{Rim} leads to the total free energy of the crystal, Δg_{Total} , which is also inserted in Fig. 5. While Δg_{Total} increases at first, indicating thermodynamic instability, it reaches a maximum value at a certain nucleus size referred to as the critical nucleus size. After reaching this critical size, the integration of further molecules to the crystal becomes exergonic and the nucleus is stable.

The correlation between the crystal nucleation and the concentration of the precursor, $c_{precursor}$ can well be identified for a physical vapor deposition (PVD) experiment where the precursor for a 2D crystal is continuously dosed onto a surface without backreaction to the gas phase (Fig. 5b). At first, $c_{precursor}$ increases linearly, passing the equilibrium

concentration $c_{equilibrium}$ of the bulk crystal without nucleation. To form the stable nucleation seeds, a certain supersaturation $c_{nucleation}$ is needed on the surface. After reaching this supersaturation, crystal seeds start to form on the surface and continuously integrate precursor particles into the crystal lattice. This process removes precursor particles from the surface, and a constant precursor concentration c_{growth} on the surface is reached. As $c_{equilibrium} < c_{growth} < c_{nucleation}$, no new nuclei form in this growth stage, but the present crystals grow in size. In the described model experiment, this stage is only stopped if the dosing of the precursor is stopped.

The different reaction pathways between the model PVD system without backreaction (as can be for example expected for the evaporation of a metal onto a metal surface in UHV) and the CVD growth system for graphene are sketched in Fig. 6. The nucleation conditions for this CVD reaction with a possible backreaction from the surface to the gas phase are in detail analyzed in chapter 6.

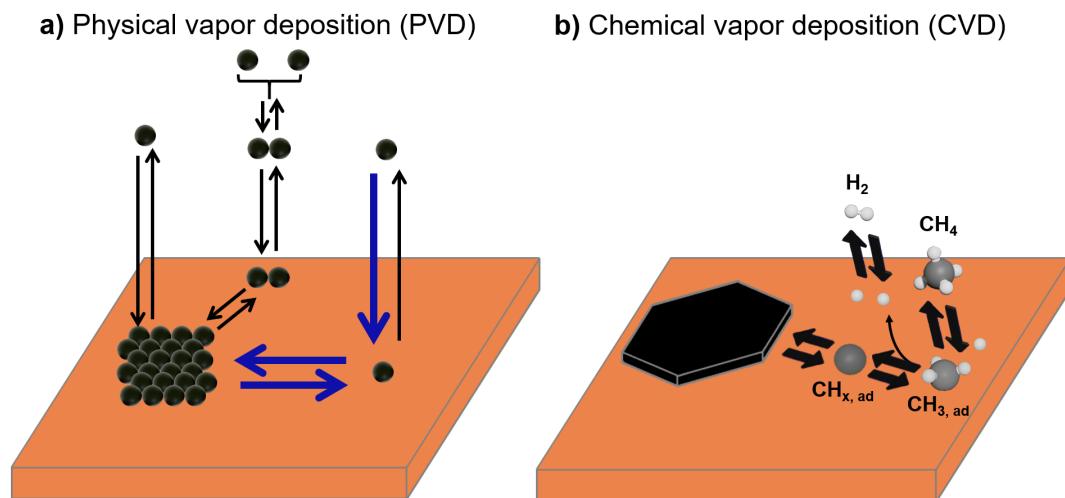


Figure 6 : Reaction pathways for PVD and CVD. a) For PVD, the precursor is directly condensed on the substrate. The main reactions in a PVD experiment (e.g. metal evaporation on a metal substrate in UHV) leading to the nucleation schemes of Fig. 5 are marked in blue. b) For CVD, the mechanism contains a chemical reaction, which in the case of graphene growth allows the backwards reaction of graphene-type carbon to the methane precursor. The sketch is restricted to the relevant pathways for the graphene CVD growth reaction.

The nucleation site: In the case of a pristine substrate, the nuclei appear statistically distributed over the whole surface, formed by statistical inhomogeneities in the concentration. This is referred to as homogeneous nucleation.

The surface often contains imperfections, such as step edges, crystal lattice defects or contaminations of a foreign species. These can form bonds to the unsaturated rim atoms of the seed, lowering Δg_{Rim} and Δg_{Total} , the critical nucleus size will then shift to a lower value of r and favor the crystal nucleation. This process is called heterogeneous nucle-

ation and requires a lower supersaturation of the precursor compared to homogeneous nucleation, but it will only appear localized at the positions of the imperfections.

2.3.2. Graphene crystal growth in a CVD reaction

In chemical vapor deposition (CVD) growth of graphene, different precursor molecules have been proposed as carbon source for the growth process. Besides methane, which is mostly used, graphene growth has been reported by using gases such as ethylene,¹⁰³ hexane,¹⁰⁴ benzene¹⁰⁵ and acetylene,¹⁰⁶ but also evaporated solid sources can be used as carbon precursor, such as polystyrene,¹⁰⁷ camphor,¹⁰⁸ paraffinic oil¹⁰⁹ or even waste plastic.¹¹⁰ Growth without any actively provided precursor from impurities and back-diffusion from a vacuum pump¹¹¹ or the impurities from the substrate foil¹¹² has also been reported, which highlights the importance of a clean reactor environment to quantitatively understand the graphene growth process. While the first CVD growth recipes using methane as a precursor molecule used no further reactive gases,^{13,113,114,115} it soon became evident that the addition of hydrogen to the gas phase allowed a more controlled and qualitatively higher synthesis of graphene, as the adsorbed hydrogen on the surface acts as a cocatalyst for the intermediate dehydrogenation reactions and enables the etching of carbon atoms from the graphene rim.¹¹⁶ This activates the backreaction of the overall methane decomposition reaction towards graphene, shown in eq. 2.1, which is otherwise inhibited by the recombination and desorption of released hydrogen atoms from the methane dehydrogenation process into the gas phase and reactor exhaust.



Despite the simple reaction equation 2.1, the hydrogen abstractions from methane proceed stepwise on the Cu surface as intermediate reaction steps. The different C_xH_y species appearing on the surface and the energetic barriers defining their abundance and diffusivity are the topic of discussion, which are compiled in chapter 2.4 (Table 1). Due to the large parameter regime for the CVD growth of graphene on copper, spanning over temperatures from 900 °C¹¹⁷ to 1120 °C,¹¹⁸ methane partial pressures between 2×10^{-4} mbar¹¹⁹ and 120 mbar¹²⁰ and hydrogen partial pressures between 0 and 500 mbar,¹²¹ the reaction rates on the sample may be controlled by different processes in specific cases. A hint towards which process is rate-limiting can be monitored by the different graphene crystal shapes resulting from different growth approaches. In addition to the formation of thermodynamically stable hexagonally shaped graphene islands, CVD growth on Cu has led to flower/star shaped flakes,¹²² quadratic flakes,¹²³ 2-lobed¹²⁴ and 4-lobed flakes¹²⁵ with either smooth¹²⁶ or dendritic rim.¹²⁷

2.4. Energetics of graphene on copper

The formation of graphene on Cu by decomposition of methane has been the basis of several theoretical studies. Therefore, a large number of different energetic calculations is available. The single reaction steps for the methane dehydrogenation and surface reaction to graphene and gaseous hydrogen are graphically presented in an energy diagram in Fig. 7.

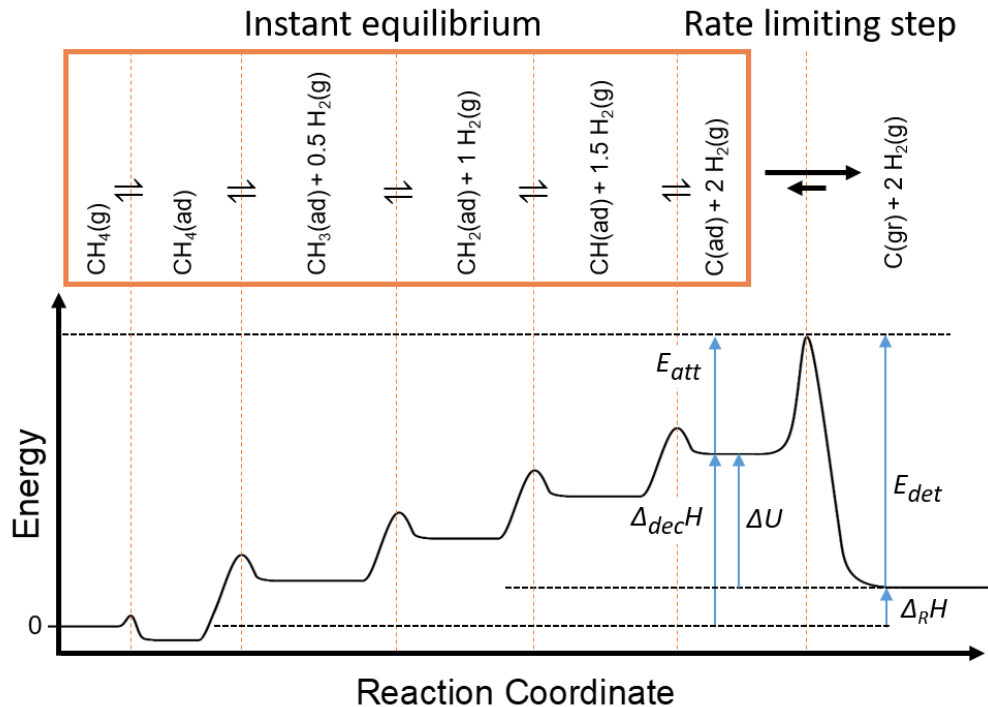


Figure 7 : Energy diagram of the single reaction steps leading from gaseous methane to graphene. The pure adsorption energy of methane on Cu is very low and commonly neglected, the first reaction step is mostly described as a dissociative adsorption, followed by dehydrogenation steps until reaching adsorbed atomic carbon, which can then be attached to a graphene edge in the last reaction step. The energetic barriers relevant for the presented experiments are marked with arrows, while all other steps are only shown schematically. The justification for this presentation is given in chapter 5. Reprinted with permission from reference ¹²⁸ . Copyright 2021 American Chemical Society.

The reaction of methane towards graphene and gaseous hydrogen begins with the dissociative adsorption on the catalytic substrate, in this case the Cu(111) surface. The non-dissociative adsorption of CH_4 is associated with an almost negligible energy difference^{137,145} and therefore mainly neglected at high temperatures. The dissociative sticking coefficient of CH_4 on Cu was measured by Alstrup *et al.*¹⁶³ to be $S_0 = 8.6 \times 10^{-9}$ on Cu(100) at 1000 K. Temperature-dependent chemisorption allowed to extract an activation energy of 201 kJ/mol which can be used to extrapolate the sticking coefficient at arbitrary temperatures. At common reaction temperatures for graphene growth between 900-1085 °C this leads to values of $S_0 = 3 \times 10^{-7} - 5 \times 10^{-6}$, respectively.

Table 1 : Summary of several relevant reported energetic values for the modelling of graphene formation on Cu from methane. All values except ref.¹²⁹ refer to calculated and not experimentally measured values. All values in eV.

	Nist ¹²⁹	Gajewski ¹³⁰	Li ¹³¹	Zhang ¹³²	Galea ¹³³	Liu ¹³⁴	Wang ¹³⁵	Various references		
$\Delta_f H [CH_4](1045^\circ C)$	0.954									
$CH_4 \rightleftharpoons CH_3 + H_{ad}(GS^*)$		0.75	0.94	0.79	0.99		0.89	0.41 ¹³⁶		
TS^*		1.57	1.63	1.77	1.94	1.88	1.56	1.31 ¹³⁶	1.95 ¹³³	1.12 ¹³⁷
$CH_3 \rightleftharpoons CH_2 + H_{ad}(GS^*)$		0.83	0.85	0.83	0.95		0.9	0.73 ¹³⁶		
TS^*		1.36	1.53	1.53	1.42	1.47	1.39	1.26 ¹³⁶		
$CH_2 \rightleftharpoons CH + H_{ad}(GS^*)$		0.41	0.48	0.48	0.47		0.61	0.53 ¹³⁶		
TS^*		0.94	1.13	1.13	1.16	1.05	1	0.93 ¹³⁶		
$CH \rightleftharpoons C_{ad} + H_{ad}(GS^*)$		1.22	0.85	1.48	1.33		1.24	1.57 ¹³⁶		
TS^*		1.84	1.65	1.97	2.11	2.21	1.87	1.97 ¹³⁶		
$C_{ad} \rightleftharpoons C_{gr}(GS^*)$			-2.1	-3.01				-0.69 ¹³⁸	-2.9 ¹³⁹	
TS^*								0.94 ¹³⁸	1.17 ¹⁴⁰	2.6 ¹⁴¹
$C_{ad} \rightleftharpoons C_{2,ad}$		-1.5	-1.25					-1.8 ¹³⁸		
TS^*		1.22	0.25					0.77 ¹³⁸	0.3 ¹⁴⁰	0.32 ¹⁴²
$C_{vac} \rightleftharpoons C_{gr}$										
Cu(111)				-7.86				-7.40 ¹⁴³		
Graphite	-7.45									
Vacuum								-7.94 ¹⁴²		
$C_{vac} \rightleftharpoons C_{ad}$										
Cu(111)		-5.11		-4.85		-5.38		-5.66 -	-4.90 ^{142, 144, 145, 146, 147, 148}	
Graphite										
$C_{gr,vac} \rightleftharpoons C_{gr,M}$										
Cu(111)								-0.035 ¹⁴⁹	-0.030 ¹⁵⁰	-0.065 ¹⁵¹
Graphite								-0.0474 ¹⁵²	-0.054 ¹⁵³	-0.044 ¹⁵⁴
<i>DiffusionBarrierCu(111)</i>										
Monomer			0.5					0.06 ¹⁴⁴	0.3 ¹⁵⁵	0.07 ¹⁵⁶
Dimer			0.49					0.44 ¹⁴⁴	0.49 ¹⁴⁰	0.5 ¹⁵⁶
$C_{gr,M}(bondlength)$								3.21Å ¹⁴⁹	2.96 Å ^{150, 157}	0.294 ¹⁵⁸
<i>Edgefreeenergy(eV/nm)</i>										
ZZ								5.52 ¹⁵⁹		
AC								7.38 ¹⁵⁹		
$H_2 \rightleftharpoons 2H_{vac}$	4.50									
$H_{vac} \rightleftharpoons H_{ad}$		-2.50				-2.51		-2.51 -	-2.12 ^{160, 133, 137, 148, 161, 162}	

This is in fairly well agreement with calculated values for the sticking coefficient on Cu(111) of $S_0 = 1.1 \times 10^{-7}$ at 1027 °C.¹³¹

The dehydrogenation reactions of CH_x on Cu have been studied by several groups, the summarized results are listed in Table 1. All dehydrogenation steps are determined to be endothermic on copper, where the last step towards adsorbed carbon C_{ad} is connected to the highest activation energy of 1.65-2.21 eV. The first two dehydrogenation steps have also been determined experimentally by iodomethane decomposition on Cu(110), leading to similar results.¹⁶⁰ The total energy necessary for the complete dehydrogenation is between 3.12 eV (Li *et al*¹³¹) and 3.74 eV (Liu *et al*¹³⁴). Gajewski *et al*¹³⁰ and Li *et al*¹³¹ also determined the formation energy of carbon dimers, which is exothermic (-1.50 eV and -1.25 eV, respectively) and should therefore be considered if the carbon coverage is high enough to enable C_{ad} collisions.

The attachment of C_{ad} to an existing graphene flake is strongly exothermic, with values ranging between -2.1 eV¹³¹ and -3.0 eV.¹³² The activation energy of this attachment step is calculated to be ≈ 1 eV.^{138,140} Theoretical calculations usually quantify the binding energy to a substrate by referencing it to the respective structure in vacuum, allowing the relative comparison to different substrate materials. As most tabulated values exist for graphite (which can be considered as graphene on graphite), these values are also added in Table 1. The adsorption of a single carbon atom onto a Cu(111) surface releases 4.85-5.38 eV. The direct formation of graphene from atomic carbon additionally releases the energy difference between C_{ad} and C_{gr} of 2-3 eV.

Here, the limits in absolute accuracy of the theoretical calculations become apparent, as the calculated energy of formation of freestanding graphene (calculated by Chen *et al*¹⁴² to be -7.94 eV) is larger than the ones for graphene on Cu(111) (-7.86 eV,¹³² -7.40 eV¹⁴³) or graphite (-7.45 eV¹²⁹). Actually, the difference between both energy values should only be the energy of adhesion, which is in both cases below 0.1 eV, as also listed in Table 1.

The reference system for the graphene formation reaction is usually the gaseous components, as shown in eq. 2.1. In this reaction, the transformation of adsorbed hydrogen to the product of gaseous H_2 species requires the knowledge of the H_{ad} desorption enthalpy, which was calculated by several groups to be between 2.12-2.51 eV. The dissociation energy of 4.5 eV is then set free when creating molecular hydrogen out of two hydrogen atoms.

The carbon diffusion on the Cu(111) surface yields very different values in theoretical calculations. The values used for calculations in this work are the ones reported by Wu *et al* (0.06 eV)¹⁴⁴ and Yazyev *et al* (0.07 eV).¹⁵⁶ The diffusion of a carbon dimer increases this diffusion barrier by about one order of magnitude.^{131,156} The interlayer distance between Cu(111) and a single graphene layer is calculated to be approx. 3 Å. The calculated lower edge free energy of zigzag (zz) edges compared to armchair (ac)

termination¹⁵⁹ correlates with the experimental results that yield mostly zigzag edges of graphene flakes grown on Cu.^{52, 116, 164, 165} While these calculated energies are valid for freestanding graphene flakes, several studies suggest that under reaction conditions the rim atoms of the graphene flakes are bound to hydrogen atoms,^{159, 166, 131} substrate atoms.^{159, 165, 166} or sunk in the Cu surface.¹⁶⁷

2.4.1. Estimation of $c[H_{ad}]$ on copper

Several studies have calculated the energetics of hydrogen adsorption on copper. While the dissociation of hydrogen molecules requires 4.50 eV, the adsorption per hydrogen atom on the Cu(111) surface releases ≈ 2.5 eV, leading to an absolute exothermic reaction for the dissociative hydrogen adsorption on Cu(111) with $\Delta H(H_2 \rightarrow 2H_{ad}) \approx -0.5$ eV. To assess the surface concentration of hydrogen on the copper surface in equilibrium at high temperatures, additionally to the adsorption energy the preexponential factors of adsorption and desorption need to be known. The adsorption rate with respect to the relative coverage of surface adsorption sites can be estimated by eq. 2.2:¹⁶⁸

$$\frac{d\theta_{ads}}{dt} = x_i * \frac{p}{N_{Cu}\sqrt{2\pi k_B T m}} S(\theta) * e^{\frac{-E_{ads}}{k_B T}} \quad (2.2)$$

In this equation, m , p and T refer to the molecular mass, partial pressure and temperature of H_2 . The factor x_i is added for the case of dissociative adsorption, as a single adsorption event creates two adsorbed particles. N_{Cu} refers to the total amount of adsorption sites on the sample, $S(\theta)$ is a coverage-dependent sticking factor, which in the case of low coverage can be neglected. The exponential term refers to the probability of a particle sticking after the impingement on the surface. The activation energy E_{ads} of 0.62 eV for hydrogen dissociative adsorption¹⁶⁹ leads to a sticking at 0.4 % of all impingement events (1045 °C).

The detachment rate on the other hand depends on the surface coverage θ^q , where q is the amount of surface adsorbates desorbing as a single molecule and the detachment energy E_{des} , leading to eq. 2.3:¹⁶⁸

$$\frac{d\theta_{des}}{dt} = -x_i * v_{des} * \theta^q * e^{\frac{-E_{des}}{k_B T}} \quad (2.3)$$

v_{des} is the pre-exponential factor, which was estimated to be $\approx 3 \times 10^{11} s^{-1}$ by Wilmer *et al*¹⁷⁰ and Genger *et al*¹⁷¹ on a catalyst similar to Cu(111). The desorption enthalpy was determined by Anger *et al*¹⁷² to be $E_{des} = 0.78$ eV. In the case of high H_2 pressures, the surface can be assumed to be in equilibrium with the gas phase, leading to equalized ad- and desorption rates. In this situation, the hydrogen surface coverage can be estimated. At typical reaction conditions ($p_{H_2} = 20$ mbar, $T = 1045$ °C), ϑ_H amounts to roughly 1% ML. Similar calculations have been performed by Kim *et al* and J. Kraus.^{173, 174}

2.4.2. Estimation of $c[O_{ad}]$ on copper

Oxygen appears as a contaminant in the used reaction gases and is introduced into the reaction system through leakages, as will be discussed in chapter 9. The dissociative sticking of O_2 on the Cu surface has an activation energy of $E_{ads} \approx 0.1 - 0.2 \text{ eV}$,^{175,176,177,178,179} significantly lower compared to H_2/Cu , which is why molecular oxygen can be dosed to Cu(111) even at temperatures of 100 K.⁹² At graphene growth conditions the surface can be assumed to be in equilibrium with the hydrogen gas phase, followingly the adsorbed oxygen is bound to react quite fast with H_{ad} and desorb from the surface. Assuming that an adsorbed oxygen atom on the Cu surface will effectively be removed from the system after collision with a single hydrogen atom (eq. 2.4), the reactive collision frequency $v_{(O,H)}$ of an adsorbed oxygen atom with a hydrogen atom can be estimated according to eq. 2.5:



$$v_{(O,H)} = d_{(O,H)} \bar{c}_{(O,H)} \frac{N_H}{A} * e^{\frac{-E_A}{k_B T}} \quad (2.5)$$

Here, $d_{(O,H)} = 2.73 \text{ \AA}$ is the sum over the radii of both atoms, $\bar{c}_{(O,H)}$ is the mean particle velocity, which can be estimated assuming a 2D-gas at high temperatures according to eq. 2.6, N_H is the number of hydrogen atoms per area A and E_A is the reactions activation energy of $E_A \approx 0.85 \text{ eV}$.^{180,179} Using the value of 0.01 ML H_{ad} coverage at reaction conditions, this leads to $N_H/A = 1.76 \times 10^{17} \text{ m}^{-2}$.

$$\bar{c}_{(O,H)} = \sqrt{\frac{\pi k_B T}{2 \mu}} \quad (2.6)$$

Equation 2.6 assumes a 2-dimensional gas on the sample surface and includes the moving of both H_{ad} and O_{ad} . Inserting all values leads to a reactive collision frequency $v_{(O,H)} = 3 \times 10^7 \text{ s}^{-1}$. Using eq. 2.6 to calculate the mean velocity of adsorbed oxygen $\bar{c}_O = 1000 \text{ ms}^{-1}$, $v_{(O,H)}$ leads to a mean free path of approximately 30 μm on the surface and a lifetime of $\tau_O = 30 \text{ ns}$. The sticking coefficient of O_2 on Cu(111) can be estimated to be $S(O_2) \approx 0.03$ for reaction temperatures by extrapolating experimental data from Habraken *et al.*¹⁷⁷ With an impingement rate according to eq. 2.7, the mean surface concentration of O_{ad} on the surface in steady state during reaction conditions will be:

$$\vartheta_O = \frac{p}{\sqrt{2\pi k_B T m_{O_2}}} * S_0 * \frac{\tau_O}{N_{Cu}} \approx 7.1 \times 10^{-11} \text{ ML} * p_{O_2} [10^{-6} \text{ mbar}] \quad (2.7)$$

At common partial pressures of O_2 up to 10^{-4} mbar (see section 3.1.3) the surface concentration would be in the range of $\vartheta_O \approx 10^{-8} \text{ ML}$. At common growth conditions ($p_{H_2} \geq 10 \text{ mbar}$, $p_{CH_4} \geq 0.01 \text{ mbar}$) the oxygen leak is therefore not expected to influ-

ence the experimental results. This may change at a lower total pressure or lower methane partial pressure, as will be discussed in chapter 8.

3. Synthesis of graphene by chemical vapor deposition of methane on copper

3.1. Reactor-Setup

The graphene reactor setup is the key component for the successful synthesis of high quality graphene in a defined, reproducible and predictable manner. The properties of the experimental setup are listed in detail, as they will be needed for several features of the subsequent data evaluation. As will become clear in the course of this dissertation, one has to be quite careful when comparing results of CVD grown graphene from different groups and it becomes almost impossible to reproduce experimental data obtained from other setups exactly. This is mainly owed to the fact that the resulting product is barely a single atomic layer of material, which is, when compared to the amount of educt and even the amount of possible impurities, barely more than a side product in the ppm range, as can be exemplarily seen in Table 2. Here, the estimated amount of different educts, substrates and also impurities are listed in relation to the amount of graphene product obtained after the reaction.

Table 2 : Educt material, substrate material and impurity material used in a typical graphene growth experiment for the formation of single layer graphene within 40 min at a total pressure of 10 mbar. The quantities are also put in relation to the amount of obtained graphene product.

Component	Flux	Total amount	Ratio to graphene
Hydrogen gas flow	20 sccm	$8 \times 10^{-2} \text{ mol}$	$6 \times 10^6 : 1$
Methane gas flow	0.02 sccm	$8 \times 10^{-5} \text{ mol}$	$6 \times 10^3 : 1$
Leak flux (air)	$4 \times 10^{-5} \text{ sccm}$	$2 \times 10^{-7} \text{ mol}$	$1 \times 10^1 : 1$
Gas impurities (O_2 & H_2O)	$1 \times 10^{-5} \text{ sccm}$	$5 \times 10^{-8} \text{ mol}$	$4 \times 10^0 : 1$
Gas impurities (C-species)	$1 \times 10^{-5} \text{ sccm}$	$5 \times 10^{-8} \text{ mol}$	$4 \times 10^0 : 1$
Copper substrate (25 μm thick)	-	$7 \times 10^{-4} \text{ mol}$	$6 \times 10^4 : 1$
Graphene product	-	$1 \times 10^{-8} \text{ mol}$	1 : 1

3.1.1. Components

The complete reactor setup is shown in Fig. 8 as a 3D model with accurate proportions of the shown components. A corresponding technical drawing is shown in Fig. 9. The

gas feed is composed by four gas lines, CH₄ (flow range 0.1-10 sccm), H₂ (flow range 1-100 sccm) and Ar (flow range 1-100 sccm) gas are inserted via a digital mass flow controller (Bronkhorst, NL) followed by a manual valve. The oxygen is dosed using a leak valve (flow range $> 10^{-11}$ sccm)(Vacgen, UK). The pressure is monitored using two baratron pressure gauges (MKS instruments, US) with a pressure range of 10^{-4} – 100 mbar and 10^{-1} – 10^3 mbar, respectively. The gas can be guided through the graphene reactor system or via a bypass directly to a vacuum scroll pump. The reactor consists of a quartz glass tube (inner diameter 14 mm) connected to the stainless steel tube system with a home-built glass-steel-connector and heated by a tube furnace. The oven activity is regulated via a home-built controller using a Type K thermocouple, which is placed in the central part of the oven between quartz glass and inner oven wall. The samples in the quartz tube can be placed on a ceramic support. Attached to Cu clamps, as shown in the inset of Fig. 8, two samples can be dragged from the hot reactor zone to the cold, outer reactor part via a magnetic transmission. One sample can be dragged in the direction of the gas stream (downstream) and one sample can be dragged in opposite direction (upstream). A third sample can remain in the hot reactor zone until complete cooling of the system, leading to a total of three independent samples obtainable per reactor cycle. Behind the reactor system, a throttle valve allows to regulate the pump speed of the connected scroll pump between 0.003 – 0.5 Ls⁻¹. This allows for independent regulation of the gas flow rates and partial pressures in the hot reactor zone.

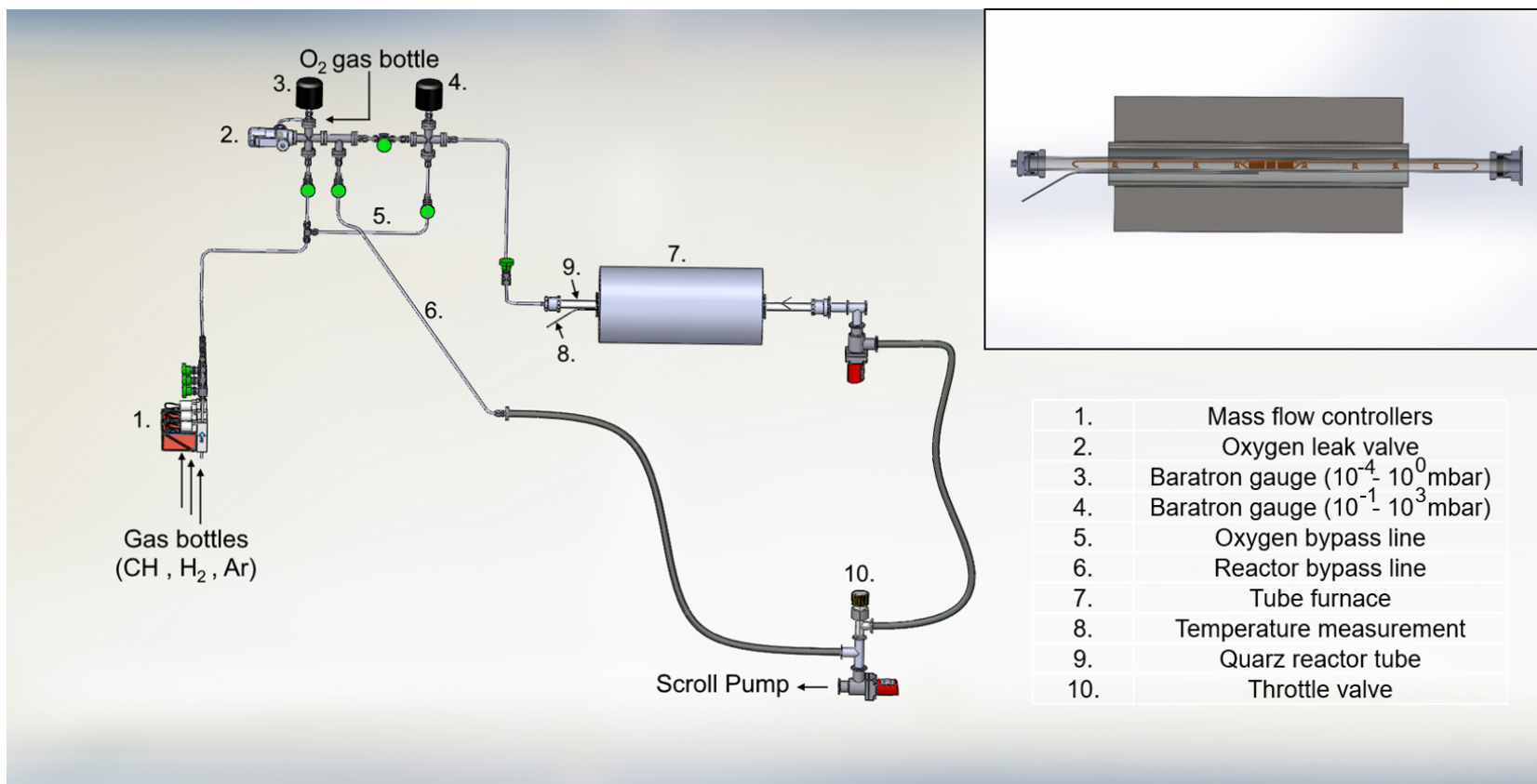


Figure 8 : 3D figure of the graphene growth reactor setup with indication of the used components. Scale approx. 1:25. The inset shows a cross section through the tube furnace, showing the position of the Cu sample pieces, the clamp system and the position of the thermocouple.

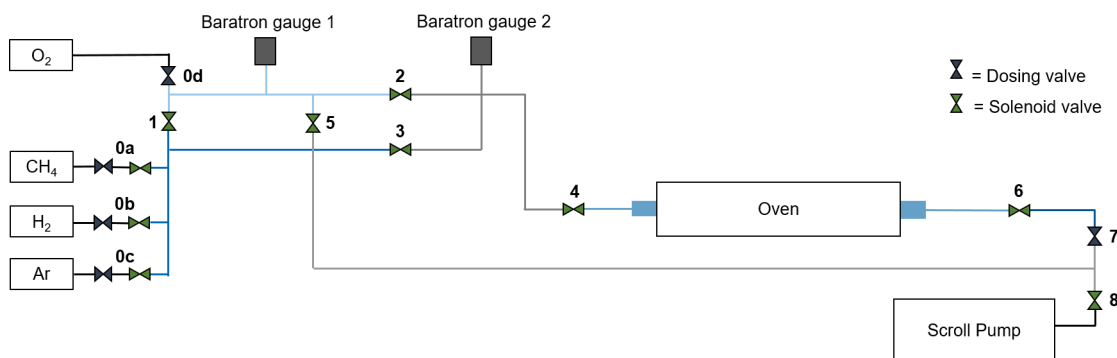


Figure 9 : Scheme of the graphene growth reactor shown in Fig. 8, most importantly showing the position of several valves and the numeration used to reference these valves in the text.

3.1.2. Temperature profile and calibration

To determine the impact of the sample position in the reactor, the heating ramp and a possible temperature offset between samples and thermocouple, a thorough calibration of the temperature was done. Using a second thermocouple, the temperature profile as a function of the distance to the quartz tube center was determined, as shown in Fig. 10a). It shows no temperature drop within the commonly used sample position distance of $\pm 2.5\text{ cm}$ to the tube center, leading to a possible sample length of 5 cm. Indicated are also ceramic and stainless steel shieldings used at the outer oven zones for a better insulation and temperature homogeneity of the hot reactor zone. Figure 10b) shows the temperature profile of a calibration experiment as a function of time. The common reaction steps associated with temperature changes are included in this diagram. The heating of the system from room temperature to $950\text{ }^\circ\text{C}$ takes 30 minutes until a constant temperature is achieved. The following heating to $1050\text{ }^\circ\text{C}$ and subsequently to $1095\text{ }^\circ\text{C}$ takes 10 min each. The removal of the samples after the performed experiment is relevant to sustain the sample composition as present during the reaction. The fastest possibility of sample removal is using the implemented clamp-chain-system. These samples can be removed within one minute (green curve) from the reaction zone to the outer quartz tube segment at room temperature. In contrast, the pure cooling of the oven takes several hours without assistance (black curve). The cooling rate can be enhanced using additional ventilation (blue curve) to allow cooling of the sample area by $100\text{ }^\circ\text{C}$ in one minute. Below temperatures of $900 - 950\text{ }^\circ\text{C}$ the graphene islands are commonly not affected in size or shape in a $\text{CH}_4 + \text{H}_2$ atmosphere.

The melting point of Cu was used as anchoring point for the absolute temperature calibration of the system at high temperatures. For this calibration, a piece of Cu foil was placed on a quartz glass slide and inserted in the sample area. The tested maximum temperatures of the oven with/without melting of the Cu foil (see Fig. 10c) lead to an absolute temperature calibration with an error of $\pm 1.5\text{ }^\circ\text{C}$.

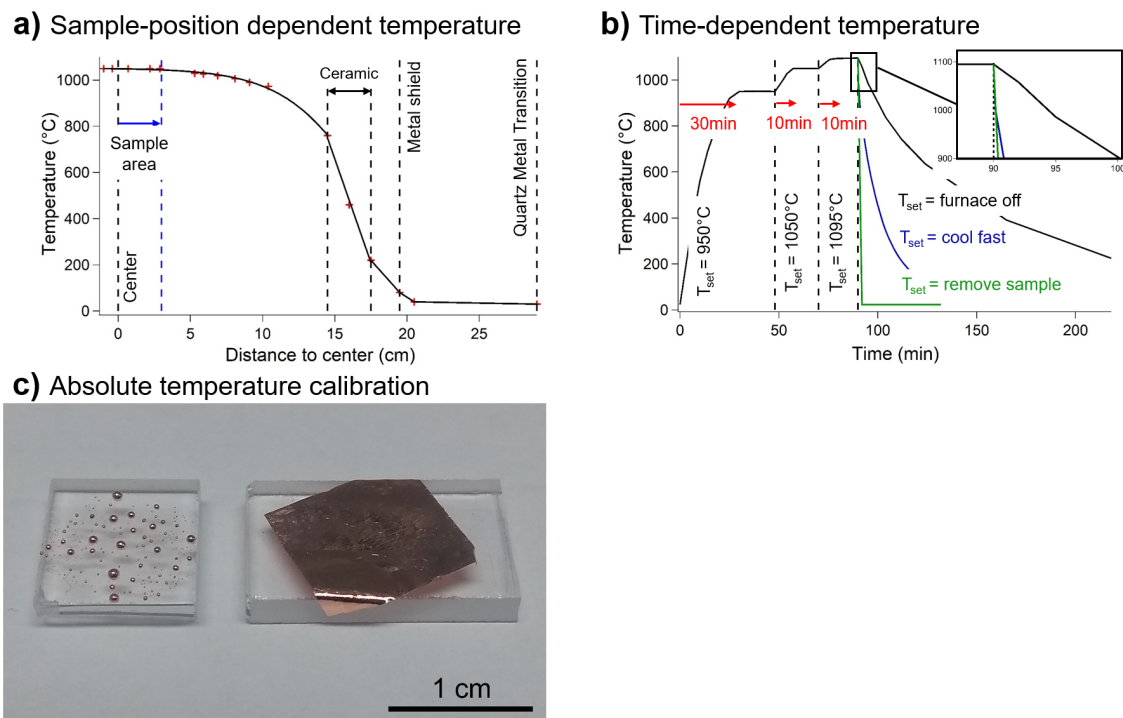


Figure 10 : Temperature calibration curves: a) Position-dependent temperature of the reactor quartz tube related to the reactor center. Dashed lines indicate commonly used sample positions and positions of isolation shields. b) Time-dependent temperature profile of the heating and cooling intervals commonly used for graphene growth. The colored curves show the possible ways of sample cooling, either by removing the samples with the described clamp system (green curve), by additionally ventilating the reactor during cooling (blue curve) or by simply turning off the tube furnace without additional cooling (black curve). c) Samples used to calibrate the absolute reactor temperature in the center of the quartz tube. The left sample shows a Cu foil heated above the melting point of Cu, while for the right sample the melting point was not surpassed.

3.1.3. Volumes, leaks and pump rates

The reactor system can be sub-classified into single sections separated by valves, as shown in Fig. 9. Using an external defined volume, the volumes of these sections were determined and are listed in Table 3. The sum over all reactor sections leads to a total volume of $745 \pm 4 \text{ mL}$. Using the same reactor division, the leak rate of gas into each segment in static vacuum was measured. The determined leak rates show either values up to the low 10^{-7} sccm range for segments purely connected with Swagelok- or ConFlat-(CF)-connectors or values up to 10^{-5} sccm for segments using ISO-KF (KF) or viton-sealed connections. The only regularly opened connections are the two metal-quartz transitions to and from the quartz tube. The inserted leak rate for this segment in Table 3 is a mean value, the total leak rate of the system is controlled for each reactor run. Assuming an idealized reactor system consisting of a chain of circular tubes with different diameters and a conductance according to eq. 3.1, it is possible to estimate the

residence time of gas molecules in the quartz reactor system:¹⁸¹

$$L = 12.1 d^3 l^{-1} \quad (3.1)$$

The conductance L in L/s is calculated by inserting the tube diameter d and length l in cm .

Table 3 : Reactor volumes and leak rates. The single reactor segments are separated by the valves shown in Fig. 10 with their determined reactor volumes and leak rates. The segment volumes were determined by expansion of a defined volume into the reactor system, while the leak rates were determined by resting in static vacuum for up to several days. The only segment which is manipulated on a regular basis is the quartz reactor, which must be removed after each reaction for sample removal and new sample placement. The leak rate of this segment is therefore only a reference value, the absolute leak rate is determined before each reactor run. The overall volume of the reactor system amounts to 745 mL, while the overall leak rate is commonly below 1×10^{-4} sccm. Notice that a majority of the leak rate stems from the reactor segments behind the sample position, where the introduced impurities should be removed through the exhaust before back-diffusion to the sample is possible.

#	Part	Enclosing valves	Volume (mL)	Leak rate (sccm)
I 	Gas Inlet	0a-c, 1, 3	24.4	3.7×10^{-8}
II 	O ₂ Inlet & Low Pres. Meas.	0d, 1, 2, 5	67.3	1.2×10^{-7}
III 	High Pressure Measurement	2, 3, 4	51.1	2.5×10^{-7}
IV 	Quartz Reactor	4, 6	161	4.4×10^{-5}
V 	Reactor Bypass	5, 7, 8	196	8.3×10^{-6}
VI 	Exhaust	6, 7	245	1.4×10^{-5}
	Complete System	-	745 ± 4	6.7×10^{-5}

Different typical reactor settings and their respective residence times are listed in Table 4. With a completely open throttle valve the residence time is below one second (Argon/O₂ pretreatment and H₂ heating ramp), while it can strongly increase for reaction conditions with higher pressures while maintaining low gas flux.

Table 4 : Commonly used gas flow settings, partial pressures and retention times. As the pressure measurement device is placed before the sample in the reactor, a pressure drop may be present during the growth process between these two positions. The indicated values for different reactor settings show that a possible pressure offset can become relevant with a completely opened throttle valve (Part Nr. 10 in Fig. 8). For common graphene growth settings, this is only used during the sample pretreatment, while the range of used reaction settings shows no large offset between measured and real pressures. Significant change is observed for the sample retention times, which increases with reduction of the effective pump speed.

Reaction settings	Total flux	pressure at baratron	pressure in reactor	time in reactor
Low pressure reaction settings	20 sccm	20 mbar	19.8 mbar	8 sec
High pressure reaction settings	40 sccm	150 mbar	150 mbar	33 sec
Argon/O ₂ pretreatment	20 sccm	5 mbar	1.1 mbar	0.5 sec
H ₂ heating ramp	20 sccm	3 mbar	1.3 mbar	0.6 sec

3.1.4. Impurities

Several sources of impurities are introduced into the reactive system during the graphene formation reaction. These can roughly be divided into two subgroups, the contaminations stemming from leakages in the reactor system and the impurities introduced together with the reactant gases. The first group contains the leakage caused by the used fittings, as described above, adsorbates on the reactor walls, contaminations arising from reactor components and back-diffusion from the used vacuum pump. The leak of the overall reactor system must be seen as a constant gas flux during the reaction, which cannot be neglected and will be addressed further below together with the impurities from the used gases. The overall leak rate used for calculations is $6.7 \times 10^{-5} \text{ sccm}$, which is assumed to consist of common air. As can be extracted from Table 3, most larger sources for leakage are positioned behind the reaction space (exhaust, reactor bypass, half of the quartz reactor), which allows the conclusion that this assumed leakage value is the upper limit affecting the grown samples. With every changing of the samples in the reactor, the system must be vented with air, which introduces several gaseous species into the reactor, including water vapor and carbonaceous species. These are typically adsorbed to the reactor walls and only desorb at a low rate without heating the complete tubing system, which is not possible in this reactor setup. The typical evacuation procedure therefore consists of an elaborate sequence of cleaning steps, listed in the following:

- Evacuation of the reactor system overnight
- Multiple purging of the reactor with the reaction gases
- Heating of the quartz tube in H_2 and Ar gas

Typically, the measurable leak rate of the reactor does not drop any more after 12 h of evacuation, indicating that volatile adsorbates are mainly pumped off. Possible remaining residues can be dissolved by the purging of the (dry) gases. Additionally, the quartz tube is typically heated in hydrogen gas (30-45 min up to 950 °C) and an extensive pretreatment procedure of several hours in argon gas is performed before the actual graphene growth step. It can therefore be assumed that the reactor walls in immediate vicinity to the samples are purely composed of fused silica and no substantial amount of impurities arises from wall desorption after this extensive pretreatment.

The reactor component crucial for the contamination-free treatment of the Cu samples is the above-mentioned quartz tube, which is also heated to reaction temperature together with the samples. While the heating procedure reliably removes additional contaminations from the reactor walls, the quartz material itself is subject to interaction with the copper samples. Several literature references have identified silicon impurities as a relevant contamination for the grown graphene samples, although the source is often also assumed to be from immanent impurities in the Cu foil. Due to the large impact on the outcome and quality of the grown graphene samples, the topic of silicon impurities in the samples is discussed separately in chapter 9.1.

Common scroll vacuum pumps are based on oil lubrication for proper functioning. These heated hydrocarbons commonly possess a relatively high vapor pressure of $\approx 10^{-4} - 10^{-3} \text{ mbar}$,¹⁸² which may back-diffuse into the reactor system without the proper precautions. To prevent back-diffusion, a zeolite trap is installed between reactor and scroll pump. Additionally, during the graphene formation step, an installed throttle valve reduces the conductance between the two systems and the flowing reaction gases inhibit the diffusion in opposite direction.

Impurities independent of the reactor setup are the ones introduced together with the reactants. The absolute purities and the contained main impurities (O₂, H₂O, C-containing species) are listed in Table 5 according to the data provided by the respective provider. The purity of the Cu foil (Alfa Aesar, US), is only stated regarding the contained metal-based impurities, which are also listed in Table 5. It does not include oxygen, as this naturally forms an oxide layer while in contact with air, or carbon-based impurities, which may be introduced into the sample during the milling process of the foil. An oxidative pretreatment procedure as introduced by Kraus *et al*¹⁸³ is used to remove this impurity from the sample before starting the graphene growth.

Combining the reactor leak rate and impurities introduced by the reaction gases, the present partial pressure of oxygen during the graphene formation under typical conditions (1045 °C, $flux_{Total} \approx flux_{H_2} = 20 \text{ sccm}$, $p(H_2) = 20 \text{ mbar}$, $p(CH_4) = 0.02 \text{ mbar}$, $H_2 : CH_4 - ratio : w = 1000$) can be estimated. At these conditions, the oxygen partial pres-

Table 5 : Materials used for the graphene growth process and their purities as stated by the producers. If given, the maximum amount of oxygen, water and carbon based impurities is also inserted. The Cu foils used in this work are mainly from batch "2", while batch "1" was used in former studies.¹⁷⁴

Component	Purity	Impurity content			
		O ₂	H ₂ O	C-species	other impurities (ppm)
Cu foil batch 1	99.8%	nat. oxide	adsorbates	see chapter 9.2	Ag(15), Ni(2), Fe(1.3), S(2.5), Si (0.31)
Cu foil batch 2	99.9%	nat. oxide	adsorbates	see chapter 9.2	Ag(8), Ni(5), Fe(5), S(5), Si (-), As(1), Sb(1), Pb(<2)
H ₂ gas	99.9999%	< 0.1 ppm	< 0.5 ppm	< 0.3 ppm	-
CH ₄ gas	99.95%	< 30ppm	-	< 300 ppm	-
Ar gas	99.999%	< 2.0 ppm	< 2.0 ppm	< 0.4 ppm	-
O ₂ gas	99.999%	-	2 ppm	0.4 ppm	-

sure can be calculated according to eq. 3.2 as the sum of O_2 from all impurity sources and amounts to $p(O_2) = 1.67 \times 10^{-5} \text{ mbar}$:

$$p(O_2) = \rho_{O_2_in_air} * \frac{flux_{Leakage}}{flux_{Total}} * p_{total} + p(H_2) * \rho_{O_2_in_H_2} + p(CH_4) * \rho_{O_2_in_CH_4} \quad (3.2)$$

In this equation, $\rho_{O_2_in_air}$ is the oxygen content in air of $\approx 21\%$, $flux_{Leakage}$ is the total reactor leak rate of $6.7 \times 10^{-5} \text{ sccm}$, $p(X)$ and $\rho_{O_2_in_X}$ are the partial pressure of a species and the respective oxygen impurity content in the respective gas.

Assuming a relative humidity of 50% at 25 °C ($p(H_2O) \approx 15.6 \text{ mbar}^{184}$), the water partial pressure can be calculated accordingly following eq. 3.3 to be $p(H_2O) = 1.1 \times 10^{-5} \text{ mbar}$.

$$p(H_2O) = \rho_{H_2O_in_air} * \frac{flux_{Leakage}}{flux_{Total}} * p_{total} + p(H_2) * \rho_{H_2O_in_H_2} + p(CH_4) * \rho_{H_2O_in_CH_4} \quad (3.3)$$

The oxygen partial pressure is far below the needed pressure for the formation of Cu-oxides, which above 950 °C is between $10^{-4} - 10^{-3} \text{ mbar}^{185}$. The influence of surface oxygen on the reaction process is rather difficult to disprove, as no threshold concentration is known to trigger a certain reaction. The average concentration of adsorbed oxygen atoms on the Cu surface O_{ad} can be estimated knowing the respective partial pressure. An estimation of the oxygen coverage on the sample surface is given in section 2.4, resulting in $\approx 10^{-8} \text{ ML}$ coverage at common reaction conditions.

It is important to consider that the hydrogen surface concentration strongly decreases with decreasing temperature, leading to a stronger impact of oxygen impurities at lower temperatures, mainly during the cooling of the samples after the reaction.

3.1.5. Comparison UHV/reactor

As described in the previous sections, there are several differences between the described reactor system and a classical ultrahigh vacuum (UHV) chamber. The base pressure, the lack of temperature-based cleaning ("bakeout"), the leak rates and applied pressure regime strongly differ from common UHV setups. Several critical points must therefore be considered for the evaluation of samples originating from this setup.

As already described above, the lower limit of oxygen-based impurities is inherent to the reactor setup and cannot be further reduced. Demonstrating the negligible impact of these impurities can therefore only be done by showing that an additional increase does not affect the reaction outcome, as is shown for oxygen in chapter 4.2.1.

It is not possible to freeze the growth process and possible intermediate reaction products, as even the fastest sample removal takes roughly 60 s, in which the sample surface is subject to change by temperature-dependent reactions and diffusion from the cooling Cu-bulk. This must be kept in mind for subsequent surface-specific examinations.

3.2. Graphene growth recipes

To ensure the growth of reproducible graphene samples with high quality, a standard reaction recipe consisting of 6 main reaction steps has been developed, which is shown in form of a diagram in Fig. 11. The pretreatment steps executed before the beginning of the graphene formation are necessary to set the reaction temperature and clean the used Cu foil. As the first moments after introduction of a reactive $CH_4 + H_2$ mixture crucially affect the nucleation of graphene flakes, a fixed reaction procedure is kept during this time. After the CVD growth of graphene, the subsequent cooling step is very important for the final surface composition of the cooled sample. The six preparation steps can be summarized as follows:

1. The quartz tube loaded with up to three samples is heated in a H_2 atmosphere at $p(H_2) \approx 1 \text{ mbar}$ to $950 \text{ }^\circ\text{C}$. As further described in chapter 9.2, modification of the gas phase during this first heating phase already has a strong impact on the reaction outcome.
2. Following a protocol introduced by Kraus *et al.*,¹⁸³ an oxidative pretreatment step is performed to remove any carbon-based impurities present on the sample surface or in the Cu bulk. Oxidizing agent is O_2 gas added at a flux of about $5 \times 10^{-4} \text{ sccm}$

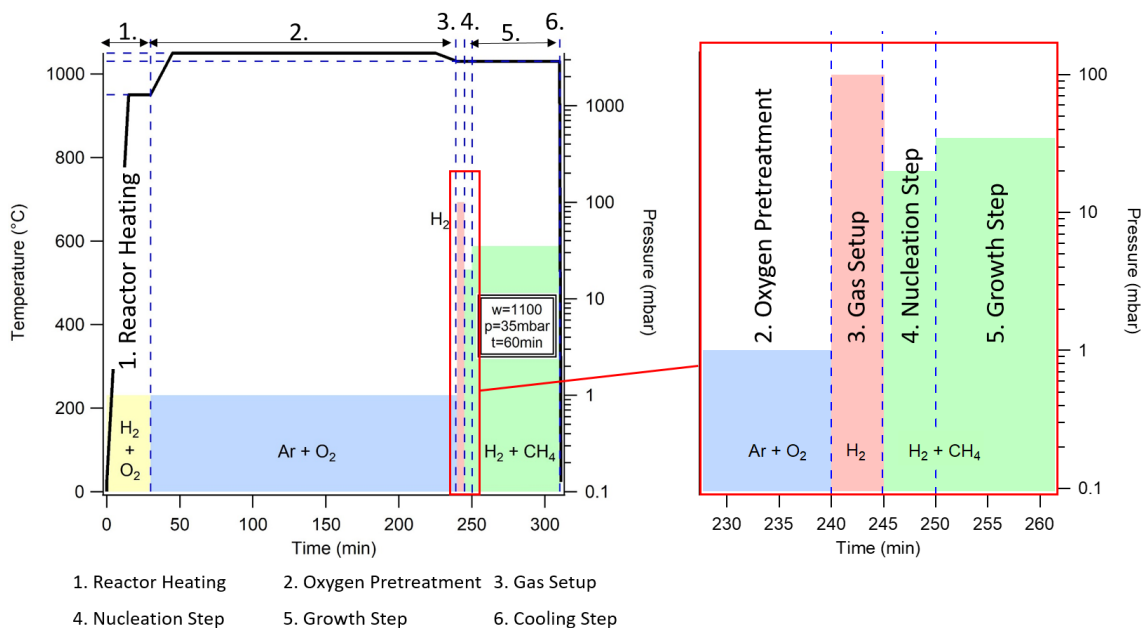


Figure 11 : Example for a used reactor recipe. The common reactor run consists of six consecutive reaction steps, where the main part of the reaction time is used to ensure that the used substrates are reproducibly cleaned before the synthesis. Step 3 consists of a defined succession of steps to exchange the oxidative pretreatment gases by the reaction gases. While these gases are set and purged through the reactor bypass, the samples are exposed to high hydrogen pressure of 100 mbar to prevent the accumulation of impurities from the gas phase and allow a defined transition to growth conditions. The following nucleation step is relevant for the formation of graphene nucleation seeds. The subsequent growth step defines the size of the produced graphene islands and in the final cooling step the samples are cooled to room temperature. Reprinted with permission from ref. ¹²⁸. Copyright 2021 American Chemical Society.

diluted in Argon gas. The partial pressure of O_2 over the samples amounts to $\approx 10^{-5} - 10^{-4}$ mbar. During this procedure, the sample is heated to $1045^\circ C$ and kept at this temperature for 60-300 min depending on the planned graphene growth reaction. After this time, the temperature of the setup is set to the planned graphene growth temperature and left to level off.

- At the destined temperature, the oxygen flux is turned off and the argon is exchanged by a H_2 flux, which is used to fill the reactor segment with a static gas phase of 100 mbar. In the meantime, the desired methane and hydrogen flux for the graphene formation reaction can be set and pumped via the reactor bypass. After achieving stable flow conditions, the flow can be guided through the reactor towards the scroll pump, while the desired total pressure is regulated via a throttle valve installed behind the quartz reactor. For proper results, it is important that the methane concentration slowly increases over the samples by mixing with the residual gas from the H_2 purge. The total pressure at first must exceed the final growth pressure and approximate this desired level by a gentle pressure decrease.

The fulfillment of this requirement is essential, as starting from a low purge pressure and raising the reactor pressure towards the CVD settings favors the increased and uncontrolled nucleation of graphene flakes.

4. The first CVD step of the graphene growth reaction is important to control the number of formed graphene flakes, the nucleation density, as evaluated in detail in chapter 6. The ideal nucleation conditions are kept for 2-5 min before changing the conditions to the actual growth conditions, where further flake nucleation during growth should be avoided. Directly after setting the growth conditions, one of the grown graphene samples can be removed from the hot reactor zone to serve as a reference. Following modification of the CVD growth conditions in step 5 can be monitored on the samples that remained in the reactor.
5. The CVD growth step is the key step for the evolution of the graphene flakes nucleated in step 4. Exposed to a specific gas phase composition, the effect on the growing graphene flakes can be monitored by removing a sample after a defined time from the hot reactor zone. In the case of three loaded samples, the third sample can be used to monitor the effect of an additional parameter change on the samples.
6. The cooling steps of each sample is at different instants of the experiment as described above. The procedure nevertheless always consists of rapid cooling of the samples in the unchanged reactive atmosphere. This is done in case of the first two samples by dragging the samples into the cold reactor zone using the Cu chain introduced in section 3.1, for the third sample the complete reactor setup is cooled rapidly.

3.3. Characterisation techniques of graphene

3.3.1. Raman Spectromicroscopy

Raman spectroscopy is a very powerful method to identify graphene sheets due to their characteristic Raman bands that result from specific electron-phonon coupling as displayed in Fig. 12. The Raman spectra obtained from single- and bilayer graphene are shown in Fig. 13 with their most prominent bands, the so-called D, G and 2D peaks. The G-band originates from a first-order scattering process of the doubly degenerate in-plane transverse optic (iTO) phonon branch and the longitudinal optic (iLO) phonon branches close to the Γ -point of graphene (the center of the Brillouin zone), marked with an arrow in Fig. 14.^{34,46} The second signal typical for graphene is the 2D-band (also referred to as G-band in literature) originating from a second-order scattering process involving two iTO phonons near the K- and K'-point. The D-Band is caused by the combination of

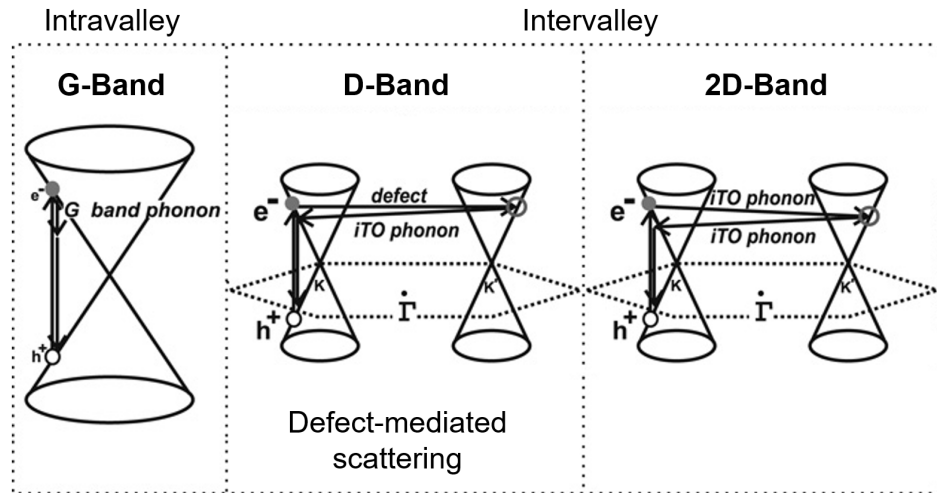


Figure 12 : Processes in the electronic structure of graphene leading to the observed Raman bands. The intravalley G-band is created by resonant excitation of an electron in the Dirac cone and includes a phonon from the *i*TO or LO branches close to the center of the Brillouin zone (Γ -point) with vanishing wave vectors. Both intervalley Raman processes leading to the D and 2D band combine processes at the K and K' points of the graphene Brillouin zone. The associated scattering processes are either an *i*TO phonon+defect scattering (D-band) or two *i*TO phonons (2D-band). Adapted from reference³⁴, with permission from Elsevier.

an inelastic phonon-scattering (*i*TO phonon) and an elastic scattering at a lattice defect, leading to half the energy loss compared to the 2D-band. The symmetric requirement of the defect-mediated scattering process is only allowed on armchair-type defect structures or point defects.⁵²

Due to the special electronic structure of graphene around the K-point referred to as Dirac cone, the absorption of the incident laser radiation is always a resonant process, as shown in Fig. 12, which greatly increases the intensity of the Raman signal.³⁴ The shift of the excitation position in the electronic structure nevertheless leads to a dispersion of the Raman-Bands with incident laser energy,³³ which is relevant for the quantitative analysis of Raman spectra. The defect-mediated D-band intensity is also strongly dependent on incident laser energy, which is relevant to correctly assess the spectral information.^{47, 186, 187}

Besides the examination of the graphene quality using the D-Band, the 2D-peak shape and G/2D intensity ratio are typically used to determine the graphene layer number. This quantized parameter is comparably easy to analyze in the case of Bernal-stacked, laterally homogeneous graphene samples.³⁴ Increasingly difficult to distinguish is the layer number for graphene stacks rotated at different angles up to rotation of 30° , where the interaction between the single graphene layers strongly changes.^{188, 189, 44, 190} For turbostratic graphene, the single layers are electronically decoupled from each other and, hence, the spectrum resembles the one of single layer graphene, complicating the assignment.^{19, 191}

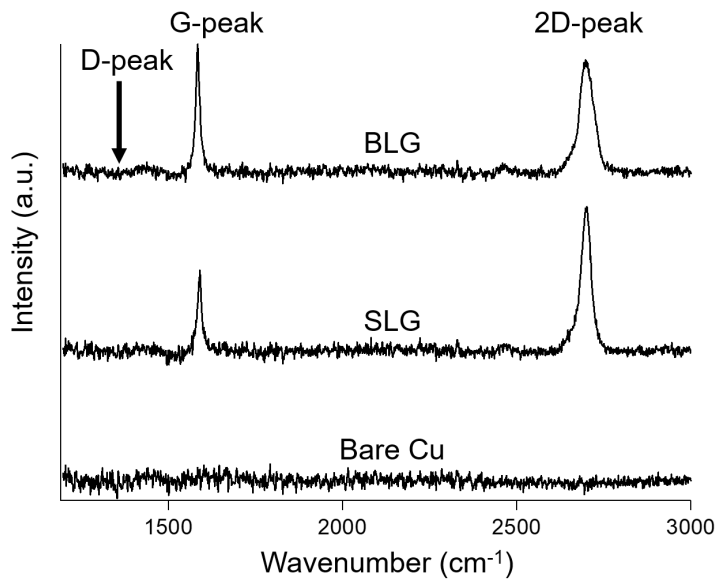


Figure 13 : Exemplary Raman spectra of a bare Cu surface, single layer graphene (SLG) and bilayer graphene (BLG). The most prominent peaks are the G- and 2D-peak. The expected position of the defect-mediated D-band is shown with an arrow. The respective fits to these spectra are shown in reference¹⁹.

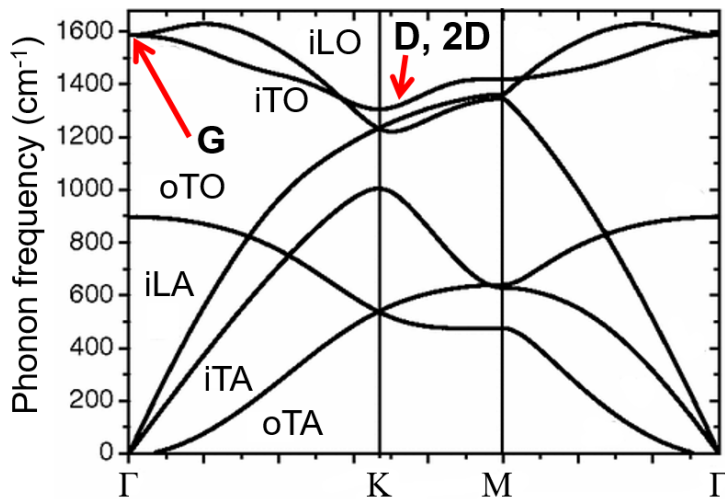


Figure 14 : Reduced representation of the phonon dispersion of graphene along high-symmetry lines. Marked with arrows are the phonons associated with the Raman transitions from the G-band (close to the Brillouin zone center) and the D/2D-bands (around the K-point). Adapted from reference⁸¹. Copyright 2008 American Physical Society.

Electronic doping, e.g. caused by the interaction with an underlying substrate, can change the peak positions of the Raman bands.⁴⁹ This shift is always towards higher photon energies, regardless of whether or not the graphene is acting as electron-donor or electron-acceptor.^{192, 193, 194}

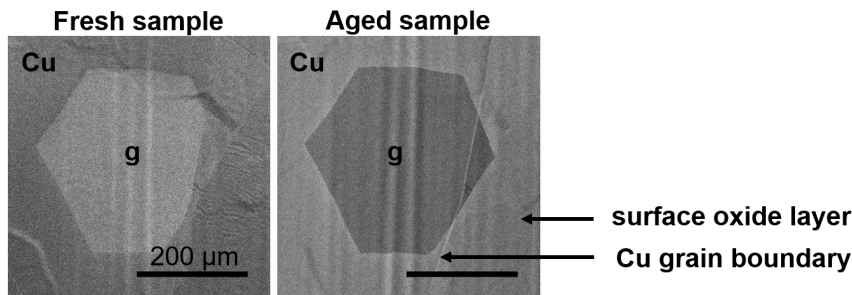
Lastly, the Raman signatures are also affected by the compressive/tensile strain acting on the graphene sheet. Distortions in the graphene lattice lead to a modification of the phonon frequencies and hence a phonon dispersion differing from the ideal case as shown in Fig. 14.¹⁹⁵ This effect is described by the Grüneisen-parameter, which links a change in crystal expansion to a change in phonon dispersion.¹⁹⁶ This strain can either be applied unidirectional, in which case a splitting of the Raman bands is observed.^{197, 198} For biaxial strain, the symmetry is retained and a shift of the complete peak is observed, where the shift of the 2D-peak is roughly doubled compared to the shift of the G-peak.^{199, 49, 200} This effect can also be used to measure stretching of freestanding graphene membranes or accordingly a pressure difference acting on a graphene membrane.⁴⁸

To track all parameters influencing the Raman spectra of graphene, it is important to combine this method with complementing characterization techniques, such as scanning electron- or optical microscopy for the lateral information. The rastering of the recorded Raman spectra on a sample enables the imaging of lateral spectral changes (Spectromicroscopy). As graphene samples are often strongly inhomogeneous, laterally resolved Raman Imaging has turned into a standard technique for graphene characterization.^{201, 202, 203, 204}

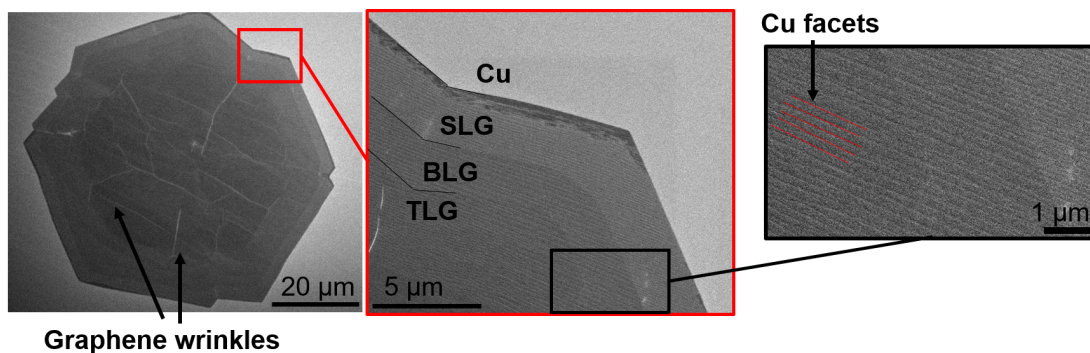
3.3.2. Scanning electron Microscopy (SEM)

Scanning Electron Microscopy (SEM) uses the differences in backscattering behavior of matter when irradiated with high-energy electrons. A focused electron beam is rastered over the sample surface while a detector records the subsequently emitted secondary electrons of low kinetic energy (0 – 50 eV) originating from the surface-near region and yielding a high topographic contrast. The escape depth of secondary electrons in condensed matter depends on the electron kinetic energy. For a mean kinetic energy of 10 eV this leads to an escape depth of approximately $\approx 1 \text{ nm}$.²⁰⁵ Additional to the topographic contrast, the differences in emission between elements, which is most distinct between metals and insulators leads to a material-specific contrast.²⁰⁵ Contrast in SEM images is created by differences in the surface work function Φ_{sample} , which is the measure between the Fermi energy E_F of the material and the vacuum energy E_{vac} outside of the material. A higher value of Φ_{sample} leads to a retaining of secondary electrons in the sample and hence less brightness in the image. Exemplary SEM images acquired by secondary electron collection are shown in Fig. 15. As the work function of graphene ($\Phi_{\text{graphene}} = 4.3 \text{ eV}$)²⁰⁶ is lower than that of Cu(111) ($\Phi_{\text{Cu(111)}} = 5 \text{ eV}$),²⁰⁷ it appears brighter in the SEM image.

a) Single layer graphene on Cu



b) Single – and Multilayer Graphene



c) Freestanding graphene

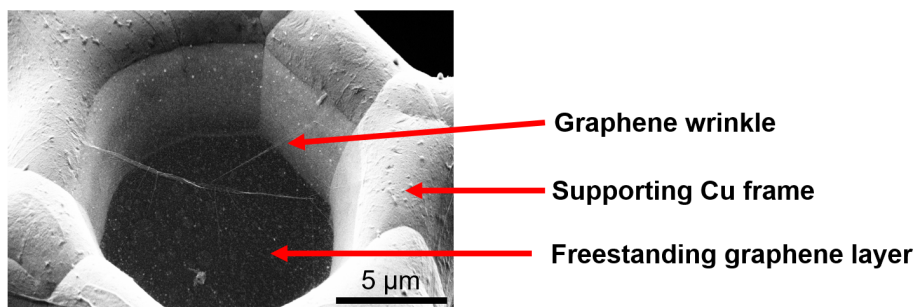


Figure 15 : Exemplary SEM images (secondary electron collection) of graphene islands synthesized on Cu (a+b) and freestanding, spanning over holes in a supporting Cu grid (c). a) Change of contrast in SEM images between single layer graphene and Cu for fresh samples and samples aged in air. For fresh samples, graphene has a lower work function than Cu(111) and, hence, allows the emission of more secondary electrons (see text). An aged sample has an oxidized surface copper layer with a higher secondary electron yield, appearing brighter than graphene.²⁰⁸ Note that the change in the brightness of graphene is caused by the adaptation of the image contrast. b) Differentiation between bare copper, single- and multilayer graphene is possible by observing the stepwise contrast changes in the SEM image combined with the hexagonal graphene structure. The stepwise increase in graphene layer number in the SEM image can be accurately followed by Raman-spectroscopy, as shown in chapter 7. Visible in these images are also graphene wrinkles and the Cu facets forming below the graphene layers, marked with arrows. c) SEM image of a freestanding graphene membrane. The graphene membrane can mainly be identified by impurities on the layer and wrinkles, appearing bright in the image.

The work function of bi- and trilayer graphene increases slightly compared to SLG to $\Phi_{multi-LG} = 4.5 \text{ eV}$, which is why these appear darker in the SEM images.²⁰⁶ Higher layer numbers show no more change in Φ_{sample} and cannot be clearly distinguished. Cu samples stored in air form an oxide layer, which has a higher secondary electron yield than the bare metal, leading to a change in contrast compared to an unoxidized graphene flake.

SEM also allows to image wrinkling of the graphene islands and facetting of the Cu substrate, as marked with arrows in Fig. 15. A large amount of secondary electrons is created by energetic losses of higher energy electrons when interacting with the sample, also in deeper layers than the mean escape depth of secondary electrons. Therefore, a single freestanding graphene membrane shows almost no secondary electron image at all (Fig. 15c). The Membrane can only be identified by impurities on the membrane and foldings in the graphene layer.

The detection of high-energy backscattered electrons (BSE) gives mainly information on the element-specific material contrast caused by the atomic-number Z dependent backscattering behavior of the elements.²⁰⁹ The higher energy of the observed electrons leads to an increased mean free path in the solid⁸⁸ and is therefore less surface sensitive.

Energy-dispersive X-ray spectroscopy (EDX) The element-specific characterization of samples parallel to the imaging in a scanning electron microscope is possible by using energy-dispersive X-ray analysis. Atoms irradiated with high-energy electrons are ionized, creating electron holes in the core shells. The subsequent relaxation of electrons with higher energy leads to the release of element-characteristic photons in the X-ray energy regime. The detection of these X-rays therefore allows the elemental analysis with the lateral resolution of the focused electron beam when using it as excitation source. More information can be found in literature.²¹⁰

BSE-SEM and EDX are not surface sensitive enough to detect SLG, but can be used to analyze the substrate composition and identify contaminations.

3.3.3. Optical Microscopy

Optical microscopy has turned out to be a very fast method to analyze grown graphene samples. Even though single layer graphene itself absorbs 2.3% of light in the visible range,⁸⁹ which is exceptional for a single atomic layer, it is rather difficult to identify optically. Using a high magnification, it is possible to distinguish the faint contrast arising from the stepwise increase in graphene layers and the connected change in the Cu foil support surface reconstruction and facetting.^{199,211} An exemplary optical image is shown in Fig. 16 a) without and in Fig. 16 b) with enhanced contrast after image capture. A stronger contrast usually develops after the exposure to air, when with time a thin oxide layer forms on the bare Cu, enabling the differentiation between no graphene and graphene areas on the sample. This contrast can easily be made unambiguous by

heating the sample in air to 200 – 300 °C, forming a thick oxide layer on the uncovered Cu foil, which is prevented underneath graphene-covered Cu.³⁷ Thus, after heating to 250 °C, the contrast allows an easy distinguishing between graphene covered and uncovered areas (see Fig. 16c)). Heating to 300 °C usually damages single layer graphene (SLG) while preserving multilayer areas, giving an insight about the layer distribution in the sample, as shown in Fig. 16 d).

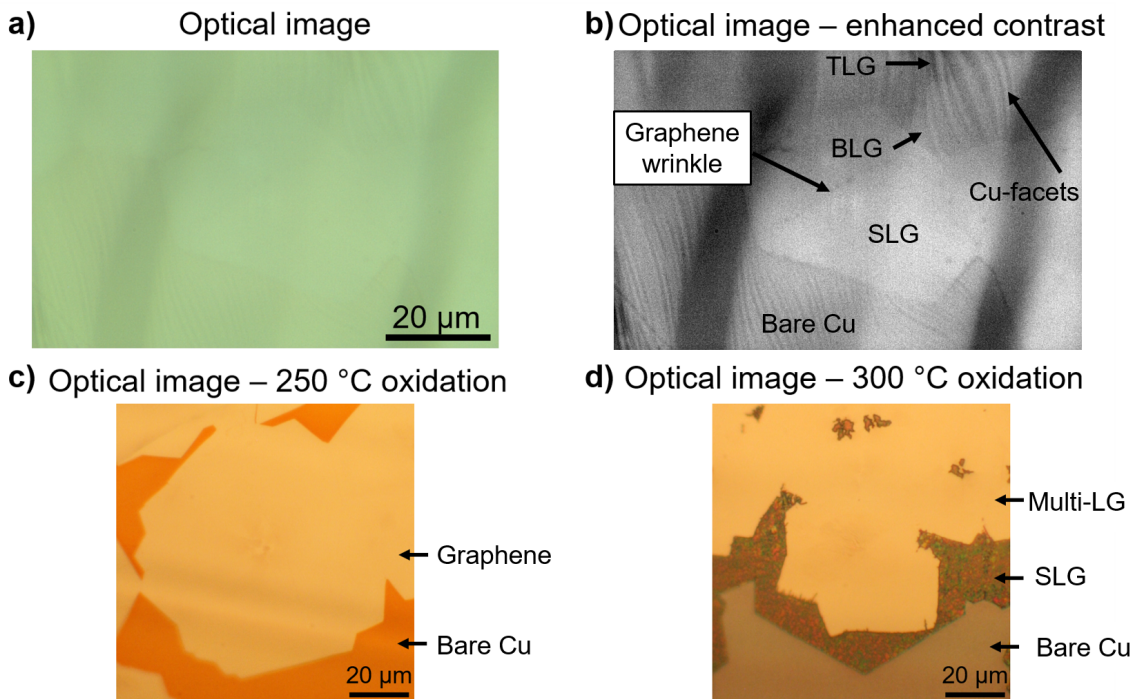


Figure 16 : Graphene samples on Cu after different modification steps. a) Optical image of fresh graphene on Cu, as directly obtained from the microscope, allowing the faint differentiation of graphene covered/uncovered graphene. After digital contrast enhancement shown in b), the differentiation is clearly easier, allowing also the identification of multilayer areas, as marked in the figure. c) The oxidation of the sample in air at 250 °C creates an intensive coloring of uncovered substrate areas, allowing the easy identification of graphene-covered sections. d) Heating of the sample to 300 °C mostly destroys single layer graphene areas, while multilayer areas remain unharmed. This creates an additional contrast between graphene areas of different thickness. (Experimental details: E. 1)

In the case of transferred, freestanding graphene membranes, the identification of continuous graphene layers is only possible through a slight contrast in the optical image. This identification can be simplified by illuminating the sample with a focused laser beam through the optical path of the microscope and observing a reflection on freestanding graphene membranes. This is shown exemplarily in Fig. 17 a) and b). The respective Raman spectrum acquired at this point is shown in Fig. 17c).

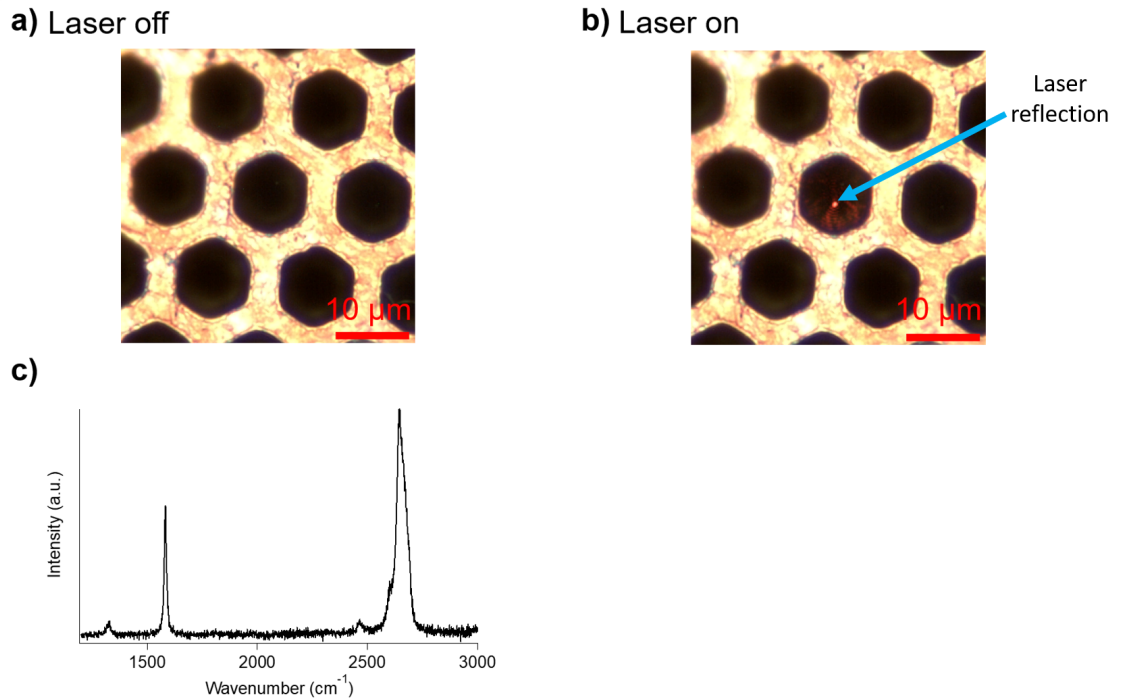


Figure 17 : Raman spectra obtained from freestanding graphene membranes. a-b) Optical images of the graphene membrane with/without laser irradiation, which allows the identification of spanned grid holes (see arrow). c) Raman spectrum at the position marked in b). (Experimental details for graphene growth: E. 2)

3.3.4. Photoelectron spectroscopy

Photoelectron spectroscopy uses the photoelectric effect to release photoelectrons from a sample surface through irradiation with X-rays. These photoelectrons are then energy-filtered by an electron analyzer and detected using a photoelectron multiplier.¹⁶⁸ These photoelectrons contain element-specific information, allowing the retrieval of information on the elemental composition and oxidation state of the uppermost atomic layers of the sample.

The surface sensitivity is especially helpful when dealing with 2D-materials, which only account for a negligible amount of the total sample atoms but are completely located on the sample surface. Depending on the kinetic energy of the analyzed electrons, the inelastic mean free path (IMFP) of the electron in the solid sample for Cu ranges between 4.88 Å at 50 eV and 20.95 Å at 1400 eV.²¹² Common laboratory-based setups use the characteristic X-ray emission from an anode material irradiated with high-energy electrons. This anode material is typically either magnesium ($Mg_{K\alpha} = 1253.6 \text{ eV}$) or aluminum ($Al_{K\alpha} = 1486.6 \text{ eV}$). The kinetic energy of the released photoelectrons in front of the sample surface is composed by the difference between the energy of the incoming photon ($E = h\nu$) and the sum of the binding energy of the electron in the sample (E_B) and the work function Φ_{Sample} needed to release the electron from the solid into the vacuum

level, as calculated in eq. 3.4.

$$E_{kin} = h\nu - (E_B + \Phi) \quad (3.4)$$

The kinetic energy as filtered by the analyzer however references to the vacuum level of the electron analyzer material, so that the measured kinetic energy refers to $\Phi_{Analyzer} = \Phi$. The work function of the analyzer, Φ , can be determined once and then be used to calculate the corrected kinetic and binding energies.

The created electron holes can be filled with electrons of higher energy. The energy released during this process can be transferred to an emitted photon (X-ray fluorescence, see EDX) or it can be transferred in a radiationless process to a further electron, which is then released from the sample. This second decay mechanism is called Auger process and the ejected electron is known as Auger electron. The original photon wavelength does not influence the kinetic energy of the Auger-electron, which is why these signals appear at fixed kinetic energies in contrast to photoelectrons appearing at fixed binding energies when changing the energy of the excitation source.

Changes in the chemical environment of an atom commonly also lead to slight changes in the binding energy of core electrons in the range of few $10^{-1} - 10^0$ eV, which are known as chemical shift. By analyzing such binding-energy shifts it is possible to extract chemical information of the observed elements.²¹³

The photoelectron signal of an XPS signal is acquired by the electron analyzer in the geometry sketched in Fig. 18. In the so-called magic angle of $\gamma = 54^\circ$ ²¹⁴ geometry the signal intensity is calculated as:

$$I = I_0 * N_{Irradiated} * \tau * \omega(\alpha) * \frac{\sigma}{4\pi} * \Delta\Omega \quad (3.5)$$

Here, I refers to the total intensity of the signal, which is directly proportional to the area under the peak curve in the acquired spectrum corrected by the respective underground line. I_0 is the intensity of the X-ray light source, $N_{Irradiated}$ is the number of irradiated sample atoms. For XPS, the penetration depth of the X-rays (≈ 250 nm at 30° incident angle in Cu^{215}) is much larger than the inelastic mean free path (IMFP) of the released photoelectrons. Thus, the intensity loss of the irradiating light for deeper layers can be neglected. τ refers to the transmission function of the analyzer. Each electron analyzer model filters electrons of different kinetic energies with a particular yield, which must be considered for comparison. The photoemission cross section σ relates to the ionization probability between the incoming photon and the released photoelectron. These values are specific for each element and electron orbital and can be extracted from tabulated data.²¹⁶ $\Delta\Omega$ is the acceptance angle of the electron analyzer. The last factor $\omega(\alpha)$ relates to the escape probability of the created photoelectron from the sample. This value is

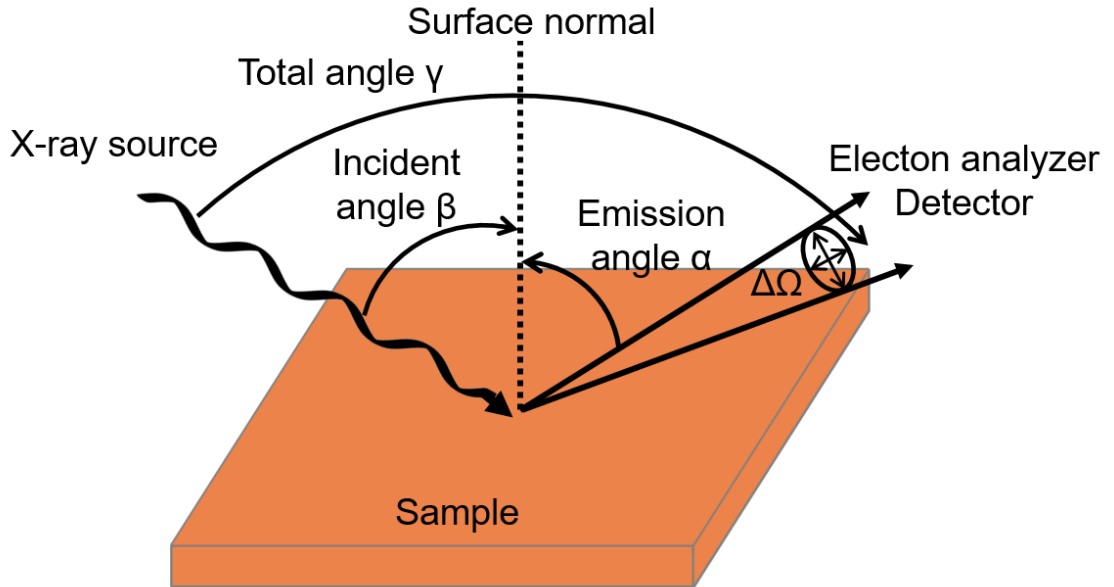


Figure 18 : XPS sample geometry, clarifying the incident angle β and emission angle α with respect to the surface normal. The total angle between X-ray source and electron analyzer is referred to as γ with an analyzer acceptance angle of $\Delta\Omega$.

mainly defined by the IMFP λ and the emission angle α of the ejected electron of the sample material following the relation:

$$\omega(\alpha) = e^{-\frac{x}{\lambda \cos(\alpha)}} \quad (3.6)$$

If the electron analyzer is placed at a certain emission angle α with respect to the sample normal, the effective escape depth amounts to $x_{eff} = x/\cos(\alpha)$. In the case of normal emission, the term $\cos(\alpha)$ in eq. 3.6 becomes 1 and $x_{eff} = x$. The depth contribution to the overall XPS signal is shown in a diagram in Fig. 19a) and graphically in Fig. 19b). As an example for the carbon C 1s photoelectron (binding energy $E_B = 284 \text{ eV}$, kinetic energy $E_{kin} = 1200 \text{ eV}$) released by an Al $K\alpha$ photon, the IMFP in Cu is $\lambda_{Cu}(1200 \text{ eV}) = 18.6 \text{ \AA} \approx 9 \text{ atomic layers}$). 63% of the carbon C 1s signal originates from the uppermost 9 atomic layers.

The absolute quantification of an elemental species based on the acquired signal requires complete knowledge of all device-specific characteristics and the sample geometry. To simplify the quantification, usually internal or external calibration samples are used as standards. In the case of a sample composed of only two elements, one species can often be referenced to the second one. For a bulk sample with a flat surface, three sample structures as sketched in Fig. 20 can be calculated.

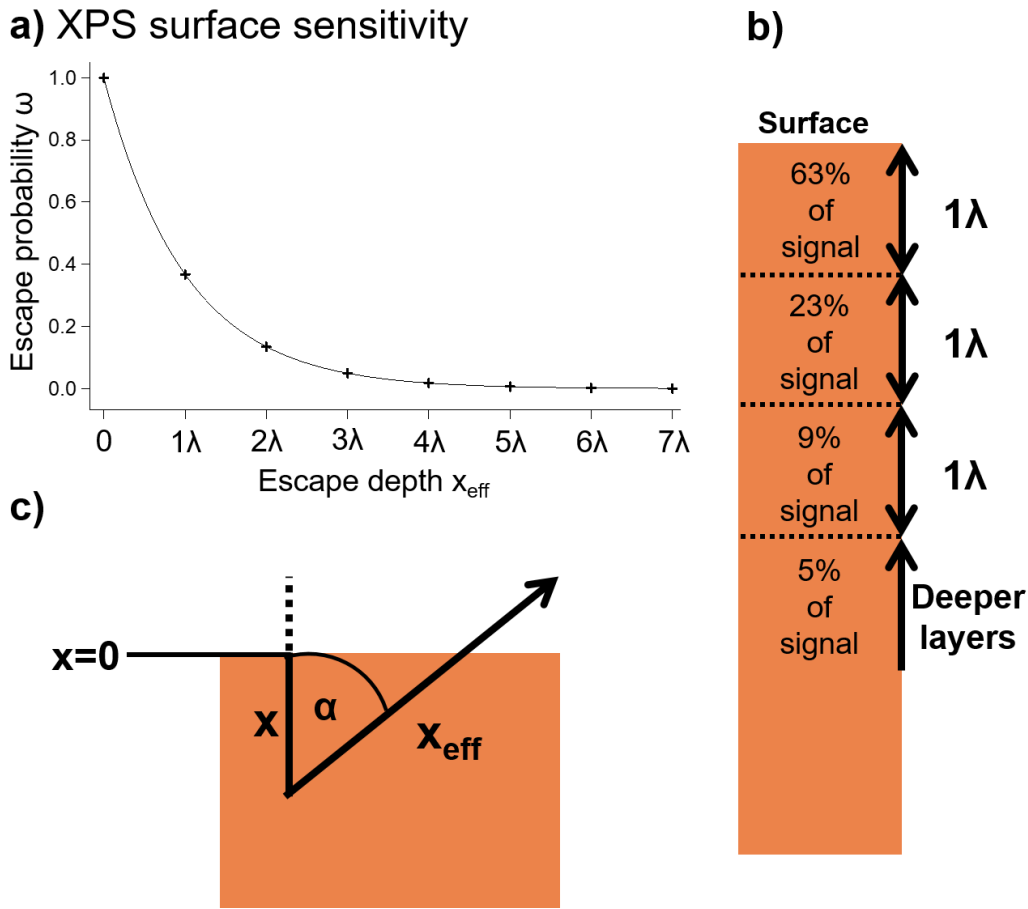


Figure 19 : XPS escape probability ω as a function of escape depth and emission angle α . a) Exponential decay of the escape probability with escape depth x_{eff} in units of the inelastic mean free path (IMFP) λ of the photoelectron. b) Illustration of the XPS signal origin. I. e., 63% of the signal originates from a sample depth of 1λ . c) The effective escape depth x_{eff} is enlarged if photoelectrons are detected at an emission angle α deviating from normal emission.

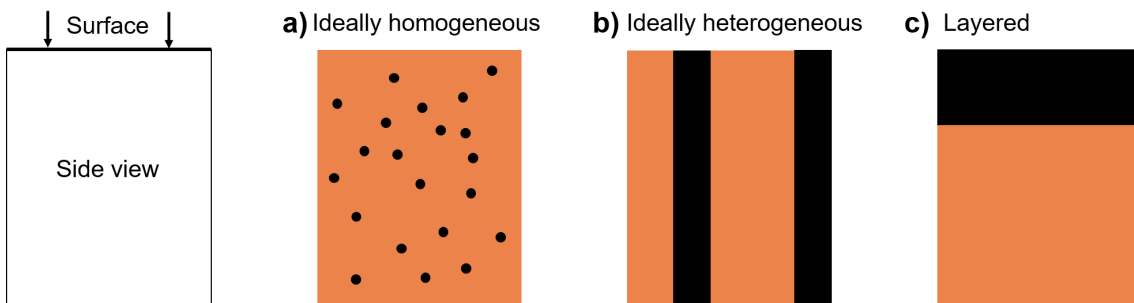


Figure 20 : Possible sample compositions leading to different photoelectron signal ratios in photoelectron spectra. Two species can be present in one sample either a) in an ideal homogeneous mixture b) completely separated laterally c) in a layered manner. The photoelectron spectra obtained for these cases are discussed in the text.

Case a): The first case refers to an ideally mixed sample. In this case, the escape probability ω can be neglected, as the sample composition does not change with the sample depth. When comparing the obtained signal intensities of both sample components (in this case named i and k), the incoming light source intensity is equal and cancels in the intensity ratio. The amount of irradiated atoms can be replaced by the atomic fraction x_i and x_k of each species. In the special case of a two-component system, component x_k can be replaced by $1 - x_i$, as $x_i + x_k = 1$. The resulting intensity ratio is determined as shown in eq. 3.7.

$$\text{Case a) : } \frac{I_i}{I_k} = \frac{x_i * \sigma_i * \tau_i}{(1 - x_i) * \sigma_k * \tau_k} \quad (3.7)$$

In the case of similar kinetic energies of the evaluated photoelectrons, this relation simplifies to:

$$\text{Case a) : } \frac{I_i}{I_k} = \frac{x_i * \sigma_i}{(1 - x_i) * \sigma_k} \quad (3.8)$$

Case b): This case represents a completely separated system, as would be the case if large particles of component i are present on the sample surface that are thicker than $\approx 3 \times IMFP$ of the released electrons. Modifications in the surface geometry are neglected in this case. Equally to case a), I_0 cancels. The total number of irradiated atoms $N_{Irradiated}$ is now dependent on the relative surface area coverage of each component, y_i , and the molar volume of each species, $V_{(m,i)}$:

$$\frac{N_i}{N_k} = \frac{y_i * V_{(m,i)}}{y_k * V_{(m,k)}} \quad (3.9)$$

The escape probability ratio ω_i/ω_k between both components can be calculated by integrating over the complete sample depth from the sample surface ($x = 0$) to the sample bulk ($x = \infty$). As shown in eq. 3.10, this integral equals λ , which leads to the ratio ω_i/ω_k to be the ratio of the respective IMFP λ_i/λ_k at the measured wavelength.

$$\int_0^{\infty} \omega dx = \left[-\lambda e^{-\frac{x}{\lambda}} \right]_0^{\infty} = \lambda \quad (3.10)$$

Within this simplified model, N and ω are not correlated. All these factors lead to eq. 3.11.

$$\text{Case b) : } \frac{I_i}{I_k} = \frac{y_i * V_{(m,i)} * \sigma_i * \tau_i * \lambda_i}{(1 - y_k) * V_{(m,k)} * \sigma_k * \tau_k * \lambda_k} \quad (3.11)$$

In the case of similar kinetic energies of the photoelectrons, this relation simplifies to:

$$\text{Case b) : } \frac{I_i}{I_k} = \frac{y_i * V_{(m,i)} * \sigma_i * \lambda_i}{(1 - y_k) * V_{(m,k)} * \sigma_k * \lambda_k} \quad (3.12)$$

Case c): Most interesting for 2D-materials is the case utilized to describe layered systems. Assuming that species i covers species k with a layer of defined thickness d , we must differentiate between both species. The surface species i can be calculated analogously to case a), with the sample ratio being $x_i = 1$ and the special case that the total signal is only obtained from the surface to the depth d . The integral over ω_i from $0 - d$ is:

$$\int_0^d \omega_i dx = \left[-\lambda_i e^{-\frac{x}{\lambda_i}} \right]_0^d = \lambda_i * (1 - e^{-\frac{d}{\lambda_i}}) \quad (3.13)$$

The signal of species k can also be calculated according to case a) with $x_k = 1$ and the addition that only the fraction $\omega_k = \omega(x = d, E_{kin,k}) * \omega_0$ leaves the sample. This leads to the relation:

$$\frac{\int_0^d \omega_i dx}{\int_d^\infty \omega_k dx} = \frac{\lambda_{(i,1)} * (1 - e^{-\frac{d}{\lambda_{(i,1)}}})}{\lambda_k * e^{-\frac{d}{\lambda_{(i,2)}}}} \quad (3.14)$$

Please note that $\lambda_{(i,1)}$ refers to the IMFP of an electron with kinetic energy relating to signal i through material i , while $\lambda_{(i,2)}$ refers to the IMFP of an electron with kinetic energy relating to species k through material i . Only if $E_{kin,i} \approx E_{kin,k}$ can these two values be seen as equal. For the ratio between both signal intensities, these relations lead to:

$$Case\ c) : \frac{I_i}{I_k} = \frac{V_{(M,i)} * \sigma_i * \tau_i}{V_{(M,i)} * \sigma_k * \tau_k} \frac{\lambda_{(i,1)} (1 - e^{-\frac{d}{\lambda_{(i,1)}}})}{e^{-\frac{d}{\lambda_{(i,2)}}}} \quad (3.15)$$

In the case of similar kinetic energies of the photoelectrons, this relation simplifies to:

$$Case\ c) : \frac{I_i}{I_k} = \frac{V_{(M,i)} * \sigma_i}{V_{(M,i)} * \sigma_k} \frac{\lambda_i}{\lambda_k} (e^{\frac{d}{\lambda_i}} - 1) \quad (3.16)$$

Note that in case of non-normal emission d has to be replaced by $d/\cos(\alpha)$, with α being the emission angle (see Fig. 20).

Experimental Setup

A commercial XPS setup provided by VSW was used for sample characterization. A load lock was attached to the setup for sample insertion into the vacuum system. The used X-ray source (TA10, VSW) was not monochromatized. Unless otherwise stated, spectra were recorded using the $Al - K\alpha$ irradiation. Photoelectrons were analyzed using a hemispherical analyzer (HA100, VSW, $\Phi_{analyzer} = 5.15\ eV$) with a constant pass energy of $22.4\ eV$ and detected using a channeltron multiplier.

The transmission function of the analyzer was experimentally determined to be:¹⁷⁴

$$\tau \sim (E_{kin})^{-0.7} \quad (3.17)$$

Additionally to the XPS measurement in this vacuum chamber, the sample surface cleaning was possible by Ar-ion-sputtering and the sample could be heated up to $650\ ^\circ C$.

Calibration to a single graphene layer

The XPS setup was calibrated to obtain the carbon/copper signal ratio for SLG. For this calibration procedure, several completely covered graphene film samples were synthesized and analyzed using the XPS spectrometer. The calibration procedure is described in detail in Appendix 12.1.

3.4. Analysis and modification of grown graphene samples

After the graphene growth procedure, grown graphene flakes can be evaluated using optical microscopy and the degree of recrystallization of the Cu substrate can also be determined. An essential part of the preparation of graphene-based devices is the detachment from the growth-substrate and the respective transfer of the graphene layer to the desired final substrate. These post-growth analyses and treatments are introduced in this section.

3.4.1. Flake density and size analysis

The graphene flake size distribution of the final sample contains information about the temporal evolution of the graphene flakes in the reaction atmosphere. In literature, mostly either individual graphene flakes are chosen to illustrate the acquired results²¹⁷ or the graphene-covered area (regardless of the individual flakes) is determined as a measure of growth progress.¹⁷³ In this work I separate the evaluation of the nucleation process strictly from the following graphene flake evolution. The grown graphene samples are oxidized in air to visualize the graphene flakes and allow analysis via optical microscopy. The nucleation density is analyzed by determining the total amount and position of the formed graphene islands. Dividing the sample surface into squares of 1x1 mm size and color-coding them regarding the number of graphene flakes formed in this area, as shown in Fig. 21, allows checking if the nucleation points are statistically distributed. The total amount of nucleated flakes divided by the sample size leads to the nucleation density η_{nuc} . The flake sizes of the graphene flakes are measured by determining the hexagon's outer circle diameter D (see Fig. 22) and converting it into the inner radius r of a regular hexagon according to equation 3.18.

$$D = 2 * R = 2 * \frac{2}{\sqrt{3}} * r \quad (3.18)$$

The flake area of the hexagonally shaped graphene islands can be calculated by eq. 3.19:

$$A = 2\sqrt{3} r^2 \quad (3.19)$$

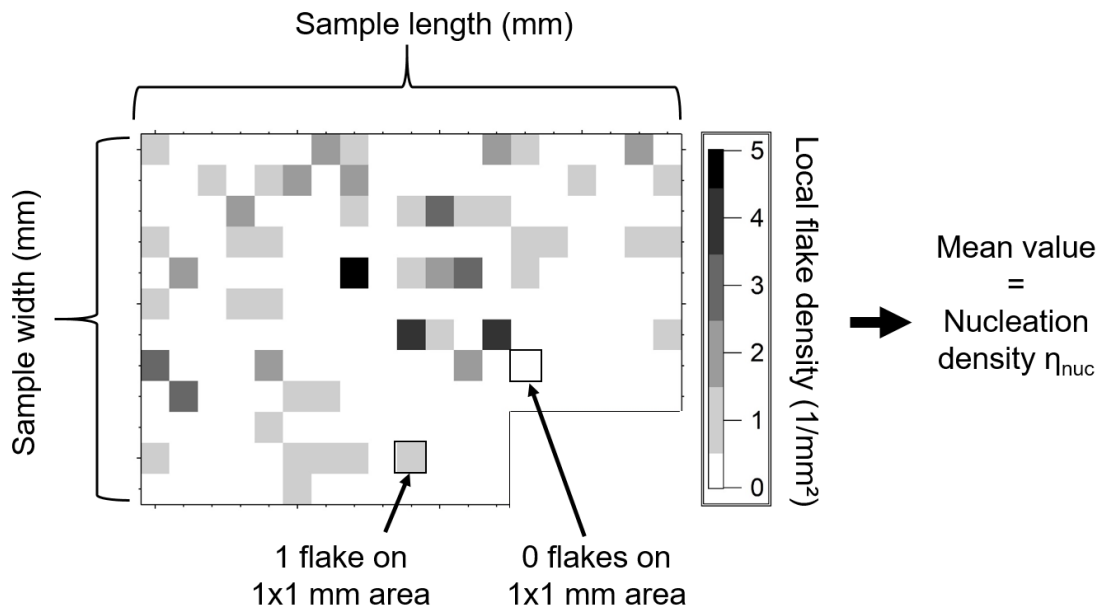
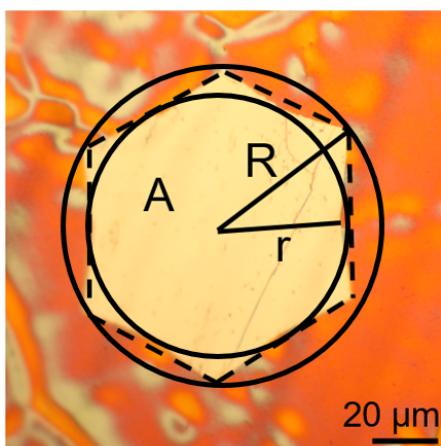


Figure 21 : Exemplary illustration of a statistically evaluated graphene flake sample. The sample is divided in squares of $1 \times 1 \text{ mm}$ size and the graphene flakes in each square are determined, visualized in different grayscales in the figure. This allows the assessment if a statistical distribution of the flakes is present on the sample, as is the case for the shown sample. The nucleation density of the complete sample is η_{nuc} .



A = Flake area
 r = Radius of the inner circle
 R = Radius of the outer circle

Figure 22 : Geometry of a hexagonal graphene flake and the relevant parameters for its description.

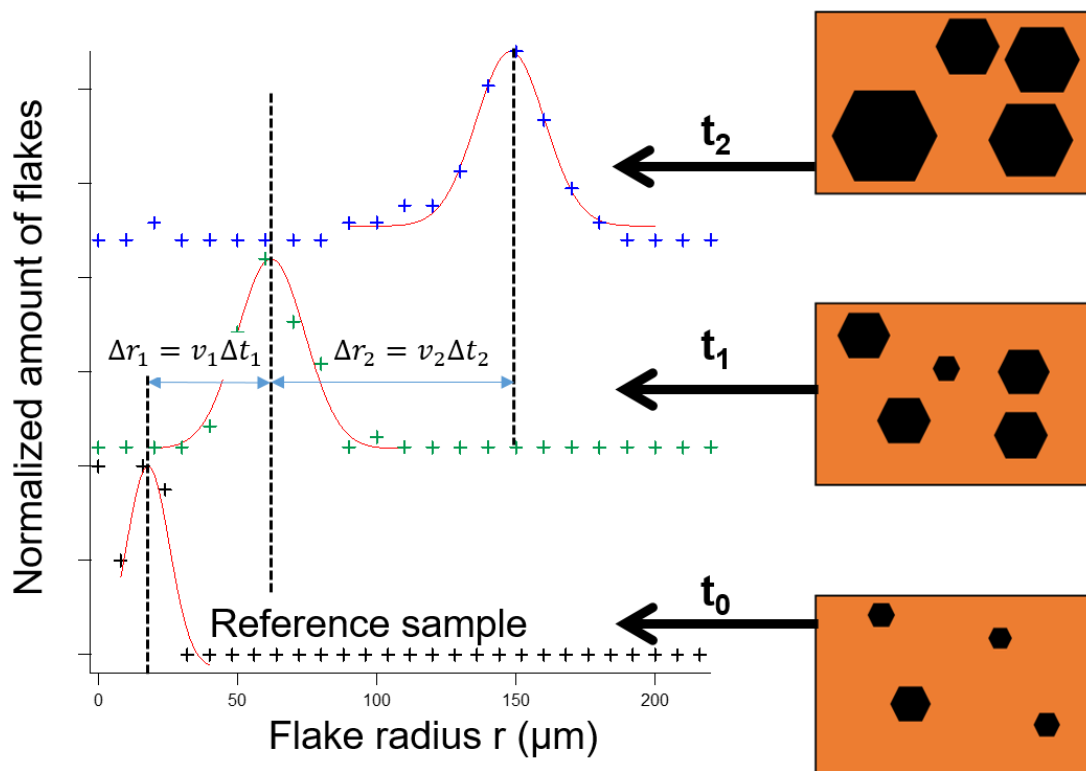


Figure 23 : Flake size distribution histograms for three samples grown for different times t , normalized to the respective maximum value. The graphene growth velocity can be extracted from the difference in distribution maxima from two samples divided by the respective additional growth time. Adapted with permission from ¹²⁸. Copyright 2021 American Chemical Society.

Counting the appearance of flakes of a given radius r enables one to derive a histogram of the grown graphene flakes on Cu, as shown in Fig. 23. The most precise method to determine the graphene flake size evolution is to determine the differences in flake size distribution between samples before and after the exposure to a specific growth condition. As described in the chapter Reactor setup, the experimental procedure allows the parallel growth on three Cu samples, which can be removed from the growth atmosphere at different times. On each sample, the monitored flakes are evaluated regarding their flake radius, as shown in Fig. 23. The difference Δr divided by the difference in growth time is defined as the growth velocity v . While the first extracted graphene sample serves as a zero-point reference, growth velocities can be extracted for both following samples. In most growth experiments the new formation of graphene flakes can be expected to happen at the start of the reaction, leading to Gaussian curves as shown in Fig. 23. Exceptions to this case are determined in chapter 6.

3.4.2. Cu surface analysis

Several literature studies have reported treatment protocols for the complete recrystallization of the copper foil prior to graphene growth, leading to a single-crystalline substrate.^{31,218,219,26,220,221,222} Mainly, the procedure proposed by Reckinger *et al.*³¹ is associated with the formation of copper oxide particles on the surface during the pretreatment phase, which pin the underlying Cu grain boundaries, inhibiting their coalescence. Sudden changing of the condition to a reductive H₂ atmosphere removes the oxide particles and enables abnormal grain growth, during which a very fast grain growth towards (111)-type grains is observed.

This type of grain growth is similarly observed when applying the treatment outlined in Fig. 11: At first the sample is heated in a hydrogen atmosphere to 950 °C and then undergoes an oxidative treatment in an Ar + O₂ atmosphere. After this treatment, the reaction gas phase is quickly changed to a reductive hydrogen atmosphere again. In the first moments after this reduction, the strongest grain growth in the Cu foil is observed, as also described by Reckinger *et al.*³¹

If a sample is removed after the oxidative pretreatment step, slight oxidation is observed in the form of round particles distributed over the sample. Such a sample is shown in Fig. 24a), where the Cu grains do not exceed 100 μm and the oxide particles are often found at the grain boundaries. Already after a short exposure to hydrogen, the Cu grain growth sets in and most Cu grains merge to one grain of several mm-cm in size. The change of the sample shown in Fig. 24a) after 5 min exposure to 100 mbar H₂ is shown in Fig. 24b). While the morphology still keeps the remainders of the original Cu grains, the coloring during oxidation and the orientation of the enlarged minor facets grains²¹⁸ (here referred to as twin crystals)^{223,224} in angles of 60° and 120° over a wide distance proves the merging to one large Cu grain. This recrystallization process is strongly dependent on the reaction temperature, below 1000 °C it is comparatively slow, at 1045 °C (≥ 5 min reduction) mostly about 80% of the sample consist of such ultra-large grains and at temperatures above 1060 °C the sample mostly consists purely of such grains. After graphene growth in H₂ + CH₄ atmosphere at 1045 °C, the Cu foil shows strong recrystallization, as is shown exemplarily in Fig. 24c). This optical image shows an oxidized Cu sample. The main Cu grain obtained from the recrystallization stretches over most of the central Cu foil.

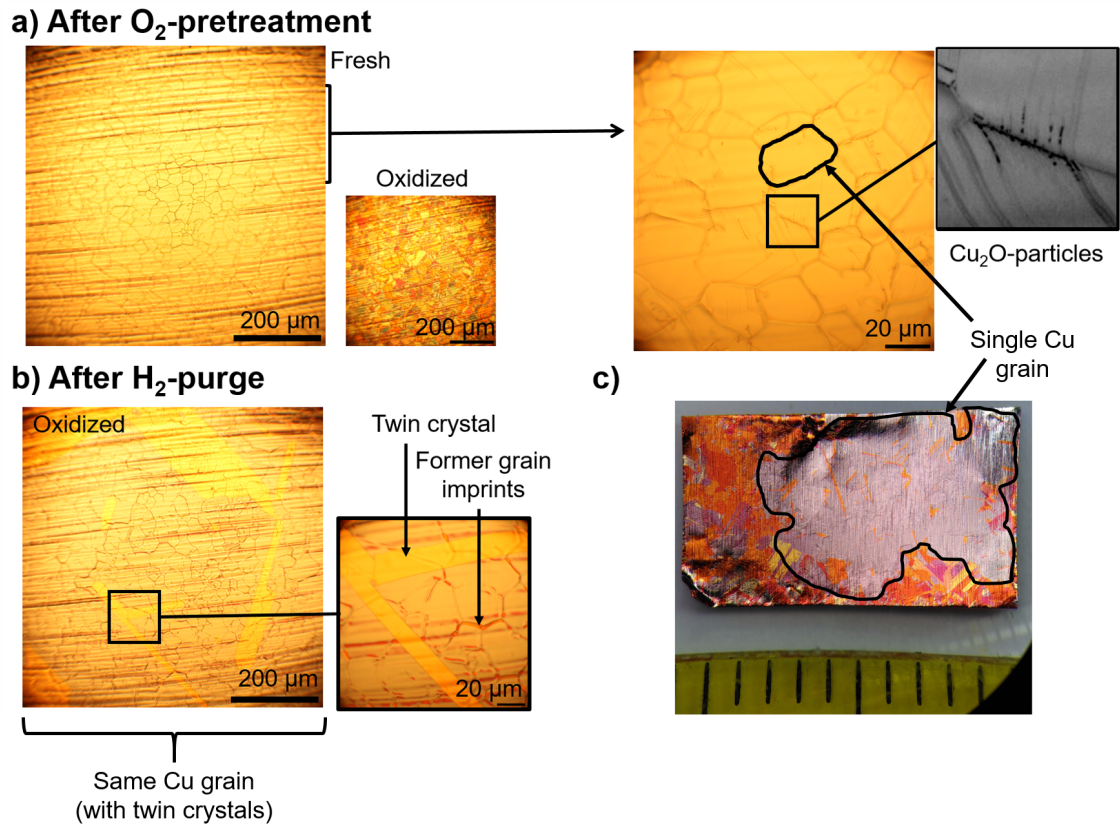


Figure 24 : Copper substrate composition in dependence of the gas phase of the last treatment step. a) In case of a purely oxidative atmosphere, the Cu grains remain in the diameter regime below $100\ \mu\text{m}$ (marked with an arrow in the magnification). The grain boundaries can be identified by the coloring after oxidation (inset), where all individual grains show slightly different coloring. The magnified image shows slight formation of copper oxide particles, which may grow during the cooling of the sample in the oxidative atmosphere, as the formation of copper oxide particles is favored at lower temperatures.¹⁸⁵ b) After the purging of the O_2 -pretreated sample with H_2 , the former grain boundary imprints remain in the surface morphology. The uniform coloring of the foil upon oxidation shows that all small grains merged to one large Cu grain. The formation of twin crystals of identical orientation over large distances backs this up.^{223,224} c) Low magnification image of the common grain distribution of a pretreated Cu foil. One large Cu grain extends over most of the sample area, while the grain restructuring is typically lower at the sample edges. (Experimental details: a,b: E. 3 , c: E. 4)

From empirical observations, the recrystallization of the Cu grains seems to be sensitive regarding:

- The switching temperature (increasing recrystallization with temperature)
- The applied pressure of hydrogen during abnormal grain growth (increasing recrystallization with hydrogen pressure)
- Residual impurities in the Cu foil (reduced recrystallization through pinning with impurities)
- Deformations in the Cu foil, e.g. at the foil borders where the foil has been cut (reduced recrystallization at stronger deformations)

For most of the experiments performed in this work, Cu grain recrystallization conditions were chosen similar to the ones leading to the sample shown in Fig. 24c), which was grown according to the reaction recipe shown in Fig. 11.

3.4.3. Transfer techniques

If the synthesized graphene sheet shall be used on a different substrate than the Cu foil for its final application, the graphene layer must be separated from the Cu substrate and transferred onto a new target. The separation of graphene from the underlying Cu mainly follows two different approaches. The graphene can be detached from the surface while both the graphene sheet and the substrate material are preserved. This separation is achieved by the so-called bubbling transfer method.^{225,226} The other option is to chemically or electrochemically decompose the growth substrate. Both processes are described in Fig. 25 and in detail also in reference¹⁹. In the usually executed approaches of both transfer procedures, the graphene must be protected by a polymeric layer, such as polymethyl methacrylate (PMMA). Then the graphene+polymer stack can be separated from the underlying substrate by using the Cu foil and a Pt foil as electrodes for the electrolysis of water, where the hydrogen evolution reaction (HER) on the Cu side softly lifts the graphene from the metal substrate (see Fig. 25, step iii [a]). The second possibility is to remove the entire substrate either by electrochemical transport of Cu to a Cu counter electrode, or by etching the Cu in a reactive solution, such as aqueous iron(III) nitrate ($Fe(NO)_3)_3(aq.)$,²²⁷ iron chloride ($FeCl_3(aq.)$)²²⁸ or ammonium persulfate ($(NH_4)_2S_2O_8(aq.)$)⁶⁹ (see step III [b] in Fig. 25). In both cases, the protected graphene layer remains floating on top of the solution, which can be exchanged several times by deionized water. The stack can then be fished with the desired new substrate, dried to remove any water trapped in between the layers and finally, the protection layer can be dissolved in hot acetone.

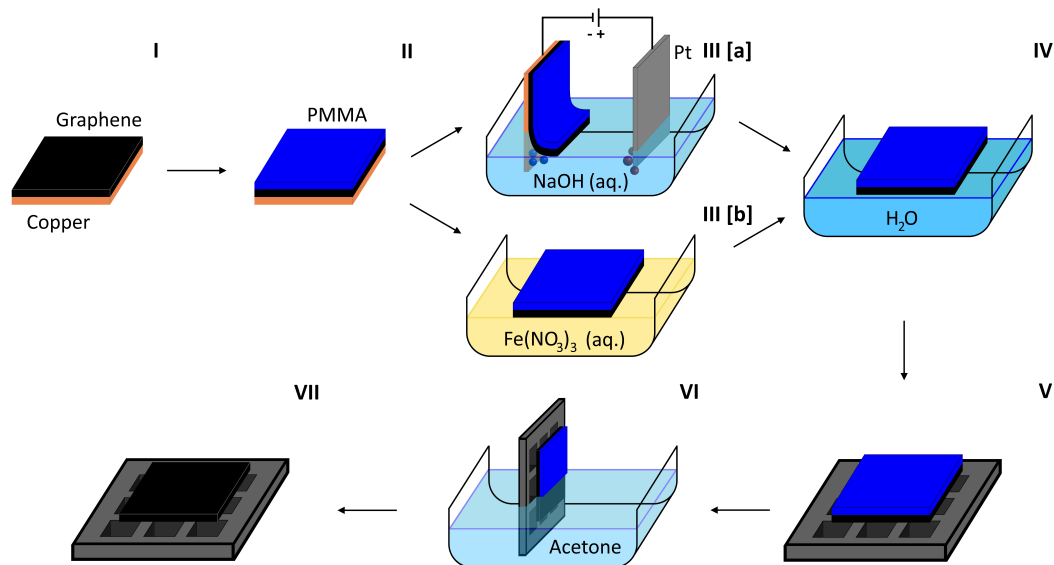


Figure 25 : Typical transfer protocols for the formation of freestanding graphene membranes after synthesis by CVD on Cu (Step I). The graphene is protected by a polymer layer (Step II) and then separated from the Cu substrate either by gas formation in between graphene and Cu (so-called "bubbling transfer", Step III a) or by etching of the metal (Step III b). After cleaning in different solutions and their exchange with water (Step IV), the floating graphene-polymer stack can be fished with the desired holey substrate (Step V), dried, and the polymer can be removed e.g. by dissolution in organic solvent (Step VI), leading to the final product (Part VII). Reprinted with permission from reference ¹⁹.

These transfer techniques have been often modified to increase the yield, quality or purity of the obtained membranes. The etching approach for example imposes less stress on the graphene membrane, which is why it is possible to remove the growth substrate while only partly protecting the graphene layer with a protective frame.^{87,229} Other groups performed the etching transfer procedure by protecting the complete graphene layer with an ultra-thin evaporated metal layer²³⁰ or by placing the destination substrate on top of the g/Cu stack while etching the Cu layer.²³¹ The dissolution of the substrate though is often also associated with an increased amount of impurity particles remaining attached to the graphene membrane after transfer.⁷² This may be caused by insoluble impurities in the original foil or residues of the etching solution.

The graphene transfer using the 'bubbling transfer' approach is usually performed with thicker protection layers, so that the removal of this layer after transfer is especially delicate. A thicker polymeric layer leads to a stiffening of the PMMA/graphene stack, lowering the mechanical contact between stack and target and reducing the stability of the graphene membrane. In order to reduce the stress acting on the membrane, drying of liquid wetting films with high surface tension has shown to be critical, therefore the drying by gradual exchange of the solvent with liquids of lesser surface tension⁷¹ or by passing over the critical point of the solvent²³⁰ (liquid to gaseous transition without boiling) have

been used. As especially successful has proven a combination of solvent-exchange with a special sample geometry avoiding the formation of solvent-filled cavities.⁷²

Several studies have tried to pinpoint the path leading to the cleanest results.^{232,233} Nevertheless, these modification steps in air and even in solution require additional post-treatment steps before the samples are suited for UHV-applications. Precleaning steps have been proposed, including the heating in presence of activated carbon,²³⁴ the heating after deposition of Pt nanoparticles²³⁵ or a very long and mild annealing step to desorb any unwanted species from the sample.⁷¹

Apart from these approaches, a large number of transfer procedures have been developed for very specialized cases, e.g. for graphene on transparent polyethylene terephthalate (PET)²³⁶ and other polymers,²³⁷ graphene/h-BN stacks²³⁸ or graphene on hydrophobic surfaces.²³⁹ To omit the transfer procedure, the direct growth of graphene is often proposed on several substrates made possible by evaporating a thin Cu layer on the substrate before growth.^{240,241}

This excerpt shows that a large number of transfer procedures are described in literature. Their evaluation is difficult, as the exact transfer failure mechanisms are mostly unknown. In this work, I map out the parameters relevant for a successful graphene transfer and design transfer recipes targeted precisely for the required sample features. These are described in chapter 10.

4. Thermodynamics of the graphene formation reaction

For the experiments regarding the thermodynamic equilibrium of graphene, the starting system always consists of pre-grown, isolated graphene flakes, as sketched in Fig. 26. This allows the modeling of the growth geometry as an isolated, single graphene flake if the islands are at sufficient distance from each other. A detailed analysis on how to achieve this starting position by controlling the graphene nucleation density is performed in chapter 6. The implemented measures to suppress the influence of contaminants are discussed in chapters 8 (oxygen) and 9 (silicon and carbon).

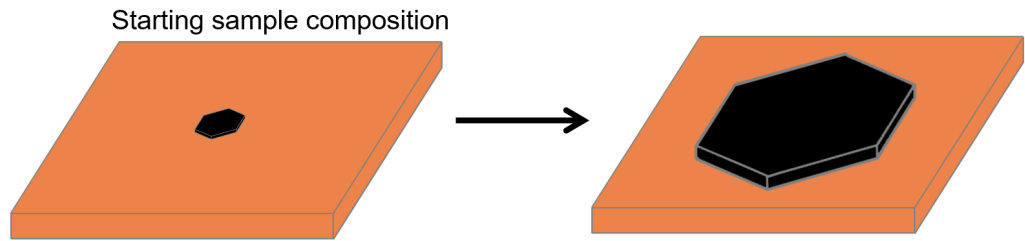


Figure 26 : The experiments performed regarding the thermodynamics and kinetics of the graphene formation reaction use pre-grown graphene flakes as starting geometries to monitor changes in the sample composition after exposure to specific reaction conditions.

4.1. Graphene decay in the reactive gas atmosphere of $CH_4 + H_2$

According to the relations given in section 2.2, the equilibrium constant of the graphene formation reaction, K_{eq} , is defined over the Gibbs free energy $\Delta_R G^\circ$, or the ratio between the activity of products and educts, as shown in eq. 4.1:

$$K_{eq} = \exp\left(-\frac{\Delta_R G^\circ}{RT}\right) = \frac{a(g)_{eq} * a(H_2)_{eq}^2}{a(CH_4)_{eq}} = \frac{1 * [p(H_2)_{eq} p^\ominus]^2}{p(CH_4)_{eq} p^\ominus} = \frac{p(H_2)_{eq}}{p^\ominus} w_{eq} \quad (4.1)$$

In eq. 4.1, $a(X)$ is the respective activity of the species X. The activity of solid species present in the reaction volume, in this case graphene, equals 1, and the one of gaseous species can be approximated by the respective partial pressure divided by the standard pressure p^\ominus of 1 bar. The ratio between hydrogen and methane partial pressure is abbreviated with the acronym w . The product of pressure and w -ratio set in an experiment is

defined as mass action constant Q_{exp} :

$$Q_{exp} = \frac{p(H_2)}{p^{\varnothing} - w} \quad (4.2)$$

Setting reaction conditions $Q_{exp} < K_{eq}$ thermodynamically favors the growth of graphene flakes, reaction conditions above equilibrium ($Q_{exp} > K_{eq}$) lead to graphene decay. When plotted logarithmically in a diagram with $p(H_2)$ and the w -ratio as axis, the condition $Q_{exp} = K_{eq}$ is fulfilled along a diagonal from the upper left to the lower right corner. This is schematically shown in Fig. 27.

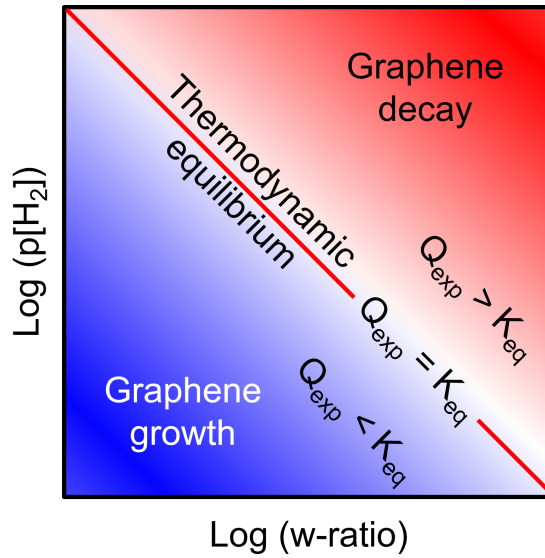


Figure 27 : Graphene formation diagram with a logarithmic plot of the hydrogen partial pressure and the w -ratio of hydrogen to methane. The thermodynamic equilibrium K_{eq} of the graphene formation reaction from methane at a certain temperature shows as a straight line in the logarithmic $p(H_2) - w$ -plot. At experimental conditions found below this line in the diagram (blue zone), graphene formation is expected, while above the K_{eq} -line (red zone), graphene should decay.

An experimental series with stepwise increasing values of Q_{exp} was conducted to visualize the effect of the reaction atmosphere on the graphene flake evolution and to localize the position of K_{eq} . Graphene flakes were nucleated at conditions far away from equilibrium for 2-5 min and then exposed to a certain value of Q_{exp} . A reference sample was removed from the growth reactor after changing to growth conditions, a second sample was left in the reactive atmosphere for 120 min.

Figure 28 shows optical images of representative flakes before and after this growth step, as well as a histogram showing the complete distribution of measured graphene radii on the sample. The mean graphene flake size clearly increases for the samples exposed to Q_{exp} values of 57 (a), 81 (b) and 88 (c), while a decrease is observed for $Q_{exp} = 102$.

Here, the flake sizes after 120 min of exposure to the reactive conditions are smaller than the originating nucleated graphene flakes. This leads to the conclusion that the value of K_{eq} at 1045 °C must lie somewhere in between 88 and 102. The precise value determination is specified in the next chapter, whereas in the following the different observed shapes are described. Since Raman spectroscopy identifies more than 90% of the formed flakes as single layer graphene (SLG), the experiments reflect the thermodynamics of the SLG formation on Cu.

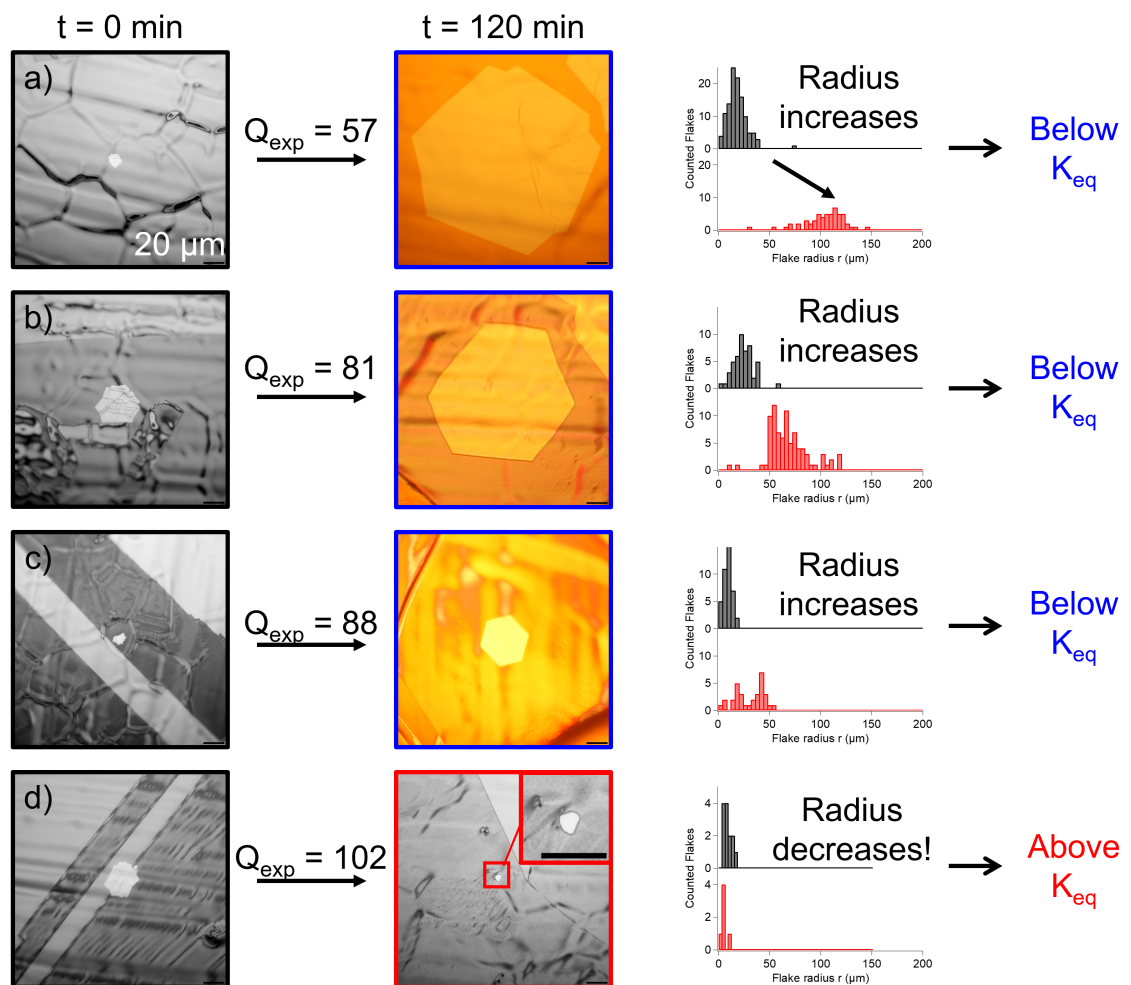


Figure 28 : Experimental determination of the thermodynamic equilibrium line K_{eq} . Pre-grown graphene flakes ($t = 0 \text{ min}$) are exposed to defined reaction conditions to explore the growth/decaying behaviour at certain points in the $p(H_2) - w$ -diagram. Growth or decay are identified by the development of the mean graphene flake radii over a reaction time of 120 min. While the graphene flake evolution towards larger flakes is very clear in sample a), it continuously diminishes for samples b) and c), grown at higher values of Q_{exp} . For sample d) grown at $Q_{exp} = 102$, the flake radii decrease during exposure to the reactive atmosphere, leading to the conclusion that the thermodynamic equilibrium is surpassed in this experiment. (Experimental details: a: E. 60 , b: E. 63 , c: E. 5 , d: E. 6)

Graphene flakes exposed in the last step of the experiment to growth conditions show an overall hexagonal shape. It was observed that the ideal hexagonal shape is strongly favored closer to K_{eq} , while at conditions far away from equilibrium $Q_{exp} \ll K_{eq}$ also in some cases more dendritic shapes are observed.

Thermodynamically, the crystal edge with the slowest attachment rate (energetically most favorable) will define the edge shape of the developed flake.^{242,243} On the opposite, the decomposition shape of crystals is defined by the edge with the highest detachment rate.²⁴² For graphene on platinum²⁴³ and on copper²⁴² in the literature dodecagonal shapes are predicted for decaying graphene flakes in an intermediate phase, while the favored final structure should be armchair-like. Regarding this aspect, the results obtained in this group rather show an overall rounded flake shape when changing to decaying conditions, as e.g. displayed in Fig. 28d). The emerging shape can also be influenced by morphological aspects or Cu grain boundaries. In case of an emerging round flake shape, the detachment barrier for graphene rim atoms would be equal at all rim positions, without setting a preferred etching edge.

While in literature the outer shape change of graphene flakes is mainly described for conditions without methane ($Q_{exp} = \infty$)^{244,242} or far away from the thermodynamic equilibrium ($Q_{exp} \gg K_{eq}$)^{245,126} the presented results show that this shape modification already takes place close to K_{eq} and can therefore be used as a criterion to determine the precise position of the thermodynamic equilibrium. Experiments as shown in Fig. 28d) are difficult to realize due to the major drawback that the overall graphene flake growth or decay at conditions close to the equilibrium slows down to zero, which consequently requires extremely prolonged exposure times to measure an unambiguous flake size change. As the flake shape changes from hexagonal to round happens according to the absolute attachment- and detachment rates (which are not zero close to the equilibrium, only the resulting overall reaction rate goes towards zero), it allows a faster determination of the growth regime.

4.2. Determination of the thermodynamic equilibrium constant K_{eq}

4.2.1. Determination at constant temperature $T = 1045^\circ\text{C}$

Using the flake shape criterion introduced in the previous chapter as feature for identification of growth/decaying conditions, an experimental series was conducted to determine the position of the thermodynamic equilibrium at $T = 1045^\circ\text{C}$. In these experiments, the graphene reactor was loaded with three Cu foil samples, allowing the investigation of two reaction conditions in one experiment, together with a referencing sample removed directly after the nucleation step. The procedure is schematically illustrated in Fig. 29. SLG flakes are at first nucleated far away from equilibrium ($Q_{exp} = 10 - 25$), then they are

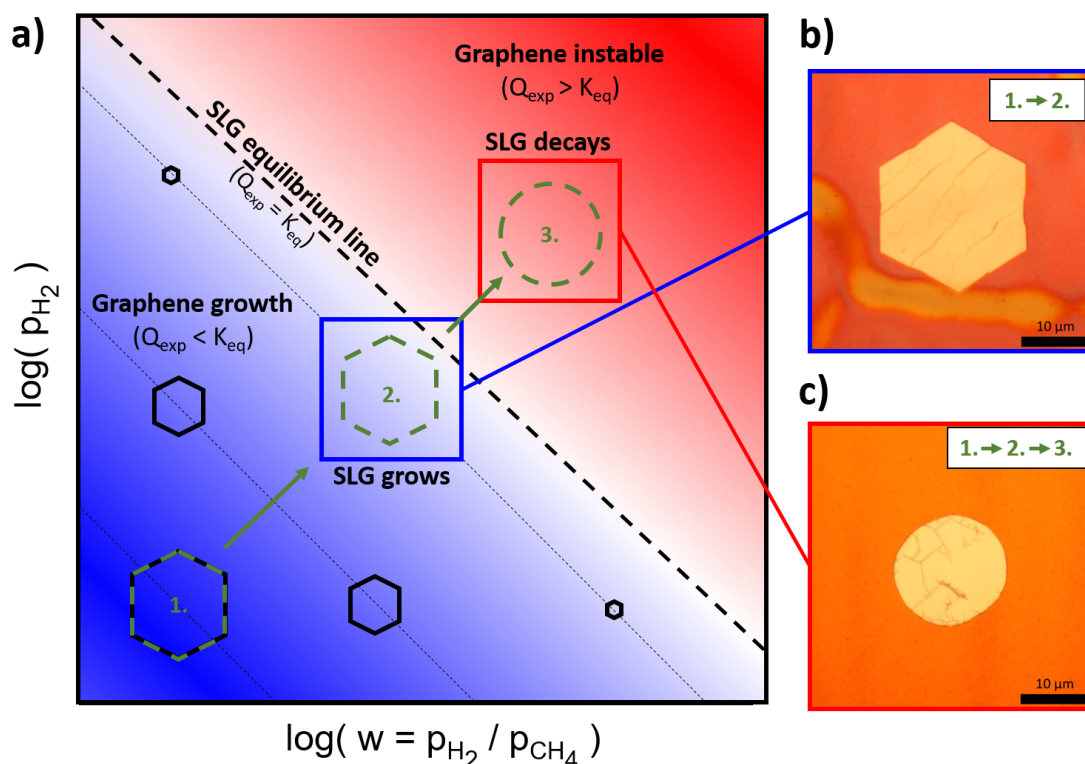
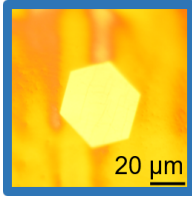
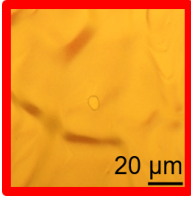
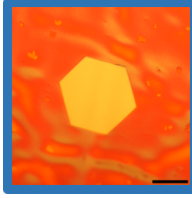
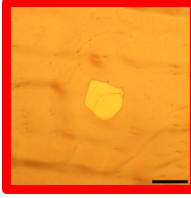
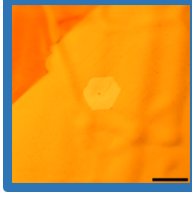
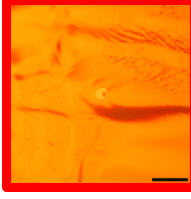
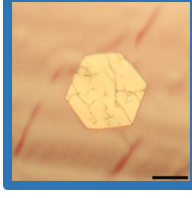
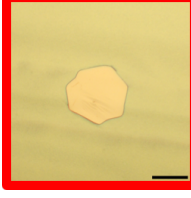
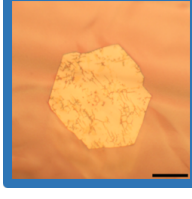
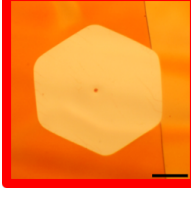
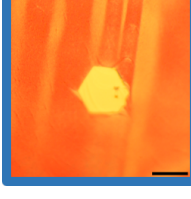
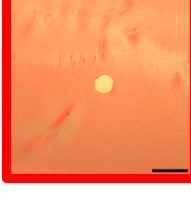


Figure 29 : Scheme for the proceeding to accurately pinpoint the equilibrium line below and above K_{eq} in a single reactor experiment. 1. Graphene flakes must be pregrown further away from equilibrium to enable sufficient nucleation events on the sample. 2. The reaction conditions are modified to conditions expected to be slightly below K_{eq} in the "growth-zone". Immediately after setting these conditions, the first sample is removed from the hot reactor zone. After a certain reaction time, the second sample can as well be removed from the reactor. 3. Changing the reaction conditions again to higher values of Q_{exp} leads to the acquisition of a third data-point, slightly above thermodynamic equilibrium. The observed morphological change indicates the crossing of the equilibrium. Reprinted with permission from reference ²⁴⁶. Copyright 2021 American Chemical Society.

exposed to conditions expected to be closely below the equilibrium, where the graphene growth should diminish to an almost undetectable value, nevertheless maintaining its hexagonal shape. Subsequently, modification of the growth atmosphere to slightly higher Q_{exp} values above the equilibrium concentration will trigger the shape change (step 3), which can be detected by optical microscopy after the reaction, as shown exemplarily in Fig. 29b) and c). The procedure is designed in this particular way, as it combines the possibility of testing two growth points per experiment with a simplified sample characterization. As was discussed in the previous chapter, graphene growth very close to the equilibrium produces flakes of almost ideal hexagonal symmetry, allowing a precise determination of shape changes.

The results of the experimental series are summed up in Table 6.

Table 6 : Experiments conducted to pinpoint the thermodynamic equilibrium for the SLG formation reaction at 1045 °C with exemplary optical images. Reactions below K_{eq} are marked blue, above red.

#	Reaction steps 1+2		Reaction steps 1+2+3	
	p (mbar) w-ratio Q_{exp}	Optical image	p (mbar) w-ratio Q_{exp}	Optical image
Exp. E. 5	p = 47.6 mbar w = 1839 $Q_{exp} = 87.5$		p = 49.1 mbar w = 2095 $Q_{exp} = 102.9$	
Exp. E. 7	p = 37.4 mbar w = 2458 $Q_{exp} = 91.9$		p = 39 mbar w = 2619 $Q_{exp} = 102.1$	
Exp. E. 8	p = 28.7 mbar w = 3381 $Q_{exp} = 97.0$		p = 30.1 mbar w = 3641 $Q_{exp} = 109.6$	
Exp. E. 9	p = 43 mbar w = 2256 $Q_{exp} = 97.0$		p = 44.5 mbar w = 2429 $Q_{exp} = 108.1$	
Exp. E. 10	p = 33.6 mbar w = 2919 $Q_{exp} = 98.1$		p = 34.6 mbar w = 3237 $Q_{exp} = 112.0$	
Exp. E. 11	p = 123 mbar w = 631 $Q_{exp} = 77.6$		p = 125.1 mbar w = 678 $Q_{exp} = 84.9$	
Exp. E. 12	p = 127.8 mbar w = 650 $Q_{exp} = 83.1$		p = 140.1 mbar w = 707 $Q_{exp} = 99.1$	

Each growth sample is listed with the corresponding hydrogen partial pressure, the w -ratio and the mass action constant Q_{exp} , as well as an exemplary optical image of one flake on the oxidized sample. The border color of the image shows whether graphene growth (blue) or decay (red) was observed. Each reactor run lead to two evaluable graphene samples, which are displayed in the left column (sample removed after steps 1+2) and the right column (sample removed after steps 1+2+3) of the table. All first samples show a pronounced hexagonal shape, while the second samples mostly show a stronger deviation from the ideal towards rounded shapes. This was not observed for sample E. 11 in Table 6, where the second sample kept its pristine shape, which is why this sample was also assigned to be in the graphene growth regime.

The resulting values for Q_{exp} were inserted in a $p(H_2)$ - w -diagram shown in Fig. 30 using the same color coding (*growth = blue, etching = red*).

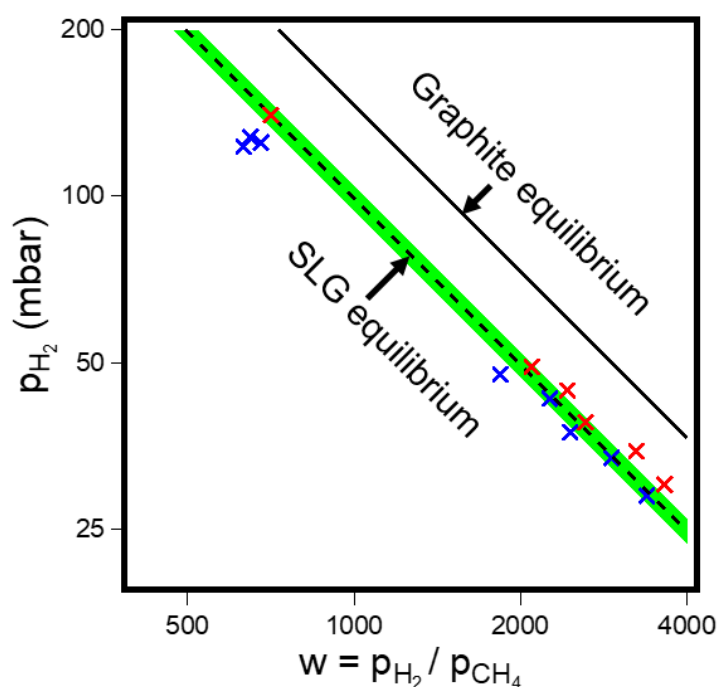


Figure 30 : Experimental results from the reactions listed in Table 6 in a $p(H_2) - w$ -diagram. Colored crosses mark the spots where experiments showed graphene growth (blue) or decay (red). The resulting SLG equilibrium line is shown as a dashed line, surrounded by the green highlighted confidence interval. The equilibrium line for the formation of graphite as extracted from literature shows a clear shift towards higher stability (continuous line).²⁴⁷ Reprinted with permission from reference ²⁴⁶. Copyright 2021 American Chemical Society.

Based on the mean value of Q_{exp} of each growth/etch pair and a standard deviation based on the distance between both data points, a value for K_{eq} was determined to be $K_{eq}(1045\text{ °C}) = 99 \pm 5$. This value is inserted in Fig. 30 in form of a dashed line, with the standard deviation shown in form of a green highlighted area. These experiments

emphasize the fact that at each temperature one specific value for K_{eq} exists, while only the product and not the individual values of its two components $p(H_2)$ and w -ratio is relevant. This value for the thermodynamic equilibrium can be converted into the Gibbs Free Energy $\Delta_R G^\circ$ using equation 4.1, which leads to $\Delta_R G^\circ (1045^\circ C) = -50.4 \pm 0.5 kJ mol^{-1}$. No values were found in literature for the Gibbs free energy $\Delta_R G^\circ$ nor for the related reaction enthalpy $\Delta_R H^\circ$ or entropy $\Delta_R S^\circ$. As the interaction between the copper substrate and the covering graphene layer is known to be low, the value for the comparable case of graphite (which can be described as graphene on graphite) was used instead.¹²⁶ This value, tabulated in the NIST-Janaf tables amounts to $\Delta_R G^\circ_{Graphite} = -54.6 \pm 0.5 kJ mol^{-1}$, which leads to a value for $K_{graphite}(1045^\circ C) = 146$. The Gibbs free energy lower by about $4 kJ mol^{-1}$ compared to single layer graphene on copper means that the formation of graphite is thermodynamically favored. The magnitude of this shift becomes optically visible by inserting the graphite equilibrium line in the $p(H_2) - w$ -diagram of Fig. 30, where a clear shift can be observed compared to the data points acquired for g/Cu.

4.2.2. Influence of O_2 on the position of the equilibrium

The results compiled in chapter 8.2 show that, under certain conditions (namely in combination with oxygen), impurities affect the growth of graphene flakes. The presence of impurities typically leads to the formation of holes in the central area of graphene flakes, while the outer rim remains unaffected. Thus, using the outer rim as flake shape criterion for thermodynamic equilibrium of the graphene formation reaction should remain valid. However, it might be possible that oxygen impurities cause the observed shift of the equilibrium line of g/Cu and g/g in Fig. 30 by influencing the equilibrium concentration of C_{ad} on the substrate.

The concentration of adsorbed oxygen under typical CVD conditions during graphene growth was estimated in chapter 2.4 to have a negligible value, which should not affect the outcome of a CVD growth experiment. In order to prove this, graphene was grown close to equilibrium conditions with additional dosing of oxygen ($1 \times 10^{-4} sccm$), resulting in a partial pressure of $1.4 \times 10^{-4} mbar O_2$ (see chapter 3.1.3). Compared to the inherent contamination of oxygen in the gas feed of $O_2 (imp) \approx 1.7 \times 10^{-5} mbar$ this is an increase by a factor 7. The used growth parameters are added in form of a black square to the $p(H_2) - w$ -diagram in Fig. 31 and optical images of the grown graphene flakes are also shown, depicting hexagonal graphene flakes without the evidence of etching at these conditions very close to the determined equilibrium conditions.

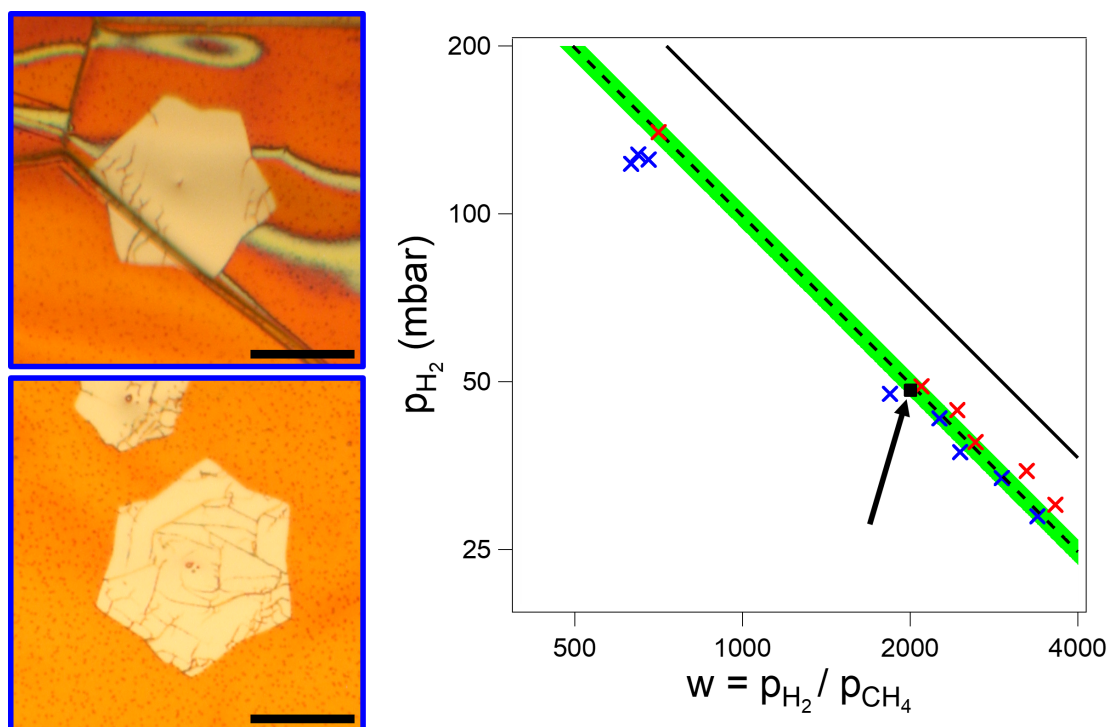


Figure 31 : Graphene growth under an increased oxygen partial pressure of $1.4 \times 10^{-4} \text{ mbar } O_2$. The used experimental conditions are marked with a black square and arrow. Growth of graphene at these conditions (see also optical images on the left side) shows that the addition of oxygen to the reactive atmosphere cannot be responsible for the shift between the equilibrium lines of graphene and graphite, as shown by the dashed and continuous lines, respectively. Scale bars amount to $20 \mu\text{m}$. Adapted with permission from reference ²⁴⁶. Copyright 2021 American Chemical Society. (Experimental details: E. 13)

Thus, the performed experiment shows added oxygen impurity 7 times larger than the one present in a clean experiment does not noticeably shift the equilibrium line. This control experiment proves that the observed shift of the g/Cu equilibrium with respect to g/g truly reflects the thermodynamics of the methane decomposition reaction on Cu towards graphene.

4.2.3. Determination of the temperature dependence of the equilibrium line

To disentangle the respective contributions of the reaction enthalpy and entropy to the Gibbs free energy, an experimental series at different temperatures was conducted analogously to the experiments at $1045 \text{ }^\circ\text{C}$ shown above. The experiments were conducted at temperatures between $970 \text{ }^\circ\text{C}$ and $1080 \text{ }^\circ\text{C}$, closely below the melting point of copper at $1085 \text{ }^\circ\text{C}$.²⁴⁷ Results of the experiments are displayed in a van't Hoff plot in Fig. 32. The respective data points are also marked in color, depending if the sample showed graphene growth (blue) or decay (red). Similar to experiments at $1045 \text{ }^\circ\text{C}$, the pressure and gas

phase ratio can be substituted by the mass action constant Q_{exp} in the diagram, which allows the temperature-dependent plot in a $\ln(Q_{exp}) - T$ -diagram of the performed experiments. The results of experiments conducted at 1045 °C compiled in panel a) appear as crosses at the respective point on the x-axis in panel b).

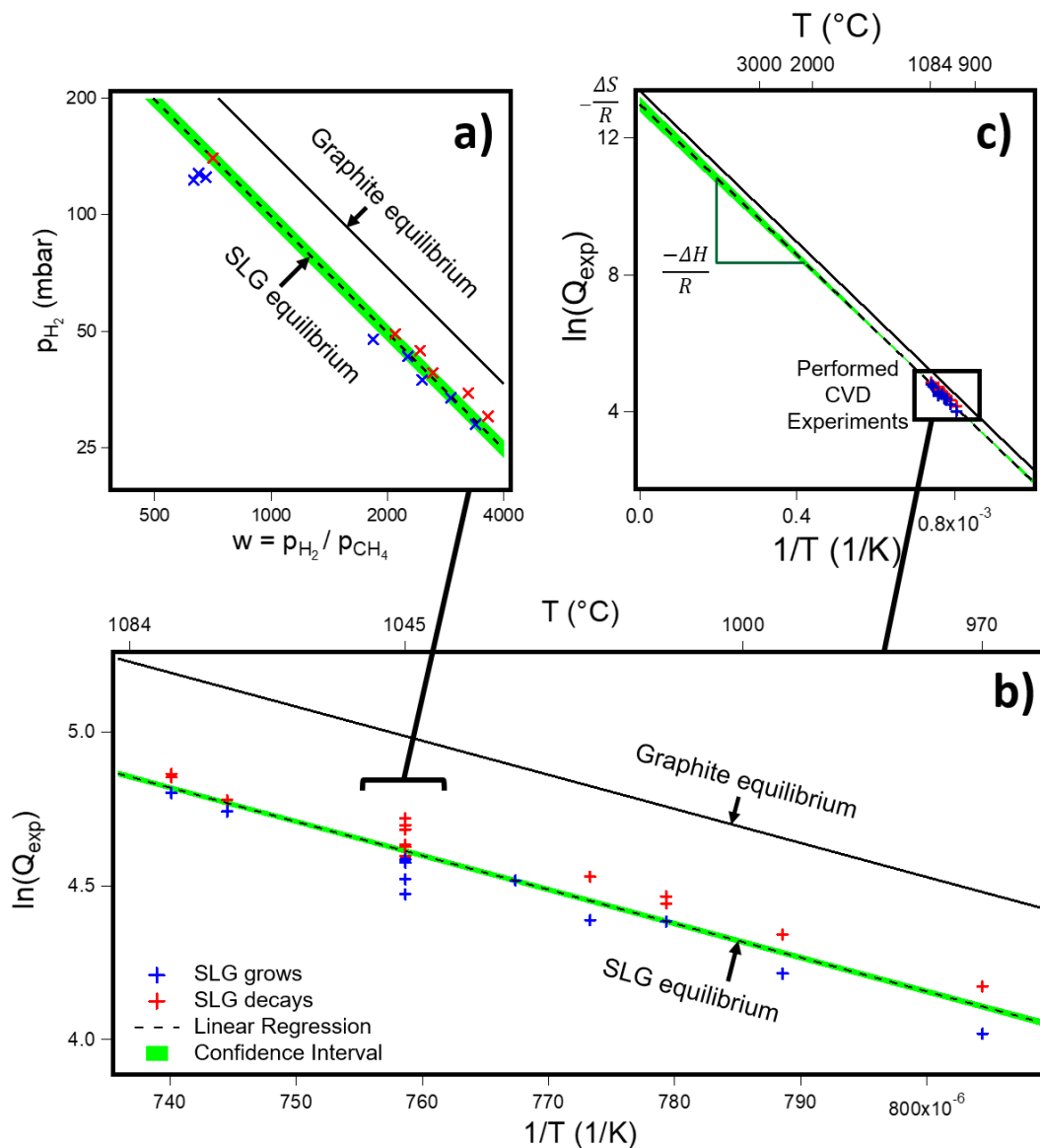


Figure 32 : Temperature dependency of the thermodynamic equilibrium of the SLG/Cu formation reaction. The data points presented in a) acquired at a single temperature merge into a single x-axis value in the $\ln(Q_{exp}) - 1/T$ -diagram shown in b). Additional experiments conducted at temperatures between 970-1080 °C are also inserted in b), restricting the possible course of the T-dependent equilibrium line. Evaluation of the slope of the equilibrium line in c) leads to the reaction enthalpy and the y-axis intercept to the reaction entropy. Confidence intervals of the analysis are sketched as green area in the respective plots. Reprinted with permission from reference²⁴⁶. Copyright 2021 American Chemical Society.

The temperature dependence of the thermodynamic equilibrium K_{eq} can be derived from

the Gibbs-Helmholtz equation 4.3, leading to equation 4.4.

$$\frac{d \Delta G}{dT T} = -\frac{\Delta H}{T^2} \quad (4.3)$$

$$\ln(K(T)) = \frac{\Delta S}{R} - \frac{\Delta H}{R T} \quad (4.4)$$

The derivation of eq. 4.4 can be found in reference ²⁴⁶ and appendix 12.2, assuming H and S to be temperature independent. In the range of the performed experiments, this leads to an error of $\pm 1\%$ for the tabulated value of graphite and therefore marks the lower limit of any calculated error to these values. A linear regression to the obtained datapoints leads to values of $\Delta_R H^\circ = 91.8 \pm 2.4 \text{ kJ mol}^{-1}$ and $\Delta_R S^\circ = 108.0 \pm 1.8 \text{ J mol}^{-1} \text{ K}^{-1}$. The obtained regression is inserted in Fig. 32 in form of a dashed line. The fit error is marked by a green highlighting. Graphically, the values for the enthalpy can be deduced from the slope of the line according to:

$$\frac{d \ln(K(T))}{d \frac{1}{T}} = -\frac{\Delta_R H}{R} \quad (4.5)$$

And the entropy according to the y-axis intercept amounting to:

$$\ln(K(T)_{1/T \rightarrow +0}) = \frac{\Delta S}{R} \quad (4.6)$$

Both values are visualized in Fig. 32c) showing an extrapolation to $1/T \rightarrow +0$, where also the values extracted for graphite are inserted. Note that the experimentally deduced values all refer to the temperature range in which the experiments were performed. The reference graphite data also refer to this temperature range and amount to $\Delta_R H^\circ_{\text{graphite}} = 92.0 \pm 0.9 \text{ kJ mol}^{-1}$ and $\Delta_R S^\circ_{\text{graphite}} = 111.2 \pm 1.1 \text{ J mol}^{-1} \text{ K}^{-1}$. All thermodynamic values are summarized in Table 7. The table shows that both evaluations, temperature-independent and temperature-dependent are in accordance with each other while in clear difference to the reference graphite values. While the fitted values for the reaction enthalpy are, within the standard deviation, equal to the graphite reference, the deviation of $\Delta_R G^\circ$ seems to stem from a lower value in reaction entropy.

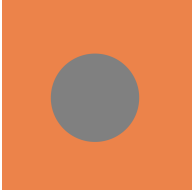
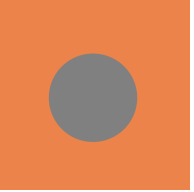
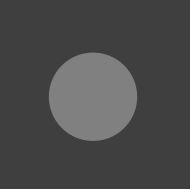
The Gibbs free energy $\Delta_R G^\circ$ is directly related to the value of $K_{eq}(T)$. As displayed in Fig. 32c), graphene on graphite is more exergonic than graphene on copper in the complete temperature interval from 0-2000 °C. If multilayer graphene on copper energetically resembles graphite, then the formation of multilayer graphene on copper should be thermodynamically favored compared to SLG. It can be concluded that the formation of SLG/Cu is purely caused by kinetic restrictions and not due to the reactions thermodynamics.

Table 7 : Thermodynamic data extracted from the performed experiments of the van't Hoff analysis, the analysis of SLG at a fixed temperature and the reference values for graphite from literature. Reprinted with permission from reference ²⁴⁶. Copyright 2021 American Chemical Society.

DATA ANALYSIS	$\Delta_R S^\circ [J mol^{-1} K^{-1}]$	$\Delta_R H^\circ [kJ mol^{-1}]$	$\Delta_R G^\circ [kJ mol^{-1}]$
g/Cu vant Hoff	108.0 ± 1.8	91.8 ± 2.4	50.6 ± 0.1
g/Cu (1045 °C) (p(H ₂)-w-diagram)			50.4 ± 0.5
g/graphite NIST-Janaf	111.2 ± 1.1	92.0 ± 0.9	54.6 ± 0.5

The expected results for growth experiments in different parameter regimes, illustrated in Table 8, show that there exists a specific parameter range between both equilibrium constants where single layer graphene growth is expected to decay while graphene on graphite should continue growing. As already stated, the properties of multilayered graphene on Cu should resemble more and more the case of graphite with increasing layer number. Multilayered graphene islands should hence grow a little bit faster at $Q_{exp} \leq K_{eq}(SLG)$ and decay with a certain shift at $Q_{exp} \geq K_{eq}(SLG)$. Experiments concerning the verification of this prediction are in detail described in chapter 7.

Table 8 : Graphical display of the different behavior of graphene on Cu and graphite substrates at the exemplary temperature of $T = 1045^\circ C$. Below $K_{eq}(g/Cu) = 101$, graphene is expected to be stable on both substrates. Between both equilibria, graphene is observed to decay on Cu substrate while expected to remain stable on graphite. Multilayered graphene islands on Cu are expected to resemble an intermediate between both structures. Above $K_{eq}(graphite) = 146$, graphene should decay in both cases.

$T = 1045^\circ C$	$Q_{exp} < 101$	$101 < Q_{exp} < 146$	$Q_{exp} > 146$
SLG on Cu			
SLG on graphite			

4.2.4. Comparison of the thermodynamic data with literature data

Related to the equilibrium concentrations of graphene growth on copper, Lewis *et al*²⁴⁸ tried to determine the equilibrium concentration for methane decomposition to graphene in a $CH_4 + H_2$ atmosphere. The determination of the sum of all gas partial pressures ($p(CH_4) + p(H_2)$) as crucial parameter for K_{eq} nevertheless makes the analysis of the results wrong. The experimental parameters used to find areas without graphene growth (low temperature, low total pressure, equal w-ratio) leads to the interpretation that the absence of graphene formation was caused by the lack of enough methane for nucleation rather than the crossing of the equilibrium concentration, which would be expected at higher pressures according to $Q_{exp} = w * p(H_2)$.

Safron *et al*²⁴⁹ performed experiments with graphene pre-covered Cu samples, analyzing the methane concentration at which the graphene film grew complete/ remained in partial coverage/ decayed after the performed reaction. The data points were collected over the large temperature range between 850-1050 °C and were used to pinpoint the position of the graphene equilibrium line. Comparison to our findings shows that these experiments observe graphene growth at higher values of Q_{exp} where graphene should already decay according to our results. The lack of control over C_xH_y impurities and carbon contaminations in the Cu foil in the performed experiments at that time might explain this shift. These contaminations may deliver supplementary carbon to artificially support graphene growth in unstable regions. At lower temperatures, the slow rate of graphene formation/decay is expected to introduce a hysteresis, which postpones the observation of growth/decaying effects.

For the reaction entropy $\Delta_R S^\circ$ no other comparable values could be found in literature. For the reaction enthalpy on the other hand, theoretical predictions and comparable experimental results are more numerous. In theoretical studies, the reaction which is commonly calculated is:



To be able to compare these literature values with our results they were combined with the NIST-data for the reactions of ($C_{vac} \rightarrow C_{graphite}$) and the formation enthalpy of methane ($CH_4 \rightarrow C_{graphite} + 2H_2$), as also listed in section 2.4.²⁴⁷ The values found in Literature by Zhang *et al*,²⁵⁰ Kittel,¹⁴³ and Li *et al*¹³¹ are listed in Table 9 and show strong scattering. Essentially, all derived values are not precise enough to allow constructive comparison with our determined values.

More information is available on the delamination energy of graphene on both, Cu and graphite, also summarized in Table 9. The main adhesion of graphene on weakly interacting surfaces is caused by the van-der-Waals forces,^{251,252,253,254} which means that possible differences between both substrates should be inherently included in the adhesion energy as an areal value in [$J \times m^{-2}$] or the equivalent atomic specification of the

delamination energy in [$eV/atom$]. Experimentally and theoretically determined values are summarized in Table 9.

Table 9 : Summary of reference values found in literature to contrast the obtained value of the reaction enthalpy/formation energy. The experimentally derived value of $\Delta_R H^\circ - 91.8 kJ/mol$ relates to $-0.951 eV$, which can be compared to the compiled values. Theoretical calculations of this value show enormous variations of $\pm 100\%$. Indirectly, contrasting the formation energy on both substrates g/Cu and g/g can be done by comparing their respective adhesion energies. Several literature references for the experimental and theoretical determination of these values are listed in this table.

Graphene on Cu		Reference Graphene on graphite	
$CH_4 \rightleftharpoons C_{gr,X} + 2H_2$			
Formation Energy ($eV/atom$)		Formation Energy ($eV/atom$)	
Results from this work ²⁴⁶	-0.951 ± 0.025	NIST Database	-0.954 ± 0.009
Calculations			
Zhang 2011 ²⁵⁰	-0.544		
Kittel 1986 ¹⁴³	-1.004		
Li 2017 ¹³¹	-2.000		
$C_{gr,X} \rightleftharpoons C_{gr,vac}$			
Predicted value from experimental results compared to NIST-data: $E_{ad}(graphite) - E_{ad}(g/Cu) = 0.00 \pm 0.03 eV/atom$			
Adhesion Energy (J/m^2) ($eV/atom$)		Adhesion Energy (J/m^2) ($eV/atom$)	
Experimental values			
Yoon 2011 ²⁵²	0.72 1.18×10^{-1}	Wang 2016 ²⁵⁵	0.221 ± 0.011 3.62×10^{-2}
Das 2013 ²⁵⁶	12.75 2.09×10^0	Xia 2019 ¹⁵²	$0.31 - 0.34$ 5.40×10^{-2}
Xin 2016 ²⁵⁷	$0.74 - 1.53$ 1.86×10^{-1}	Benedict 1998 ²⁵⁸	0.21 ± 0.09 3.44×10^{-2}
Na 2015 ²⁵⁹	6 9.82×10^{-1}	Liu 2012 ²⁶⁰	0.19 ± 0.01 3.11×10^{-2}
Na 2016 ²⁶¹	1.54 2.52×10^{-1}	Wang 2015 ²⁶²	0.33 ± 0.06 5.40×10^{-2}
Cao 2014 ²⁶³	0.51 8.34×10^{-2}	Li 2014 ²⁶⁴	0.227 ± 0.005 3.71×10^{-2}
Calculations			
Vanin 2010 ¹⁴⁹	0.21 3.50×10^{-2}	Xia 2019 ¹⁵²	0.29 ± 0.06 4.74×10^{-2}
Gong 2010 ¹⁵⁰	0.18 3.00×10^{-2}	Girifalco 1955 ²⁶⁵	0.33 5.40×10^{-2}
Xu 2010 ¹⁵¹	0.40 6.50×10^{-2}	Weippert 2018 ²⁶⁶	0.27 4.40×10^{-2}

It shows that the experimental determination of graphene adhesion on Cu is bound to severe scattering of the results, which are all much higher than the respective theoretical predictions or the values determined for the detachment of a single graphene layer from a graphite crystal. Theoretical predictions for the energy of cohesion of g/Cu ($0.03 - 0.06 \text{ eV/atom}$) and both theoretically and experimentally determined values for the energy of cohesion of g/g ($0.03 - 0.05 \text{ eV/atom}$) would lead to differences of $\Delta = -0.03 - +0.03 \text{ eV/atom}$ between g/Cu and g/g . These values are in very good agreement with my presented experimental results, which assume the difference between g/Cu and g/g to be $0.00 \pm 0.03 \text{ eV}$. We can in summary confirm that the interaction between g/Cu and g/g is very similar regarding the enthalpy, additionally stating that there might be a difference in entropy between both cases, causing a shift in thermodynamic stability at reaction temperatures.

It is possible to additionally validate the received thermodynamic values with all literature references in which graphene growth is reported by CVD on Cu in a $CH_4 + H_2$ atmosphere, as long as the needed values of temperature and mass action constant Q_{exp} are stated. 81 literature references satisfying these requirements were analyzed and the results inserted in the $\ln(Q_{exp}) - 1/T$ -plot of Fig. 32. The result, shown in Fig. 33, consists of a large number of growth conditions mainly far away from equilibrium conditions. Fewer are closely below K_{eq} ; the area commonly used in this work ($Q_{exp} > 20$, $\ln(Q_{exp}) > 3$) is shown magnified in Fig. 33b).

Six references marked i-vi are in contradiction to the proposed thermodynamic limit, which is also shown in the graphic in form of K_{eq} as a dashed line. Graphene growth at these values could only be possible if there was an additional carbon source in the reaction zone or the parameter calibration was not fully accurate. For the samples grown in references i,¹²¹ ii,¹⁵⁵ iii²⁶⁷ and iv¹⁶⁴ as marked in Fig. 33, the slight surpassing of K_{eq} and the low reported growth rates indicate that the calibration of the fluxes may be slightly wrong, but rather emphasize the position of the thermodynamic equilibrium in this area. In the case of sample v²⁶⁸ graphene was grown after melting of the Cu foil on a tungsten substrate foil and subsequent cooling to resolidify the molten Cu. In the case of present tungsten carbide (WC), this may lead to a continuous release of carbon, influencing the carbon concentrations on the sample surface. The authors of reference vi²⁶⁹ show graphene growth at a high offset to K_{eq} and even report large graphene flakes of $80 \mu\text{m}$ flake diameter (without stating a reaction time). Comparison to our reported results and all evaluated literature references indicates that the stated growth conditions are wrong. Other than this outlier, all growth conditions presented in literature coincide with the determined thermodynamic growth limit.

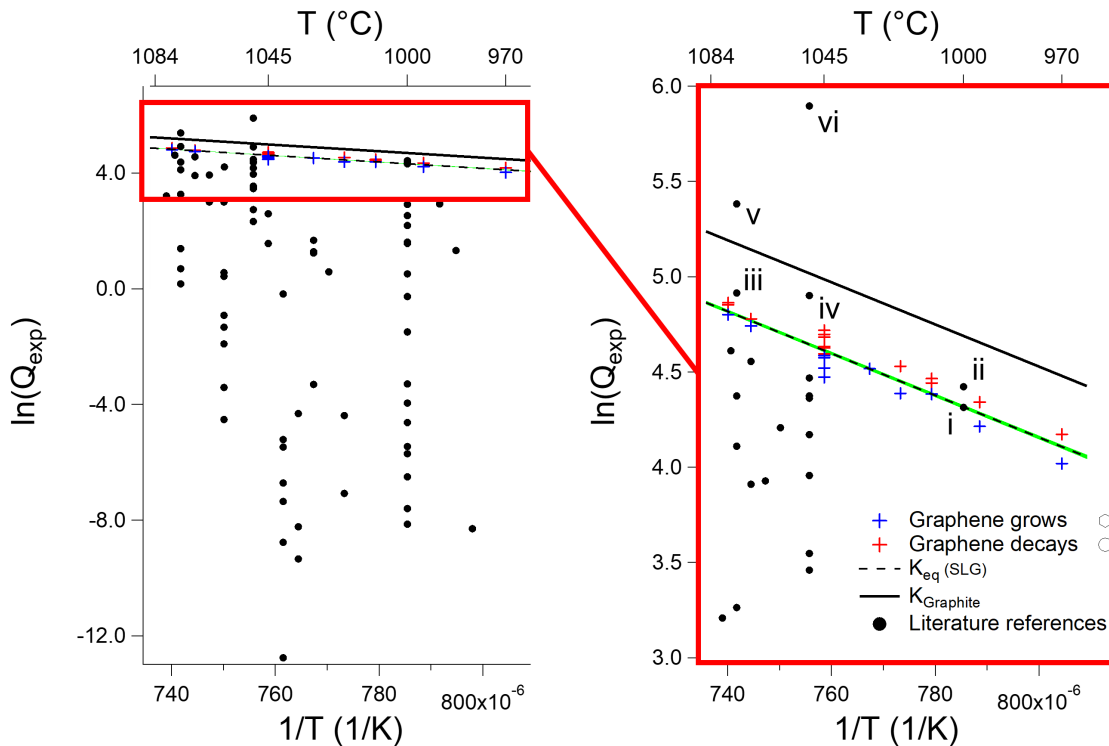


Figure 33 : Discussion of graphene growth conditions presented in literature and their respective results compared to the values presented in this chapter. Six literature references declare graphene growth at conditions where, according to our thermodynamic results, graphene decay should be observed (see numeration in the magnification to the right). These references are discussed in the main text.

The presented experiments enable the comparability and calibration of CVD graphene growth reactors. I. e., when performing the CVD growth on Cu in an arbitrary reactor, the applied growth conditions can be related to a universal standard. The outlined experiments explicitly determined thermodynamic data for SLG/Cu different to SLG/graphite, which can be used for a qualitative discussion of SLG formation on support metals other than Cu.

While theoretical calculations for the interaction energies between graphene and several metal substrates exist,^{149, 175, 270, 271, 151} this is not the case for data affecting the reaction entropy.

The gained insight is directly transferable for the growth by CVD on Cu using other precursor molecules. As the thermodynamic potentials of the formation reaction of other hydrocarbon molecules, such as C_2H_6 , C_2H_4 and C_2H_2 are tabulated in literature databases,¹²⁹ the prediction of graphene growth regimes is straightforward by exchanging the thermodynamic data of methane by the ones of other hydrocarbons. The different thermodynamic equilibria are plotted in Fig. 34 in addition to the experimentally determined equilibrium K_{eq} for methane. While the continuous line shows the equilibrium for the reaction towards graphite, the dashed line for the reaction to single layer graphene

on Cu shows in each case a significant offset. Sparsely available literature values for reactions with these precursor molecules are inserted in form of color-coded triangles. Due to their higher sticking coefficient and reactivity, larger hydrocarbons are often used in UHV experiments¹⁰⁶ where the graphene growth is kinetically controlled via the total carbon input and not by the equilibrium with the gas phase. Since the thermodynamic equilibrium is strongly shifted towards the graphene formation for these molecules, already traces of larger hydrocarbons in the reactive CVD atmosphere of a reactor experiment may lead to graphene growth. This becomes visually evident in the offset between the equilibrium lines of methane and higher hydrocarbons in Fig. 34. Within the indicated temperature-regime for the hydrocarbons already Q_{exp} values more than 1000 times larger than for the methane decomposition reaction should enable graphene formation on Cu. Also note that the T^{-1} dependency of the equilibrium constant relates to the entropy difference of the decomposition reaction for the different hydrocarbon precursor molecules, which is dominated by the impact of a different amount of released H_2 molecules per carbon atom.

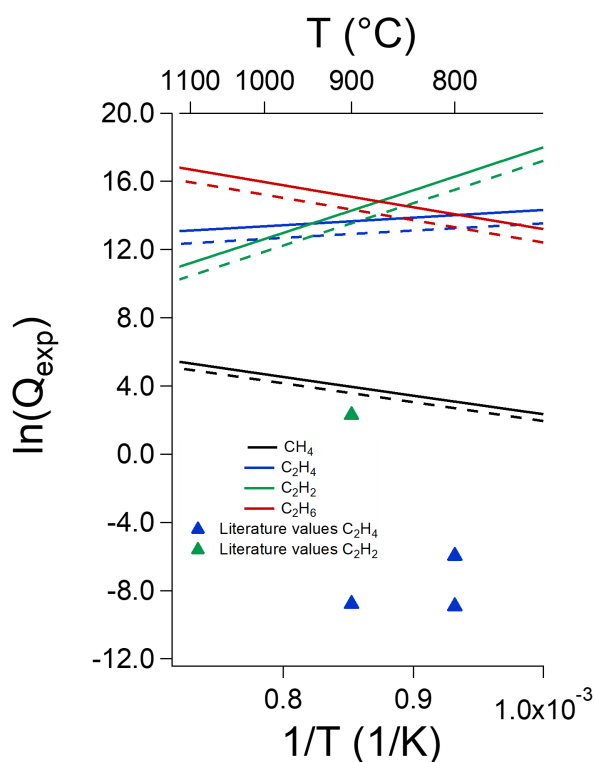


Figure 34 : Thermodynamic equilibrium lines for graphene growth from different hydrocarbon precursors. Dashed lines show the expected equilibrium line for the growth of graphene on Cu substrate, while the continuous line shows the expected equilibrium on graphite, color-coded according to the inserted legend. As can be seen, graphene formation for larger hydrocarbons is expected to strongly favor the graphene formation reaction. Already traces of these gases are sufficient to maintain the graphene growth at values of $\ln(Q_{exp}) > 10$. The different slopes depend on the amount of formed hydrogen gas per carbon atom in the precursor molecule. Colored triangles mark literature references for graphene growth using other precursors than methane.^{106,272,273}

5. Growth kinetics

5.1. Modelling of graphene growth on copper

Graphene growth on Cu by CVD consists of several individual elementary reaction steps, the dissociative adsorption of methane on the Cu surface, the dehydrogenation of the CH_x species and the integration of carbon to the graphene flake.¹⁷⁴ Although there are several studies about the kinetics and energy barriers of individual reaction steps already discussed in chapter 2.4, the modeling of the complete reaction chain is bound to large uncertainties.¹⁷⁴ Several theoretical studies have tried to determine the concentrations of reaction intermediates as well as the pathways of carbon attachment to the graphene flake, proposing either the formation of carbon dimers,^{130,140,142} subsurface carbon¹⁴⁵ or CH_{ad} as graphene feeding adsorbate species^{145,131} in addition to the graphene growth fed from a C_{ad} surface phase.^{126,173}

Several literature studies listed in the following tried to comprehend and predict graphene growth kinetics using different approaches and simplifications to the reaction process:

- Loginova *et al*^{271,274} experimentally investigated *in situ* the graphene growth process on Ru(0001). Due to the large adsorption energy of C_{ad} on Ru, the carbon surface concentrations can be measured before and during graphene nucleation and growth. *In situ* tracking of the surface carbon coverage allows the extraction of the concentration necessary for graphene nucleation, the oversaturation during graphene growth and the equilibrium saturation between C_{ad} and graphene after turning off the carbon source. The growth velocity was found to scale according to the attachment of C_5 clusters to the graphene islands.
- Kim *et al*^{141,173} presented a very early graphene growth model in which the overall reaction was split into three parts: The methane adsorption and dehydrogenation process, the hydrogen recombination and desorption step and the attachment of the carbon species to the graphene flake. Due to the early presentation of this model, graphene growth recipes lacked control over the nucleation process and reaction conditions were usually set very far from equilibrium conditions (e.g. $Q_{exp} = 0.04$ and $T = 720 - 1000^\circ C$), leading to a high nucleation density, continuous nucleation and a fast graphene covering of the copper surface. These reaction conditions moved the focus of the publication to the question at which conditions an incomplete graphene layer is expected.

- Mehdipour *et al*²⁷⁵ transferred insights gained from the growth process of low-pressure CVD on Ru and Ir to a growth model on the Cu surface, trying to imply all relevant reactions to model the graphene nucleation and subsequent growth process. However, the calculations for very low partial pressures ($p(H_2) < 10^{-2}$ mbar) do not match experimental graphene growth conditions.
- Confronted to similar problems as Kim *et al* (saturated coverage, uncontrolled nucleation, fast decay of growth rate), Celebi *et al*²⁷² tried to incorporate the process of continuous nucleation into the growth model, finding that the plot of the total graphene coverage versus the growth time can be fitted by a Gompertzian sigmoidal function. As this conclusion is strongly limited to the used parameter space, the transfer to further growth conditions is not possible.
- Xing *et al*²⁷⁶ assume additionally to the model by Kim *et al* that the overall graphene growth rate (coverage increase per time) is directly proportional to the amount of bare Cu foil, leading to a corrected growth speed α . As this assumption is only correct if a fixed percentage of the adsorbing methane molecules on the surface is incorporated into the graphene islands, this model does only work for an extremely high nucleation density where every arriving carbon atom is included in the graphene lattice. This is not at all the case in most experiments conducted on copper.
- Safron *et al*²⁴⁹ presented a growth model based on work by Zinsmeister²⁷⁷ for growth of 2D surface layers upon constant intake of precursor material. The graphene growth rate was determined to be dependent on the supersaturation above the equilibrium concentration, referred to as critical methane concentration (CMC). The mean growth rate of a single graphene flake was determined by calculating the ratio between overall graphene coverage and formed nuclei, as the processes of continuous nucleation could not be suppressed. Using this evaluation method, they experimentally found a linear correlation between the flake growth rate and the difference between $p(CH_4) - \text{''CMC''}$ and a correlation according to $p(H_2)^{-3/2}$ regarding the influence of the hydrogen partial pressure. Due to this correlation, CH_{ad} was assumed to be the rate-determining building unit (BU) for the growth reaction.
- Eres *et al*¹²⁷ could show that modification of the graphene growth atmosphere comes along with a severe change in nucleation characteristics, leading to the insight that the nucleation process should be observed separately from the subsequent growth process.

- Cabrero-Vilatela *et al*²⁷⁸ tried to experimentally detect the influence of a large number of parameters, including precursor partial pressure, catalyst thickness, exposure time and cooling rate, hoping to locate a trend of these parameters on the resulting graphene growth. Due to the low amount of experimental data and only qualitative evaluation, no generalized information can be extracted from this publication.
- Weatherup *et al*²⁷⁹ examined the possible reaction pathways for ethylene on Pt, observing surface features that may influence the growth process (diffusion into the bulk, accumulation along grain boundaries). These observations are mainly not applicable directly to the growth process of graphene on copper.
- Kraus *et al*.¹²⁶ proposed a growth model based on the elementary reactions listed by Kim *et al*, but expanded to focus the growth template on a single, isolated graphene flake instead of the entirety of graphene flakes on a sample. The proposed growth model assumed the C_{ad} -attachment to the grown graphene flake as rate-limiting step, while all appearing surface species (C_{ad} , $CH_{x,ad}$, H_{ad}) were assumed to be in equilibrium with the respective gas phase species during CVD.

5.2. Presentation of the current graphene growth model

The model presented here is an advanced version of the model by Kraus *et al.*, which is in detail described in literature.^{126,174} Several new specifications were added to increase the precision of the model and verify the validity of the model assumption. The kinetic growth model uses the situation of an isolated, hexagonal graphene flake on the bare Cu substrate to approximate the real growth conditions. The extended, bare Cu surface allows to assume the gas phase species CH_4 and H_2 to be in equilibrium with its corresponding dissociated surface species H_{ad} , $CH_{3,ad}$, $CH_{2,ad}$, CH_{ad} and C_{ad} . A single graphene flake on this substrate does not significantly reduce the surface concentrations when growing close to the thermodynamic equilibrium as determined in chapter 4.2. Note that the kinetic model describes the growth of graphene flakes, while the nucleation of new flakes during CVD is separately discussed in chapter 6. Starting with the impingement of diffusing C_{ad} atoms on the grown graphene island edge along its perimeter L , with an attachment energy barrier E_{att} to be overcome, leads to the following attachment rate of C_{ad} atoms to the flake:

$$\frac{dN_C(att)}{dt} = \frac{dC_{ad}}{dx} D^* L^* e^{-\frac{E_{att}}{RT}} \quad (5.1)$$

Here, the first term relates to the diffusion of the C_{ad} -species on the Cu surface according to Ficks first law within the approximation of a 2-dimensional lattice gas. It includes the concentration drop of C_{ad} from the equilibrated Cu surface ($[C_{ad}] = [C_{ad}]_{eq}$) to the edge of the graphene rim ($[C_{ad}] = 0$) and the diffusion coefficient D . $[C_{ad}]$ in this case relates to the total amount of carbon atoms per area unit, while the related quantity ϑ_C relates to the amount of C_{ad} atoms per substrate unit cell ($[C_{ad}] = \vartheta_C A_{Cu}$). According to several literature references^{126, 138, 140, 165} the attachment energy barrier E_{att} is in the order of 1 eV or 100 kJ/mol. Assuming this to be the correct order of magnitude, only a small fraction (at 1045°C approximately 0.1%) of the impinging carbon atoms will be attached to the graphene lattice, which justifies approximating that the concentration drop will take place within just one atomic distance a_{Cu} . This leads to:

$$\frac{d[C_{ad}]}{dx} = \frac{[C_{ad}]_{eq}}{a_{Cu}} = \frac{\vartheta_C}{a_{Cu} A_{Cu}} \quad (5.2)$$

The diffusion coefficient on a 2-dimensional lattice is given by:

$$D = 14 a_{Cu}^2 v_{ad} e^{-\frac{E_{diff}}{RT}} \quad (5.3)$$

with a_{Cu} being the nearest neighbor distance on the substrate lattice (in this case Cu(111)), v_{ad} the hopping attempt frequency (typically $10^{13} s^{-1}$) and E_{diff} the activation energy for the hopping event. This energy barrier is approximately 60 meV (5.8 kJ/mol) on Cu(111).¹⁴⁴ Inserting the diffusion coefficient D and eq. 5.2 into eq. 5.1 leads to:

$$\frac{dN_C(att)}{dt} = 0.25 * v_{ad} a_{Cu} \vartheta_C \frac{1}{A_{Cu}} L e^{-\frac{E_{diff}}{RT}} e^{-\frac{E_{att}}{RT}} \quad (5.4)$$

Additional to the attachment of C_{ad} to the flake, the detachment of carbon atoms from the flake edge is also taken into account in this model. Due to the lack of unambiguous results regarding the detachment procedure, a simple, vibration-based detachment of a carbon atom without interaction with external adsorbed species is assumed. The detachment rate is therefore determined by the flakes rim atoms, the respective atoms vibrational frequency representing the detachment attempt frequency v_{gr} and the detachment barrier E_{det} to be:

$$\frac{dN_C(det)}{dt} = -\frac{2L}{a_g} v_{gr} e^{-\frac{E_{det}}{RT}} \quad (5.5)$$

The processes for carbon att- and detachment are illustrated in Fig. 35 and the energetic barriers are shown in the energy diagram in Fig. 36, which was already shown in chapter 2. It is possible to describe the indicated energy barrier of the final attachment step according to: $E_{att} = E_{det} + \Delta_R H^\circ - \Delta_{dec} H^\circ$, where $\Delta_R H^\circ$ is the previously determined (chapter 4.2) reaction enthalpy of graphene and $\Delta_{dec} H^\circ$ is the decomposition enthalpy of

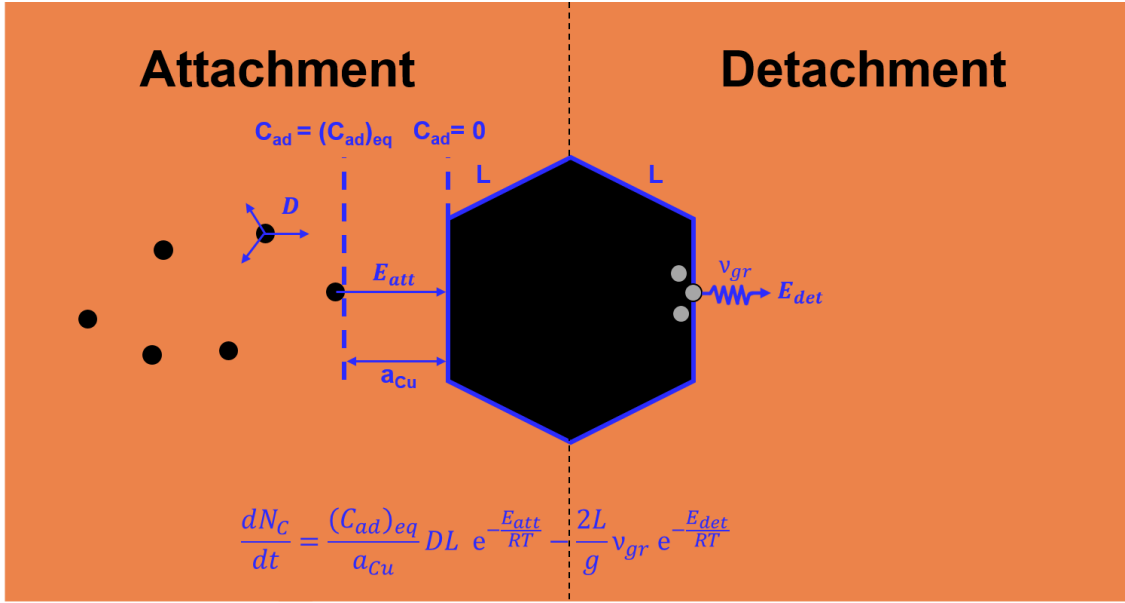


Figure 35 : Graphical illustration of the parameters determining the graphene attachment and detachment reaction rates. For the attachment reaction, the relevant terms are the concentration gradient of C_{ad} around the graphene flake, the diffusion coefficient D , the possible interaction perimeter L of the island and the attachment energy barrier E_{att} . For the detachment of graphene, the graphene rim atoms possibly detach from the island at each vibration (in this case called the attempt frequency ν) if overcoming the necessary detachment energy E_{det} .

methane towards C_{ad} .



This decomposition reaction also defines the surface concentration of carbon, which can be either given in absolute numbers ($[C_{ad}] = atoms/m^2$) or relative to the Cu packing density ($[\vartheta_C] = ML$). The equilibrium constant of eq. 5.6 at low C_{ad} coverage amounts to:

$$K_{dec} = e^{-\frac{\Delta_R G_{dec}^0}{RT}} = \frac{\vartheta_C * a(H_2)^2}{a(CH_4)} = \vartheta_C * Q_{exp} \quad (5.7)$$

Here, C_{ad} is treated as a non-interacting 2-dim gas with an activity approximated by ϑ_C , since:

$$\vartheta_C \approx \frac{\vartheta_C}{1 - \vartheta_C} \quad (5.8)$$

According to estimations made by Li *et al*¹³¹ and Mattevi *et al*,¹⁷³ ϑ_C on Cu(111) is below 10^{-7} or 10^{-8} monolayers, respectively. The free Cu adsorption sites $*$ = $1 - \vartheta_C$ can therefore straightforwardly be assumed to be $*$ ≈ 1 , which justifies eq. 5.7.

The increase of graphene atoms over time dN_C/dt leads to the size increase of the growing flake, which is treated as regular hexagon. As a result, the flake radius of a grown hexagon with circumference L relates to the C atom increase per time:

$$\frac{dN}{dt} = \frac{A_g}{2} \frac{dA}{dt} = \frac{A_g}{2} \frac{dA}{dr} \frac{dr}{dt} = \frac{A_g}{2} L \frac{dr}{dt} \quad (5.9a)$$

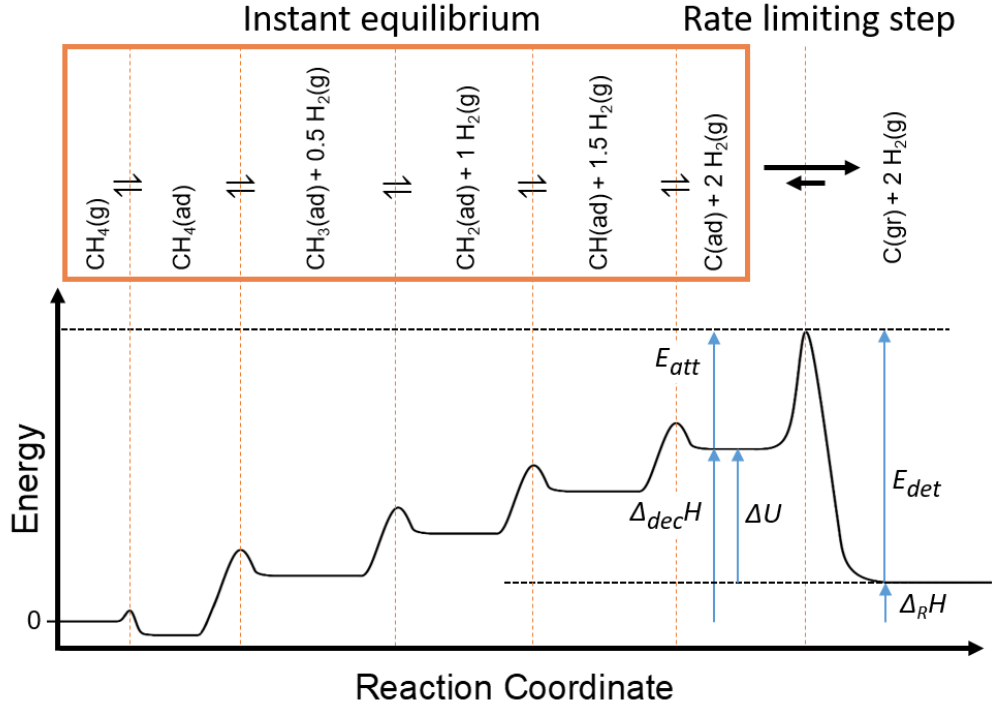


Figure 36 : Energy diagram of the elementary reaction steps as used in the presented growth model. As all adsorption and dehydrogenation steps are assumed to be immediately equilibrated, the rate-limiting step on which the growth model focuses is simply the last reaction step of the carbon integration in the graphene crystal. Only the energy values relevant for use in the kinetic model as presented are indicated in the diagram. Reprinted with permission from reference ¹²⁸. Copyright 2021 American Chemical Society.

$$\text{with: } \frac{dA}{dr} = \frac{d(2\sqrt{3}r^2)}{dr} = 4\sqrt{3}r = L \quad (5.9b)$$

Merging the attachment and detachment rate from eq. 5.4 and eq. 5.5 into one equation and substituting dN/dt by dr/dt allows the cancellation of the flake perimeter L on both sides of the resulting equation. The graphene growth velocity $v = dr/dt$ as used in this work is then defined as:

$$v = \frac{dr}{dt} = \left[\frac{A_g}{8A_{Cu}} v_{ad} a_{Cu} e^{-\frac{E_{diff}}{RT}} e^{\frac{\Delta_{dec}S^\circ}{R}} e^{-\frac{\Delta_R H^\circ}{RT}} \frac{1}{Q_{exp}} - \frac{A_g}{a_g} v_g \right] e^{-\frac{E_{det}}{RT}} \quad (5.10)$$

Both unit cell areas A_g and A_{Cu} for Cu(111) amount to $a_X^2 * \sqrt{3}2$ with a_X being the lattice constant ($a_g = 2.46 \text{ \AA}$, $a_{Cu} = 2.55 \text{ \AA}$). As known from the thermodynamic considerations in chapter 4.2, the net growth at thermodynamical equilibrium K_{eq} is zero, i. e. att- and detachment rates are equal. The detachment term can therefore be replaced by the negative attachment term at $Q_{exp} = K_{eq}$, which amounts to:

$$K_{eq} = e^{-\frac{\Delta_R H^\circ - T\Delta_R S^\circ}{RT}} \quad (5.11)$$

Table 10 : Parameters and constants relevant in the presented kinetic growth model and their respective values and units.

Known parameters	Value	Fit parameters	Unit
Gas constant R	$8.314 \frac{J}{molK}$	Decomposition entropy $\Delta_{dec}S^\circ$	$\frac{J}{molK}$
Graphene lattice constant a_g	2.46 \AA	Detachment energy E_{det}	$\frac{kJ}{mol}$
Copper lattice constant a_{Cu}	2.55 \AA		
Attempt frequency v_{ad}	$\approx 10^{13} s^{-1}$		
Diffusion energy E_{diff}	$5.8 \frac{kJ}{mol}$	Variables	Unit
Reaction enthalpy $\Delta_R H^\circ$	$91.8 \frac{kJ}{mol}$	Temperature T	K
Reaction entropy $\Delta_R S^\circ$	$108 \frac{J}{molK}$	Mass action constant Q_{exp}	<i>unitless</i>

As a result, the growth velocity v calculates as:

$$v = \frac{dr}{dt} = \frac{a_g^2}{8a_{Cu}} v_{ad} e^{-\frac{E_{diff}}{RT}} e^{\frac{\Delta_{dec}S^\circ}{R}} e^{-\frac{\Delta_R H^\circ}{RT}} \left[\frac{1}{Q_{exp}} - e^{\frac{\Delta_R H^\circ - T\Delta_R S^\circ}{RT}} \right] e^{-\frac{E_{det}}{RT}} \quad (5.12)$$

The only two fit parameters remaining to be determined in this eq. 5.12 are the methane decomposition entropy $\Delta_{dec}S^\circ$ and the detachment energy barrier E_{det} of carbon from the graphene rim. All other values are known constants or are determined during the reaction, as listed in Table 10. The determination of the two unknown parameters requires a large dataset of determined growth velocities v at different conditions T and Q_{exp} to enable a plausible fit.

5.3. Verification of the time independency of $v(t) = dr/dt$

According to the correlation described in eq. 5.12, the growth velocity v only depends on the set reaction temperature and mass action constant Q_{exp} . Keeping these two parameters constant should hence lead to the same growth speed v , i. e. a linear increase of flake radii with growth time. This assumption was tested to verify the fundamental validity of the proposed growth model. Graphene was grown in the described reactor setup with three loaded Cu samples, which could be removed individually from the hot reactor zone at different times, as described in chapter 3.1. Using the first sample as reference, the flake size evolution of the second and third sample in the subsequent growth intervals was determined with high precision, as already described in chapter 3.4. Graphene samples were grown after standard oxidative pretreatment and a short nucleation step at $T = 1045 \text{ }^\circ\text{C}$ and $Q_{exp} = 45$ for different times between 5-120 min. The radii of the observed flakes on

the samples were statistically evaluated and a mean flake radius r was determined. The mean flake radius is plotted versus the growth time t in Fig. 37. Exemplary optical images of single graphene flakes of each sample clarifying the flake size increase are shown in Fig. 38. The evolution of the graphene flakes can be fitted with a linear equation leading to a growth speed at these conditions of $v(T = 1045^\circ\text{C}, Q_{\text{exp}} = 45) = 92 \pm 3 \mu\text{m h}^{-1}$.

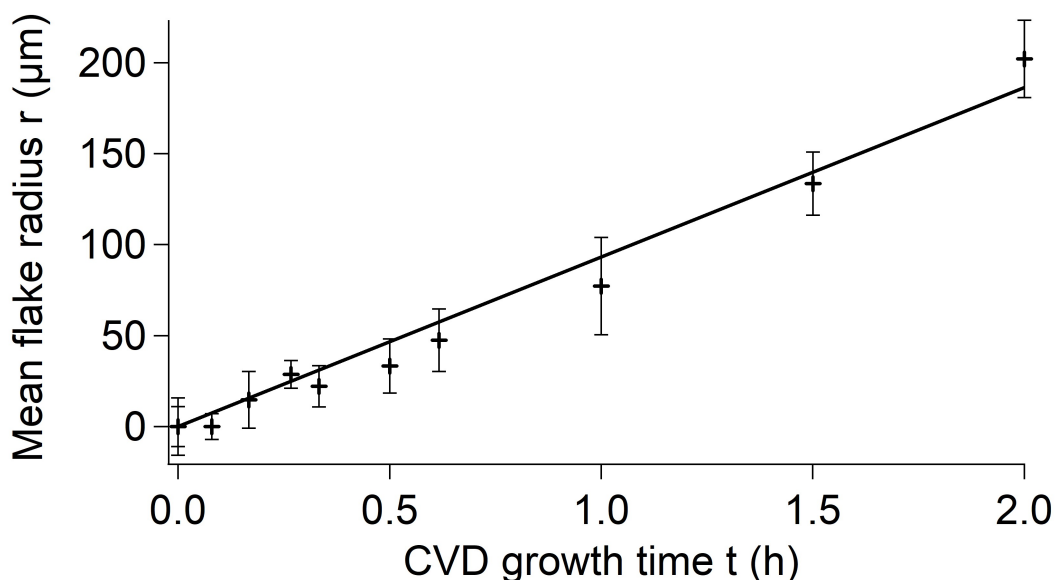


Figure 37 : Graphene flake radius evolution at fixed growth conditions in dependence of the reaction time. The respective linear regression through $r(t = 0 \text{ min}) = 0 \mu\text{m}$ is added, indicating the expected linear evolution of the flake radius in time. Adapted with permission from reference ¹²⁸. Copyright 2021 American Chemical Society.

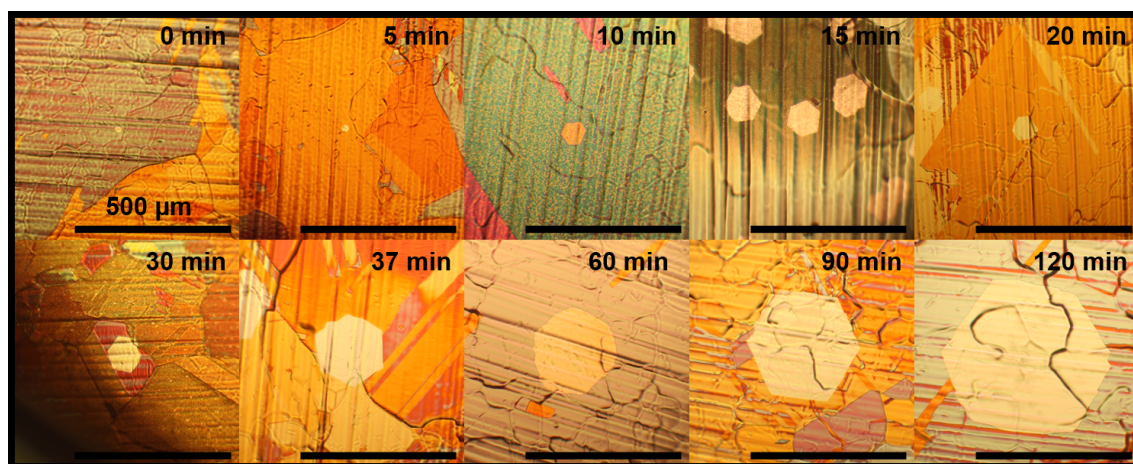


Figure 38 : Exemplary optical images of the graphene flakes as evaluated to determine the data points shown in Fig. 37. Note that the mean flake radius is not determined from single graphene flakes, but from the overall flake size distribution found on each sample. (Experimental details: 0+5+10min: E. 4 , 15min: E. 49 , 20+30min: E. 14 , 37+90min: E. 15 , 60+120min: E. 16)

The described experiments prove the time independency of v , as predicted by the proposed growth model. The increase in required carbon atom incorporation with increasing flake radius at constant v is counterbalanced by the likewise increasing number of collisions between diffusing C_{ad} and the graphene flake rim. The increasing depletion of surface carbon species by the flake attachment process does not influence the growth procedure due to the large bare Cu surface allowing an equilibrated decomposition reaction (eq. 5.6) of methane.

5.4. Graphene growth at conditions leading to equal Q_{exp} -values

While the graphene samples shown in Fig. 38 are grown at equal mass action constant Q_{exp} originating from equal $H_2 : CH_4$ -ratio $w = 1250$ and $p(H_2) = 36 \text{ mbar}$, the variation of these parameters with unchanged mass action constant should lead to unchanged graphene growth rates, as only the combined value Q_{exp} is represented in the growth equation 5.12. An experimental series was conducted at $Q_{exp} = 45$ with varying relations of $p(H_2)$ and w . The used conditions are summarized in Table 11 together with the resulting growth speed values.

Table 11 : Graphene growth velocity determined for four samples grown at different combinations of $p(H_2)$ and w – ratio, but leading to the same mass-action constant Q_{exp} . Additionally stated is the methane partial pressure for each reaction, which varies over more than one order of magnitude.

	w-ratio	$p(H_2)$ (mbar)	Q_{exp}	v ($\mu\text{m}/h$)	$p(CH_4)$ (mbar)
Exp. E. 51	300	147	44.1	75 ± 16	0.49
Exp. E. 17	498	90.9	45	120 ± 30	0.18
Exp. E. 17	747	60.9	45	88 ± 30	0.08
Exp. of Fig. 37 and 38	1200	36	45	92 ± 3	0.03

The evaluated reactions are performed in a broad parameter range between $w = 300 - 1200$ and $p(H_2) = 36 - 150 \text{ mbar}$. Regardless of the large spreading of the CVD parameters, the resulting Q_{exp} -value remains constant and so does the detected growth speed v , which remains between $70 - 120 \mu\text{m} h^{-1}$. It is particularly noted that the methane partial pressure during the reaction shows large variations for the performed experiments, spanning over more than one order of magnitude, as also listed in Table 11. The methane impingement rate on the Cu sample, being directly proportional to its partial pressure, is

therefore not relevant under these growth conditions. This correlation also agrees well with the expectations from the derived kinetic growth model.

5.5. Fitting the unknown reaction parameters $\Delta_{dec}S^\circ$ and E_{det} to experimental data

Variation of the growth parameters T and Q_{exp} and monitoring of the growth speed v allows estimating the unknown parameters $\Delta_{dec}S^\circ$ and E_{det} . In order to receive a large dataset from experiments spanning over a large parameter space, experiments were performed at conditions according to the following four conditions:

- Exposure to conditions close to the thermodynamic equilibrium (see dataset from chapter 4.2)
- Graphene growth at varying values of Q_{exp} and constant temperature $T = 1045^\circ\text{C}$
- Graphene growth at varying temperatures and constant mass action constant $Q_{exp} = 45$
- Graphene growth at combinations of T and Q_{exp} that lead to graphene growth speed of about $v = 100 \mu\text{m h}^{-1}$. The value was chosen, since graphene flakes grown at these conditions lead to a low statistical error in the flake size evaluation while maintaining fairly short growth times.

The extracted growth speeds v from the conducted experiments are summarized in Table 12. The experiments acquired at one temperature can be displayed in a single $p(\text{H}_2) - w$ -graph as shown in Fig. 39a) for $T = 1045^\circ\text{C}$. The growth speed is illustrated by the area of the inserted hexagons. In this diagram, the experiments at equal $p(\text{H}_2)$ and w merge in one point. The experiments shown in Fig. 37 therefore merge in the hexagon marked with an arrow, while the experiments at equal Q_{exp} are shown on one diagonal. Experiments, in which no absolute growth speed was measured, but only whether the graphene sample was exposed to conditions above or below the thermodynamic equilibrium line K_{eq} are shown with green (growth detected) or red markers (decay detected). The equilibrium line as determined in the experiments in chapter 4.2 is marked with a red line. The growth speed of all performed experiments was used collectively to perform a Levenberg-Marquardt fit to the fit parameters of $\Delta_{dec}S^\circ$ and E_{det} . The resulting global fit leads to a value of v for each pair of T and Q_{exp} . Regarding the experimental series at $T = 1045^\circ\text{C}$ with varied Q_{exp} , described above, the fit leads to an inverse proportional relationship between v and Q_{exp} , which is shown in the red curve of Fig. 39b). The experiments performed at 1045°C are shown with black markers in the same figure, showing the same inverse proportional relationship as the fit.

At variable temperature, as done in series $Q_{exp} = const.$, the term regarding the carbon detachment from the graphene island is also altered, which leads to a deviation from the linear relationship between T and $\log(v)$, as shown in Fig. 39c). The corresponding experimental values show a slight overestimation by the fit at lower temperatures, which is counterbalanced by a slight underestimation at higher temperatures. Note that the fits shown in Fig. 39b) and c) are extracted from the same global fit taking into account all acquired experimental results. The result of the fit is displayed as 3D-plot of v vs Q_{exp} & T in Fig. 39d), where the respective lines of constant Q_{exp} and constant T are marked in color. Growth speeds extracted from experiments are marked as black spheres, where a cut-through shows the superposition with the fit-surface and a potential displacement to the surface is shown with lines parallel to the axis. The offset between predicted and determined growth speed v is commonly lower than a factor 2, the exact values are also listed in Table 12.

Table 12 : Experiments used for the determination of the kinetic growth model.

Temperature (°C)	Q_{exp} -value -	Determined growth speed v ($\frac{\mu m}{h}$)	Predicted growth speed v ($\frac{\mu m}{h}$)	Deviation -	Experiment #
1084	45	1050±105	451.46	130%	Exp. E. 50
1075	45	545±80	316.49	70%	Exp. E. 18
1060	45	360±60	172.12	110%	Exp. E. 19
1045	42.7	89±11.6	100.27	11%	Exp. E. 15
1045	42.7	98.9±27.9	100.27	1%	Exp. E. 15
1045	45.5	101.3±10.6	89.56	13%	Exp. E. 16
1045	45.5	77.5±17.2	89.56	13%	Exp. E. 16
1045	70.7	34.7±15.8	31.38	11%	Exp. E. 20
1045	20.2	312±88.8	294	6%	Exp. E. 20
1045	92	6.8±7.2	7.06	4%	Exp. E. 7
1045	87.9	10.1±6.9	10.83	7%	Exp. E. 21
1045	87.5	6.9±1.7	11.21	38%	Exp. E. 5
1045	81.4	19.4±8.8	17.57	10%	Exp. E. 63
1045	66	34.5±5.4	38.86	11%	Exp. E. 22
1045	56.6	47.2±9.1	57.55	18%	Exp. E. 60
1020	29.52	118.5±13.2	62.68	90%	Exp. E. 23
1020	45.1	26.4±13.2	29.66	11%	Exp. E. 23
1015	45	12±20.8	23.54	49%	Exp. E. 24
1000	24.57	72.2±13.4	34.64	110%	Exp. E. 25
1000	45.1	9.6±5.3	11.19	14%	Exp. E. 25
975	21.69	41.7±6	13.56	200%	Exp. E. 26
975	45	1.2±0.64	2.85	< 2 μm	Exp. E. 26
950	5.86	57±14.6	23.08	150%	Exp. E. 27
950	45.2	-0.8±1.2	0.47	< 2 μm	Exp. E. 27
900	1.4	66±13.2	10.48	530%	Exp. E. 28
1078	125.85±2.15	0	-3.47	-	Exp. E. 28
1070	116.75±2.15	0	1.48	-	Exp. E. 29
1045	91.1±8	0	7.86	-	Exp. E. 12
1045	105.05±6.95	0	-2.97	-	Exp. E. 10
1045	102.5±5.5	0	-1.21	-	Exp. E. 9
1045	103.3±6.3	0	-1.77	-	Exp. E. 8
1045	97±5.1	0	2.9	-	Exp. E. 7
1045	95.2±7.7	0	4.35	-	Exp. E. 5
1020	86.65±6.15	0	-0.34	-	Exp. E. 30
1010	82.5±2.4	0	-0.65	-	Exp. E. 31
995	72.25±4.55	0	0.04	-	Exp. E. 32
970	60.3±4.6	0	0.05	-	Exp. E. 33

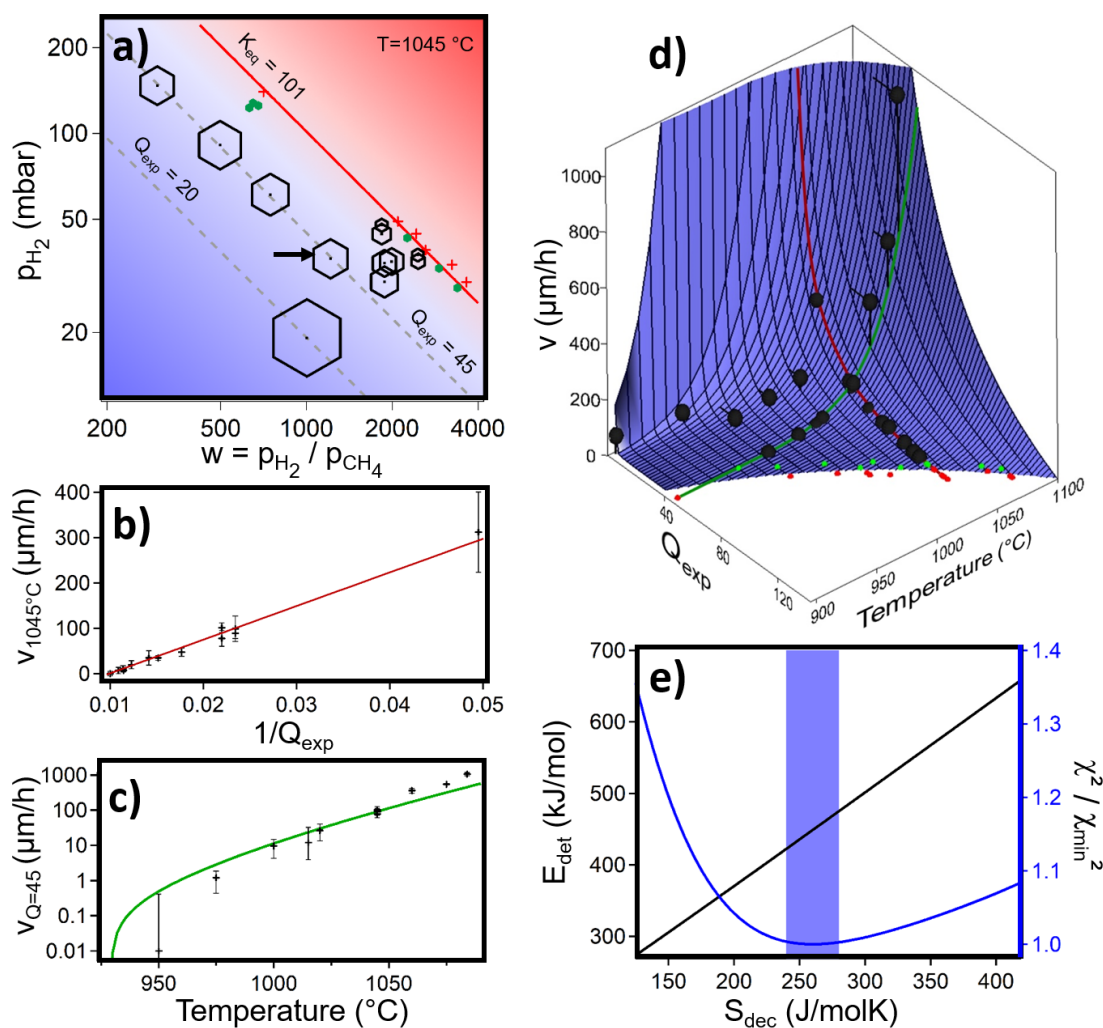


Figure 39 : Experimental results and respective expected growth values of the single universal fit to the kinetic growth model as presented in this chapter. a) $p(H_2) - w$ -diagram at 1045 °C as also used for the determination of the thermodynamic equilibrium in chapter 4.2 enhanced by experiments with determined graphene growth velocity v , imaged by hexagons of different sizes according to the determined growth velocity v . At $Q_{exp} = 45$ the experiments listed in Table 11 and Fig. 37 are presented. This diagram shows the increase of the growth velocity v with increasing distance to the equilibrium line K_{eq} . b) Excerpt of the universal fit at $T = 1045\text{ °C}$ and the respective acquired experimental data. Both fit and data points show a linear evolution of $v(1/Q_{exp})$. c) Excerpt of the universal fit at $Q_{exp} = 45$ and the respective acquired data points. While the fit to the universal growth model shows a slight overestimation at low temperatures, it underestimates the growth velocity at high temperatures slightly below the melting point of the Cu substrate. d) 3-D-plot of v vs Q_{exp} & T , derived by the global fit. All data points are inserted as black spheres, possible offsets from the fit surface are marked with horizontal/vertical lines. Red and green spheres mark the thermodynamic experiments pinpointing K_{eq} at $v = 0$. Red and green lines mark the excerpts shown in b) and c), respectively. e) Best-fit result of the detachment energy E_{det} as a function of the decomposition entropy S_{dec} (black curve), showing a linear compensating relationship of one from the other. The least-squares χ^2 value shows a universal minimum, indicating the best fit result. Highlighted in blue is the area of confidence of the fit. Reprinted with permission from reference ¹²⁸. Copyright 2021 American Chemical Society.

Fig. 39d) also displays the full parameter range of the conducted experiments. Between $T = 900 - 1080 \text{ }^\circ\text{C}$, $p(\text{H}_2) = 20 - 200 \text{ mbar}$, $w = 300 - 4000$ and $Q_{exp} = 1 - 125$, the applicability of this growth model has been proven. The agreement of the growth velocities with the model shows that several of the assumptions made are reasonable and do not influence the growth rates occurring in real experiments. These assumptions include:

- **The equilibrated decomposition reaction of methane towards C_{ad} on the Cu surface:** If the pre-equilibrated surface species was a hydrogenated species C_xH_y , then a different scaling relation of the growth velocity with respect to the hydrogen partial pressure would have been expected, as also shown by Kraus *et al.*¹²⁶
- **The carbon species attached to the graphene flake is C_{ad} :** The carbon species attached to the graphene flakes in these experiments is assumed to be the monomer C_{ad} . Literature references estimate a C_{ad} concentration below 10^{-7} ML ,^{131,173} which almost inhibits the statistical collision of two carbon atoms on the surface. Literature studies suggesting the dimer formation on Cu calculated with hydrogen to methane ratios that are not related to experimental data. For example the argumentation of Li *et al.*¹³¹ is based on calculations with a $\text{H}_2 - \text{CH}_4$ w-ratio of 0.01 and a mass action constant $Q_{exp} = 10^{-8}$.
- **The diffusion on the Cu surface lattice can be modeled by a 2D lattice gas at the common reaction temperatures:** The effect of surface inhomogeneities or anisotropies in the diffusion is not found to be of defining relevance at these conditions

Additionally, the performed fit provides values for the decomposition entropy of methane $\Delta_{dec}S^\circ = 260 \pm 20 \text{ J mol}^{-1} \text{ K}^{-1}$ and the detachment energy barrier of carbon atoms from the graphene flake $E_{det} = 451 \pm 26 \text{ kJ mol}^{-1} = 4.7 \pm 0.3 \text{ eV}$. In eq. 5.12, both values have a compensating effect, which accounts for the relatively high errors of the two correlated values. Variation of one parameter leads to an almost linear change of the other parameter, as shown in Fig. 39e). The χ^2 error value of the fit indicates a shallow minimum, which is highlighted in Fig. 39e), where the standard deviation is visualized as blue hatched area.

Both fit parameters can be indirectly compared to literature data. The detachment energy E_{det} can be calculated via the C_{ad} attachment energy barrier towards graphene E_{att} and the energy difference ΔU for carbon in the C_{ad} and in the SLG phase, respectively, according to:

$$E_{det} = E_{att} + \Delta U \quad (5.13)$$

The value ΔU can be estimated to range between 2.5 eV and 2.9 eV ,¹²⁸ which leads to $E_{att} = 1.8 - 2.2 \text{ eV}$ when using the fitted value $E_{det} = 4.7 \text{ eV}$. The energy barrier of about 2 eV for carbon attachment to SLG on Cu very much matches the one experimentally

found for g/Ru(0001). Again, theoretically computed values for SLG/Cu reported in the literature strongly differ and range between values of $E_{att} = 1 \text{ eV}$,^{138,145} 1.2 eV ¹⁴⁰ and 2.6 eV .¹⁴¹

When not providing attaching C_{ad} atoms, the fitted energy barrier $E_{det} = 4.7 \text{ eV}$ relates to a nominal flake decay with a flake radius decrease per time according to:

$$v_{det} = -\frac{A_g}{a_g} v_g * e^{-\frac{E_{det}}{RT}} \quad (5.14)$$

The value for g/Cu leads to a radius decrease in time between $1 \mu\text{m h}^{-1}$ at $900 \text{ }^\circ\text{C}$ and $\approx 100 \mu\text{m h}^{-1}$ close to the melting point of Cu. Figure 40 displays the respective plot of the temperature range between $800 \text{ }^\circ\text{C}$ and $1080 \text{ }^\circ\text{C}$, which will be further discussed in chapter 5.6.

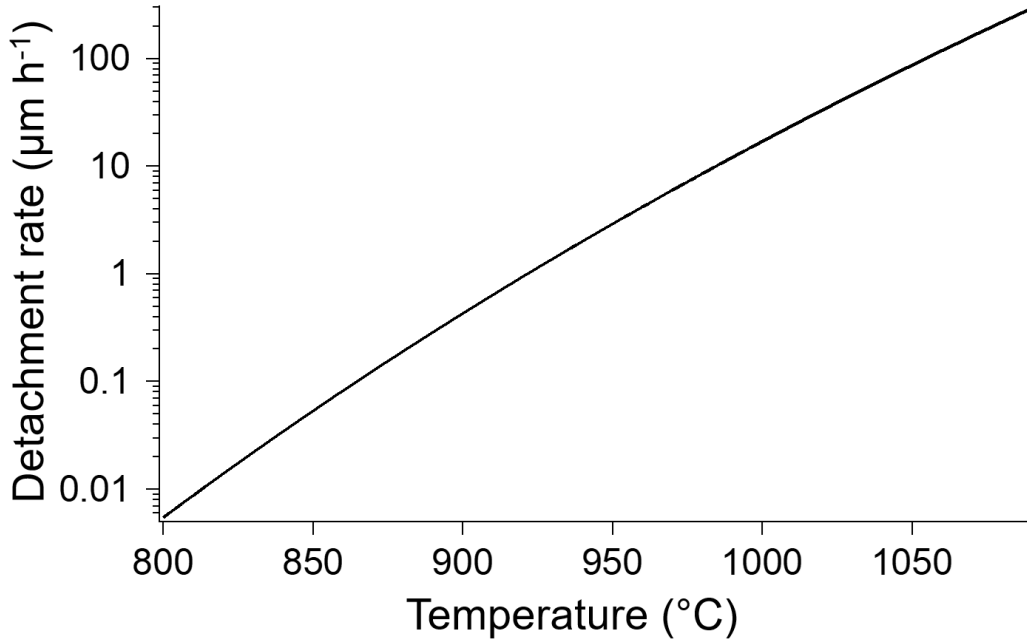
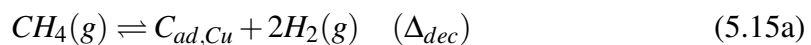
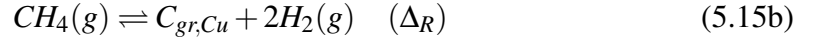


Figure 40 : Graphene decomposition rate assuming only the graphene detachment reaction as a function of the reaction temperature, spanning over 4 orders of magnitude in the relevant temperature regime.

The fitted decomposition entropy $\Delta_{dec}S^\circ = 260 \pm 20 \text{ J mol}^{-1}\text{K}^{-1}$ can be used to calculate ΔU in an alternative estimation and also to derive the C_{ad} concentration ϑ_C in thermodynamic equilibrium with graphene flakes. Subtracting the entropy of the CH_4 decomposition reaction towards C_{ad} from the one towards graphene leads to the formal reaction:





$$\Rightarrow C_{gr,Cu} \rightleftharpoons C_{ad,Cu} \quad (5.15a - 5.15b) \quad (5.15c)$$

This reaction equation describes the phase coexistence of 2-dim graphene flakes and the 2-dim C_{ad} gas on Cu. At thermodynamic equilibrium ($\Delta G = 0$) eq. 5.15c leads to the following relations:

$$\Delta H - T\Delta S = 0 \quad (\text{with } \Delta = \Delta_{dec} - \Delta_R) \quad (5.16a)$$

$$\text{or: } T(\Delta_{dec}S - \Delta_RS) = (\Delta_{dec}H - \Delta_RH) = \Delta U \quad (5.16b)$$

With the knowledge of $\Delta_RS = 108.0 \pm 1.8 \text{ J mol}^{-1} \text{ K}^{-1}$ and the fitted value of $\Delta_{dec}S^\circ = 260 \pm 20 \text{ J mol}^{-1} \text{ K}^{-1}$ this leads to a value of $\Delta U = 2.1 \pm 0.3 \text{ eV}$, which is in fair agreement with the estimated value of $\Delta U = 2.5 - 2.9 \text{ eV}$ as described above and other values received from theoretical calculations showing strong variations ($\Delta U = 0.69 \text{ eV}$,¹³⁸ 2.1 eV ,¹³¹ 2.9 eV ,¹³⁹ 3.0 eV ¹³²). With the known value $\Delta_RH = 0.95 \text{ eV}$, the resulting value for $\Delta_{dec}H = 3.0 \pm 0.3 \text{ eV}$ is slightly lower than the respective values found in literature ranging between $\Delta_{dec}H = 3.7 \text{ eV}$ and 4.6 eV .^{280, 131, 130, 132, 133, 136}

For adsorbed atoms on surfaces, the entropy is mainly defined by the configurational entropy of the adsorbed species on the substrate lattice. The entropy therefore diminishes with increasing coverage due to a lower amount of distribution possibilities. This relation allows to determine a surface coverage with the knowledge of the respective entropy. In the case of C_{ad} on a Cu(111) lattice, the only additional degree of freedom (DOF) to the 2 translational DOF is the out-of-plane substrate- C_{ad} bond length. As this bond is quite strong ($E_{ad} = 4.9 - 5.2 \text{ eV}$), the respective vibrational contribution to the entropy is assumed to be low. Relation 5.16b for the phase equilibrium 5.15c can then be used to calculate the entropy difference between C_{ad} and SLG/Cu as $\Delta_{dec}S - \Delta_RS = 152 \text{ J (mol K)}^{-1}$, which equals to $S_{C_{ad}/Cu} - S_{g/Cu}$. Since the graphene formation entropy $\Delta_RS = 108 \text{ J (mol K)}^{-1}$ has been determined and the one for graphite formation is calculated as $\Delta_RS_{graphite} = 111 \text{ J (mol K)}^{-1}$ from NIST tabulated values, where also the absolute entropy of graphite $S_{graphite} = 30.7 \text{ J (mol K)}^{-1}$ is found, the one for g/Cu results as $S_{g/Cu} = 27.7 \text{ J (mol K)}^{-1}$. As a result, $S_{C_{ad}/Cu}$ calculates as: $S_{C_{ad}/Cu} = S_{g/Cu} + \Delta_{dec}S - \Delta_RS = 180 \text{ J (mol K)}^{-1}$

The configurational entropy of the N adsorbed carbon atoms on the M possible substrate sites can be calculated by:

$$S_{Config} = k * \ln\left(\frac{M!}{N!(M-N)!}\right) \quad (5.17)$$

Including the difference in atomic density for the graphene and the Cu(111) lattice of $\rho = 2.15$ and using Stirlings approximation, the configurational entropy can be determined as:

$$S_{Config} = R \left[\ln \left(\frac{1 - \vartheta_C}{\vartheta_C} \right) + \frac{1}{\rho} \ln \frac{1}{1 - \vartheta_C} \right] \quad (5.18)$$

The derivation of this equation from eq. 5.17 is shown in Appendix 12.2, which allows to relate the entropy $S_{Cad/Cu}$ to the equilibrium C_{ad} coverage ϑ_C by approximating $S_{Config} \approx S_{Cad}$. The applicability of this relation was tested in reference ¹²⁸ for the case of graphene on Ru(0001), where both the surface coverage ϑ_C and the entropy S_{Cad} are available as experimental data.^{98,274} For graphene on Cu with the derived value of $S_{Config} \approx S_{Cad} = 180 \text{ J mol}^{-1} \text{ K}^{-1}$ at a temperature of 1045 °C, the concentration ϑ_C of C_{ad} in thermodynamic equilibrium is $\approx 4 \times 10^{-10} \text{ ML}$. Using the slightly shifted values for graphite ($S_{graphite} = 30.7 \text{ J mol}^{-1} \text{ K}^{-1}$), a similar value of $3 \times 10^{-10} \text{ ML}$ is estimated. This low equilibrium concentration is even lower than the predicted values of $< 10^{-7} \text{ ML}$ ¹³¹ and $< 10^{-8} \text{ ML}$ ¹⁷³ reported in literature. This finding explains the high sensitivity of the CVD synthesis route with respect to carbon based impurities, where even the possibility to grow graphene using the oil vapor pressure back diffusing from a downstream positioned vacuum pump was reported.¹¹¹ Note that using the equilibrium constant for the methane decomposition reaction on Cu (eq. 5.6), the evolution of the surface carbon concentration can be determined also for deviations from K_{eq} :

$$K_{dec} = \frac{\vartheta_C * (p(H_2)/p^\ominus)^2}{(p(CH_4)/p^\ominus)} = \vartheta_C * w * (p(H_2)/p^\ominus) = \vartheta_C * Q_{exp} = Q_{dec} \quad (5.19)$$

The concentration evolves linearly with Q_{exp} , as this decomposition reaction is assumed to always be in equilibrium ($Q_{dec} \stackrel{!}{=} K_{dec}$). Commonly used parameter settings between 1-0.01 times K_{eq} consequentially lead to concentrations of C_{ad} between $4 \times 10^{-10} - 4 \times 10^{-8} \text{ ML}$. Using the proposed model for the graphene growth on Cu it is therefore not only possible to correctly predict the graphene growth velocity over a large parameter range, it is also possible to issue a statement about the detachment energy $E_{det} = 4.7 \pm 0.3 \text{ eV}$ and to quantify the C_{ad} concentration on the Cu surface during CVD growth

5.6. Experimental exploration of the decay term in the kinetic model

After having identified the rate limiting reaction steps for the attachment of adsorbed carbon atoms to the graphene flakes the question arises if the model also correctly predicts the decay rate of graphene when exposing a sample to conditions above the thermodynamic equilibrium K_{eq} . As already discussed in chapter 4.2, no quantitative determination of the decay rate has been performed up to now in literature. When exposing grown graphene flakes to a pure hydrogen atmosphere, the vanishing methane partial pressure

leads to a mass action constant approaching $Q_{exp} \rightarrow \infty$, inhibiting the new attachment of carbon to the graphene flake. The back-reaction of carbon detachment from the graphene flake should be the only factor determining the flake size change.

To explore the behavior of graphene flakes in pure hydrogen atmosphere, an experiment was conducted where graphene flakes were pre-grown at $Q_{exp} = 46$, $T = 1045^\circ\text{C}$ and subsequently exposed to pure $36.5\text{ mbar } H_2$ atmosphere for 15 minutes. A graphene sample was extracted before and after the exposure to pure H_2 . The graphene flakes detected on the sample after oxidation in air were examined by optical microscopy and the flake size distribution of the flakes was determined, as shown in Fig. 41. Before exposure to pure hydrogen, the sample shows graphene flakes of a regular hexagonal shape and a mean radius of $35 \pm 9\ \mu\text{m}$. After etching in hydrogen atmosphere, the flakes show an overall rounded shape as described in chapter 4.2. The flake radii were also determined and corrected by the factor $\sqrt{\pi/2\sqrt{3}}$ to calculate the radius of the equivalent ideal hexagon hosting the same amount of carbon atoms as the observed circular flakes. The appearing hexagonal holes on the inside of the graphene flakes were not subtracted from the total area, as these holes can be attributed to reactions with oxygen impurities on the surface (as will be discussed in chapter 8.1.1).

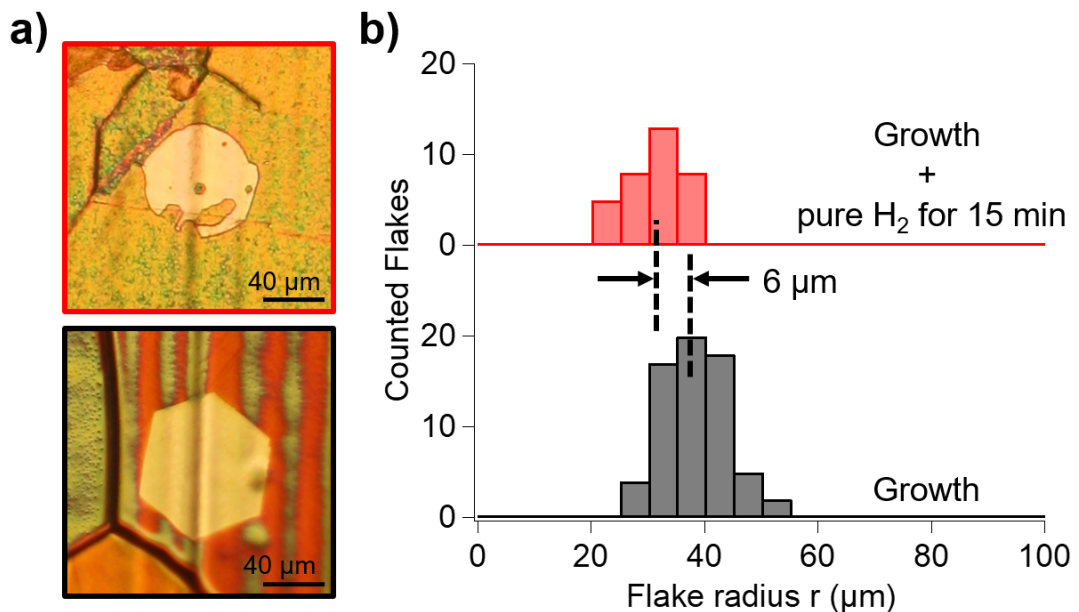


Figure 41 : Determination of the graphene decomposition rate without the addition of methane to the gas phase. Black: Exemplary optical image and histogram showing the flake size distribution as determined before the exposure to pure hydrogen gas phase. Red: Optical image and flake size distribution after exposure to $36.5\text{ mbar } H_2$ atmosphere for 15 min at 1045°C . A decay rate of $v = -24\ \mu\text{m h}^{-1}$ is determined for this step. (Experimental details: E. 48)

Omitting the oxygen induced hole formation inside the flakes and determining the mean flake radius as $35 \pm 9 \mu\text{m}$ and as $29 \pm 8 \mu\text{m}$ after the 15 min H_2 exposure leads to a decay rate of $dr/dt = -24 \mu\text{m h}^{-1}$. According to the nominal detachment rate at $1045 \text{ }^\circ\text{C}$ (see Fig. 40), a detachment rate of $-74 \mu\text{m h}^{-1}$ would be expected. The observed detachment rate of $dr/dt = -24 \mu\text{m h}^{-1}$ is about 3 times lower than expected but of the correct order of magnitude. The discrepancy can be attributed to two different causes. If during growth a certain amount of carbon is diluted in the Cu bulk in a sort of steady-state, this carbon might migrate to the surface and refill the surface concentration when changing the gas phase conditions. This would lead to a certain delay in the graphene flake size decay until the Cu bulk is carbon free. At these reaction conditions, all impurities in the reactor system affect the outcome of the experiment, traces of carbon in the gas feed or from the reactor walls may also lead to a virtual methane partial pressure above zero.

It is also possible that the graphene decay rate is lower than expected if the detachment of carbon from the graphene flake is not the rate-determining step. The following hydrogenation steps as well as the associative desorption from the surface may limit the formation rate of methane as well. J. Kraus estimated the maximum desorption rate of methane by recombination of $CH_{3,ad}$ and H_{ad} under common reaction conditions ($T = 1075 \text{ }^\circ\text{C}$, $p(H_2) = 10 \text{ mbar}$, $p(CH_4) = 0.01 \text{ mbar}$) to be in the order of $10^{-4} \text{ ML s}^{-1}$ on Cu(110).¹⁷⁴ This is about 0.4 ML decay per hour or 0.1 ML decay in 15 min as in the performed experiment. With a graphene coverage on the sample of approximately 5-10%, this hydrogenation may influence the observed decay rate of graphene flakes.

However, the performed experiment shows that the introduced kinetic growth model also predicts the correct order of magnitude decay rate for samples above the thermodynamic equilibrium K_{eq} , where the detachment rate outplays the C_{ad} attachment to the flakes.

5.7. Evaluation of the literature graphene growth coincidence with the proposed growth model

Several literature references have been explored to extract the used growth parameters and the resulting growth velocity for comparison with the predictions of the kinetic growth model.

Table 13 : Literature data of ambient pressure CVD (APCVD) growth studies and extracted growth velocities in comparison with the prediction of the kinetic growth model (see text). Supplementary explanations are provided on the next pages. Table data adapted with permission from reference ¹²⁸. Copyright 2021 American Chemical Society.

APCVD	Year	T (K)	p_{CH_4} (mbar)	p_{H_2} (mbar)	Q_{exp}	t_{CVD} (min)	flake radius r (μm)	Nuc. dens. $1/\text{mm}^2$	$\frac{v_{theo}}{v_{expt}}$	$\frac{N_{C,provided}}{N_{C,consumed}}$	v_{theo} ($\mu\text{m}/\text{h}$)
Gao ¹²¹	2010	1273	3.32	498	75	1	0.9	40000	0.0041	137	0.22
Han ²⁸¹	2011	1333	2.96	9.87	3.00E-02	0.05	8.7	3600	38	1.7	392910
Robertson ²⁸²	2011	1273	3.28	246	18	10	2.2	40000	3.9	227	51
Wu ²⁸³	2011	1263	3.32	249	19	3	0.2	250000	8.2	1151	32.8
Yu ¹⁶⁴	2011	1323	0.00774	32.3	135	15	6.5	2500	g should decay	3	
Nie ²⁸⁴	2012	1223	0.0296	12.8	6	30	5.2	8000	2.3	2.6	24.4
Mohsin ²⁶⁸	2013	1348	0.046	100	217	300	433	0.2	g should decay	1376	
Vlassiok ²⁸⁵	2013	1323	0.0266	48.2	87	75	21.7	195	1.0	58	17.2
Wu ²⁸⁶	2013	1353	9.9	495	25	8	13	400	9.0	4673	873
Ogawa ²⁸⁷	2014	1348	0.00976	24.4	61	20	17.3	200	3.6	12	185
Suzuki ²⁸⁸	2014	1323	0.00982	17.7	32	20	8.7	1000	7.4	7	194
Li ²⁸⁹	2015	1348	0.025	10	4	180	650	0.005	25	7978	5426
Nguyen ²⁹⁰	2015	1348	0.0286	47.6	79	180	303	1	1.0	210	100
Zhang ²⁹¹	2015	1323	0.00735	19.6	52	30	21.7	80	2.0	16	85.6
Chen ⁷²	2016	1318	0.476	47.6	5	7	10.4	1000	17	77	1475
Chen ⁷²	2016	1333	0.485	29.1	2	7	23.8	400	36	46	7293
Ding ²⁹²	2016	1348	0.0147	19.6	26	120	433	1	3.1	35	676
Jung ¹⁵⁵	2016	1273	0.0469	62.5	83	15	6.5	900	g should decay	25	
Phan ²²	2016	1323	0.0286	47.6	79	240	650	0.25	0.2	175	27.6
Ta ²⁹³	2016	1333	27.3	63.6	1.50E-01	0.083	3.2	10000	38	68	87184
Wang ²⁹⁴	2016	1348	0.965	33.8	1	60	217	0.25	87	18478	18770
Wu ⁵⁰	2016	1323	0.0222	27.8	35	2	8.7	400	0.7	3.9	171
Wu ²⁴⁰	2016	1303	0.075	20	5	60	650	0.1	1.1	218	731
Xu ²⁷	2016	1273	9.8	9.8	9.80E-03	0.05	52	1	2.1	242	128021
Zhang ²⁴⁵	2016	1323	0.0049	19.6	78	15	17.3	400	0.4	1.7	28.8
Zhang ²⁹⁵	2016	1323	0.00735	19.6	52	30	21.7	4	2.0	315	85.6
Stehle ²⁴²	2017	1338	0.0117	24.4	51	60	10.8	400	16	49	171
Burton ²⁹⁶	2019	1338	0.5	100	20	10	108	4	1.0	350	643
Zheng ¹¹⁸	2019	1393	6.17	6.17	6.17E-03	0.067	48.5	50	407	23	1.80E+07

Table 14 : Literature data of low-pressure CVD (LPCVD) studies (see text).¹²⁸ Copyright 2021 American Chemical Society.

LPCVD	Year	T (K)	p_{tot} (mbar)	p_{CH_4} (mbar)	p_{H_2} (mbar)	Q_{exp}	t_{CVD} (min)	flake radius r (μm)	Nuc. dens. ($1/mm^2$)	$\frac{v_{theo}}{v_{expt}}$	$\frac{N_{C,provided}}{N_{C,consumed}}$	v_{theo} ($\mu m/h$)
Liu ²²⁷	2011	1253	0.5	0.25	0.25	2.50E-04	20	1.3	50000	562676	59	2.20E+06
Vlassiouk ¹¹⁶	2011	1273	na	0.00013	0.466	2	30	3.5	2500	105	0.17	735
Jia ³⁷	2012	1293	0.13	0.0165	0.127	9.78E-04	6	21.7	400	13187	0.94	2.90E+06
Kim ¹⁴¹	2012	1273	4.1	0.373	3.73	3.73E-02	0.017	0.9	250000	10.6	0.04	33623
Wang ¹²³	2012	1318	13	0.0133	13.3	13	15.5	156	1	0.8	21	481
Yan ²⁹⁷	2012	1333	143	0.308	144	67	80	173	2	0.6	1265	76.5
Zhang ²⁹⁸	2012	1273	0.27	0.0197	0.267	3.62E-03	30	4.3	900	40316	48	346725
Hao ²¹	2013	1308	0.13	0.00132	0.133	1.34E-02	150	346	1	2704	3.6	374716
Regmi ²⁹⁹	2012	1273	0.67	0.167	0.5	1.50E-03	1	2.2	10000	6349	4.6	838166
Vlassiouk ²⁸⁵	2013	1298	6.7	0.000566	1.01	2	75	13	600	177	0.8	1851
Wu ³⁰⁰	2013	1308	0.07	0.022	0.044	8.80E-05	1	6.5	2500	146334	0.46	5.70E+07
Eres ¹²⁷	2014	1313	0.2	0.00952	0.19	3.79E-03	120	217	3	14825	19	1.60E+06
Han ³⁰¹	2014	1273	275	0.05	25	13	5	26	100	0.3	4.9	83.8
Yan ²⁴	2014	1343	146	0.225	146	95	115	52	25	1.5	1341	40.2
Ghosh ³⁰²	2015	1273	24	0.119	23.9	5	2	1.1	10000	7.4	26	245
Liang ¹¹⁹	2015	1293	0.05	0.000199	0.0498	1.25E-02	5	2.2	2500	8501	0.15	224427
Miseikis ³⁰³	2015	1333	25	0.0271	0.543	1.09E-02	10	47.6	10	4162	37	1.20E+06
Zhao ³⁰⁴	2015	1303	na	0.0146	0.732	3.67E-02	360	433	1	1569	57	112716
Cabrero-Vilatela ²⁷⁸	2015	1323	50	0.00217	4.71	10	15	8.7	900	23	1.3	786
Chaitoglou ³⁰⁵	2016	1313	0.2	0.04	0.16	6.40E-04	20	13	1000	243821	11	9.50E+06
Cheng ³⁰⁶	2016	1333	na	0.00345	2.3	2	60	108	3	77	18	8320
Hao ²⁸⁰	2016	1308	na	0.0667	0.133	2.65E-04	8	17.3	400	145951	9.8	1.90E+07
Hao ²⁸⁰	2016	1308	na	0.00133	0.133	1.33E-02	60	17.3	800	21824	0.73	377555
Hsieh ³⁰⁷	2016	1313	1.3	0.00213	1.33	1	80	433	1	22	2.1	7266
Jung ¹⁵⁵	2016	1273	0.67	0.000583	0.666	1	10	2.2	10000	127	0.16	1633
Kraus ¹⁸³	2016	1348	2	0.002	2	2	60	86.6	4	127	15	11036
Li ³⁰⁸	2016	1333	100	0.249	9.98	4.00E-01	1	3.5	2500	153	25	32222
Yin ³⁰⁹	2016	1303	6	0.00998	5.99	4	40	8.7	3600	85	3	1106
Agrawal ³¹⁰	2017	1350	144	0.205	144	101	480	650	0.1	0.5	8951	44.2
Das ³¹¹	2017	1273	933	0.222	44.4	9	14	6.1	500	4.8	223	125
Huet ³¹²	2017	1323	750	0.08	72	65	30	106	1	0.25	573	52.6
Kraus ¹²⁶	2017	1233	15	0.06	15	4	60	21.7	1	2.7	5638	58.2
Luo ³¹³	2017	1313	0.13	0.0121	0.121	1.21E-03	20	10.8	400	155233	12	5.00E+06
Qi ³¹⁴	2018	1313	0.17	0.005	0.165	5.45E-03	30	130	5	4301	4.2	1.10E+06

Supplementary information to Tables 13 and 14:

Literature references in which all necessary information was given to predict graphene growth velocities according to the outlined kinetic growth model and where experimental data were provided from which experimental graphene growth velocities could be deduced. Due to the lack of statistical information, the extracted data points are subject to large variations and no error margins can be given. In the case of several given growth conditions, one or in some cases two representative growth conditions were used. All parameters used to determine experimental and predicted growth speed are listed in the tables, as well as an estimation of the observed nucleation density. The ratio between predicted and experimentally observed growth speed is listed in column $\frac{v_{theo}}{v_{expt}}$. As discussed in the main text, the ratio of the provided impinging and consumed surface carbon atoms for graphene growth are listed in column $\frac{N_{C,provided}}{N_{C,consumed}}$. The predicted growth speed is listed in the last column.

Colorcode:

Red: Data with conflict - provided carbon supply ($N_{C,provided}$) does not match the carbon required for the reported graphene growth ($N_{C,consumed}$), i. e. $\frac{N_{C,provided}}{N_{C,consumed}} < 1$ or graphene growth was reported at CVD conditions where graphene formation is thermodynamically unstable. Such cases result from wrong CVD parameter readings or carbon impurities of the system. These cases can be disregarded for obvious reasons.

Green: Reported flake growth velocity v_{exp} does not deviate from the predicted value v_{theo} by more than an order of magnitude.

Yellow: Methane overdosing by more than a factor of 100 compared to carbon amount required for the observed graphene growth.

Blue: v_{theo} lower than 1000 $\mu\text{m/h}$.

Sum: 63 data sets from 59 studies reported in literature.

A total of 63 growth conditions from 59 literature references were found in which all relevant parameters were listed to enable comparison with the kinetic growth model. The graphene growth can be done using reactor systems at atmospheric pressure without the use of a vacuum pump (also known as Ambient Pressure CVD), or the graphene can be grown in a leak-tight system with a constant pumping of the reactive gases at $p_{tot} < 1\text{bar}$ (also known as Low Pressure CVD). The partial pressures of H_2 and CH_4 are often quite similar between APCVD and LPCVD, as Argon gas is used to fill the reactor system to ambient pressure for APCVD. Nevertheless, literature references report differences in growth behavior for both growth techniques.²⁸⁵ These differences mainly refer to parameters, such as the nucleation density and Cu evaporation, which need to be discussed separately from the graphene growth velocity. All references and the used growth parameters are listed in Table 13 for APCVD growth conditions and Table 14 for LPCVD conditions.

The applied growth parameters of the literature data are visualized in Fig. 42 in form of a $Q_{exp} - T$ -graph. The fixed graphene equilibrium line and the predicted growth velocities are inserted in the graph. The used markers for the literature data indicate the used growth system (APCVD = circle, LPCVD = cube). The color-coding is used to inform about the accordance between predicted and experimentally observed growth velocity. Black markers show concordance with less than one order of magnitude deviation, red markers show experimentally observed growth velocities that are more than one order of magnitude lower than the predicted values and blue markers are used for experiments grown at conditions where graphene should be thermodynamically unstable according to the results presented in chapter 4.2.

Experiments reported at growth conditions that lead to a growth velocity of up to 1mmh^{-1} show coincidence within the predicted order of magnitude. At growth conditions further away from equilibrium the predicted growth velocity exceeds the experimentally observed one by more than a factor of 10. These observations are independent of the used growth system. Thus, at growth velocities above $v = 1\text{mmh}^{-1}$, there seems to be an additional limitation occurring for larger growth velocities. In several cases, the kinetic growth model predicts growth velocities larger than 10 cm per hour. For these large growth velocities, the available carbon from the methane decomposition on the Cu surface may be insufficient to feed the demand of the growing graphene flakes. In order to clarify this potential limitation, a rough comparison of provided and consumed carbon is done in the following. The consumed carbon on the Cu surface can be estimated by the average flake size and the determined nucleation density on the sample. These values were extracted from provided images in the respective publications. The number of consumed carbon atoms per flake is given by eq. 5.20:

$$N_{C,consumed} = r^2 * 2\sqrt{3} * \frac{\rho}{A_{Cu}} \quad (5.20)$$

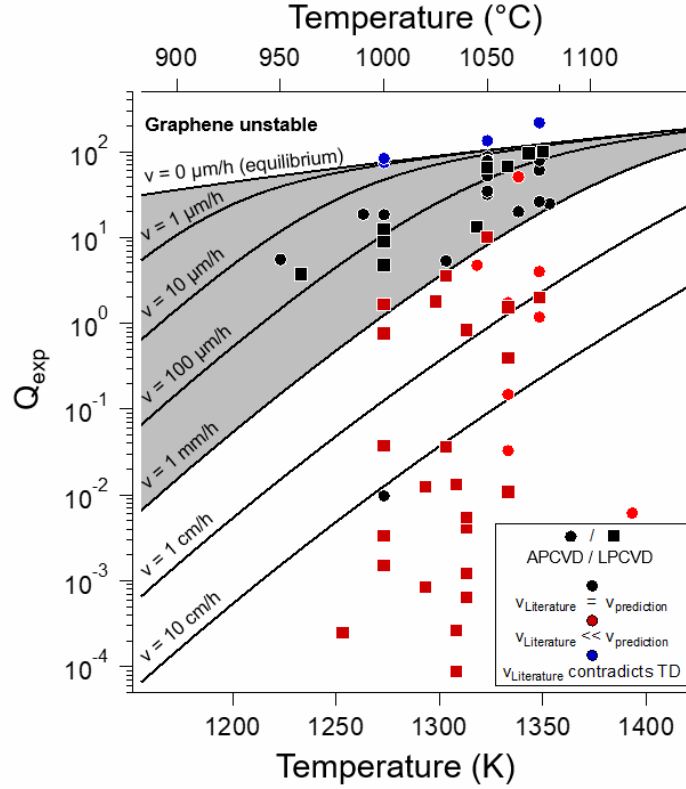


Figure 42 : Presentation of literature data according to our graphene growth model. The reaction conditions used in the literature references are inserted in a $Q_{exp} - T$ -diagram. The logarithmically plotted mass action constant relates to the orders of magnitude of the growth velocity according to our model, as inserted in form of (mostly) parallel lines. Coloring of the data points indicates either agreement of literature and predicted values in the same order of magnitude (black), stronger deviations than one order of magnitude (red) or the disagreement between growth/etching behavior at the respective reaction conditions (blue). All data-points are listed in Tables 13 and 14. Highlighted in grey is the growth regime where prediction and experimental results fit very well. Reprinted with permission from reference ¹²⁸. Copyright 2021 American Chemical Society.

Here, r is the inner radius of the graphene flake hexagon, ρ is the difference in atomic density between graphene and Cu(111) of 2.15 and A_{Cu} is the Cu(111) unit cell size. The provided amount of C atoms on the surface is determined by the amount of methane impingement on the surface (eq. 5.21) multiplied by the sticking coefficient S_{CH_4} of methane on Cu(111) at the reaction temperature.

$$N_{provided} = \frac{P_{CH_4}}{\sqrt{2\pi * m_{CH_4} * k_B * T}} * S_{CH_4} \quad (5.21)$$

The sticking coefficient S_{CH_4} is extrapolated from the value of 8.6×10^{-9} at 1000 K with an apparent activation energy of 201 kJ mol^{-1} .¹⁶³ These values were measured for Cu(100) but are assumed to be similar for Cu(111). The resulting ratio between $N_{C,provided}$ and $N_{C,consumed}$ is listed in Tables 13 and 14. All experiments in which the growth velocity v is overestimated by the model show a respective ratio lower than 100.

I. e., in the respective cases less than 100x more methane molecules are dissociatively adsorbed on the Cu surface than are required for the growth of the observed graphene islands. Thus, the failure of the growth model in predicting the growth velocity seems to require an overdose of about a factor 100. Note that the estimated ratio does not include the surface blocking by the already grown graphene flakes, which limits the actual carbon supply at high coverage. In many literature studies high total coverage is reached, which increases the discrepancy between carbon supply and consumption ($N_{C,provided}/N_{C,consumed}$) in the respective experiments. One exception is the experiment by Xu *et al.*²⁷ In this study, the chosen CVD parameter conditions ($Q_{exp} \approx 10^{-2}$) would lead to a predicted growth velocity of 13 cm h^{-1} in agreement with the experimentally observed value of 6 cm h^{-1} . In this study, a very high partial pressure of methane of 9.8 mbar provided a carbon supply 250 times larger than the used carbon.

Thus, within the order of magnitude the kinetic growth model seems to correctly predict high growth rates as long as the overdosing requirement is fulfilled. All in all, the kinetic growth model seems to work very well and deviations of the predicted growth rates seem to occur due to:

- Growth rates larger than predicted by the growth limitation of the attachment process to the graphene flake can only be explained by mis-calibration of the reactor system or an additional carbon source in the system. This may be present in the form of contaminations in the gas phase or contaminations originating from the growth substrate (in this case the Cu foil).
- Growth rates lower than predicted may arise in parameter regimes where a different reaction than the attachment of C_{ad} to the graphene flake becomes limiting, as these situations are not included in the current growth model. In these cases, including all red marked literature references in Fig. 42, the predicted growth speed may only state an upper limit to the possible growth speed.

5.8. Growth velocities observed at deficient gas phase supply

The comparison of experimental values with the ones reported in literature predicts a correlation between the maximum possible growth velocity v and the applied methane partial pressure, i. e. the carbon atoms arriving on the Cu surface. To examine this hypothesis, an experimental series was done at $T = 1045^\circ\text{C}$ with a constant methane partial pressure of $p_{CH_4} = 0.01 \text{ mbar}$ but an increasing distance to the thermodynamic equilibrium, i. e. Q_{exp} -values of 10, 5 and 2.5. Each experiment was conducted with either two or three Cu samples, removed after different reaction times t to increase the significance of the respective data points. In order to account for the effect of continuous graphene

flake nucleation throughout the experiment at these conditions (see chapter 6), the size increase of the largest graphene flakes was determined rather than using a mean island size distribution, which would underestimate the growth rate. In Fig. 43, the determined growth speed values are added to the predicted growth rate expected at sufficient carbon supply. The three growth values far away from equilibrium show equal growth speeds of $\approx 500 \mu\text{m h}^{-1}$, regardless of their Q_{exp} -values. While this value roughly coincides with the expected growth speed at $Q_{exp} = 10$ (first data point), growth speeds at sufficient carbon supply would amount to 1400 and $2900 \mu\text{m h}^{-1}$ for $Q_{exp} = 5$ and $Q_{exp} = 2.5$, respectively.

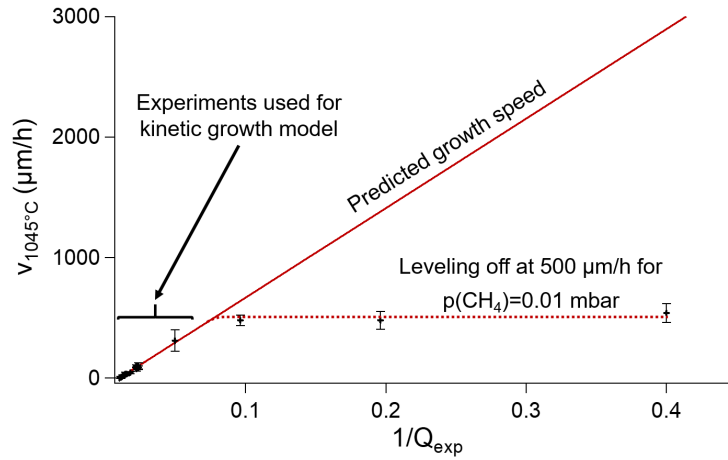


Figure 43 : Deviation of predicted growth velocity v by the growth model and experimental results at particularly low methane partial pressures. The diagonal line shows the growth speed v predicted by the kinetic growth model, while the experiments at differing Q_{exp} and $p(\text{CH}_4) = 0.01 \text{ mbar}$ show a levelling off at a growth velocity of $v \approx 500 \mu\text{m h}^{-1}$. (Experimental details: E. 34 , E. 35 , E. 36)

In order to examine in more detail the correlation between methane partial pressure $p(\text{CH}_4)$ and the limiting growth velocity, an expanded experimental series was done by variation of $p(\text{CH}_4)$ and Q_{exp} at a constant temperature of 1045°C . The extracted growth speeds are plotted against $1/Q_{exp}$ in Fig. 44a) and against $p(\text{CH}_4)$ in Fig. 44b). Again, the levelling off in dependence of the methane partial pressure is observed. The chart shown in Fig. 44b) proves that v scales linearly with $p(\text{CH}_4)$ at low methane pressure ($p(\text{CH}_4)$ -limitation). The fitted line for $p(\text{CH}_4)$ -limitation up to $p(\text{CH}_4) = 0.02 \text{ mbar}$ leads to the empirically determined formula:

$$v_{max}[p(\text{CH}_4), 1045^\circ\text{C}] = 500 \pm 30 \frac{\mu\text{m}}{\text{h}} * \frac{p_{\text{CH}_4}}{0.01 \text{ mbar}} \quad (5.22)$$

For values larger than $p(\text{CH}_4) = 0.02 \text{ mbar}$ the limiting growth velocity slightly changes its slope, indicated by dashed lines.

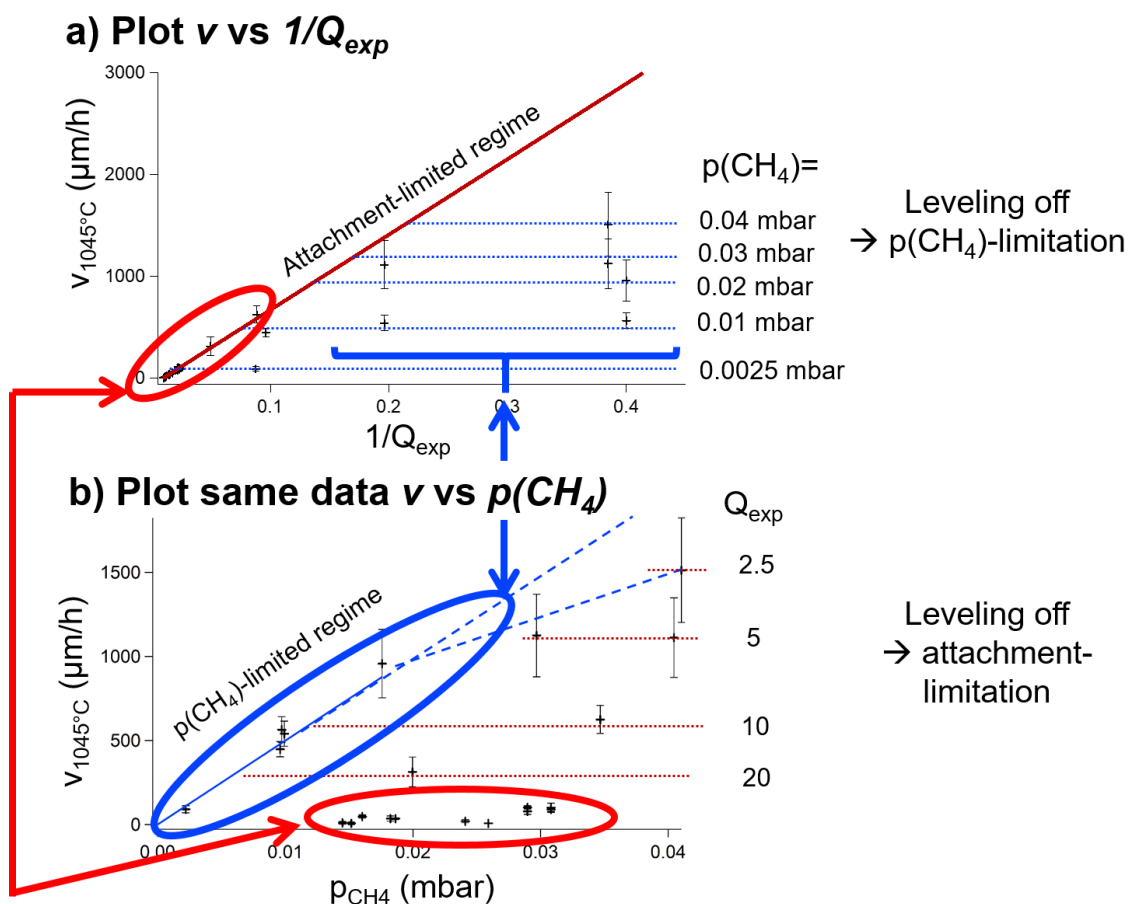


Figure 44 : Experiments conducted at 1045 °C indicating a growth velocity levelling off at low methane partial pressures. a) Plotting v vs $1/Q_{exp}$ shows a leveling off directly related to the methane partial pressure, as indicated in the diagram. At enough provided methane, the attachment limitation leads to growth velocities as predicted in the growth model. b) Plotting the same data against the methane partial pressure shows the linear dependence of v related to $p(\text{CH}_4)$ and a leveling off if the attachment limitation is reached. (Experimental details: E. 34 , E. 35 , E. 36 , E. 37 , E. 38 , E. 39 , E. 40 , E. 41 , E. 42)

The presented results clearly show that, while the attachment of C_{ad} is the limiting growth step at sufficient supply of carbon to the surface, the growth limitation can also change towards a $p(\text{CH}_4)$ -limitation type. Once this limiting growth regime is reached, changing the kinetic driving force (the distance to thermodynamic equilibrium) does no longer have an impact on the observed growth speed. Most interestingly, this limiting graphene growth velocity is not dependent on:

- The total nucleation density: At samples with different nucleation densities and also in the course of a single reaction with significant continuous nucleation of new flakes during CVD growth (see chapter 6), the determined growth speeds remained unaffected by the flake density on the Cu foil.

- The reaction time: The growth velocity $v = dr/dt$ remains constant over time also in the $p(\text{CH}_4)$ -limited growth regime. All data points shown in Fig. 44 were at least measured for two different growth times t , as is shown in Fig. 45.

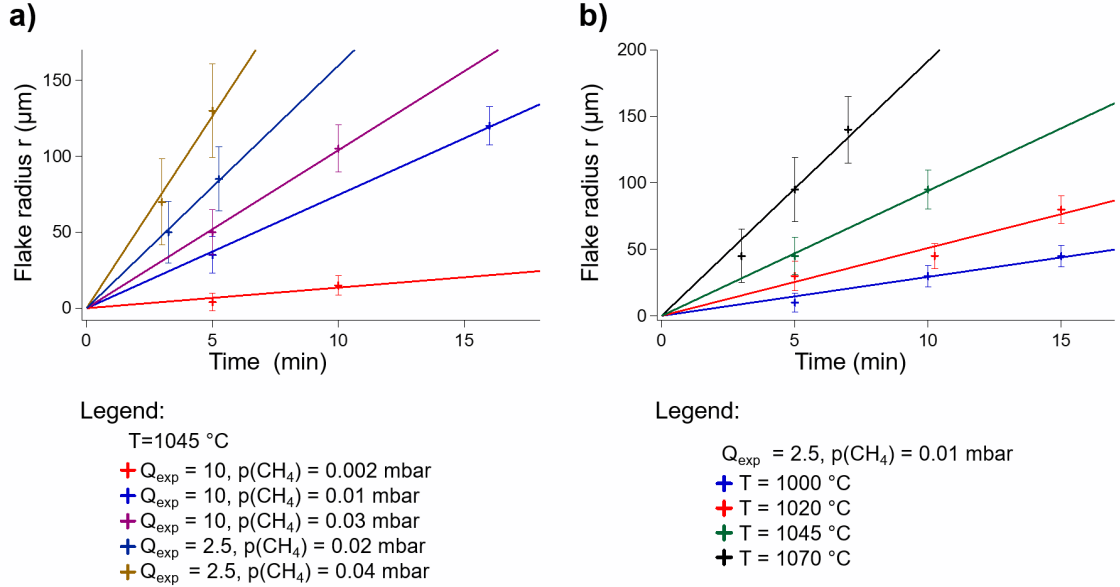


Figure 45 : Flake radius increase over time for CVD experiments performed at $p(\text{CH}_4)$ -limited growth conditions. No nucleation step was included in the reaction sequence and the largest graphene flakes were used to determine the flake radii. The straight lines show linear fits through the data points, fixed at $r(t = 0) = 0$. a) Reactions performed at constant temperature of $1045\text{ }^\circ\text{C}$. Only an excerpt is shown for sake of clarity. b) Experiments performed at constant $Q_{\text{exp}} = 2.5$ and $p(\text{CH}_4) = 0.01\text{ mbar}$, at varying temperature.

Combining these two findings of strong dependence on $p(\text{CH}_4)$ coupled with independency of the sample surroundings and the overall flake size leads to the hypothesis that the carbon atoms effectively feeding the graphene growth are exclusively the ones arriving within a certain distance of the graphene rim. This defines a certain area of capture around each graphene flake, where methane molecules arrive and feed the growing island. This situation is sketched in Fig. 46.

Assuming a constant width λ of the capture zone around each island rim leads to an effective feeding area of $\lambda * L_{\text{rim}}$ where methane molecules can adsorb from the gas phase. If each adsorbing gas phase molecule landing in the capture zone feeds the growing flake with the required carbon atoms, the carbon attachment rate is proportional to the flake rim L_{rim} . Since also the flake radius is proportional to L_{rim} , the resulting growth velocity $v = dr/dt$ should not depend on the island size.

The argument of a constant growth velocity v works similar as during the derivation of eq. 5.12 and provides the explanation of the experimental finding of the linear flake radius increase per time plotted in Fig. 45 for the $p(\text{CH}_4)$ -limited growth regime. Other reaction limitations can be excluded:

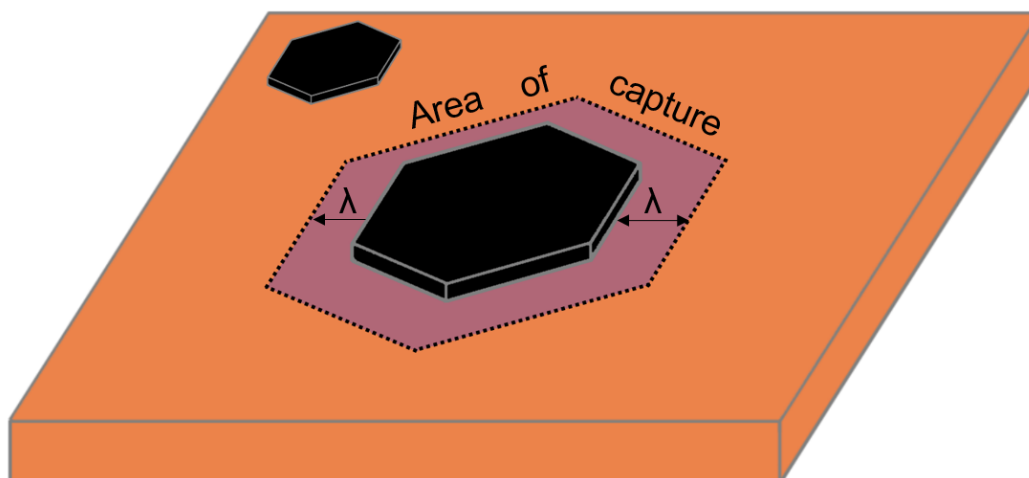


Figure 46 : Proposed model for the observed $p(\text{CH}_4)$ –limitation of the growth speed at low methane partial pressures. If the carbon atoms relevant for the growth of a graphene island are the ones arriving in a certain distance to the island rim, then a so-called "area of capture" around each graphene flake determines the growth rate of the flake. As this "area of capture" increases equal to the island rim length, this leads to a constant island growth until merging with neighboring islands. This scenario would for example be expected if the mean lifetime of an adsorbed carbon atom on the Cu surface is limited by the backreaction to gaseous methane.

- A broad C_{ad} concentration gradient between the graphene rim and the bare Cu area. With changing value of Q_{exp} the C_{ad} equilibrium concentration on bare Cu should also increase, which then leads to an increased amount of diffusion and attachment to the graphene flake. The experiments show that a reduction of Q_{exp} by a factor of 4 (see Fig. 44), which leads to a quadrupled equilibrium concentration of C_{ad} , has no impact on the graphene growth velocity.
- Feeding of the graphene flake growth reaction from the Cu volume has been shown not to be the case.¹⁷ Additionally, the carbon dissolution in the Cu volume must also be fed by the adsorbing methane molecules, which would thus also depend on the surface coverage and nucleation density.

The radius of the predicted area of capture can be estimated by comparing the amount of dissociatively adsorbed molecules with the carbon atoms incorporated in the graphene island. Using the already introduced estimation of the sticking coefficient by Chorkendorff *et al*¹⁶³ and the fitted growth limit dependency on $p(\text{CH}_4)$ (eq. 5.22) leads to an area of capture of $\approx 100 \mu\text{m}$ at 1045 °C. The calculation of this value is outlined in

Appendix 12.4. The estimated value of $\lambda = 100 \mu\text{m}$ at $1045 \text{ }^\circ\text{C}$ depends on the reactive sticking coefficient of methane, which was extrapolated in the approximation and therefore only leads to an order of magnitude estimation. However, since no decrease of the growth speed was observed for graphene flakes that approach neighboring flakes at distances of about $50\text{-}100 \mu\text{m}$, the estimation seems to deliver a slightly overestimated, but reasonable value for λ .

Temperature dependency of the $p(\text{CH}_4)$ - limited growth velocity An experimental series with a constant gas phase composition ($p(\text{H}_2) = 5 \text{ mbar}$, $p(\text{CH}_4) = 0.01 \text{ mbar}$) at varying temperatures was conducted in order to give an insight into the apparent activation energy of the limited growth process. The determined growth speed is plotted in form of black markers in Fig 47a) plotted against the reaction temperature T . Plotted in blue are the growth speeds predicted by the kinetic growth model assuming the pre-equilibrium of the C_{ad} -phase. Plotted in black is a fit to the data points implicating the temperature-dependent impingement rate of methane molecules on the surface (first term in eq. 5.23) and an apparent activation energy E_{app} for the decomposition of methane on the surface and attachment to the graphene island (second term in eq. 5.23).

$$v \sim \frac{p(\text{CH}_4)}{\sqrt{2\pi * m_{\text{CH}_4} * k_B * T}} * e^{-\frac{E_{app}}{RT}} \quad (5.23)$$

Here, m_{CH_4} refers to the molecular mass of the methane molecule of $m_{\text{CH}_4} = 2.66 \times 10^{-26} \text{ kg}$. Fig. 47b) shows the Arrhenius plot used for the determination of the apparent activation energy E_{app} . The fit leads to an apparent activation energy of $E_{app} = 382 \pm 8 \text{ kJ mol}^{-1} = 3.96 \pm 0.09 \text{ eV}$.

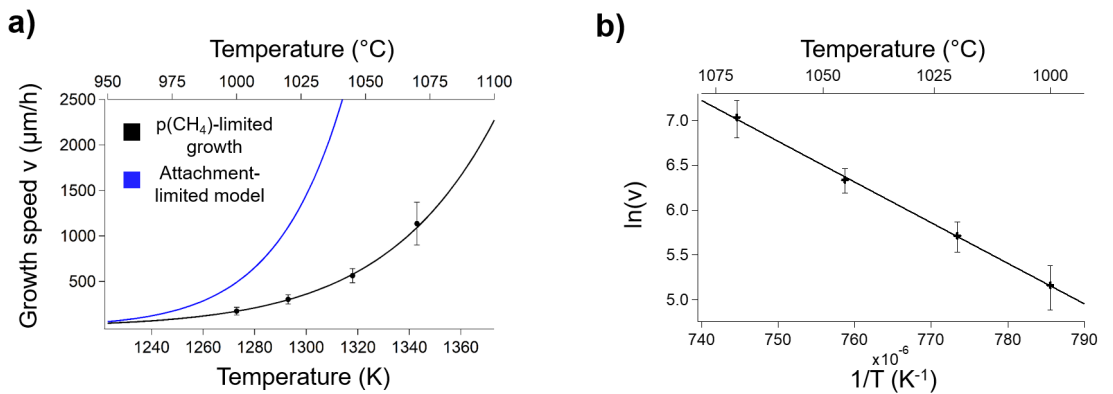


Figure 47 : Temperature dependence of the methane limited growth velocity. a) Graphene island growth velocity of the $p(\text{CH}_4)$ -limited growth conditions (black points) compared to the expected values from the kinetic growth model of eq. 5.23 (blue line). $p(\text{CH}_4)$ -limited growth was conducted at $p(\text{H}_2) = 5 \text{ mbar}$ and $p(\text{CH}_4) = 0.01 \text{ mbar}$. b) Arrhenius plot of the growth velocity $\ln(v)$ against the inverse temperature $1/T$. The fit leads to an apparent activation energy of $382 \pm 8 \text{ kJ mol}^{-1}$. (Experimental details: E. 43 , E. 44 , E. 45)

Comparison of the $p(\text{CH}_4)$ -limited growth with literature data

Having identified an additional CVD growth regime for the CVD growth of graphene on Cu provides the possibility to re-evaluate the literature data compiled in Tables 13 and 14 and shown in Fig. 42. As discussed in chapter 5.1, a large amount of literature values in which graphene was grown far away from thermodynamic equilibrium did not match the growth velocities predicted. As primarily evaluated, the provided carbon for these cases was particularly low compared to the consumed carbon for the graphene flake growth. Assuming a $p(\text{CH}_4)$ -limitation of the growth kinetics, as done in the model of eq. 5.23, the measured growth kinetics can be discussed to be either attachment-limited or $p(\text{CH}_4)$ -limited. The information is added in the Tables 15 and 16, in which color coded markers refer to the used limitation ($a = \textit{attachment} - \textit{limited}$, $b = p(\text{CH}_4) - \textit{limited}$).

Colorcode:

a: Growth limited by carbon attachment to graphene island (attachment-limitation)

b: Growth limited by deficiency of the provided methane ($p(\text{CH}_4)$ -limitation)

TD: Growth thermodynamically prohibited

Green: Deviation by less than a factor 10 (between predicted and experimentally observed value)

Yellow: Deviation by more than a factor 10

Red: Deviation by more than a factor 50

Table 15 : Literature data of ambient pressure CVD (APCVD) growth studies as shown in Table 13, extended by the predictions of the $p(CH_4)$ -limited growth model. Table data adapted with permission from reference ¹²⁸. Copyright 2021 American Chemical Society.

APCVD	Year	T (K)	P_{CH_4} (mbar)	$v_{CH_4,limit}$	Limit	$v_{resulting,theo}$	v_{expt}	$\frac{v_{res,theo}}{v_{expt}}$
Gao ¹²¹	2010	1273	3.32	47544	TD	0.22	54	0.004
Han ²⁸¹	2011	1333	2.96	220382	b	220382	10440	21
Robertson ²⁸²	2011	1273	3.28	46971	a	51	13	3.9
Wu ²⁸³	2011	1263	3.32	35580	a	33	4	8.2
Yu ¹⁶⁴	2011	1323	0.00774	442	TD	G should decay	26	
Nie ²⁸⁴	2012	1223	0.0296	95	a	24	10	2.3
Mohsin ²⁶⁸	2013	1348	0.046	5055	TD	G should decay	87	
Vlassiuk ²⁸⁵	2013	1323	0.0266	1520	a	17	17	1.0
Wu ²⁸⁶	2013	1353	9.9	1.23637e+06	a	874	98	9
Ogawa ²⁸⁷	2014	1348	0.00976	1073	a	185	52	3.6
Suzuki ²⁸⁸	2014	1323	0.00982	561	a	194	26	7.4
Li ²⁸⁹	2015	1348	0.025	2747	b	2747	217	13
Nguyen ²⁹⁰	2015	1348	0.0286	3143	a	100	101	1.0
Zhang ²⁹¹	2015	1323	0.00735	420	a	86	43	2.0
Chen ⁷²	2016	1318	0.476	23800	a	1475	89	16
Chen ⁷²	2016	1333	0.485	36110	a	7293	204	36
Ding ²⁹²	2016	1348	0.0147	1615	a	676	217	3.1
Jung ¹⁵⁵	2016	1273	0.0469	672	TD	G should decay	26	
Phan ²²	2016	1323	0.0286	1635	a	28	162	0.2
Ta ²⁹³	2016	1333	27.3	2.03257e+06	a	87184	2313	38
Wang ²⁹⁴	2016	1348	0.965	106048	a	18770	217	87
Wu ⁵⁰	2016	1323	0.0222	1269	a	171	261	0.7
Wu ²⁴⁰	2016	1303	0.075	2496	a	731	650	1.1
Xu ²⁷	2016	1273	9.8	140340	a	128021	62400	2.1
Zhang ²⁴⁵	2016	1323	0.0049	280	a	29	69	0.4
Zhang ²⁹⁵	2016	1323	0.00735	420	a	86	43	2.0
Stehle ²⁴²	2017	1338	0.0117	993	a	171	11	16
Burton ²⁹⁶	2019	1338	0.5	42426	a	643	650	1.0
Zheng ¹¹⁸	2019	1393	6.17	2.07417e+06	b	2.07417e+06	43432	48

Table 16 : Literature data of low-pressure CVD (LPCVD) studies as shown in Table 14, extended by the predictions of the $p(CH_4)$ -limited growth model. Table data adapted with permission from reference ¹²⁸. Copyright 2021 American Chemical Society.

LPCVD	Year	T (K)	P_{CH_4} (mbar)	$v_{CH_4,limit}$	Limit	$v_{resulting,theo}$	v_{expt}	$\frac{v_{res,theo}}{v_{expt}}$
Liu ²²⁷	2011	1253	0.25	1996	b	1996	3.9	512
Vlassioug ¹¹⁶	2011	1273	0.00013	1.9	b	1.9	7	0.3
Jia ³⁷	2012	1293	0.0165	416	b	416	217	1.9
Kim ¹⁴¹	2012	1273	0.373	5342	b	5342	3176	1.7
Wang ¹²³	2012	1318	0.0133	665	a	481	603	0.8
Yan ²⁹⁷	2012	1333	0.308	22932	a	77	130	0.6
Zhang ²⁹⁸	2012	1273	0.0197	282	b	282	8.6	33
Hao ²¹	2013	1308	0.00132	50	b	50	139	0.4
Regmi ²⁹⁹	2012	1273	0.167	2392	b	2392	132	18
Vlassioug ²⁸⁵	2013	1298	0.000566	16	b	16	10	1.6
Wu ³⁰⁰	2013	1308	0.022	839	b	839	390	2.2
Eres ¹²⁷	2014	1313	0.00952	416	b	416	108	3.8
Han ³⁰¹	2014	1273	0.05	716	a	84	312	0.3
Yan ²⁴	2014	1343	0.225	21738	a	40	27	1.5
Ghosh ³⁰²	2015	1273	0.119	1704	a	245	33	7.4
Liang ¹¹⁹	2015	1293	0.000199	5	b	5	26	0.2
Miscikis ³⁰³	2015	1333	0.0271	2018	b	2018	286	7.1
Zhao ³⁰⁴	2015	1303	0.0146	486	b	486	72	6.7
Cabrero-Vilatela ²⁷⁸	2015	1323	0.00217	124	b	124	35	3.6
Chaitoglou ³⁰⁵	2016	1313	0.04	1748	b	1748	39	44.8
Cheng ³⁰⁶	2016	1333	0.00345	257	b	257	108	2.4
Hao ²⁸⁰	2016	1308	0.0667	2545	b	2545	130	19.6
Hao ²⁸⁰	2016	1308	0.00133	51	b	51	17	2.9
Hsieh ³⁰⁷	2016	1313	0.00213	93	b	93	325	0.3
Jung ¹⁵⁵	2016	1273	0.000583	8.3	b	8.3	13	0.6
Kraus ¹⁸³	2016	1348	0.002	220	b	220	87	2.5
Li ³⁰⁸	2016	1333	0.249	18539	b	18539	210	88
Yin ³⁰⁹	2016	1303	0.00998	332	b	332	13	25.5
Agrawal ³¹⁰	2017	1350	0.205	23713	a	44	81	0.5
Das ³¹¹	2017	1273	0.222	3179	a	125	26	4.8
Huet ³¹²	2017	1323	0.08	4572	a	53	212	0.3
Kraus ¹²⁶	2017	1233	0.06	262	a	59	22	2.7
Luo ³¹³	2017	1313	0.0121	529	b	529	32	16.3
Qi ³¹⁴	2018	1313	0.005	218	b	218	260	0.8

For reactions conducted far away from the thermodynamic equilibrium, the attachment limitation predicts large growth velocities, 18 experimental conditions predict growth speeds larger than $10^5 \mu\text{m h}^{-1}$. As is shown in Table 15 and 16, in most of these conditions the methane partial pressure is not high enough to support these large growth speeds. Combining the information from attachment- and $p(\text{CH}_4)$ -limitation, only two graphene growth conditions reported by Xu²⁷ and Zheng¹¹⁸ lead to predicted growth speeds larger than $10^5 \mu\text{m h}^{-1}$, and these are also the largest reported experimental growth speeds, only slightly falling short of $10^5 \mu\text{m h}^{-1}$. Fig. 48 shows the updated $Q_{\text{exp}} - T$ -diagram with the correctly predicted $p(\text{CH}_4)$ -limited growth speed colored in green using an acceptance factor of $\pm 50x$ to the experimentally observed growth value. Additionally, the literature data is also plotted in a $p(\text{CH}_4) - T$ -diagram using the methane dependence as shown in eq. 5.22 and the temperature dependence of eq. 5.23 with $E_{\text{app}} = 382 \text{ kJ/mol}$. Only three literature references cannot be correctly predicted using the described kinetic models of attachment- or $p(\text{CH}_4)$ -limited graphene growth.

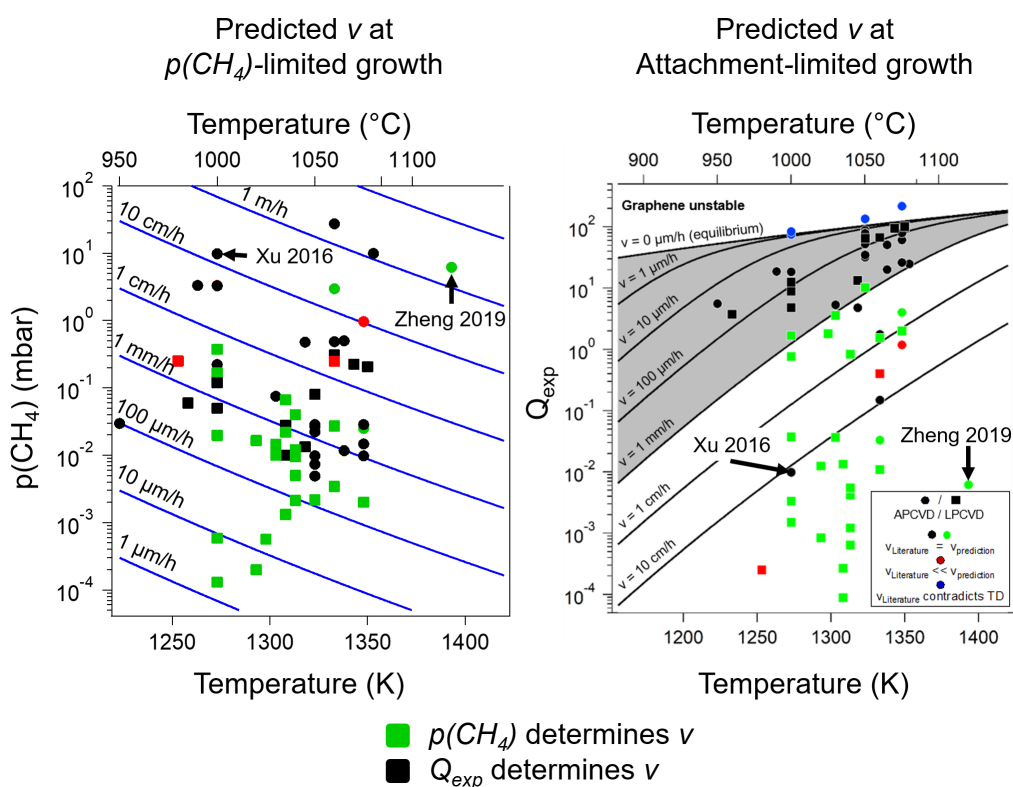
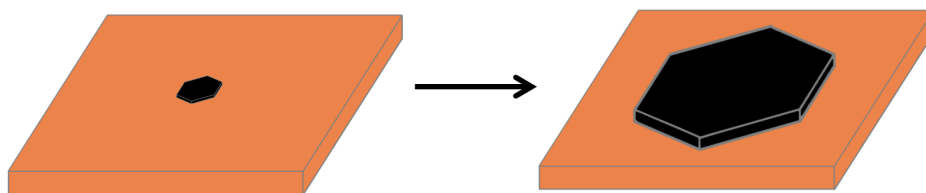


Figure 48 : Literature data discussed in the framework of a $p(\text{CH}_4)$ -limited (left panel) and attachment-limited growth kinetics (right panel). In addition to Fig. 42, the diagram indicates in green color literature growth speeds that can be explained with the $p(\text{CH}_4)$ -limitation assuming an error factor of ± 50 . Only three data points contradict the proposed growth limitations (red). Literature references by Xu *et al*²⁷ and Zheng *et al*¹¹⁸ referred to in the text are marked with arrows. The right diagram is adapted with permission from reference¹²⁸. Copyright 2021 American Chemical Society.

6. Understanding and controlling the nucleation of graphene flakes

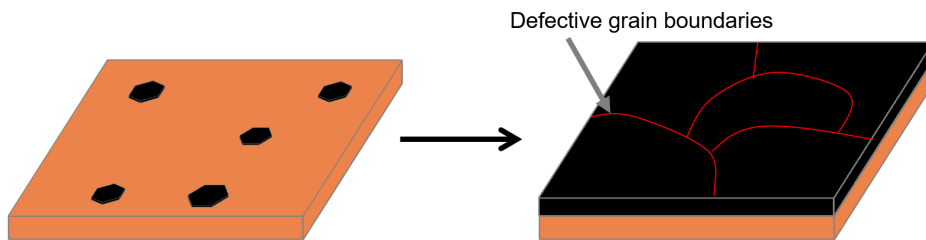
The growth of graphene crystals through chemical vapor deposition on a catalytic substrate begins by the fusion of several carbon atoms to a new nucleus, which can then grow by the incorporation of further carbon atoms. The nucleation density determines whether single graphene flakes or a continuous graphene film form during CVD (see Fig. 49).

a) Minimum nucleation



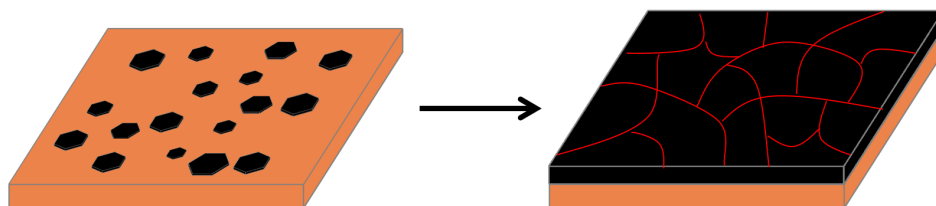
Application: Analyze flake size evolution, growth speed v , growth kinetics + thermodynamics

b) Low nucleation



Application: Graphene transfer, devices

c) High nucleation



Application: (low quality graphene)

Figure 49 : Relevance of the nucleation density for the outcome of graphene growth experiments. a) Minimum graphene nucleation leads to the evolution of very large single graphene flakes, mainly used for the examination of graphene growth. b) Low nucleation leads to a closed graphene film in an accessible time range, which is mainly required for graphene-based applications. c) Too high nucleation leads to a high amount of defective graphene grain boundaries, which decrease the graphene quality.

A very low nucleation density allows the growth of large, isolated graphene flakes, while a higher nucleation rate can ease the formation of a closed graphene layer within rea-

sonable time. At a very high nucleation density however, a large number of coalescing crystallites with a large number of grain boundaries appear if the graphene flakes are not aligned (see Fig 49). These grain boundaries deteriorate the mechanical stability of the grown graphene film.

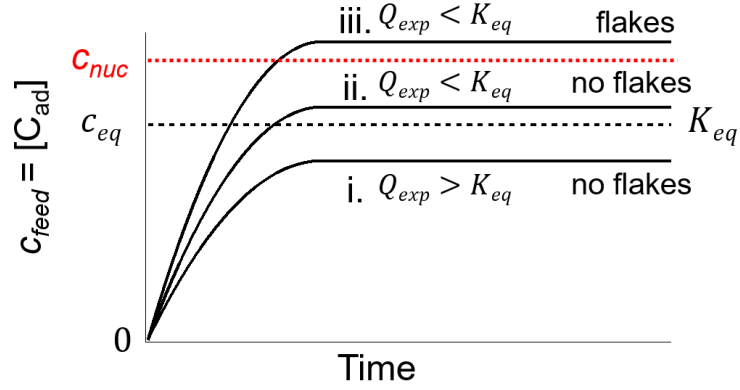


Figure 50 : Schematic evolution of the $[C_{ad}]$ concentration over time for different mass action constants Q_{exp} . If the set Q_{exp} lies above the equilibrium constant K_{eq} , no graphene growth should be allowed. For $Q_{exp} < K_{eq}$ graphene flakes should grow over time. As long as $[C_{ad}]$ does not exceed the concentration needed for nucleation, c_{nuc} , no graphene flakes will form. Case ii will show no graphene flakes, while case iii will enable the nucleation and subsequent growth of graphene flakes. According to the results obtained from chapter 5, the growth feeding phase is assumed to be $[C_{ad}]$.

An important difference between the outlined nucleation processes for physical vapor deposition (PVD) in Fig. 6 and the CVD g/Cu system is the dosing of the precursor. If carbon atoms are dosed in a PVD experiment, carbon is delivered to the surface by direct evaporation and consumed by incorporation to the graphene crystals. The CVD synthesis route also allows the backreaction of dehydrogenized carbon C_{ad} from the surface to gaseous methane. An equilibrium C_{ad} concentration can form without graphene growth on the surface, as outlined in the $[C_{ad}] - t$ -diagram in Fig. 50 (case i). No graphene will form if the established C_{ad} concentration on the surface stays below the threshold for nucleation, c_{nuc} . Note that c_{nuc} may be above the graphene equilibrium concentration $c_{eq}(K_{eq})$ and it is possible that no graphene will form even at parameters where already formed graphene flakes would grow (case ii.). Only when applying case iii. of Fig. 50 graphene flakes would nucleate and form on the Cu surface.

In this case, the C_{ad} consumption on the surface would be shared by the backreaction to methane and the graphene flake attachment, the C_{ad} concentration should therefore decrease after the nucleation of graphene flakes. Comparing both reaction pathways shows that at common reaction conditions ($T = 1045^\circ\text{C}$, $Q_{exp} = 10$, $p(\text{H}_2) = 20\text{ mbar}$, $p(\text{CH}_4) = 0.02\text{ mbar}$), the carbon input on the surface from the gas phase is approximately 2 ML/min ($S_0(1045^\circ\text{C}) \approx 3 \times 10^{-6}$). After graphene growth at these

conditions for 60 min, the sample is approximately half covered with graphene, which corresponds to less than 1% ML/min. If the adsorbed carbon concentration C_{ad} on the bare Cu surface is constant during the reaction, eq. 6.1a must be valid and the rate of desorbing carbon atoms $\dot{N}_{desorption}$ must be approximately 2 orders of magnitude larger than the carbon atoms incorporated into graphene crystals, $\dot{N}_{graphene\ growth}$. The graphene nucleation therefore does not significantly influence C_{ad} on the bare Cu surface.

$$\dot{N}_{adsorption} = \dot{N}_{desorption} + \dot{N}_{graphene\ growth} \quad (6.1a)$$

$$\dot{N}_{desorption} \gg \dot{N}_{graphene\ growth} \quad (6.1b)$$

Several studies have dealt with the graphene nucleation topic from a theoretical point of view, mainly focusing on the case of homogeneous nucleation on pristine surfaces^{315,316} or the nucleation on substrate anomalies such as atomic step edges.³¹⁷ For the samples grown in this work, the envisioned nucleation density is so low in the range of 1-10 flakes/mm² - that at these length scales further impurities are commonly present on the catalyst surface that may catalyze the nucleation process. In these cases heterogeneous nucleation is expected to take place. While homogeneous nucleation is a purely statistical process and should solely depend on the set growth conditions, heterogeneous nucleation is localized to defects or the impurity particles and strongly dependent on their condition. As the exact composition and origin of impurity particles is commonly not known unless they are artificially placed on the sample,^{318,319} it is very complicated to predict their appearance and activation other than in an empirical manner. Pretreatment methods to remove potential contaminations from the sample prior to growth have been developed, for example by an oxidative pretreatment as introduced by Kraus *et al.*¹⁸³ This kind of pretreatment is also used for most samples shown in this work, as in detail described in the methods-section 3.2. It is also possible that the active addition of a further component (in this case the addition of O_2) inhibits the nucleation process as suggested in ref.²¹. According to the authors, the oxygen passivates the nucleation sites on the Cu surface and strongly reduces the nucleation density.

The as-received industrial Cu substrate foils used in this work show a large amount of surface contaminations, as well as surface oxidation.²¹ Photoelectron spectra of the untreated Cu sample as received from the provider show contaminations of carbon (organic contamination, oil residues, carbonaceous species), oxygen (surface oxidation) and nitrogen (possibly organic contaminations). Especially high amounts of oxygen are detected, as shown in Fig. 51. Note that the concentration of impurities influencing the nucleation process may well be below the detection limit of the XPS setup, which means that the detected impurities shown in Fig. 51 may have nothing to do with the nucleation rate of graphene flakes during CVD growth.

A sample cleaned by the oxidative pretreatment step and subsequently shortly exposed to a reductive hydrogen atmosphere, such as commonly performed before the growth of graphene samples, is shown in Figure 52. The optical appearance shows only features assigned to the copper foil, such as the milling marks running in parallel lines from top to bottom remaining from the foil rolling and a copper grain boundary in Fig. 52a). Almost not visible in the optical image are single black dots in the sub- μm size regime, marked with arrows in Fig. 52a) and b), respectively. Raman spectra acquired at these positions show the presence of further materials, among others amorphous carbon³²⁰ or remaining particles of oxidized copper Cu_2O .

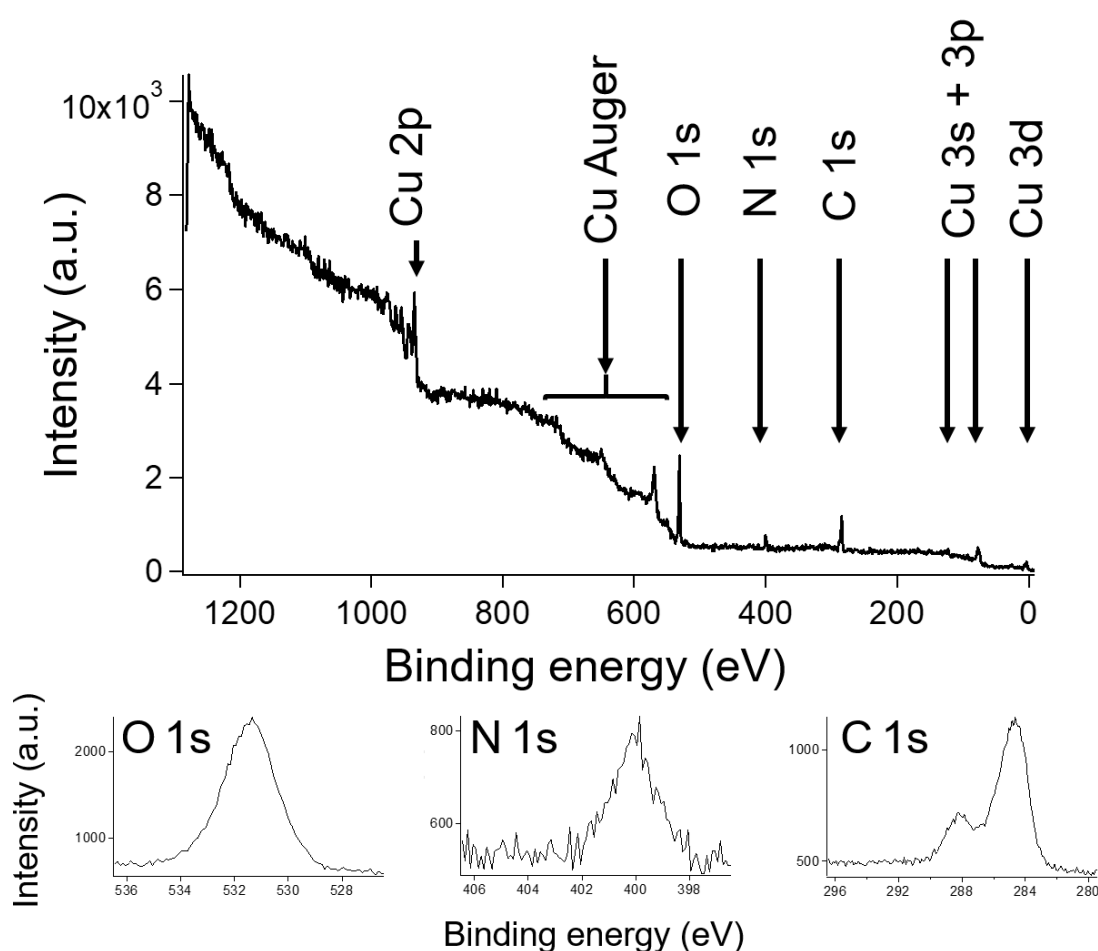


Figure 51 : XPS spectrum of an as-received Cu foil without any pretreatment. Apart from the Cu-related signals a significant amount of oxygen, nitrogen and carbon can be identified, as shown in the magnifications below.

Such dark spots are often found in the center of graphene flakes, where the graphene growth originates in the first moments during the growth phase.

In the case of heterogeneous nucleation, a cluster of carbon atoms may form around

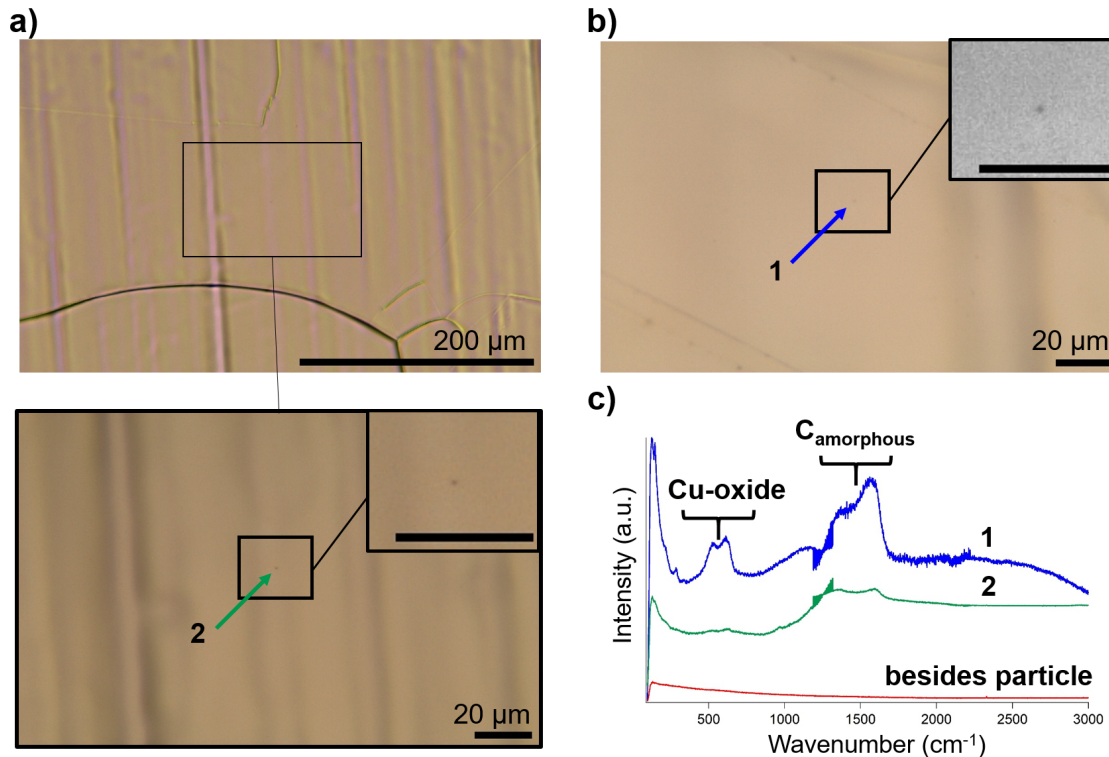


Figure 52 : Impurity particles remaining on the sample surface after pretreatment followed by a short hydrogen purge. Particles identified as black dots in a) and b) indicate the rare remainders of accumulated impurities after sample cleaning. These particles are very scarcely found on the sample surface (all other features in image b) can be attributed to grain boundaries) with similar density as the subsequent graphene flake nucleation during CVD growth (not shown). c) Raman analysis of these particles (colors of the spectra according to the colors of the arrows in a-b)) shows an increased amount of carbon (around 1500 cm^{-1}) and copper oxide (around 600 cm^{-1}), while the reference spectrum acquired at a featureless site shows no Raman features at all. All scale bars amount to $20\text{ }\mu\text{m}$ unless otherwise noted. (Experimental details: E. 2)

an impurity, which is energetically unstable until reaching a critical size where the carbon attachment becomes energetically favorable.³²¹ This critical nucleus size defines at which $[C_{ad}]$ nucleation sets in. As the carbon cluster may be energetically stabilized at impurities, the critical nucleus size is lower for heterogeneous nucleation, which leads to an island formation at a lower supersaturation of C_{ad} .

The nucleation behavior under different starting conditions was studied in a series of experiments. The conditions under which growth was performed, are summarized in Fig. 53 in a $p(H_2) - w$ -diagram. $[C_{ad}]$ increases from the upper right to the lower left corner with further deviation from the thermodynamic equilibrium, leading to a higher chance of graphene flake nucleation at individual defects/impurity particles. The results of the experiments marked as colored triangles in the diagram are shown in Figs. 54 (sample 1), 55 (sample 2) and 58 (sample 3). At the temperature of $1045\text{ }^\circ\text{C}$, graphene nucleation was not observed above a Q_{exp} value of approximately 80. This coincides with

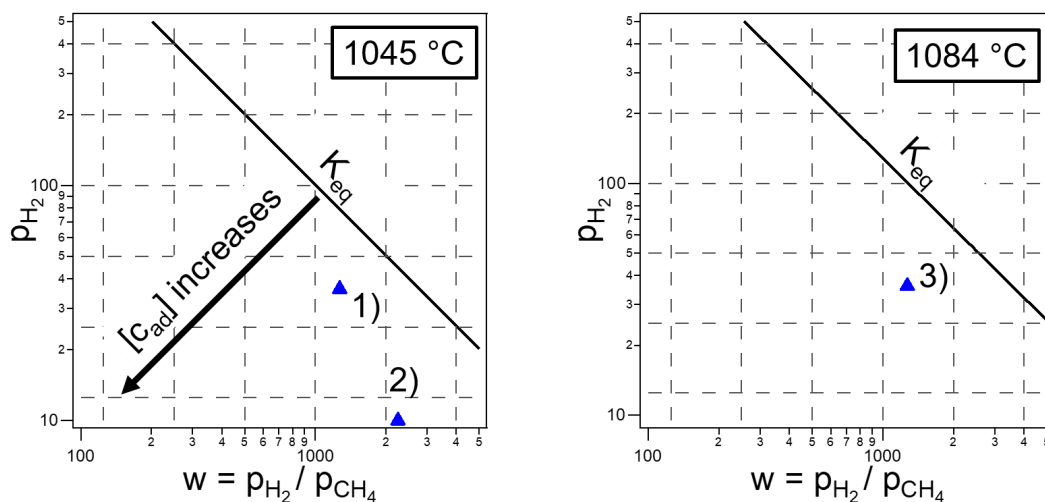


Figure 53 : Graphene growth conditions of samples discussed in this chapter, plotted in a $p(H_2) - w$ -diagram. This type of diagram indicates the distance of the growth conditions to the thermodynamic equilibrium (solid line), as described in the text. The temperature and distance to equilibrium are used as parameters to characterize the nucleation behavior on the sample.

findings by Kraus *et al.*,¹²⁶ who did not observe graphene formation at these conditions, nevertheless without pinpointing this phenomenon to the nucleation of flakes.

Sample 1: ($T = 1045\text{ }^\circ\text{C}$, $Q_{exp} = 45$) At a Q_{exp} value of 45 and $T = 1045\text{ }^\circ\text{C}$ nucleation is observed on the sample in a very scarce and almost unrecognizable manner. As shown in Fig. 54, over a sample area of 30 mm^2 only 3 graphene flakes formed at these conditions. Nucleation at high values of Q_{exp} commonly leads to a low amount of nucleated graphene flakes which cannot guarantee a high enough absolute number of flakes for proper statistical evaluation. After growth under such conditions, the flakes are often only found at the sample rim or around large impurity particles (see Fig.54b-c). Remarkably, the nucleated graphene flakes can be grown for an arbitrary time without the nucleation of additional graphene flakes. Fig. 54c) shows graphene flakes grown for 30 and 60 min to a diameter of about $500\text{ }\mu\text{m}$ size on an almost empty Cu foil (nucleation density of $\approx 0.1\text{ flakes/mm}^2$).

Sample 2: ($T = 1045\text{ }^\circ\text{C}$, $Q_{exp} = 22$) When choosing a parameter set with lower Q_{exp} , thus favoring the formation of graphene through a higher concentration of C_{ad} on the surface, the amount of graphene flakes statistically formed on an oxygen pretreated sample increases further. For sample 2) grown at $Q_{exp} = 22$, the graphene flake formation is statistically evaluated in Fig. 55. Figure 55a) shows the position-dependent flake density of the sample in a 2D-diagram, where a single square stands for an area of 1 mm^2 . The image illustrates that the nucleation events do not appear particularly clustered and are not dependent on the position relative to the gas flow direction. The main part of the present graphene flakes is not in close vicinity to other flakes, as also clarified in

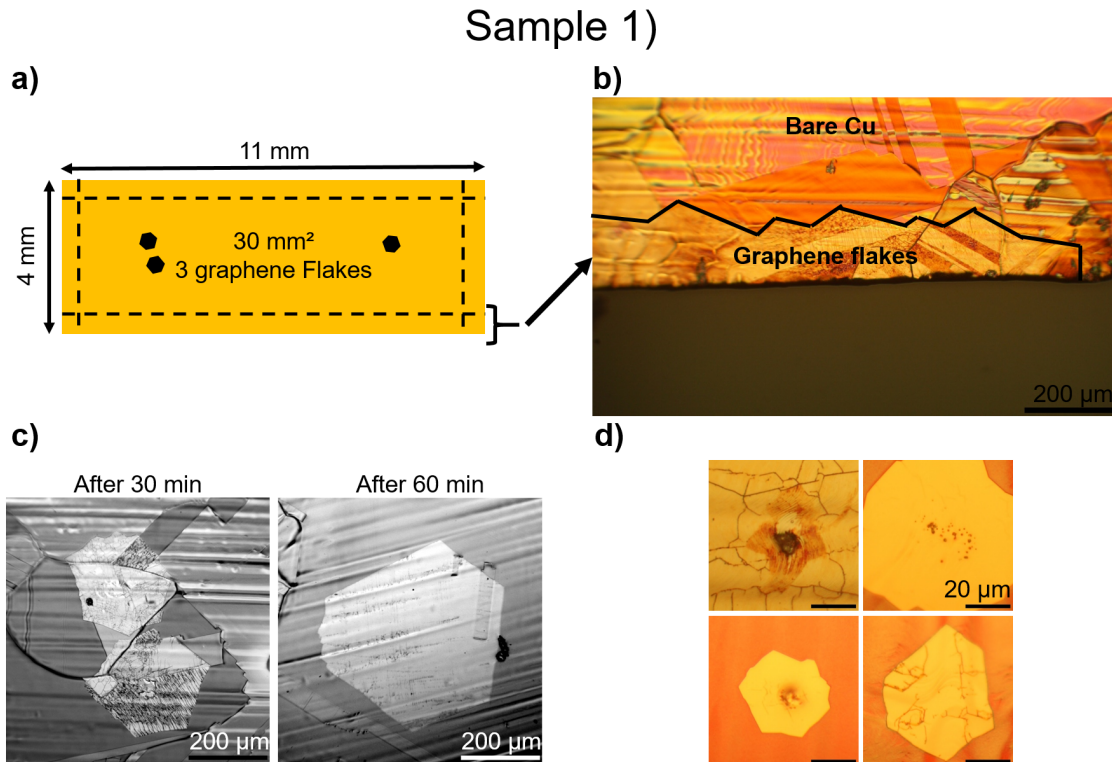


Figure 54 : Nucleation behavior of a sample grown at the conditions marked 1) in Fig. 53. a) Sample area of the characterized sample, showing nucleation of three graphene flakes over an area of over 30 mm². b) At the sample rims, enhanced nucleation is observed. Graphene flakes grow from the sample rim to the substrate area. c) Graphene flakes found in the central area of the sample after 30 and 60 min of growth time. While the nucleation density does not increase with total reaction time, the few present graphene flakes increase in size. d) Examples for graphene flake nucleation spots with clear particles (upper row), with surface inhomogeneities (lower left image) and with smaller nucleation seeds (lower right image), all images are acquired after sample oxidation, increasing the visibility of the central particle. Note: Figs. b and c) were acquired after significant storage time in air, therefore the graphene areas appear only very faint. (Experimental details: a-c: E. 46)

Fig.55c), showing a histogram of the flakes found in the 1x1 mm² area-squares. A single area fragment was found with an increased flake density, where 18 flakes were found in a single area-square. Summing up to a total of 91 flakes counted on the sample, this leads to a mean nucleation density of 0.4 flakes/mm². Exemplarily, a graphene flake is shown in Fig. 55b). It shows a hexagonal symmetry and in the center a nucleation spot is visible in form of a dark point. Evaluation of all flakes shows that at these growth conditions, 65% of all flakes contain nucleation dots detectable in the optical microscope and 96% of the graphene flakes have an overall hexagonal flake structure.

The determined flake radii r are summed up in form of a histogram in Fig. 55d), which roughly depicts a Gaussian distribution. Notably, the counted flakes drop to zero for flake sizes between 0-10 μm.

This sample formed enough graphene flakes for a statistical evaluation. Due to the low

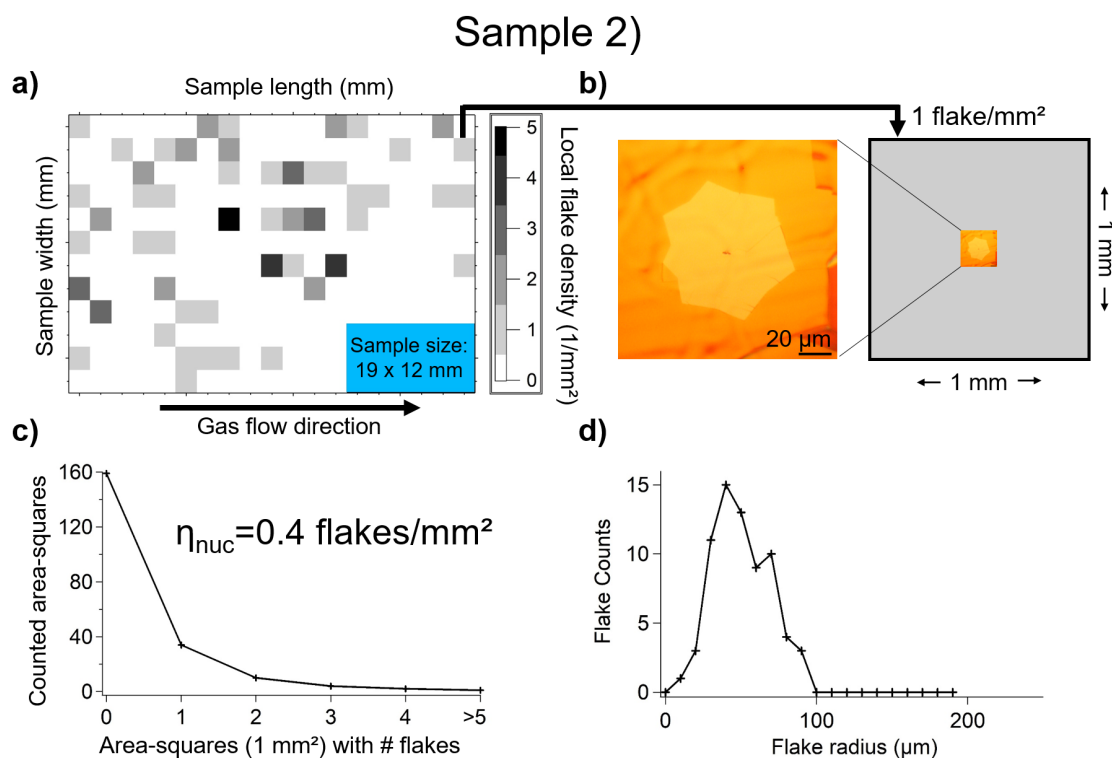


Figure 55 : Statistical evaluation of the nucleation behavior of a sample grown at CVD conditions 2) in Fig. 53. a) Scheme of the sample area divided into area segments of $1 \times 1 \text{ mm}^2$ with the respective nucleation density marked by the gray-scale intensity. No correlation of the flake nucleation positions can be identified, nor is a significant influence of the gas flow direction detected. b) Exemplary graphene flake with nucleation spot in the flake center. c) Only a single area segment contains more than five flakes, while the vast majority shows no graphene nucleation at all. d) Histogram of the flake size distribution of the identified graphene flakes, showing an almost Gaussian distribution of the flake sizes. Note: As the flakes in close proximity may influence each other in terms of growth behavior, the area segment with increased nucleation density was not used to evaluate the mean flake radius. (Experimental details: E. 47)

island density, the graphene flakes are statistically distributed over the sample and do not collide with each other during growth until reaching an island size close to the mm regime, fulfilling the desired growth geometry of isolated graphene islands.

Nucleation appears at clearly visible heterogeneous seeds and at positions without visible nucleation spots. Note that a lack of optically visible nucleation seed does not mean that homogeneous nucleation is happening, as a heterogeneous nucleus may as well be down to a single atom small. Fig. 55d) shows an overall symmetric Gaussian distribution, indicating that all graphene flakes originate from the same time period.

6.1. Distinguishing between homogeneous and heterogeneous nucleation

Figure 56 sketches an experiment which allows to decide whether graphene flakes are formed during CVD synthesis upon heterogeneous or homogeneous flake nucleation. A first sample is grown by applying the pretreatment and CVD protocol that leads to a low flake nucleation density as the one of the experiment leading to the sample displayed in Fig. 55.

The applied CVD conditions are modified after the foil pretreatment and the expected concentration of the graphene feeding phase is qualitatively plotted versus the treatment time by the dashed curve. Since the attachment limited growth regime was shown to take place from a pre-equilibrated C_{ad} 2-dim lattice gas as feeding phase, the vertical axis displays the concentration of this quantity, although the feeding phase during nucleation might consist of a different species. For simplicity, $[C_{ad}]$ will be used in the following to express the concentration of the phase that leads to flake nucleation.

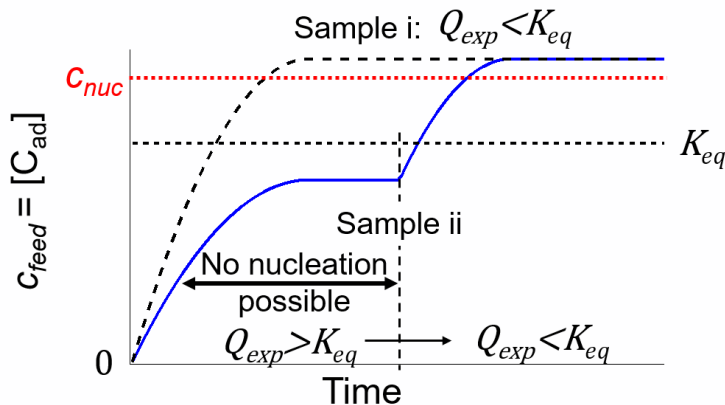


Figure 56 : Illustration of the experiment performed to distinguish between homogeneous and heterogeneous nucleation during graphene flake formation.

As sketched in Fig. 56, the concentration increases with time when applying CVD conditions with $Q_{exp} < K_{eq}$ and nucleation followed by flake growth sets in if $[C_{ad}]$ exceeds the required concentration c_{nuc} .

In comparison to sample i), a second sample ii) is synthesized by applying the identical pretreatment and CVD growth conditions, except that during CVD at first $Q_{exp} > K_{eq}$ conditions are set that, according to thermodynamics, cannot lead to graphene formation. However, the concentration of the feeding phase $[C_{ad}]$ will increase during the treatment, but since it does not exceed c_{eq} , no flake growth can occur.

If then identical CVD conditions as to ones chosen for sample i) are set, the conditions required for flake nucleation are met. In case of homogeneous nucleation an identical graphene island distribution would appear on both samples, when growing for identical times. This stems from the fact that homogeneous nucleation results from statistical events that lead to the formation of critical nuclei and - at the time when the required nucleation conditions are met - both samples i) and ii) are identical. If, however, during the treatment of sample ii), a foreign material or defect exists or is created that does not follow the thermodynamics of the clean g/Cu system, the required facilitated graphene flake nucleation during CVD synthesis at $Q_{exp} < K_{eq}$ may take place. Thus, the resulting heterogeneous nucleation would lead to an altered flake density after CVD growth of sample ii).

The experiments performed following this strategy are outlined in Fig. 57, where the applied treatment is compiled in a) and graphically sketched in b). The chart indicates that the CVD synthesis of sample i) delivered graphene flakes with an island density of 0.5 flakes/mm^2 . The resulting density obtained on sample ii) increased to 30 flakes/mm^2 . Thus, the flake nucleation increase by a factor of 60 during synthesis of sample ii) clearly demonstrates the heterogeneous nature of the flake nucleation process.

This experiment shows that the nucleation of graphene flakes on the Cu surface cannot be purely caused by the carbon intake from methane decomposition on the metal surface, which would be the case for homogeneous nucleation. In this case, both samples would require to feature similar nucleation behavior, as the evolution of $[C_{ad}]$ after surpassing the nucleation threshold (see Fig. 56) is equal and homogeneous nucleation by definition only depends on $[C_{ad}]$ and T . This identical overcritical concentration of C_{ad} on the Cu surface should lead to similar statistical growth distributions, which were not observed in the shown experiments. In this section I was able to show that the Cu substrate after pretreatment still contains (a very low amount of) optically identifiable impurity particles (Fig. 52), graphene growth on one substrate position may occur simultaneously with large graphene-free areas ($> 5 \times 5 \text{ mm}$) and that identical growth conditions can lead to significantly different nucleation behavior. The nucleation in these experiments is therefore of heterogeneous nature. Theoretical studies on homogeneous nucleation are thus not applicable in this situation.

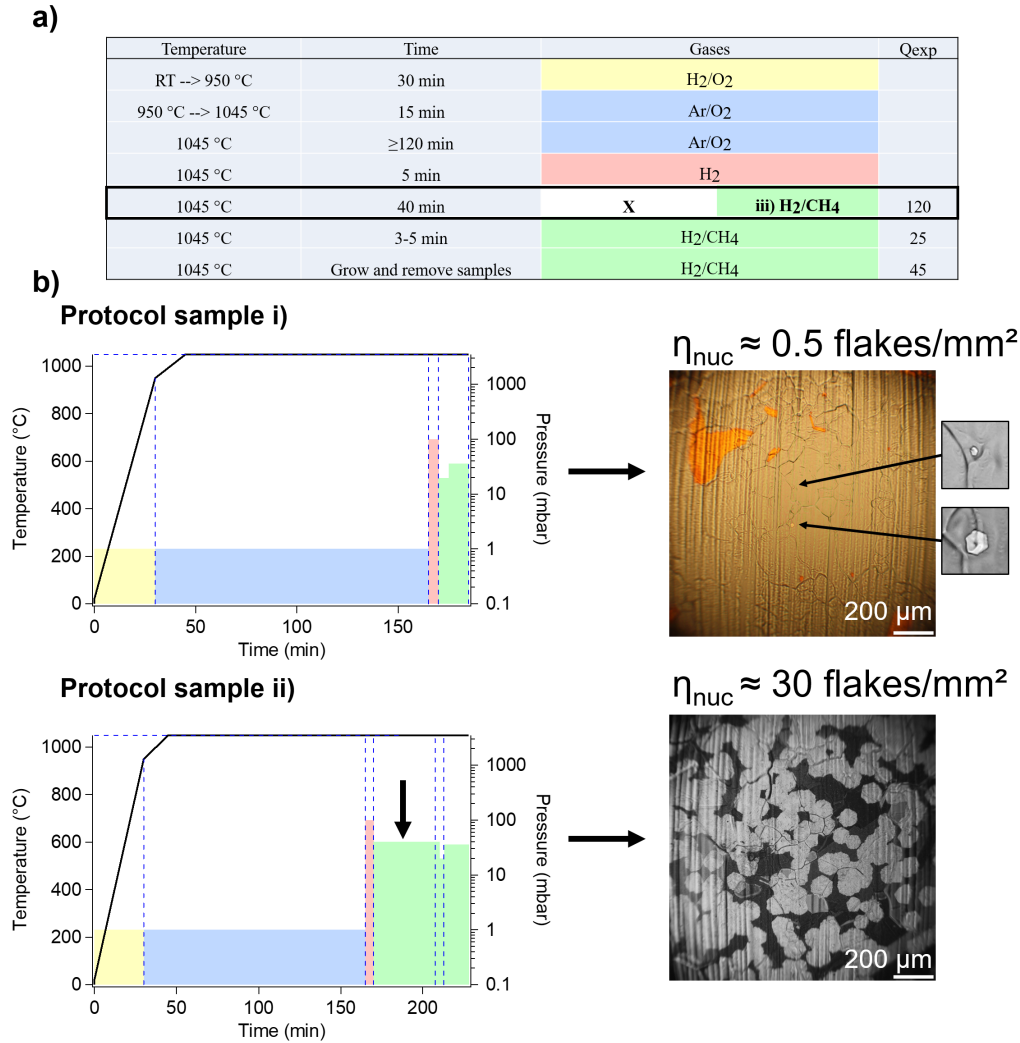


Figure 57 : Nucleation behavior dependence on the exact pretreatment succession. a) Growth protocols for the two samples evaluated regarding their nucleation behavior. While sample i) corresponds to the described common pretreatment method, in sample ii) an additional step was introduced before the graphene flake nucleation, where a H_2/CH_4 mixture was introduced, at which knowingly graphene growth does not set in ($Q_{exp} > K_{eq}(1045 \text{ }^\circ\text{C}) = 101$). Graphene nucleation therefore happens at the same gas phase composition in both samples. The growth protocols are also imaged in form of graphs below the table in b), together with the observed nucleation densities: Sample i) shows a $\eta_{nuc} < 1 \text{ flake/mm}^2$, it is significantly higher in cases ii) with $\eta_{nuc} \approx 30 \text{ flakes/mm}^2$. (Experimental details: E. 4 , E. 49)

6.2. Graphene nucleation dependence on the temperature and Q_{exp}

Sample 3: ($T = 1084 \text{ }^\circ\text{C}$, $Q_{exp} = 45$) The observed flake nucleation enters a new regime when setting growth conditions more strongly favoring the graphene growth, i. e. at lower values of Q_{exp} or at higher temperatures. The results for a sample grown at a temperature of $1084 \text{ }^\circ\text{C}$ and a Q_{exp} -value of 45 are shown in Figure 58. The histogram of the

evaluated graphene flake sizes is shown in Fig. 58a) and a typical optical image of the oxidized sample after CVD is displayed in Fig. 58b) as example. The graphene islands show a strong variation of the island size between 0-180 μm flake radius, which also appears in the flake size distribution. The resulting histogram extracted from sample 3) greatly deviates from the one of sample 2) with an almost regular Gaussian shape, also shown in Fig. 58 for comparison. Also in contrast to flakes grown following the synthesis protocol of sample 2) is the fact that now only few flakes show visible nucleation spots. Due to the larger amount of small flakes, the nucleation density is in the order of 10 flakes/ mm^2 .

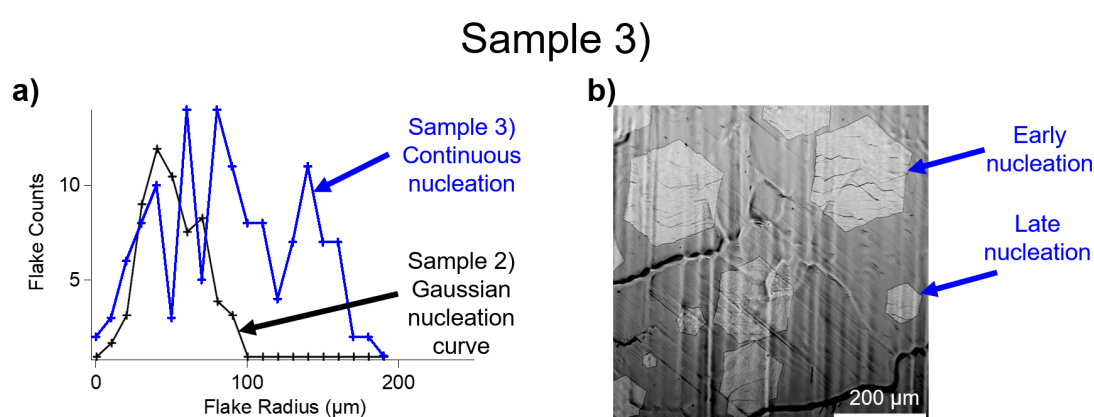


Figure 58 : Statistical evaluation of the nucleation behavior of a sample grown at conditions 3) in Fig. 53 at elevated temperatures. a) The evaluation of the flake sizes shows a broad distribution curve. For comparison, the panel also displays the distribution obtained from sample 2) b) Optical image showing that graphene flakes of all sizes are found on the sample. As all flakes are assumed to grow at equal speed, they must have formed at different times in the experiment. (Experimental details: E. 50)

The broad island size distribution indicates the presence of very large and small islands on the Cu surface (see Fig. 58b). Such a behavior can be explained when considering continuous nucleation of graphene flakes over the complete growth period. In such a case, flakes nucleated at the beginning of the CVD synthesis grow large while the ones nucleated at the end do not have the time to reach a large size. In order to extract the flake growth velocity during CVD one has to track the growth front of the largest graphene flakes, which for this sample would be approximately 180 μm . This characteristic nucleation behavior can be assigned to *continuous nucleation* and may be caused by 2 different effects:

1. At these conditions homogeneous nucleation is present on the sample
2. Further impurity particles arriving on the sample surface over time create time-

dependent heterogeneous nucleation. These particles could for example consist of particles detached from the reactor wall or diffusing to the surface from the substrate bulk.

From the experimental results presented here, both scenarios could be a possible explanation. Additional experiments with a changed sample geometry - such as shielding of the sample from the reactor walls - could resolve this question.

6.3. Evaluation of several performed experiments regarding their nucleation behavior

To achieve statistically more meaningful information about the impact of the chosen growth parameters on the nucleation process, 73 CVD experiments were evaluated regarding the nucleation processes observable on the samples. The data set stretches over a large parameter space including temperatures between 900-1084 °C, pressures up to 60 mbar and Q_{exp} -values between 1.5 and 117.

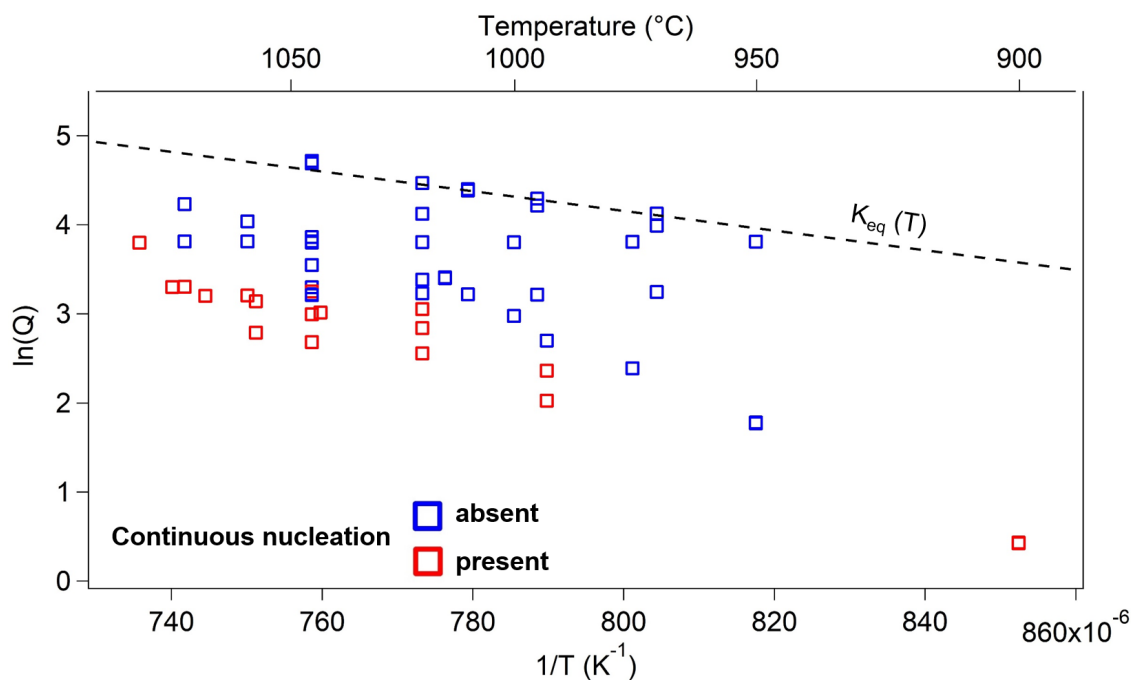


Figure 59 : Observation of continuous graphene flake nucleation depending on the used growth conditions. The $\ln(Q_{exp}) - 1/T$ -diagram shows the result of the evaluation of 73 experiments regarding the occurrence of continuous nucleation after the first phase of exposure to the reactive atmosphere. The results show a clear distinction between CVD synthesis regimes in which continuous nucleation is observed or not. The transition between both regimes follows a temperature dependence with similar orientation as the thermodynamic equilibrium of graphene growth ($K_{eq}(T)$), but with a slightly more inclined slope.

The samples were examined with respect to two aspects:

- The nucleation of new nuclei over the course of the experiment (continuous nucleation)
- The overall density of nucleated graphene flakes (η_{nuc}).

The results are shown in the diagrams of Fig. 59 and Fig. 60. The diagrams are plotted in a Vant Hoff plot type with the inverse temperature as x-axis and the natural logarithm of the Q_{exp} -value as y-axis. The dashed line at the top of the diagram shows the thermodynamic equilibrium line (K_{eq}) for graphene growth.

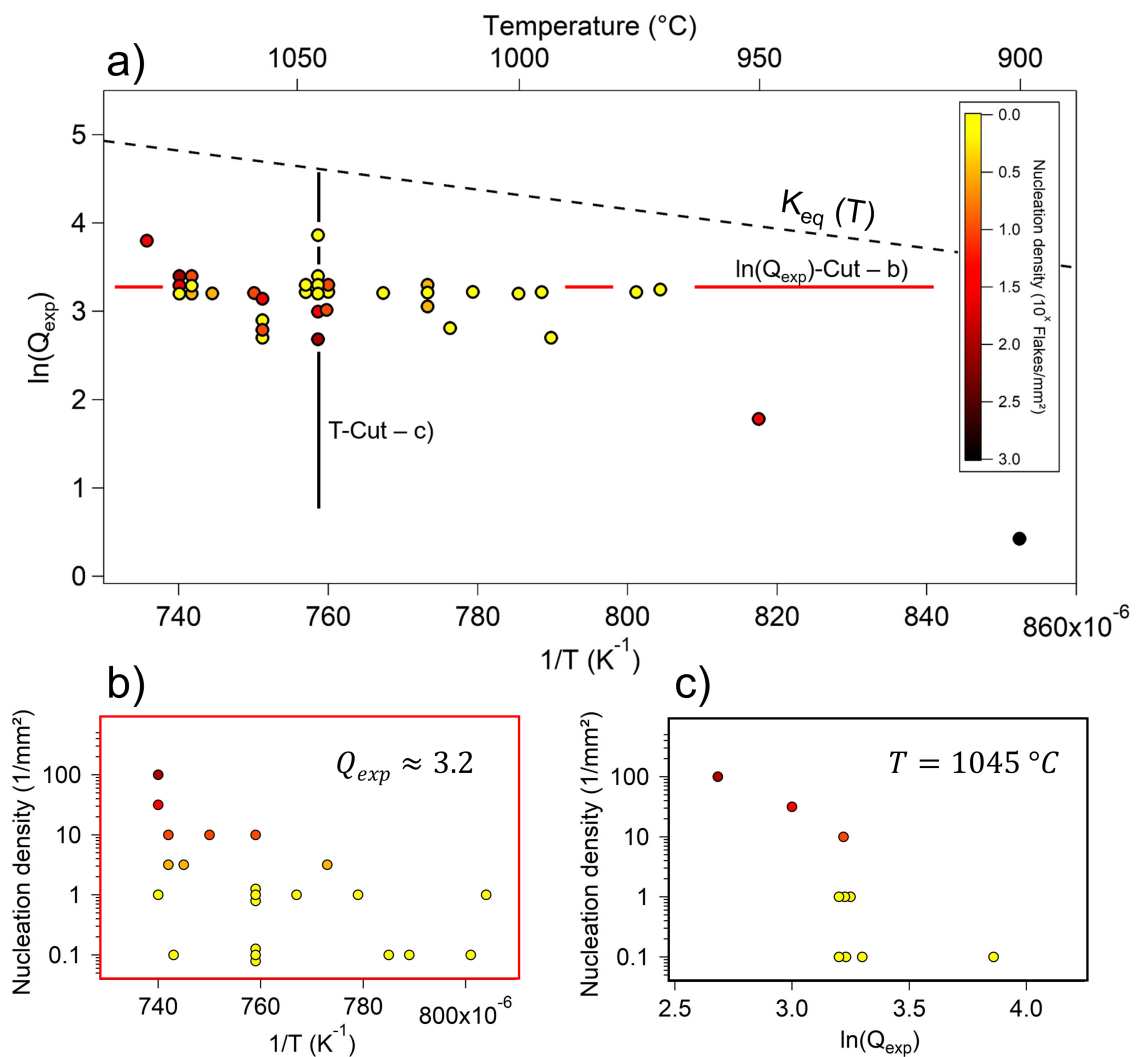


Figure 60 : Nucleation density as a function of (Q_{exp}, T) CVD parameters. The nucleation density is color coded along 10^x with $0 \leq x \leq 3$. b) Nucleation density at constant $\ln(Q_{exp}) \approx 3.2$ as a function of temperature. c) Nucleation density at constant $T = 1045^\circ C$ as function of Q_{exp} . The data subset b) and c) are indicated in panel a). All displayed samples have gone through the same pretreatment recipe as described in chapter 3.2, with variations in the overall pretreatment time, which may also account for the large variations in the results.

Figure 59 allows a clear division between a graphene growth regime without continuous graphene nucleation (blue squares) and one with continuous nucleation (red squares). The continuous nucleation is observed at conditions strongly favoring the graphene growth, at lower values of Q_{exp} . The parameter regime without continuous nucleation is observed close to the K_{eq} line with increasing temperature, limiting the possible reaction settings in which a controlled graphene growth can be executed without the formation of new graphene islands during CVD growth. Roughly, it can be stated that below a certain $Q_{exp}(T)$, continuous nucleation occurs. This means that, as shown in Fig. 61 an additional important supersaturation level can be introduced in the diagram of Fig. 50: The concentration above which continuous nucleation is observed, $c_{continuous}$.

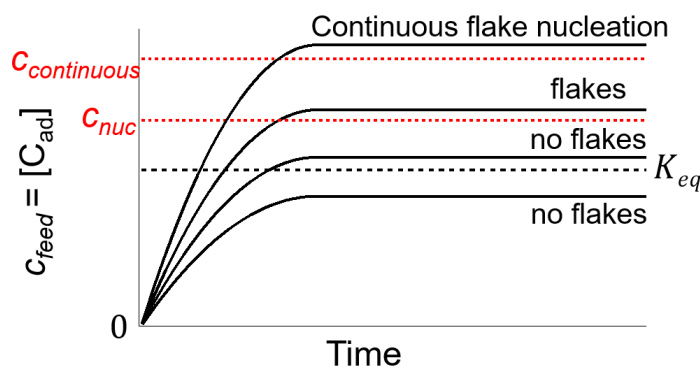


Figure 61 : $[C_{ad}]$ surface concentrations during graphene growth. Above $[C_{ad}] = c_{eq}$, two supersaturation levels seem to play a role. c_{nuc} as threshold for nucleation at the beginning of the CVD process and $c_{continuous}$ above which continuous nucleation during the complete CVD growth is observed.

Figure 60 shows the roughly estimated nucleation density of several growth experiments. All samples shown in this Figure underwent the same oxygen pretreatment procedure with slight variations regarding treatment time and oxygen content. Mainly, the observed parameter space can be divided in three separate sections. No nucleation is observed in close vicinity to the dashed equilibrium line (K_{eq}), as already described before. Experiments with graphene nucleation are observed only when applying CVD conditions sufficiently far from the $K_{eq}(T)$ -line. In a certain area of the parameter space the nucleation density stays below 1 flake/mm². Similar to the transition towards continuous nucleation, an increase in nucleation density by 1-2 orders of magnitude is found in the same parameter regime and with similar temperature dependence.

The strong spreading of the nucleation values, but also the clarity of the overall nucleation trends regarding the temperature and the Q_{exp} dependence become more apparent when looking at cuts through the 2D-plot, as shown in Fig. 60b+c). Apart from the phenomenological parameter dependency ruling the nucleation events during CVD synthesis, the charts (especially Fig. 60b+c) can be used to search for growth conditions that favor the formation of single, large flakes or growth at high nucleation density.

6.4. Nucleation conditions at high pressures

In contrast to the obtained findings described in the previous chapter for experiments conducted at $p_{total} < 60 \text{ mbar}$, another change in nucleation behavior was observed for samples grown at pressures above approximately 100 mbar H_2 partial pressure. In Fig. 62a), high pressure experiments (blue circles) are compared to low pressure experiments (yellow-red circles). These data points show a strong increase of the mean

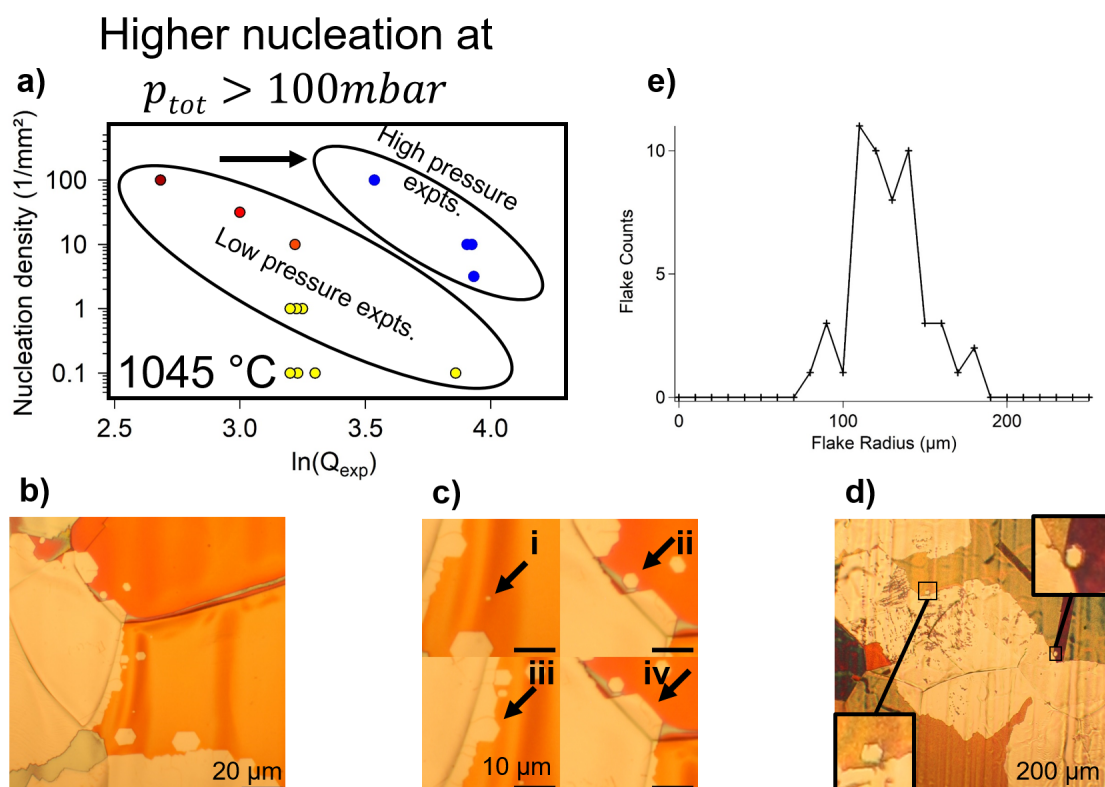


Figure 62 : Nucleation behavior of graphene samples grown at high pressures above 60 mbar. a) Blue circles mark the nucleation density of graphene flakes grown at increased pressure, which greatly exceeds the one obtained at lower pressure (red and yellow points). b-d) Optical images of graphene flakes grown at 150 mbar, $w = 300$, $T = 1045 \text{ }^\circ\text{C}$ for 100 min. (Experimental details: E. 51) b) Large islands are observed that are surrounded by small islands in their close vicinity. c-d) Close-ups show the case of isolated small flakes (i-ii) and flakes that are incorporated into the large island. e) Histogram of the flake distribution of the sample shown in d), where small flakes in the vicinity were not included. The narrow Gaussian line shape similar to the one shown in Fig. 55 indicates that the growth of the large islands seems to be unaffected by the formation of the small graphene islands.

nucleation density by two orders of magnitude in comparison to the one observed in low pressure experiments. Optical images of graphene flakes grown at high pressures also show differences to their counterparts grown at low pressures, as presented in the opti-

cal images in Fig. 62b-d). Around the rim of the grown graphene flakes, at a distance of up to 20 μm , significantly smaller graphene flakes can be identified. These are not observed at larger distances to the main flakes. Fig. 62c) shows these new flakes in different stages of incorporation into the main flake. While flake i can be barely identified with the used microscope, flake ii is already significantly larger but still separated from the main graphene island. Flakes iii and iv are then already in contact to the main, large flake with an increasing amount of the flake area being incorporated into the main flake. Figure 62d) shows a graphene flake grown for a longer time at high pressures. It shows a large graphene flake of approx. 200 μm flake-radius. When looking at the rim of this flake, one can still identify two small, newly formed graphene flakes right next to the main island rim. These are also shown magnified in the two insets in the upper right and lower left corners. While there are several small flakes formed around the rim of the large graphene flakes, the flake size distribution of the main graphene islands shows no significant broadening of the distribution, as depicted in Fig. 62e). Note that the small flakes appearing at the rim of the large flakes are subsequently incorporated into the large flakes and therefore do not form independent new graphene flakes.

When comparing high-pressure growth experiments to graphene grown at lower pressure, it becomes clear that at least one new nucleation site is activated at high pressures when regarding the increased total nucleation number at the beginning of the reaction. The fact that small graphene flakes form around the larger graphene flakes at high pressures also indicates that some processes on the molecular level are significantly changed when increasing the total pressure. This phenomenon could be explained by the presence of secondary nucleation, where the nucleation of new crystals is induced by the presence of a parent crystal.³²² However, also other processes can account for the flake nucleation, but in some form, the formation of the small nuclei must be enabled by the large flakes, as they only appear in their direct vicinity. Interestingly, this process is independent of the process referred to as continuous nucleation in the previous section.

As observed by Kraus *et al.*,¹²⁶ graphene films grown at high pressure show an increased amount of multilayer graphene areas. Similar to the nucleation of single layer graphene flakes, also the formation of bilayer graphene needs a nucleation point from which the growth sets in. At CVD synthesis below 60 mbar it is often observed that one nucleation seed acts as starting point for the first and several further graphene layers.²⁴ Whereas CVD growth at higher pressures typically leads to a multitude of small multilayer flakes below one large, single-layered graphene flake.¹²⁶ The observation of nucleation of small islands in the vicinity of large flakes might explain this, as small graphene flakes can be integrated in two ways into the main flake, which is sketched in Fig. 63:

- By over-/undergrowth of the small flake, immediately leading to a small multilayered flake

- By incorporation into the single-layer-graphene lattice. If the small graphene flakes are rotated with respect to the main flake, several defects with dangling bonds will develop along this boundary line that may lead to the nucleation of additional layers below.

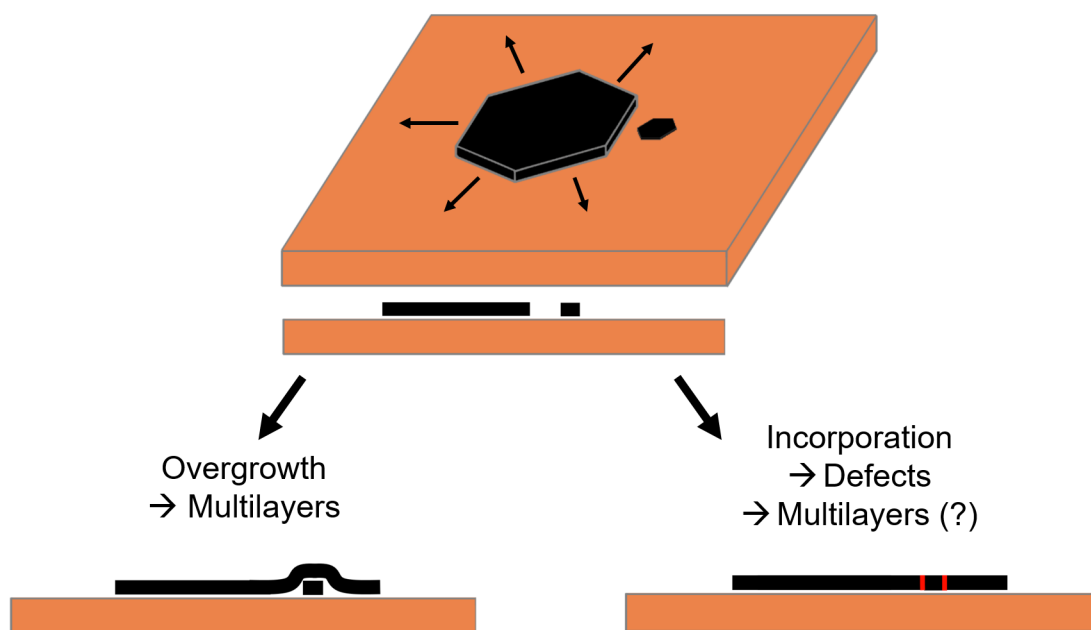


Figure 63 : Possible interaction between a large, expanding graphene flake and a small graphene flake formed close by. The small graphene flake can either be overgrown, directly leading to multilayered graphene areas. Otherwise, the small flake can be integrated into the large flake area, leading to defects at the grain boundary. These defect lines may also act as nucleation points for further graphene layers.

6.5. CVD synthesis strategies with control of the flake nucleation

To enable graphene growth with control of the resulting flake size, it is necessary to decouple the graphene nucleation from the graphene growth process itself. Such a decoupling is induced by introducing a new CVD step into the graphene growth procedure, which in the following will be called nucleation step.

The nucleation step is added to the CVD protocol after the foil pretreatment, which consists of the heating ramp and the oxidative treatment followed by the hydrogen purge. Before establishing the actual CVD growth step, the nucleation step is introduced for a short time to force the formation of graphene flakes before growing them in the subsequent growth step.

The procedure is displayed in Fig. 64. The idea behind the concept is outlined in Fig. 65, where again for simplicity the concentration of the growth-feeding phase is assigned to

$[C_{ad}]$ and plotted versus the CVD treatment time. This assignment is the most likely scenario (see chapter 5), but the arguments are independent of the actual microscopic process inducing the flake nucleation.

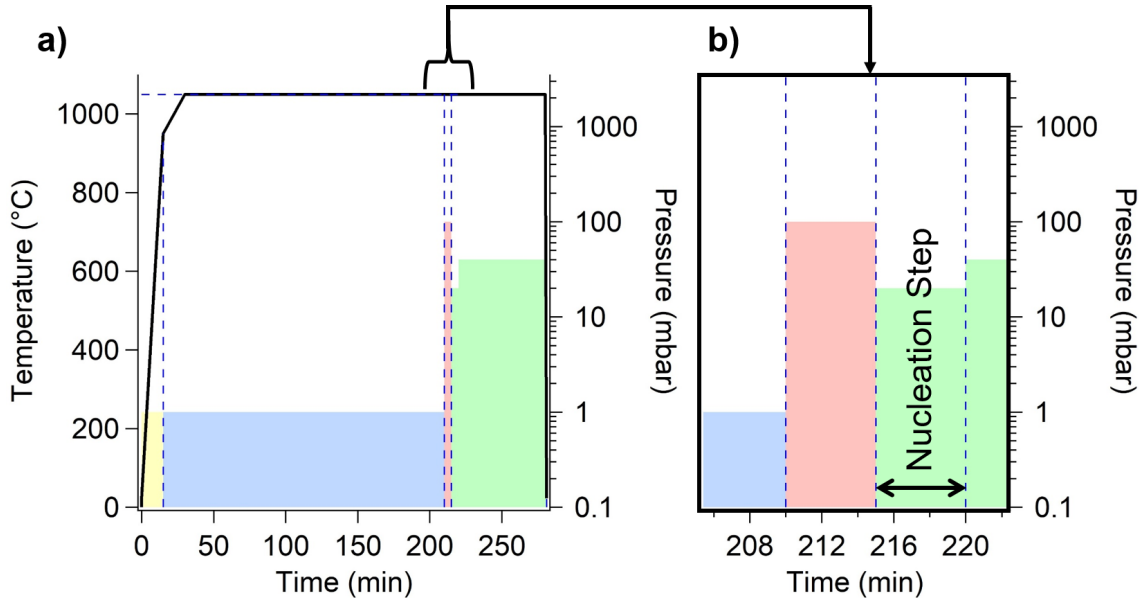


Figure 64 : Growth recipe including the introduced "Nucleation Step" to control the nucleation behavior independently from the graphene growth behavior in the subsequent growth step. The "Nucleation Step" consists of a short exposure to the reactive $CH_4 + H_2$ gas phase further away from the equilibrium concentration than the actual growth step. Hence, possible nucleation sites should grow graphene flakes in these first minutes of the reaction and no continuous nucleation should be observed after this step. The amount of expected graphene flakes is determined by the conditions set in this step, while subsequent graphene growth does not affect this value.

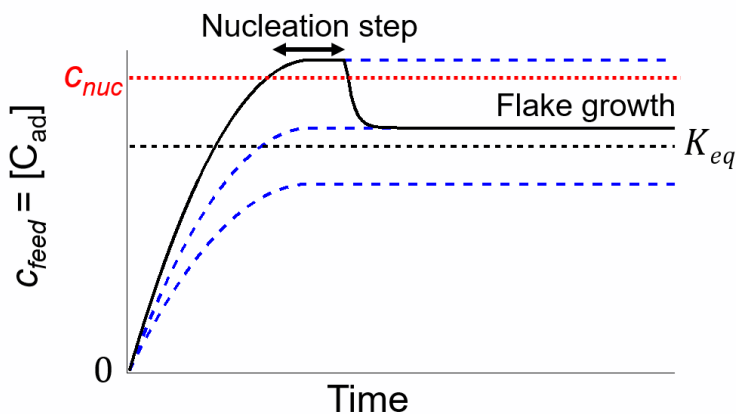


Figure 65 : C_{ad} concentration evolution for an improved synthesis protocol. At first, a nucleation step is set at conditions with $[C_{ad}] > c_{nuc}$, in which graphene nuclei form. After a certain, short nucleation time, the conditions are changed to a lower value of $[C_{ad}]$, where the formed nuclei will grow in size (see text).

As is indicated in Fig. 65, the $[C_{ad}]$ concentration rises when setting the synthesis conditions. In order to induce the controlled formation of graphene flakes the concentration has to exceed the level required for graphene nucleation, c_{nuc} . After a certain growth time, the CVD parameters are set closer to thermodynamic equilibrium, at best below $c_{continuous}$, so that no new graphene flakes are formed during the growth step. The sufficiently high $[C_{ad}]$ concentration temporarily ignites the heterogeneous seeds during the nucleation step, which is suppressed as much as possible during the subsequent growth step of the synthesis protocol. All in all, we can summarize two main issues of the concept:

1. $Q_{nuc} < Q_{exp}$: The nucleation step should always be executed at conditions further away from the equilibrium concentration than the subsequent growth. Otherwise, a lowering of the mass action constant Q_{exp} leads to an increase in the adsorbed carbon concentration C_{ad} and hence might activate new nuclei.
2. $t_{nuc} \approx 2 - 5 \text{ min}$: Generally, the nucleation step should be kept short. In case that no continuous nucleation is observed at the chosen CVD settings, it can be expected that all nucleation events take place in the first moments of the nucleation, regardless of the duration. On the other hand, if the parameter regime is entered where continuous nucleation takes place ($c_{continuous}$), the duration should be kept as short as possible to reduce the spreading of flake sizes.

The results presented in this chapter are derived by experiments that monitor the phenomenological response of the system, which is inherent when dealing with minority species that induce a condensation process. The achieved results are strictly relevant only to the used reactor. They may even change with slight modifications to the reactor setup, the gas purity, the quartz tube age or even the batch of copper foils. The basic principles of nucleation deduced from the outlined experiments can nevertheless be transferred to any similar growth reactor. After performing a calibration procedure to deduce the nucleation events observed at certain CVD conditions, the relative changes when varying the parameter space will be similar, even when using a different reactor setup.

7. Selective growth of multilayer graphene flakes

The method of graphene growth by chemical vapor deposition (CVD) on copper is known for its high yield of single layer graphene flakes enabled through the surface mediated growth on this catalyst.^{21, 13} Due to the surface-mediated growth it may be expected that the formation of second- or multilayer graphene is kinetically controlled. Indeed, it has been shown in the previous section that the formation of multilayer islands in graphene seems to require a nucleation seed.

Other metals with higher carbon bulk solubility grow graphene mainly through segregation from the bulk of the metal catalyst, allowing for additional layers to form below the first one.^{323, 15} Nevertheless, several synthesis routes for bi- and multilayer graphene on Cu have been published.^{280, 126, 114, 324} The amount of multilayers formed on the surface according to these studies can be influenced by increasing the total pressure in the system,¹²⁶ by a special cooling rate,¹¹⁴ by gradually increasing the methane partial pressure³²⁴ or by a special sample geometry.²⁸⁰

Bilayer graphene is typically relevant due to its special electronic properties. While the mechanical characteristics of few layer graphene mainly scale linearly with graphene layer number, the electronic properties are non-scalable in this thickness regime,³²⁵ including e. g. the formation of a tunable bandgap.⁷⁷ The electronic structure highly depends on the rotational alignment of the formed graphene layers and intercalated atoms inbetween.³²⁶ This opens a playground for the design of materials with novel properties, but it also requires the controlled formation of graphene with desired film thickness.

The literature instructions on how to grow primarily multilayer graphene on copper substrates^{280, 126, 114, 324} perform their growth at CVD conditions where the formation of a specific layer number is kinetically driven (see section 4.2). However, the results of the thermodynamic considerations from chapter 4.2 indicate the existence of a parameter range where the reaction thermodynamics should lead to the exclusive formation of few-layer graphene. The chart shown in Fig. 66a) displays the graphene stability regime for $T=1045$ °C. The blue colored parameter space shows the graphene growth zone (growth Regime A), whereas the red area indicates the graphene instability regime (growth Regime C). The dashed black line shows the thermodynamic equilibrium line for single layer graphene (SLG) as determined in chapter 4.2 and the continuous black line indicates the graphite equilibrium line as extracted from the NIST-Janaf tables.²⁴⁷ The discrepancy between both equistability lines is caused by slight differences, most probably in the reaction entropy of the formation reaction. The two equilibrium lines enclose a new growth Regime B, which is shown in yellow color in Fig. 66a), where SLG should decay while graphite should not.

Graphene with an increasing number of layers should rather resemble graphite energeti-

cally, which can be thought of as infinite-layered graphene. The stability of bi-, tri- and higher layered graphene stacks is assumed to lie somewhere between these two extrema. As a result, within the yellow shaded CVD parameter regime SLG would be thermodynamically unstable while multilayer graphene should still be thermodynamically stable. Figure 66b) sketches three types of experiments that were performed to prove this issue. They are outlined in the following chapter.

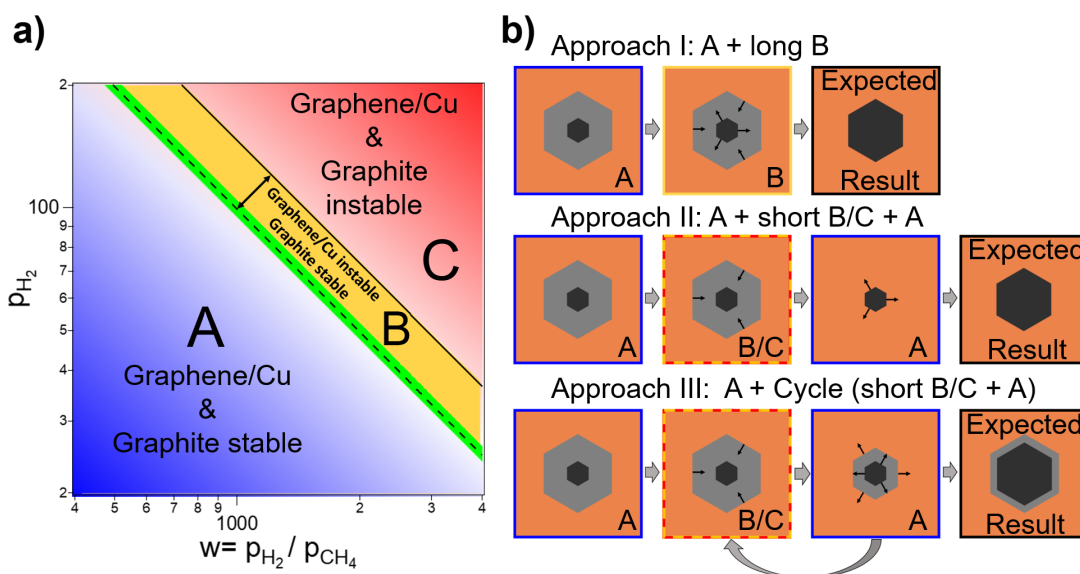


Figure 66 : a) $p(H_2) - w$ -diagram showing the different growth regimes, specifically indicating the CVD parameter regimes where SLG on Cu is stable (A), and the one where graphite turns unstable (C). Applying CVD parameters of the regime inbetween (B) should lead to the decay of SLG while keeping multilayer graphene stable (see text). b) Potential reaction designs to achieve the formation of graphene multilayer flakes in direct proximity to the bare substrate, without the formation of SLG. Starting with pre-grown graphene islands, the flakes can either be exposed to growth Regime B (yellow) for a long time, until the SLG areas are decayed while the multilayer regions are stable or even increase in size. Otherwise, the pre-grown graphene flakes can be exposed to unstable conditions (Regime C), assuming that the central multilayer region will decay after the decay of SLG. With the proper timing, the remaining multilayer islands can be exposed to growth conditions again, assuming that pure multilayers continue to grow without the evolution of a new SLG area. Lastly, a switching between growth and etching conditions can be used to selectively etch SLG areas while promoting multilayer growth.

7.1. Experimental verification of simultaneous growth and decay of graphene with different layer numbers

For the experimental verification of the proposed growth mechanisms in the yellow shaded growth Regime B of Fig. 66b), graphene flakes were pre-grown by applying CVD parameters in the growth Regime A (blue) and subsequently the conditions were changed to shift into the yellow shaded growth Regime B (as listed in Table 17 and as is sketched

in the $p(H_2) - w$ -diagram shown of Fig. 67a).

In growth Regime B no nucleation events are expected, therefore pre-grown graphene flakes were used for these experiments. The two-sample experiment was conducted at $T = 1080^\circ\text{C}$.

Table 17 : Experimental conditions for a sample exposed to SLG-unstable conditions close to thermodynamic equilibrium after nucleation (i) and pre-growth (ii) of the graphene islands. At the reaction temperature of 1080°C , $K_{eq} = 125$ and $K_{graphite} = 181$. (Experimental details: E. 52)

#	$T = 1080^\circ\text{C}$	w-ratio	$p(H_2)$	Q_{exp}	t_{grow}	Optical Image
i)	Nucleation	1361	20.0 mbar	27.2	3 min	
ii)	Regime A $Q_{exp} < K_{eq}$	3380	36.0 mbar	121.7	10 min	Fig. 67b) - blue
iii)	Regime B $Q_{exp} > K_{eq}$	3516	36.4 mbar	127.8	10 min	
iv)	Regime B $Q_{exp} > K_{eq}$	3516	36.8 mbar	129.2	10 min	Fig. 67b) - yellow

After nucleation and growth in Regime A (step i and ii in Table 17), almost perfect hexagonal graphene flakes form on the sample, as shown in the blue framed optical image in Fig. 67b). After 20 min of exposure to the conditions of growth Regime B (step iii and iv in Table 17), the remaining sample was removed from the reactor. This sample shows a strong decay of the graphene flakes, as graphene flakes turned into the rounded shape as known for decaying samples (see chapter 4.2). In several cases, additional, small hexagonally shaped graphene flakes appeared inside decaying graphene islands, attached to or in the direct vicinity of decaying graphene flakes (see Fig. 67b).

Raman measurements taken at the indicated positions in Fig. 67c) are displayed in panel d). They show a typical SLG pattern for the rounded island, and a broadened multilayer-characteristic spectrum for the smaller, hexagonal islands. These experimental results indicate that, indeed, there is evidence for the simultaneous decay of the larger SLG segments and simultaneous growth/stability of the multilayered islands at the applied CVD conditions of Regime B. Although the multilayer islands are comparatively small, as would be expected for graphene islands grown for such a short time period, it was possible to show that these are more stable than the SLG equivalent material. It cannot be unambiguously stated whether the multilayer islands are really thermodynamically stable or if the decay is kinetically hindered, as processes in this regime may be very slow. The direct vicinity to the decaying SLG graphene at a notable kinetic rate nevertheless suggests a thermodynamically driven process.

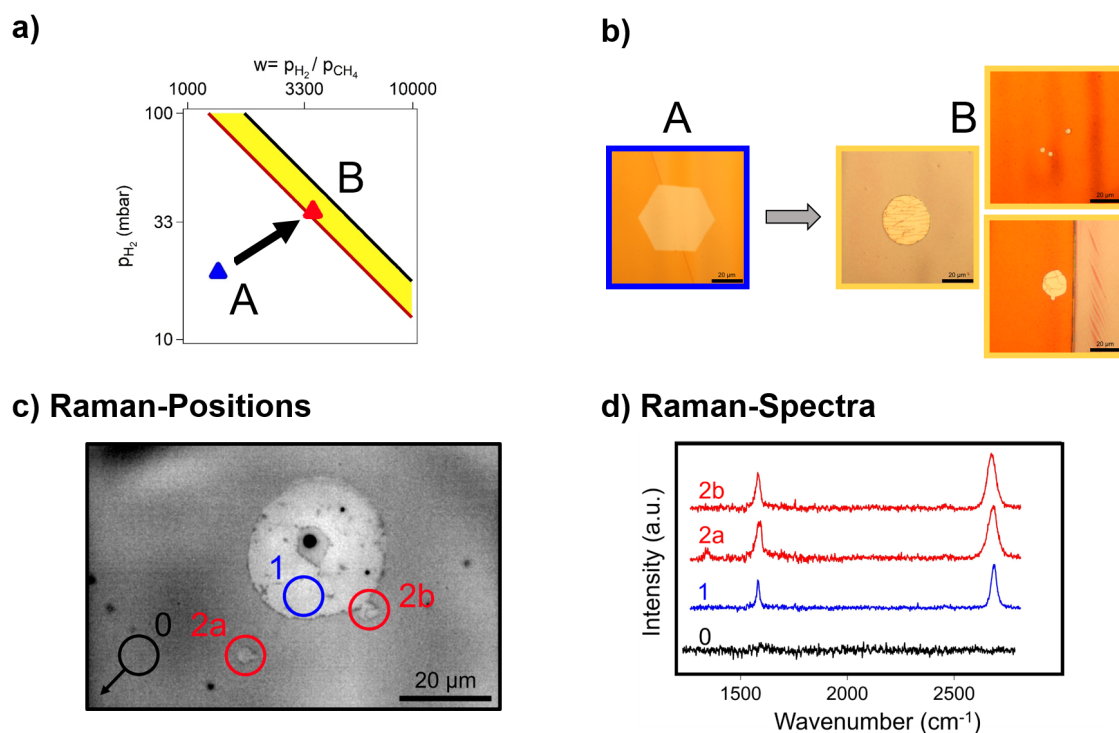


Figure 67 : Experimental results of the sample exposed to conditions according to Table 17. a) After growth (blue triangle) the graphene flakes are exposed to decaying conditions (red triangle). b) Optical images of the graphene flakes after exposure to the reactive conditions as shown in a). While the sample shows ideal hexagonal flakes after growth (blue), the flakes show the typical rounded shape after etching (yellow). Special observations in this sample are the isolated, small hexagonal islands remaining after the partial etching of the graphene flakes. c-d) Raman analysis of a decaying SLG island together with the smaller hexagonal islands, which show the Raman-fingerprint of multilayer graphene. The bare Cu surface shows no Raman signal (black). Adapted with permission from reference ²⁴⁶. Copyright 2021 American Chemical Society.

7.2. Approaches to receive large areas of multilayer graphene

The growth procedure presented in the previous section shows a way to selectively etch SLG while keeping thicker graphene intact. This observation leads to a graphene growth procedure towards the formation of multi-LG. Although exploiting this new growth regime, the resulting multilayer structures are still quite small compared to the remaining SLG areas. Technological relevance is reached only if exclusively multilayer areas can be grown at extended size.

The etching process needs a bare Cu surface in equilibrium to establish the predicted pre-equilibrium state of surface adsorbates and enable the particle exchange between gas phase, surface adsorbates and graphene flake. Therefore, it is not possible to first grow a complete graphene film and then etch away the single layers, as there would be no Cu surface left for gas adsorption. As the etching rate in Regime B (yellow area in Fig. 66) is

quite low when slightly exceeding the equilibrium concentration, it is necessary to establish a special reaction recipe to achieve the selective multilayer growth. Three different approaches depicted in Fig. 66b) to reach this goal are presented in the following:

Approach I. Nucleate graphene flakes far away from the equilibrium (Regime A), etch away the single layer fraction and simultaneously grow the bilayer fraction in growth region B. This method is quite time demanding, as most of the growth process is taking place in growth region B where all net processes are very slow due to the close vicinity to the equilibrium concentration K_{eq} . Basically, this method proposes a strongly elongated version of the experiment described in Fig. 67, in which all SLG components decay and the multilayer fraction grows at low growth speed.

Approach II. Nucleate graphene flakes far away from the equilibrium (Regime A), etch away the complete single layer fraction (Regime B) and grow the whole flake as a multilayer by applying CVD parameters of growth Regime A. This approach assumes that if the complete SLG flake is etched and only multi-LG remain, subsequent exposure to growth conditions (Regime A) does not form new SLG, as sketched in the second row of Fig. 66b).

Approach III. Nucleate graphene flakes (Regime A) and cycle phases of single layer decay (Regime B/C) and overall graphene growth (Regime A) to continuously increase the multilayer fraction of each grown flake. This method does not rely on the requirements of approach II to exactly hit the narrow CVD-Regime B. Instead, also cycling between Regimes A and C should result in a graphene film with extended multilayer fraction if the multilayer decay proceeds at a slower rate with respect to the SLG decay.

Generally, it must be noted that the planning of such experiments purely on the basis of $p(H_2) - w$ -diagrams is only possible due to the exact knowledge of the flake evolution both in thermodynamic and kinetic respect.

Different samples were grown according to the outlined synthesis approaches, which are discussed in the following:

7.2.1. Experimental realization of approach I

The synthesis of approach I follows the recipe:

Nucleate graphene flakes far away from the equilibrium, etch away the single layer fraction and simultaneously grow the bilayer fraction by applying CVD conditions of growth Regime B.

The effect of long exposure in growth Regime B was explored in this experiment. The exact conditions are listed in Table 18. Graphene flakes were nucleated at conditions far away from equilibrium, exposed for 60 min under growth conditions close to thermodynamic equilibrium for the evolution of regular hexagonal flakes and additionally kept overnight for 14.5 h at conditions in growth Regime B.

Table 18 : Applied experimental reaction conditions at 1075 °C according to synthesis approach I used to enlarge the relative multilayer ratio by long exposure to CVD reaction conditions of Regime B, which is enclosed by the thermodynamic equilibrium line for graphite ($K_{graphite} = 175$) and SLG formation ($K_{eq} = 122$). (Experimental details: E. 53)

#	$T = 1075^{\circ}C$	w-ratio	$p(H_2)$	Q_{exp}	t_{grow}
i)	Nucleation (Regime A)	320	200 mbar	64	3 min
ii)	Growth near K_{eq} (Regime A)	320	350 mbar	112	60 min
iii)	Regime B	357	425 mbar	152	14.5 h

The optical images of graphene flakes (Fig. 68b) show a regular hexagonal pattern. The observed graphene flakes have a mean radius of $32 \mu m$, which relates to a growth velocity of $1.3 \mu m h^{-1}$ during the last reaction step, as the medium flake radius after growth step ii) was $\approx 12 \mu m$.

Synthesis approach I

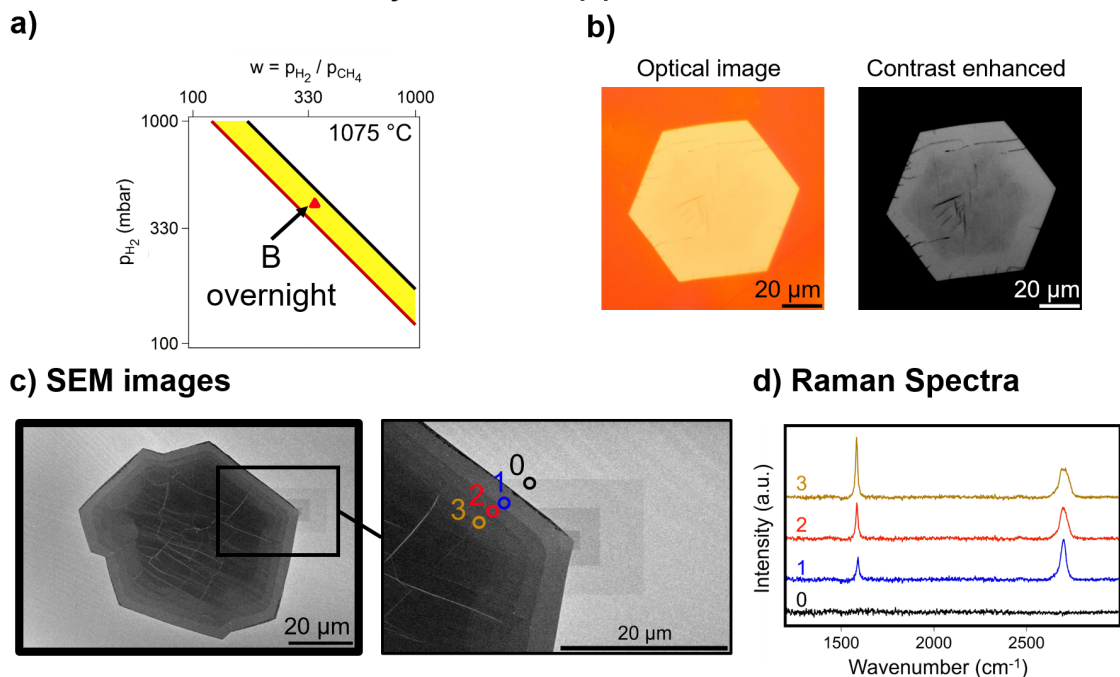


Figure 68 : Experimental results of the approach of long exposure to conditions in the growth Regime B. a) Reaction conditions maintained during 14.5 h, as shown in Table 18. b) Optical images (left: original data, right: contrast-enhanced data) of a graphene flake after exposure to the conditions in a), showing a fast increase in contrast in the central part of the graphene flake. c) SEM images of a flake treated equally to b), showing the stepwise increase in contrast (graphene layers) every $\approx 2 \mu m$. Magnification with positions of Raman-spectra measurements. d) Raman spectra acquired at the positions shown in c), showing the stepwise increase from 0 to 3 graphene layers.

Already in the optical images, at enhanced contrast, the inner part of the graphene flake appears dark. The contrast-enhanced greyscale-image shows this effect more clearly. A staircase-like contrast increase towards the graphene flake center can be observed by Scanning electron microscopy, as shown in Fig. 68c). Here, the contrast increases stepwise from the flake rim towards the flake center every $2 - 3 \mu\text{m}$. The outermost graphene edge shows a darker contrast, which can be assigned to the onset of Cu oxidation below the graphene flake during the short exposure to air in-between growth and measurement. A linescan of Raman spectra shows the evolution of the Raman-signals with increasing contrast, which correlates with an increasing layer number. An excerpt of the linescan positions is shown in Fig. 68c) and the corresponding spectra are shown in Fig. 68d). While the spectrum of the rim stripe shows the shape and intensity distribution commonly contributed to SLG, the next spectra can be fitted with the known parameters for Bernal stacked bi- and trilayer graphene, respectively, as done in reference¹²⁸. The attribution of Bernal stacked graphene layers is justified by the parallel alignment of the layer edges seen in Fig. 68.

Again, it is rather difficult to unambiguously state whether the formed, thin SLG area around the flakes is thermodynamically stabilized by the available multilayer regions nearby or if the complete decay is kinetically hindered. Nevertheless, it is unambiguous that the formation of multilayer graphene flakes is strongly favored at conditions very close to thermodynamic equilibrium. The long exposure to these conditions overnight enables the formation of extended multilayer areas, but at a very low growth rate of $1 \mu\text{m h}^{-1}$. It remains to be examined whether it is possible to steer the multilayers towards a favored number of layers by slightly changing the reaction conditions during CVD.

The exact determination of the layer number from the SEM and Raman data turns out to be rather difficult for higher layer numbers. While the stepwise increase in layer number can be observed for the first few layers in the secondary electron image, the contrast change is not distinguishable for the central part of the graphene flake. In the case of Bernal stacked multilayer graphene, the intensity of the G-peak should scale approximately linearly with the number of superimposed graphene layers. The evolution of the G- and 2D-peaks is shown in the form of a waterfall-plot in Fig. 69a). The G-peak signal area normalized to the SLG area is plotted against the spectrum number in Fig. 69b), the position of locally acquired spectra is indicated in the SEM image of Fig. 69c). The G-peak intensity increase in the first few Raman spectra can be correlated to the stepwise contrast change in the SEM image. The G-peak area of n -layer graphene is a multiple of the SLG G-peak area up to $n = 3$, as indicated in Fig. 69b). An exception is observed for the first two graphene-spectra, which show a much higher intensity due to decoupling of the SLG from the Cu substrate as a result of the oxygen intercalation along the graphene island edge.

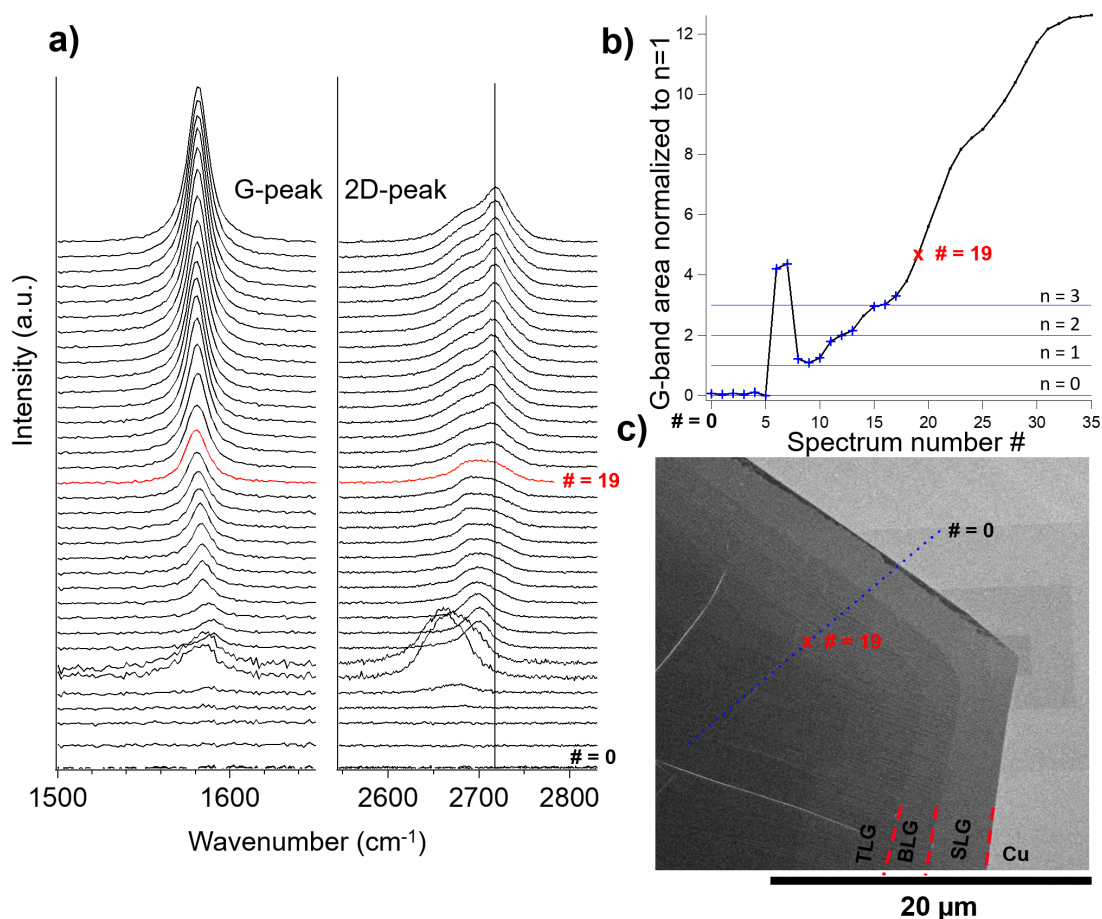


Figure 69 : Evolution of local Raman spectra acquired along a line-scan from a graphene flake on the sample described in Fig. 68. a) Waterfall plot of the G and 2D-band of the spectra from the graphene-free Cu area to the center of the island. b) Integrated G-band intensity of the respective Raman spectra normalized against the integrated peak intensity obtained from SLG, plotted against the spectrum-number #. The data set shows the stepwise thickness increase of the graphene flakes as identified by Raman-spectroscopy. While the first Raman spectra show no graphene-signal at all (bare Cu), the following spectra show a strongly increased Raman intensity, which can be explained by the decoupling of graphene by the forming oxide layer between graphene and Cu. The following spectra show a clear stepwise intensity increase along the respective increase of the flake thickness (1, 2, 3 layers), followed by a strong intensity increase of the G-band signal at higher layer numbers. This observation indicates the electrical decoupling of the out-most graphene sheet from the Cu substrate above three layers thickness. c) SEM image superimposed with the spots of the locally acquired Raman-spectra. Spectrum number 19 is marked red in each diagram to facilitate the referencing.

This is also visible in the SEM images, where oxidation between graphene and Cu substrate is initiated from the graphene flake edge after exposure to air and appears as a slight rim with dark contrast around the graphene flake in the SEM images. Note that the SEM images were measured after approximately 60 min sample exposure to air, while the Raman spectra were measured 24 h after removal from the reactor setup and exposure to air. The oxidized rim should therefore be larger in the measured Raman-spectra than

the one imaged by SEM. Above the third graphene layer, at spectrum number $\# = 19$, the Raman intensity increases much stronger per recorded spectrum than before. As the graphene island thickness increases at an increased slope, a stepwise intensity increase is not resolvable due to the lateral resolution limit of the Raman experiment. The Raman G-band reaches two more intensity plateaus (at spectra 25 and 35) before reaching the center of the linescan.

The strong increase in Raman-signal intensity for higher layer numbers may indicate that at this layer number the highest graphene sheet does not interact with the substrate metal anymore and therefore exhibits the spectral characteristics of electronically entirely decoupled graphene. This hypothesis is strengthened because in the 2D-band a new peak species appears at 2719 cm^{-1} after spectrum $\# = 19$. This species is indeed observed in highly oriented pyrolytic graphite (HOPG) by Dresselhaus *et al.*³⁴ I conclude that above four layers of graphene on Cu, the Raman spectrum approximates the one of HOPG. Using a defined graphene crystal with known layer number, it might be possible to calibrate the Raman intensity also for higher layers to reliably determine the thickness of unknown samples.

7.2.2. Experimental realization of approach II

The synthesis of approach II follows the recipe:

Nucleate graphene flakes far away from the equilibrium, etch away the complete single layer fraction and grow the whole flake as a multilayer in growth Regime A.

To test the behavior of graphene exposed to decaying followed by growth conditions, an experiment was conducted according to the parameters listed in Table 19. Graphene was nucleated and pre-grown at $Q_{exp} = 45$ (Regime A), then exposed to decaying conditions for 60 min in CVD Regime B and subsequently again to growth conditions (Regime A) for 30 min. It should be noted that the applied nucleation conditions at high pressures of 150 mbar favor the formation of multilayer graphene islands, as discussed in chapter 6.4.

Table 19 : Applied experimental reactor conditions at $1045 \text{ }^\circ\text{C}$ according to synthesis approach II. The nucleated graphene flakes were exposed to SLG decaying conditions followed by growth conditions. At the reaction temperature of $1045 \text{ }^\circ\text{C}$, $K_{eq} = 101$ and $K_{graphite} = 146$. (Experimental details: E. 54)

#	$T = 1045^\circ\text{C}$	w-ratio	$p(\text{H}_2)$	Q_{exp}	t_{grow}
i)	Nucleation (Regime A)	300	150 mbar	45	20 min
ii)	SLG decay (Regime B)	900	150 mbar	135	60 min
iii)	Grow (Regime A)	500	150 mbar	75	30 min

After exposure to nucleation and decay conditions (step ii in Table 19), the graphene flakes show the rounded shape typical for exposure to CVD conditions where SLG/Cu is unstable, as can be seen in the optical images in Fig. 70a). In case that Regime B is not hit, but the stability line of multilayered graphene is surpassed (Regime C), SLG and multi-LG decay equally. Returning to growth conditions in Regime A again leads to the formation of hexagonally shaped flakes (or flakes with hexagonally oriented angles), as shown in Fig. 70b). SEM images of these flakes, displayed in Fig. 70c), resolve a large amount of multilayer graphene in these flakes.

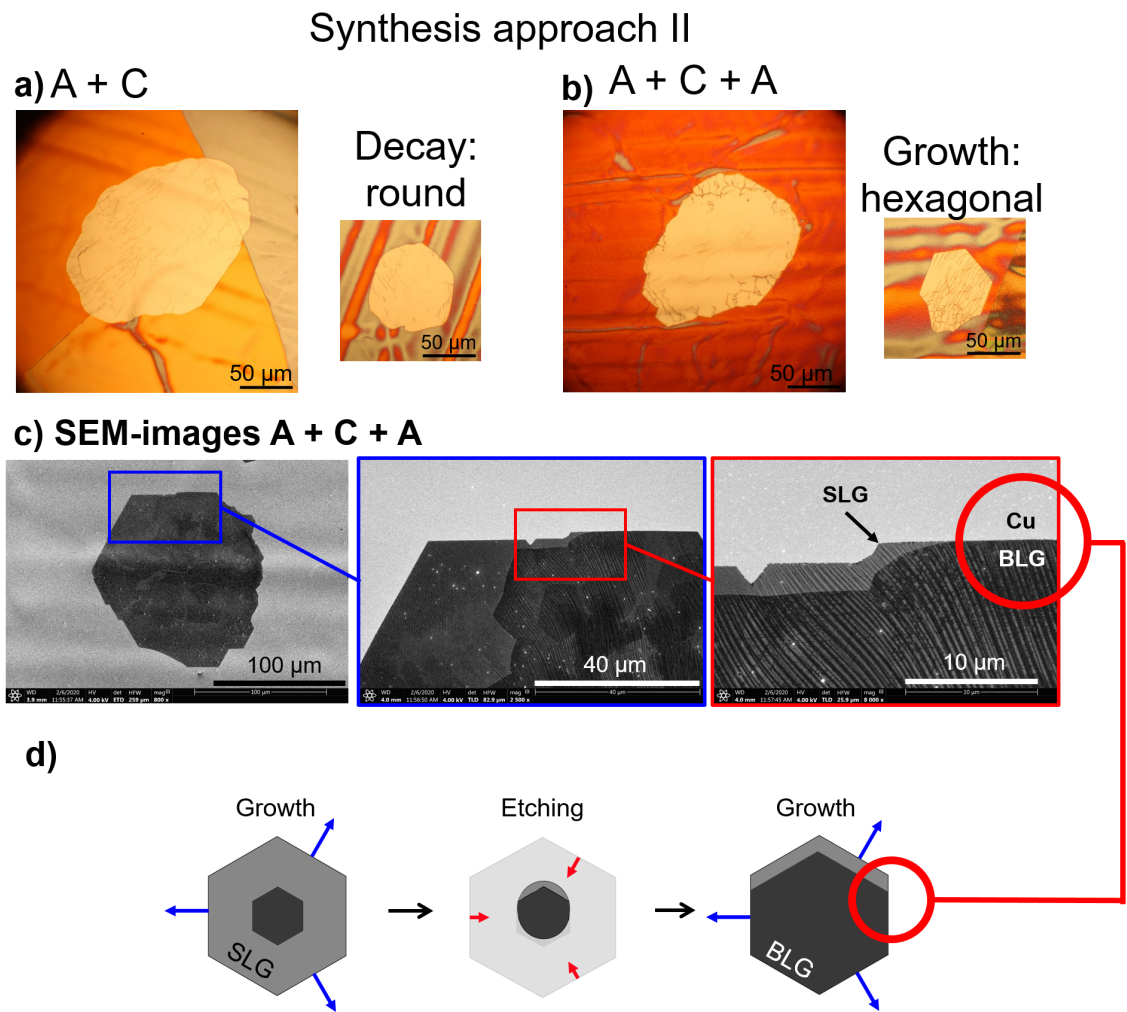


Figure 70 : Experimental results of a sample treated according to approach II. Precise reaction conditions are listed in Table 19. a) Graphene islands after exposure to etching conditions, showing overall rounded flake rims. b) Graphene flakes after subsequent exposure to growing conditions, showing again the development of straight rim lines. c) SEM images of flakes treated equally to b), showing the increased evolution of graphene multilayers and especially the direct transition from bilayer graphene to graphene-free copper substrate, which is commonly not observed for graphene flakes grown at one single reaction mixture.

Interestingly, the multilayer area of the graphene flake expands until the outer rim of the graphene flake, where a direct transition from multilayer graphene to bare Cu is observed (see magnified images of Fig. 70c). This flake geometry is not possible to achieve with one single growth step, as always SLG will form the outer graphene rim. Sketched in Fig. 70d), initial SLG flakes with multi-LG in its center will turn to flakes with direct transition from multi-LG to Cu after the first CVD treatment in Regime B. Flakes with this morphology will then continue to grow in this shape after returning to growing conditions in Regime A.

After the observation that SLG growth on Cu is only controlled kinetically in section 4.2, the outlined experiment proves that under the correct starting conditions the evolution of graphene on Cu tends to produce bi-/multilayer graphene. Using the synthesis approach II, it becomes possible to minimize the amount of SLG while simultaneously increasing the desired amount of multilayer regions. Nevertheless, the demands on the experimental precision is very high and it is almost impossible to accomplish a defined n-layer graphene film in *ex situ* growth experiments due to the natural spreading of experimental results (flake size distribution, flake density, multilayer nucleation). Achieving this goal could more easily be obtained by cycling growth and decay conditions, as discussed in the next section.

7.2.3. Experimental realization of approach III

The synthesis of approach III follows the recipe:

Nucleate graphene flakes and cycle CVD treatment phases of single layer etching and overall graphene growth to continuously increase the multilayer fraction of the graphene flakes.

The third method presented to increase the multilayer fraction in Cu-CVD grown graphene makes use of the general graphene flake build-up. In most cases, multilayer islands nucleate in the central part of the SLG flake, creating a smaller multilayer island surrounded by a larger SLG area. At CVD conditions in the unstable Regime B/C, the graphene decay starts from the flake edge towards the center. This decay therefore affects SLG areas first. Cycling growth intervals, in which entire graphene flakes expand, with decay intervals, in which selective SLG decay takes place, should lead to graphene flakes with a higher multilayer fraction in the end.

Accordingly, cyclic growth/decay conditions listed in Table 20 were applied to promote the formation of multilayer graphene. Again, a two-sample loading experiment was conducted, where the first graphene sample was removed from the reactive atmosphere after step i) and examined after oxidative contrast enhancement in air at different temperatures, as shown in Fig. 71a).

Table 20 : Applied experimental reaction conditions at 1075 °C according to synthesis approach III. The nucleated graphene flakes were cycled between growth and etching conditions. At the reaction temperature of 1075 °C, $K_{eq} = 122$ and $K_{graphite} = 175$ (Experimental details: E. 55)

#	$T = 1075^{\circ}\text{C}$	w-ratio	$p(\text{H}_2)$	Q_{exp}	t_{grow}
i)	Nucleation (Regime A)	375	200 mbar	75	5 min
ii)	Regime B	375	400 mbar	150	60 min
iii)	Regime A	375	200 mbar	75	5 min
iv)	Regime B	375	400 mbar	150	30 min
v)	Regime A/B	375	350 mbar	131	60 min

Synthesis approach III

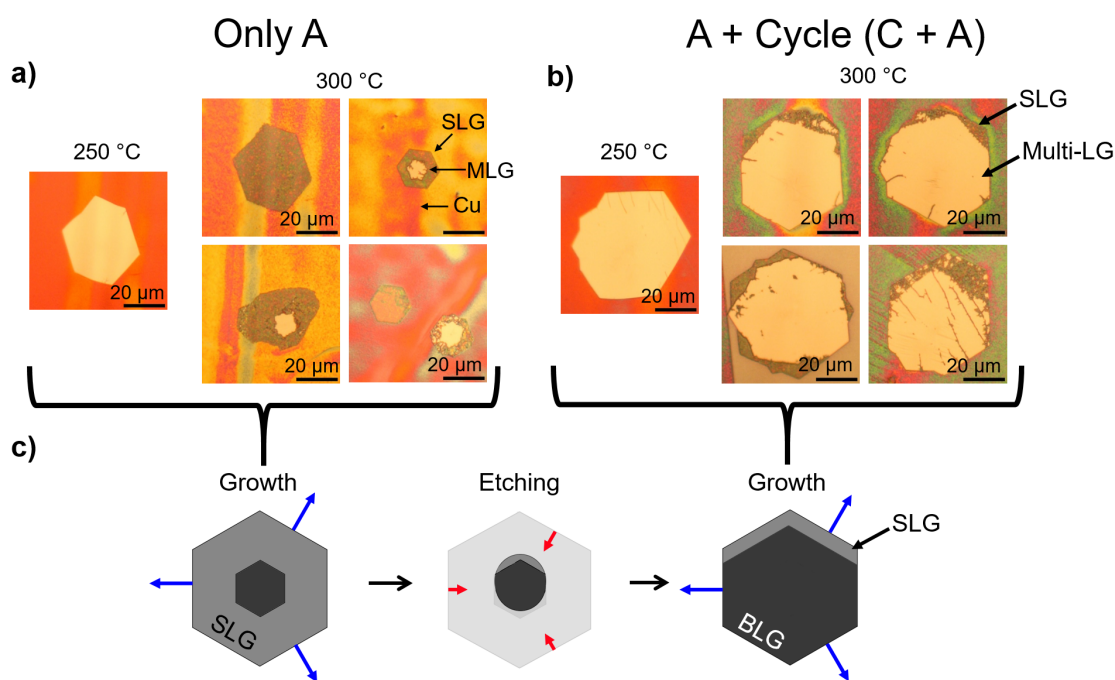


Figure 71 : Experimental results of a sample treated according to approach III, as listed in Table 20. a) Optical images of the graphene flakes after the first growth period, heated to 250 °C (left) and 300 °C (right). Samples heated to 300 °C allow the identification of small multilayer islands, covering approximately up to half the graphene island. b) Optical images after the cycling of growth and etching periods in the reaction conditions. Samples heated to 300 °C show a large multilayer fraction, surrounded by a small SLG rim. Noteworthy is the observation that several flakes show the complete absence of SLG rims along some flake edges. c) Possible reaction pathway explaining the absence of SLG areas on some of the graphene edges. This pathway implicates that if a SLG area is completely etched in the decay phase, the subsequent growth phase will enable the collective growth of the bilayer front without the separation into two growth fronts.

The oxidative contrast enhancement at 250 °C in air shows the general existence of regular hexagonal graphene flakes on the bare Cu surface. An additional heating in air to 300 °C attacks the SLG fraction of the flakes and, thus, allows distinguishing between SLG and multi-LG.

The graphene flakes after growth step i) show mainly SLG areas with partly small multilayer graphene (Multi-LG) islands in the center. Some of these multilayer areas take up a maximum of $\approx 50\%$ of the graphene area, but this ratio shows strong deviations with a large fraction of flakes also showing no multilayer area at all.

The sample exposed to two cycles of etching and growth with graphene flakes as obtained after reaction step v) was removed from the reactor and imaged by optical microscopy, as shown in Fig. 71b). The samples heated to 250 °C in air for contrast enhancement show almost no change compared to the samples of step i) regarding shape and size. More important is the distribution of SLG/Multi-LG areas in the sample, which becomes visible after heating in air to 300 °C. Small areas coloring in a darker grey color show remaining SLG areas, but the largest flake fraction is composed by yellow/orange colored multilayer areas. Through the clear transition between SLG and Multi-LG, it is possible to determine the interlayer rotation for several flakes. In the exemplarily shown graphene flakes of Fig. 71b), the interlayer rotation can be found either as Bernal stacked graphene with aligned flake layers or turbostratic rotated layers. The information can be deduced from the alignment of the respective flake edges, which are known to be zigzag edges and produced along the lattice vector of the honeycomb lattice.⁵² Regardless of the rotational alignment of the graphene layers, all flakes show areas with a direct transition from multilayer graphene to bare Cu.

Using this synthesis instruction, it becomes possible to steer the reaction results on this substrate known for its high yield of SLG samples towards graphene flakes with almost pure multilayer thickness. To explain the formation process of large Multi-LG flakes with small remaining SLG areas as visible in the optical images, I propose a mixture of the processes known from approaches I and II: At first, SLG flakes with a small Multi-LG fraction are nucleated and grown when applying CVD conditions of Regime A. However, the cycling between Regimes B and A or even between C and A will at some point deliver graphene flakes with an abrupt transition of the multilayer region towards the bare Cu support. After this process, respective exposure along the synthesis approach III will enlarge such Multi-LG flakes, maintaining its multilayer geometry.

Using the knowledge gained from the thermodynamic and kinetic analysis of graphene growth, the specific synthesis of highly defined samples becomes possible, as shown in this chapter. The formation of multilayer graphene is accessible using the approach of graphene flake exposition to conditions in the intermediate growth Regime B between the stability lines of SLG and graphite. To accomplish the full flexibility regarding the formation of samples with defined thickness, shape and size, several topics remain to be

examined more thoroughly. This includes the formation of multilayer nuclei with pre-defined interlayer rotation, the experimental differentiation between the formation of bi-, tri- and higher layers of graphene and the growth rate of bilayer graphene edges compared to the ones of single layer graphene.

8. Etching of graphene by oxygen

In the following chapter, I will discuss the decomposition reactions observed for graphene flakes by reaction with oxygen. To disentangle the contribution from oxygen and the one from the reactive methane + hydrogen atmosphere, experiments are first performed in a pure $Ar + O_2$ atmosphere and subsequently in a $CH_4 + H_2 + O_2$ atmosphere.

8.1. Graphene decay experiments reported in literature

The decomposition reaction of graphene flakes is far less studied than the opposite formation reaction. The studying of the back-reaction is particularly difficult, as the edge termination of graphene crystals in the CVD operando state is not completely understood. It is therefore not known, whether the detachment of a carbon atom from the graphene rim is either a purely statistical process, induced by the collision with an adsorbed hydrogen atom or affected by atoms bound to the flake rim, such as hydrogen or metal atoms (see section 2.4). Several experimental studies discussed the decay of graphene flakes. Mainly, such experiments consisted of exposing grown graphene flakes to a hydrogen atmosphere with^{244, 108, 245, 242, 296, 327, 328} or without^{329, 217, 330, 331} the addition of argon as carrier gas. Different approaches were only reported by Kraus *et al.*,¹²⁶ who etched by increasing the hydrogen-to-methane w-ratio and Liu *et al.*,³³² who drastically lowered the hydrogen flow after growth in an $Ar + H_2 + CH_4$ atmosphere.

Despite having applied similar CVD conditions, the reported results differ significantly. While all references report the formation of hexagonal holes inside the graphene films, Choubak *et al.*³²⁹ identified that the purification of the used hydrogen by removing the oxygen contamination prevents the formation of such hexagonal holes. All references working with graphene flakes instead of continuous graphene films observed a flake shape change when exposing the samples to a reducing hydrogen atmosphere, either interpreted as dodecagons^{217, 242} or rather an overall rounding of the flake shape.^{244, 245} While the strong increase of the hydrogen-to-methane w-ratio by Kraus *et al.* also leads to the rounding of graphene flakes, it is not observed in the experiments reported by Liu *et al.* when strongly decreasing the w-ratio. The etching of trenches in the flakes was mainly observed by Wang *et al.*²⁴⁴ and Zhang *et al.*,²⁴⁵ who cooled the sample between the growth and etching process, enabling the formation of wrinkles in the graphene flakes during the cooling process. Etching was observed along these wrinkles when reheating the sample.

In the following, a set of reactions is described, that was performed in order to disentangle the different informations obtained from the literature references. The outcome of

CVD synthesis protocols may be caused by an oxygen gas impurity in the feed, e. g. an air leakage of the reactor system. This is why I studied the graphene etching in a pure $Ar + O_2$ atmosphere as well as in a reactive $H_2 + CH_4$ mixture, to which O_2 was added intentionally.

8.1.1. Etching of graphene flakes in $Ar + O_2$

To examine the impact of possible oxygen impurities on the decomposition reaction of graphene, grown graphene flakes were exposed to argon gas (which contains oxygen contamination in the ≈ 2 ppm regime) directly after the growth of graphene flakes. An argon flow of 30 sccm and a pressure of 20 mbar (4×10^{-4} mbar O_2) was set at the growth temperature of 1045 °C for different time periods while turning off the methane and hydrogen gases. Before the Ar/O_2 treatment, the pre-grown graphene flakes have a hexagonal structure with smooth edges, as shown in Fig. 72a).

After 2 min of oxygen treatment in Ar, a large amount of hexagonal holes developed in the flake, with higher density towards the flake rim (Fig. 72b). The holes are of different sizes up to a maximum extension of about 2 μ m diameter. The flake rim remains straight, except for intersections where etched hexagons interrupt the straight flake edge.

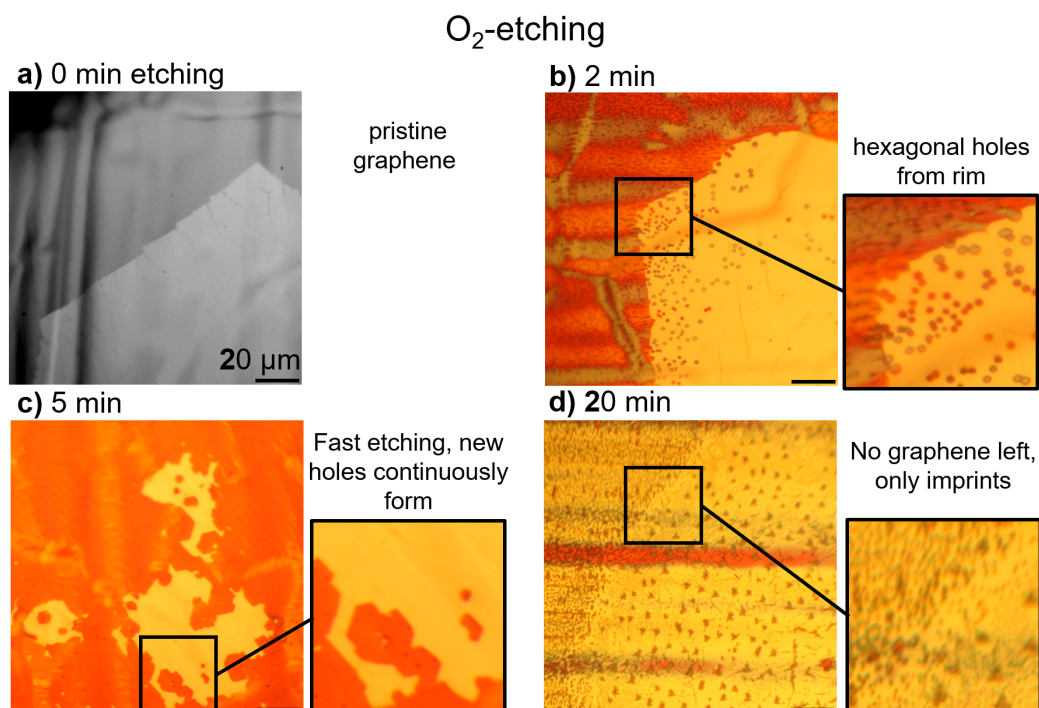


Figure 72 : Degradation of graphene after exposure to traces of oxygen (present as contamination in argon gas) at 1045 °C. The optical images show graphene flakes after a) 0 min, b) 2 min c) 5 min, d) 20 min of exposure to 20 sccm of Ar at 20 mbar. These reaction excerpts show the continuous decay of the graphene flakes with reaction time. Fig. d) shows no more graphene, the visible contrast is formed by impurities on the sample surface, as discussed in chapter 9.1. (Experimental details: a: E. 56 , b-c: E. 57 , d: E. 58)

After 5 min $Ar + O_2$ exposure, the already strongly advanced flake decay could be imaged, as shown in Fig. 72c). Only patches of the flake remained intact. Hexagonal holes with a variety of hole sizes up to a maximum of about 7 μm are shown to be distributed around the remains. Still, the rim of the flake has quite sharp edges, where at several positions partially remaining hexagonal holes can be identified in the displayed images of Fig. 72.

After 20 min exposure, there are no intact remainders of the graphene flakes on the sample (see Fig. 72d)). An imprint allows to identify the original flake position.

The reaction equation between graphene-type carbon atoms with traces of oxygen is a simple oxidation towards mostly carbon monoxide (eq. 8.1a) and to some extent carbon dioxide (eq. 8.1b).



When assuming a simple dissociative adsorption of oxygen on the bare Cu surface, followed by diffusion until collision with a carbon atom, one would expect a decay of the graphene flake beginning from the outer rim, but the decomposition advances from several point sources inside the flake area. The size distribution of the created holes indicates that the defect sites are continuously formed during the induced graphene flake decay. As will be shown in chapter 9 extensively, the center of the nucleation sites where graphene removal is ignited, mostly contains a contaminant particle. The progression of the formed hexagonal holes from the rim towards the center of the flake shows that the formation of these holes is not induced by (random) impingement of oxygen or contaminants from the gas phase, as this should create statistical hole formation on the entire graphene flake. The formation process must contain a diffusion process from the bare Cu surface below the flake, until a reaction most probably with an impurity atom or particle pins the oxidized particle to a specific location. This process is schematically presented in Fig. 73, where the impurity particle is marked in red and the diffusion path of the oxygen is indicated with arrows. Theoretical calculations indicate that the diffusion of oxygen below the graphene film might be favored after the passivation of the graphene edge.³³³ After sufficient impingement events of the diffusing O_{ad} atoms with the postulated impurity particle, either strain from the growing particle or a chemical reaction with the graphene film in contact to the particle may create a defect in the carbon lattice (Fig. 73ii) through which further gas particles may adsorb on the surface (Fig. 73iii).

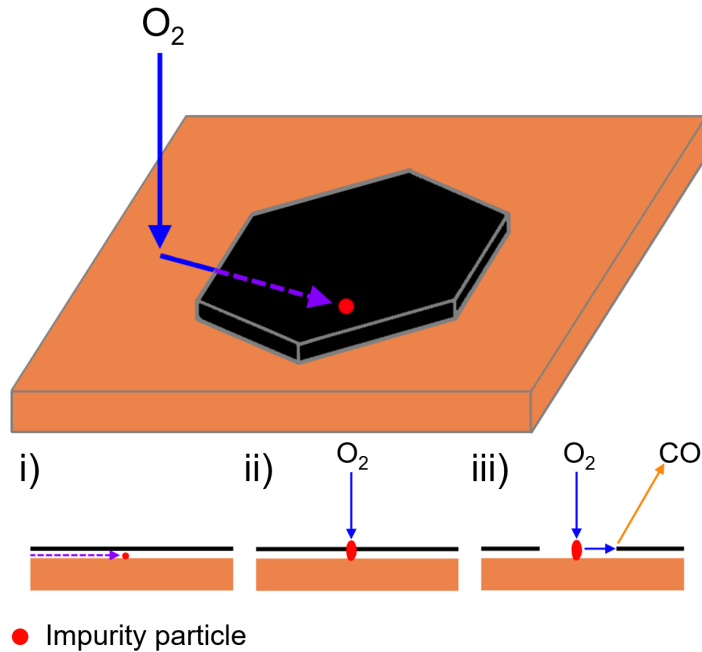


Figure 73 : Possible formation sequence of holes in the previously intact hexagonally shaped graphene island. Oxygen is dissociatively adsorbed on the Cu surface and diffuses below the graphene sheet, until reacting with an impurity particle. This particle grows until it penetrates the graphene layer. After the rupture of the graphene layer, direct dissociative adsorption is possible on the impurity particle, increasing the amount of oxygen present in the etched cavity.

The growth rate of the created holes indicates that the amount of reacting oxygen atoms is not constant for each hole, as this would expect the hole size to increase as the square root of the reaction time. This would be the case if the oxygen dissociative adsorption is focused on the impurity particle in the center of the hole. However, the maximum hole sizes of $2\ \mu\text{m}$ (2 min) and $7\ \mu\text{m}$ (5 min) indicate that with hole size an increasing amount of oxygen is provided, which can be explained by increasing adsorption on the newly created bare Cu surface, leading to exponentially accelerated hole growth. The kinetics of the two models are compared in Fig. 74 together with the experimentally extracted data points. The derivation of the two fit curves is done in Appendix 12.3. The orientation of the holes is always parallel to the graphene flake rim, which means that the holes are zigzag-terminated.³³⁰

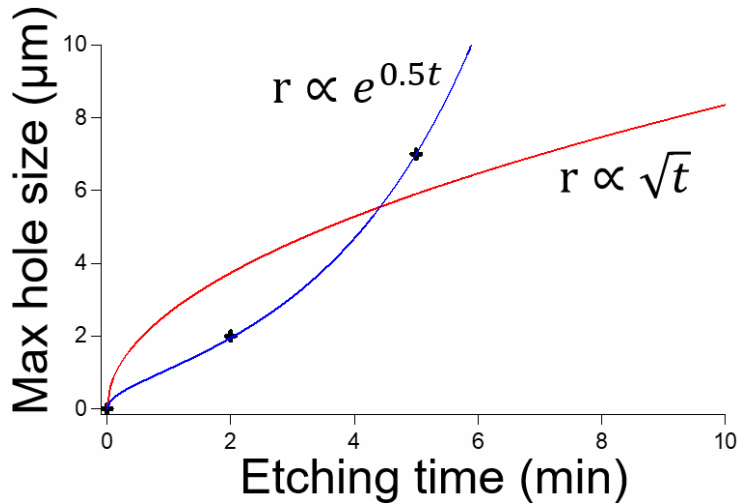


Figure 74 : Hole size evolution of the largest hexagonal holes inside the imaged graphene sheets as a function of oxygen exposure time t . The curves describe fits to these data points according to two different oxygen adsorption mechanisms. The blue curve assumes dissociative adsorption on the complete bare Cu area of the hole, which leads to hole formation with the hole radius exponentially increasing with time. The red curve assumes pure adsorption on the impurity particle in the center of the hexagonal hole, leading to hole formation with a hole radius scaling with \sqrt{t} . The models are explained in Appendix 12.3.

The outlined experiment proved that oxygen impurities create zigzag terminated hexagonal holes in the graphene flakes. The fact that the flake rim does not show a significant shape-change is important when comparing the oxygen-induced etching with the CVD-induced decay above K_{eq} .

8.1.2. Reaction of oxygen with continuous graphene layers

Figure 75 shows scanning electron microscopy (SEM) images and Fig. 76 shows optical images of a sample where a complete graphene film was grown before changing the reactive atmosphere to pure Ar and slowly cooling the sample to room temperature in this atmosphere. The largest part of the sample shows pristine, continuous graphene, but at some particular places on the sample, large holes in the graphene film can be identified, such as the one shown in Fig. 75a).

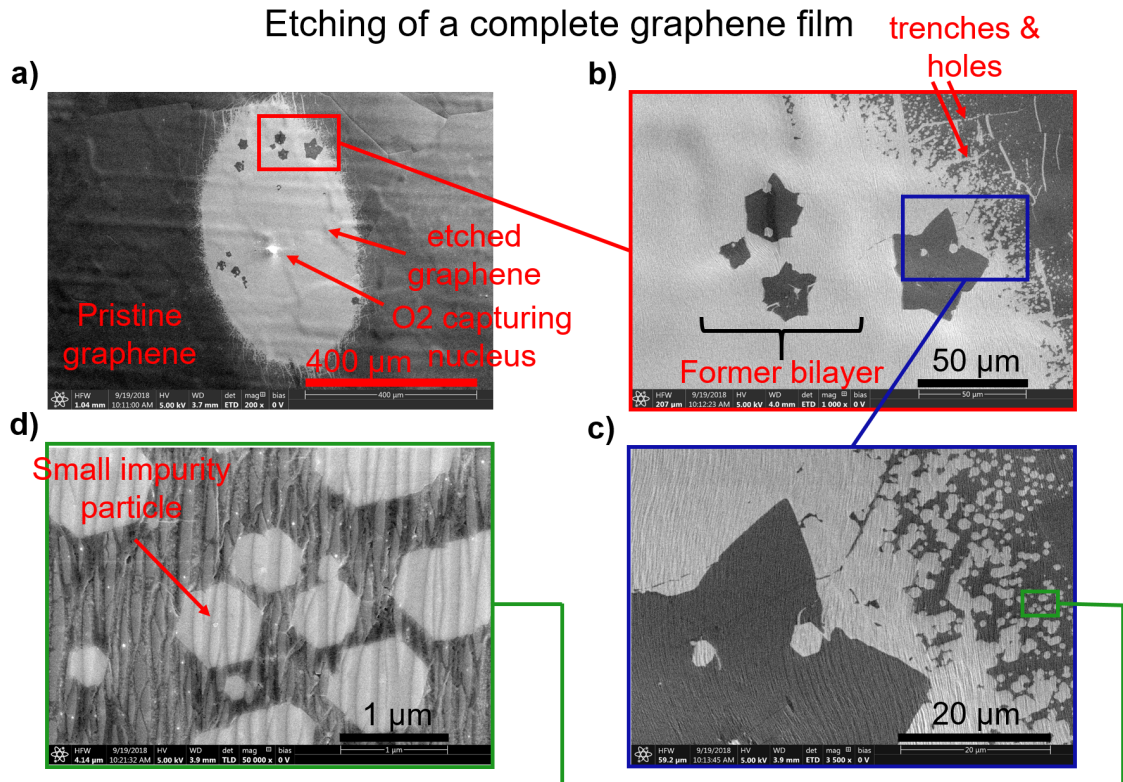


Figure 75 : SEM images of a continuous graphene film exposed to an oxidative atmosphere after synthesis at 1045 °C and subsequently cooled in the oxidative gas phase. The continuous graphene film remained intact, except for areas where visible nuclei initiated etching of the graphene film. A typical case is shown in a-c): a) The image shows an etched hole (bright feature) in the graphene layer (dark areas). A bright impurity particle is positioned in the center of the etched zone. b-d) Magnifications of the previous image. b-c) Former multilayer islands remain intact in the etched areas. The etched front proceeds in form of etched hexagonal holes and small trenches, as marked with red arrows. d) Small impurity particles seem to be present in the center of each small hole etched in the graphene film. All hexagonal holes are oriented equally, indicating a single crystalline domain. (Experimental details: E. 59)

Over an area of approximately 400x400 μm in Fig. 75a), the graphene is completely removed in an oval-shaped area, where several details can be observed. The rim of the etched area has a fractal appearance, consisting of small, hexagonal-shaped holes, as can be identified in the magnified images of Fig. 75c-d). The hexagonal holes are distributed within a 20-30 μm wide rim. Additionally to these hexagons, several almost straight trenches are identified in the graphene film, running mainly in two perpendicular directions, as can be seen in the upper right corner of Fig. 75b). Noticeably, the trenches running from the bottom to the top direction of the image, are parallel to the facets formed on the Cu surface (see section 2.2) and the overall oval shape of the large etched hole is also oriented along these trenches. The trenches running perpendicular to the copper facets are less developed and numerous.

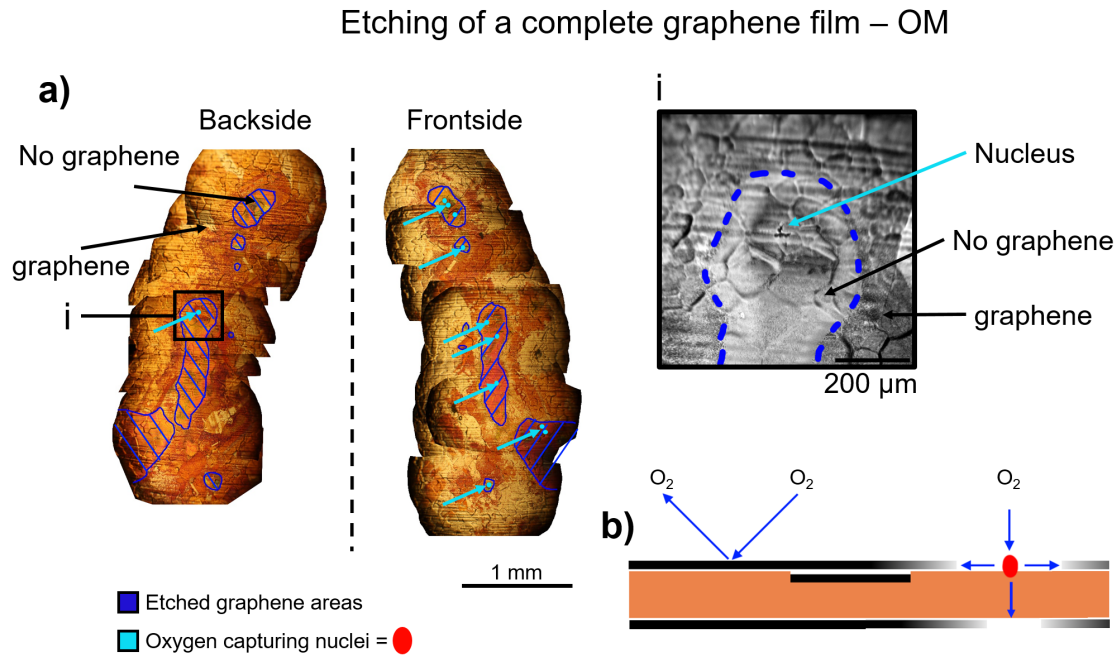


Figure 76 : Optical images of the sample shown in Fig. 75, which was exposed to oxygen atmosphere after the CVD growth of a continuous graphene layer at 1045 °C. Figure a) shows the areas of the graphene film etched by the exposure to oxygen (circled in dark blue) and impurity particles, at which the decay process may have started (marked with a teal arrow). The optical images of the front and backside of the Cu foil show matching areas of graphene etching, regardless if oxygen capturing nuclei are only found on one of the etched areas (frontside or backside). This symmetry indicates that oxygen diffusion through the Cu substrate can enable graphene decay on the opposite side. The inset i) shows a magnification of the etched area with an oxygen capturing nucleus in the center, surrounded by the intact graphene film. b) Possible mechanism of graphene etching by oxygen: Defects or large impurity particles in the graphene layer allow the dissociative adsorption of O_2 and etching of a hole in the graphene, on which further oxygen can adsorb, increasing the size of the etched hole. In addition, oxygen can diffuse through the Cu foil onto the opposite side and induce graphene etching without the presence of a nucleation seed. (Experimental details: E. 59)

Inside the graphene etched area, several star-shaped graphene islands remain present. These resemble small multilayer areas commonly sparsely present in single layer graphene films.

Figure 76a) shows optical images of a different area of the same sample. A set of several etched areas (marked blue) are stretched over an area of $\approx 4 \times 1 \text{ mm}$ and can be found in the almost identical, mirrored form on the backside of the sample, which is also shown in Fig. 76a). There are several large impurity particles in the center of the etched regions. While they are quite evenly distributed on the front side of the sample (marked with teal arrows) only one of these particles could be identified on the backside. The exclusive formation of these etched areas around large impurity particles shows the inertness of the grown graphene layer against collisions from the gas phase. Oxygen molecules present in the gas phase need bare Cu surface or defects in the graphene layer to stick to the

surface. The evolution of aligned hexagonal holes is the main type of graphene decay that can be identified. Smaller contamination particles can be found inside several of the small hexagonal holes, which most probably are formed according to the process described in Fig. 73 and subsequently increase the sticking of oxygen from the gas phase, accelerating the hole size evolution.

The symmetry of the etched graphene areas on both sides of the Cu foil shows that the diffusion of oxygen on the sample does not only happen on the surface of the metal foil, but also bulk diffusion through the metal volume is present. If the continuous graphene film is once disrupted, then the arriving oxygen will also form holes on the opposite side of the sample after oxygen bulk diffusion. The comparable sizes of the etching front on which the small hexagonal holes are found (20-30 μm) and the foil thickness (25 μm) are consistent with this picture that a volume process must be responsible for the formation of the hexagonal holes.

Noticeably, the oxygen does not equally affect SLG and Multi-LG, as thicker graphene islands remain intact for a longer time while the first layer is already decayed, as observed in the SEM images of Fig. 75.

8.2. Influence of oxygen impurities in the CVD-atmosphere

After discussion of the effect of oxygen on grown graphene samples, I want to discuss the influence of oxygen impurities in the CVD *hydrogen + methane* atmosphere on the grown graphene samples. The pure $H_2 + CH_4$ mixture is expected to induce a decay of graphene flakes if the mass action constant of the reactive gas atmosphere is increased above the equilibrium concentration ($Q_{exp} > K_{eq}$) or if the methane flux is stopped completely ($Q_{exp} = \infty$). If the reactive $H_2 + CH_4$ atmosphere contains an O_2 impurity, graphene decay may be induced by an unbalanced mass action constant or by oxygen-induced etching, depending on the O_2 impurity contamination. The separation of both effects is the topic of this section.

In literature, the hexagonal hole evolution was ascribed to the decay of graphene in a methane-deficient reaction atmosphere, showing similar results as the experiments described before in a pure $Ar + O_2$ gas phase. As estimated in section 2.4, the maximum oxygen coverage present on the Cu foil during CVD in the used reactor setup under typical reaction conditions (20 mbar, 1050 °C) should be $\vartheta_O \approx 10^{-8} ML$ within an O_2 partial pressure of $\approx 2 \times 10^{-5} mbar$.

The hexagonal shaped holes inside the graphene film can be used as an indicator for the increasing influence of oxygen during graphene growth. According to Choubak *et al.*,³²⁹ using an oxygen trap to achieve a clean gas atmosphere should completely inhibit the formation of these hexagonal holes.

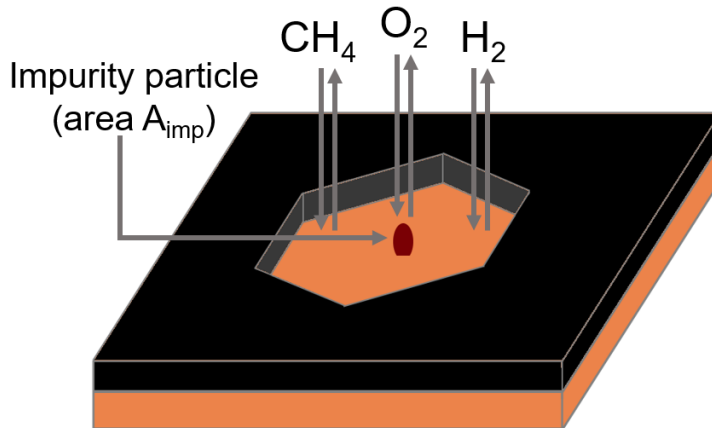


Figure 77 : Illustration of the influencing factors on the evolution of hexagonal holes in graphene layers. The size of the impurity particle determines the O_2 uptake at this position. The partial pressures of oxygen, hydrogen and methane influence the surface concentrations of each component and hence also the resulting hole size.

The sketched model of Fig. 77 displays the key processes of CVD growth in an O_2 contaminated atmosphere. In order to include the findings of the last chapter, the model considers a hexagonal hole in the graphene film with an impurity particle in its center. Due to the inertness of the graphene film and neglecting bulk diffusion, the hole represents an isolated catalyst surface enclosed by an inactive surrounding.

Oxygen is provided by the increased sticking coefficient on the impurity particle (approximated as $S = 1$) and dissociative adsorption on the bare Cu surface, and carbon is provided by CH_4 decomposition on the bare Cu surface with the known sticking coefficient used in different publications.^{163,126} Assuming the adsorbed hydrogen to be in equilibrium with the gas phase, the coverage of about 10^{-3} ML (under typical reaction conditions, see chapter 2.4) leads to a reduction of impinging oxygen before it can reach and oxidize the flake rim. In this case, the oxygen impurity of the CVD atmosphere is expected not to influence the reaction at all, i. e. the postulated carbon removal would be restricted to the impurity particle itself. This expectation is in accordance to the observation of an intact graphene film with defects in the close vicinity of impurity particles (see chapter 9.1). If, on the other hand, the O_2 influence of the impurity during CVD is increased, the hole size should increase. In the following, experiments are conducted, that determine the impact of the factors:

- Increased oxygen partial pressure
- Increased impurity content of the Cu foil in the bulk by high pressure pretreatment (see chapter 9.1)

- Increased mass action constant $Q_{exp} = 150 \gg K_{eq}(1045\text{ }^\circ\text{C}) = 101$ (reduction of the methane partial pressure)
- Closing methane valve after growth ($Q_{exp} = \infty$)

Having conducted the respective experiment, the samples were removed from the reactor and the formation of holes in the graphene film was analyzed by optical microscopy, assuming that the formed holes were not altered during the sample cooling. The respective optical images of the samples are shown in Fig. 63.

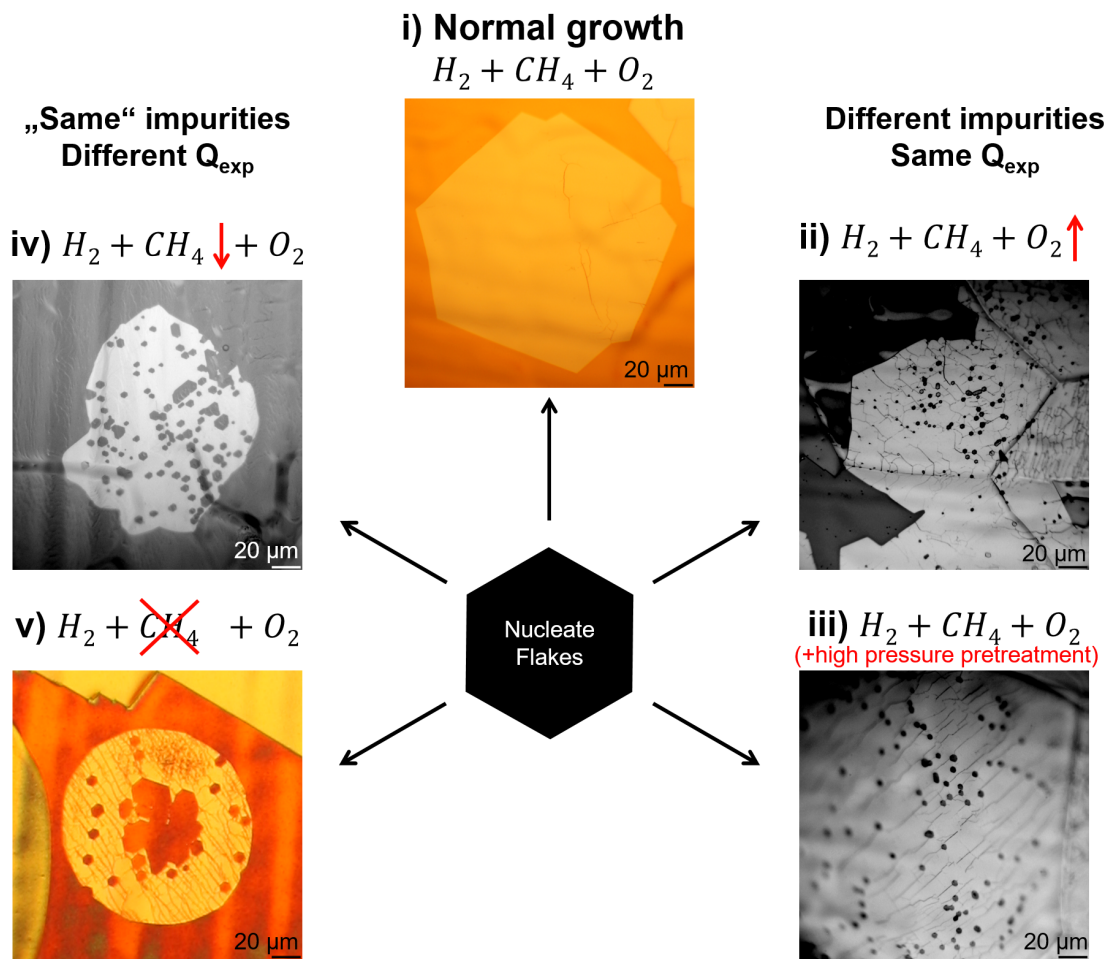


Figure 78 : Factors influencing the hole formation during CVD growth of graphene flakes. i) Optical image of a graphene flake with the shape of a regular hexagon as grown under typical CVD conditions. ii) and iii) Formation of hexagonal holes inside the graphene flake, induced by an elevated oxygen background pressure or increased impurity content in the substrate foil through a high-pressure hydrogen pretreatment (see chapter 9.1). The observed holes have narrow size distribution, peaking at few μm . Sample ii) contained an oxygen impurity of $\approx 40\text{ ppm}$, compared to an intrinsic oxygen impurity content of $\approx 1\text{ ppm}$ in the other cases. iv) and v) Applying CVD parameters far from equilibrium in the graphene instability region by lowering (iv) or stopping (v) the methane partial pressure also leads to the formation of hexagonal-shaped holes. However, also a flake shape change towards rounded flakes is observed. (Experimental details: i) E. 60 , ii) E. 61 , iii) E. 62 , iv) E. 56 , v) E. 63)

At first, a control experiment was conducted at $Q_{exp} = 56$, $1045\text{ }^\circ\text{C}$ without the intentional addition of further oxygen or other impurities to the sample. The resulting flake is shown in Fig. 63i) with straight graphene edges and no holes in the graphene flake. When keeping the resulting reactive atmosphere but adding oxygen to the gas mixture ($p(O_2) = 8 \times 10^{-4}\text{ mbar}$), hexagonal holes appear in the flakes, as shown in Fig. 63 ii). The filling of the Cu foil with silicon-based impurities (see chapter 9.1) leads to a similar result with hexagonal holes (Fig. 63iii).

The increase of the Q_{exp} -value to 170 or even the complete shutting of the methane feed also lead to the formation of such holes (Fig. 63iv and 63v), combined with the change of the overall flake shape to a rounded form. This shape change of the outer rim is not observed for purely oxygen-influenced samples and appears exclusively in combination with graphene decay at conditions above K_{eq} .

The shown experiments indicate that the parameter correlation is in accordance with the expectation of the model shown in Fig. 77:

- No hexagonal holes appear under typical growth conditions of the used reactor in a reactive atmosphere with an oxygen concentration $\leq 1\text{ ppm}$
- Increasing the oxygen partial pressure favors the hole formation
- Increasing the amount of impurity-particles favors the hole formation
- Applying reaction conditions far from K_{eq} in the graphene instability region in an O_2 contaminated atmosphere favors the hole formation in connection with a rounding of the overall graphene flake shape.

An increase in the oxygen (ii) or impurity content (iii) increases the effective oxygen flow into the defective Cu foil area and leads to the formation of optically visible holes. Also, lowering the carbon supply by reducing or total cancellation of the methane flow leads to the formation of larger holes.

The observation of hexagonal holes in graphene films is attributed to the increasing influence of oxygen and further impurities on the sample. However, the outer shape change of graphene flakes (rounding of flakes) is not caused by oxygen but by the decay in $CH_4 + H_2$.

9. Contaminations influencing the CVD growth of graphene and the characteristics of grown graphene samples

9.1. Silicon contaminations

A relevant source of contaminations during graphene growth by CVD on copper is the appearance of silicon oxide particles on the samples. These particles were observed in a large number of literature studies, such as references ^{116,281,334,335,305,336}. Although SiO_x particles are mentioned in a large number of graphene-based publications and several groups have studied their appearance, the processes leading to SiO_x particle formation on Cu are still not fully understood.

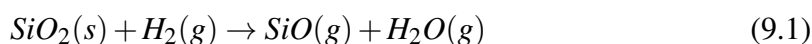
While in early studies appearing particles were not identified as SiO_x but rather referred to as "dust particles",¹¹⁶ characterization methods such as EDX and Auger electron spectroscopy (AES)³³⁷ resolved the main component to be silicon, which was confirmed in a multitude of publications by ICP-OES³³⁵ (Inductively Coupled Plasma - Optical Emission Spectrometry) and EDX.^{334,338,339}

Despite the unambiguous identification as silicon oxide particles, the origin of these contaminants is debated, as a large number of accumulation pathways for the silicon in the Cu substrate were described in literature. Several authors ascribed their origin to the inherent contaminations in the copper foil.^{335,36} However, this assignment can be excluded because Zhang *et al*²⁴⁵ and Lisi *et al*³³⁹ have shown that the shielding of the growth substrate from the outer silica reactor tubes prevents the formation of such particles. According to the manufacturers of the Cu foil (see chapter 3.1.4), the impurities present in the as bought Cu foil are less than 0.5 ppm. Assuming a Cu foil with 25 μm thickness to have approximately 10^5 atomic layers, this amounts to less than 5% of a single monolayer Si distributed over the whole Cu volume, which would also not be sufficient to explain the observed impurity particles. The silica must therefore be introduced into the copper growth substrate from the hot silica walls during the reaction.

According to Ruiz *et al*,³³⁴ the origin of these impurities may lie in the copper intercalation into the reactor tube's silica crystal structure and the subsequent "precipitation onto the sample", which is also assisted by Suzuki *et al*.²⁸⁸ Geng *et al*³³⁸ describe a direct deposition of SiO_x nanoparticles from the reactor wall in argon atmosphere without proposition of a reaction pathway, Gomez-Martinez *et al*³⁴⁰ also describe the evaporation and oxidation of silicon monoxide molecules by oxidation of a pure silicon wafer piece, though performing this reaction in a quartz tube without considering the quartz walls as

additional silicon source in the discussion. Ge *et al*³³⁶ describe the full reduction of silica from the reactor walls to atomic silicon, which is then evaporated from the reactor walls, oxidized in the atmosphere after changing to oxidative conditions and subsequently deposited on the Cu sample substrate.

While all these recent studies from the last 10 years deliver strongly diverging explanations for the appearance of silicon-based impurities related to the specific case of impurities on the graphene growth substrate, there also exist older studies by Tso and Pask^{341, 342} from 1982, who examined the reaction of fused silica and silicate glasses with hydrogen gas. At temperatures of ≈ 1400 °C in a hydrogen atmosphere, fused silica shows a mass loss of about 10 mg per hour per cm^2 , which was shown to be activated with an activation energy of 343 kJ mol^{-1} for the following reaction:



Using these results, the etching rate of fused silica from the reactor walls can be estimated at common CVD graphene growth conditions of $T = 1050$ °C and $p(\text{H}_2) = 300$ mbar. Extrapolation from 1400 °C and atmospheric hydrogen pressure using the stated activation energy leads to an etching rate of $\approx 0.01 \text{ mg (cm}^2\text{h)}^{-1}$, resulting in an etching rate of $\approx 3 \times 10^{-3} \text{ mg (cm}^2\text{h)}^{-1}$ at 300 mbar. Assuming an inner quartz tube piece of 5 cm length ($\varnothing = 15$ mm) to be equally tempered, this leads to a surface area of 24 cm^2 and an etching rate of $\approx 0.08 \text{ mg h}^{-1} = 1.3 \times 10^{-6} \text{ mol h}^{-1}$. With the common Cu surfaces of the samples used as reference ($\approx 1.2 \times 5$ cm size with front- and backside, $\approx 10 \text{ cm}^2$ total area), this would relate to approximately 40 ML per hour of silicon removed from the quartz tube, being more than enough to explain the quantities of silicon observed in several studies referred to above, even if only a fraction of the decomposed silicon is deposited on the Cu sample. At 950 °C, this amount is lowered to 2.5 ML/h at 300 mbar. At common CVD reaction conditions with 10-20 mbar H_2 , this roughly amounts to the quantity of Si-based impurities already present in the Cu substrate from the fabrication process.

The hypothesis of silicon monoxide being the volatile species transporting silicon from the reactor walls to the copper sample is backed up by the vapor pressures of the silicon-containing species at the reaction temperatures. The equilibrium vapor pressure of SiO above a mixture of silicon and fused silica is 10^{-2} mbar at 1050 °C,³⁴³ while the vapor pressure of pure silicon ranges between $10^{-8} - 10^{-6}$ mbar.³⁴⁴ SiO_2 is reported to decompose only by comproportionation of SiO_2 with Si or decomposition of SiO_2 emitting molecular oxygen and the above mentioned, volatile SiO species.³⁴⁵

Several literature studies characterize silicon oxide species by means of Raman spectroscopy and photoelectron spectroscopy. Crystalline SiO_2 structures, such as Cristobalite, show sharp Raman signals with highest intensity at 23 cm^{-1} , 420 cm^{-1} , 787 cm^{-1}

Table 21 : Several literature references for elementary silicon and different silicon oxide signals as detected by photoelectron spectroscopy.

Si 2p signal assignment				
Reference	Si	SiO	Si ₂ O ₃	SiO ₂
Nguyen 1989 ³⁴⁸	99.8	101.6	102.4	103.2
Anwar 1990 ³⁴⁹	-	101.8	-	-
Alfonsetti 1993+1994 ^{350,351}	99.8	101.9-102.2	102.7	103.8
Yamamoto 1995 ³⁵²	99.5	-	-	103.5
Grunthaner 1979 ³⁵³	-	101.8	103.1	-
NIST data base ²¹⁶				103.0-104.1
Used fit parameters	99.5-99.8	101.6-102.0	102.7-103.1	>103.5

and 1080 cm^{-1} ,³⁴⁶ while suboxides like *SiO* and *Si₂O₃* show signals at 444 cm^{-1} and 502 cm^{-1} .³⁴⁷

Literature data differ when trying to relate the oxidation number of silicon to the XPS binding energy of Si 2p. While the signal of pure silicon is assigned to the signal at 99.5-99.8 eV, signals between 103.0-104.1 eV are assigned to the fully oxidized *SiO₂* species. Table 21 shows a list of literature references for silicon with several oxidation numbers between 0 and IV. The values in the last line are used as fitting parameters for the respective species unless otherwise noted. The full width at half maximum (FWHM) of the signals is set to 1.4 eV according to Nguyen *et al.*³⁴⁸

9.1.1. Experimental procedure to determine the influence of silicon on Cu substrate surfaces:

To verify which reaction mechanism enriches the substrate foil with silicon contaminations, a reaction was performed according to Table 22 with two samples, of which sample a) was exposed to a high pressure hydrogen atmosphere of 300 mbar, while the second sample b) was not. After the reaction and cooling in identical, oxidizing conditions, the sample was analyzed using photoelectron spectroscopy. The respective Si 2p spectra are shown in Fig. 79. While the sample with high-pressure hydrogen treatment shows a clear silicon signal, the one of the purely oxidatively treated sample is at the detection limit of the spectrometer. The fitted signal components show a high amount of silicon between the oxidation numbers +II (*SiO*) and +III (*Si₂O₃*), the contamination is therefore not completely oxidized on the sample surface. Assuming, as has been shown in most literature references, that the silicon oxide contamination agglomerates to form particles of few nm diameter, the XPS signal contribution can be calculated in a simplified way assuming the complete separation between copper and silicon on the surface and no lateral inhomogeneities (see model *b* presented in Fig. 20 in the methods section 3.3.4).

Table 22 : Experimental reaction conditions for two Cu samples without graphene growth, but with either pure oxidative pretreatment (sample b) or the oxidative pretreatment followed by a high-pressure hydrogen- and subsequently an oxidative-treatment (sample a). (Experimental details: E. 64 + E. 65)

#	$T = 1050^{\circ}\text{C}$	Conditions	Sample a)	Sample b)
i)	Pretreatment	200 min, 1 mbar Ar, 10^{-3} mbar O_2	Yes	Yes
ii)	Hydrogen exposure	90 min, 300 mbar H_2	Yes	No
iii)	Re-oxidation	90 min, 1 mbar Ar, 10^{-3} mbar O_2	Yes	(Same as i)
XPS Si coverage (from Si 2p/Cu 3p signal ratio)			8%	< 1%

The ratio between the Si 2p and Cu 3p signal leads to a surface coverage of 8% SiO_x particles, using the molecular mass and density of SiO and the inelastic mean free path of the released Si 2p photoelectron from SiO_2 . For sample b), treated purely in oxidative atmosphere without the exposure to H_2 , the area coverage is $\leq 1\%$, but above the detection limit of the setup.

The sample described above shows very clearly that the silicon contamination in the

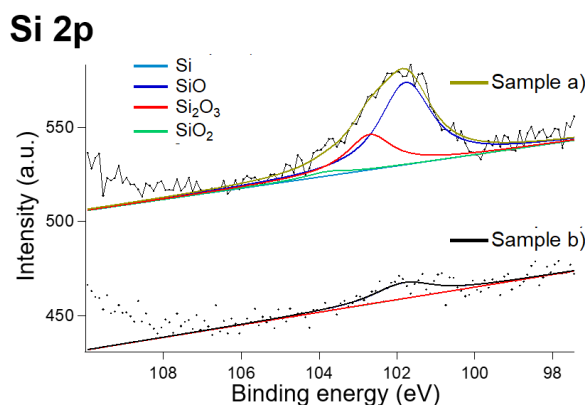


Figure 79 : XPS spectra to the samples described in Table 22. While sample a) shows a strong silicon suboxide signal, the signal of sample b) is present, but almost at the detection limit.

copper sample can be a major issue for the defined growth of graphene layers, covering almost 10% of the sample surface in this experiment. While the origin of the contamination from the reactor wall was already sufficiently proven in literature by shielding of the sample from the reactor walls, this experiment shows that the material transport process requires a high pressure hydrogen treatment to accumulate silicon in the copper substrate, completely agreeing with the results presented by Tso and Pask.^{341,342} In this experiment, a pressure of 300 mbar H_2 was used to accelerate this accumulation process. Common growth reaction protocols at lower pressures would nevertheless as well introduce silicon into the copper sample during the course of the graphene growth reaction.

The silicon detected in sample b) might be attributed to the contaminations inherently present in the copper foils. The estimation of 5% monolayers of impurities present in the sample would decrease upon agglomeration to a signal in the order of magnitude observed in b). While this amount does not play a crucial role for the overall graphene quality of the sample, this amount may already be enough to significantly influence the nucleation behavior, since small impurity clusters may act as nucleation centers during graphene growth.

Unknown is the exact distribution of the silicon in the sample and its response upon exposure to oxidative or reductive atmospheres. In the calculations above, the silicon oxide particles were assumed to form on the sample surface, as this was described in the literature sources listed above. A video recorded by Wang *et al*³⁶ during heating of a copper foil in an environmental scanning electron microscope apparatus shows the formation of such silicon particles in an atmosphere containing an increased oxygen partial pressure. These particles diffuse on the substrate surface, but are not observed to vanish into the Cu bulk.

9.1.2. Silicon reaction after accumulation in the Cu substrate:

A set of experiments was performed to clarify the response of silicon oxide particles on the substrate surface upon exposure to oxidative or reductive atmosphere. Copper foils were at first cleaned from carbon impurities by an oxidative pretreatment, followed by the enrichment with silicon in a high pressure hydrogen atmosphere. The growth conditions are listed in Table 23. After the Si filling of the copper foil, the samples were exposed to different partial pressures of oxygen in argon carrier gas. Sample c) was exposed to low (10^{-5} mbar) oxygen partial pressure and sample d) was exposed to a high partial pressure of 10^{-3} mbar. In both cases one sample (marked c1 and d1, respectively) was removed from the hot reactor zone after one hour of oxidative treatment. A second sample in each reactor run was subsequently treated in a reductive atmosphere with 300 mbar hydrogen for further 60 min and then removed from the reactor (marked c2 and d2, respectively). The experimental results are summarized in Table 24 and in more detail discussed in the following section.

Samples c1) and d1)

The samples exposed to high-pressure hydrogen followed by an oxidative treatment show large amounts of silicon oxide on the sample surface. SEM images of sample c1) (Fig. 80) show particles of up to 2 μm size and approximately 10^5 particles per mm^2 . The EDX spectra (Tab. 25) recorded on the marked spots in the SEM images prove the silicon oxide nature of these particles. A second feature can be determined in the SEM images in form of round patterns, which show an increased carbon content in the EDX spectrum. The sample d1) treated with a higher oxygen partial pressure leads to round structures of up to 20 μm size, as imaged by SEM (Fig. 81). These particles show similar features as

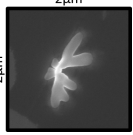
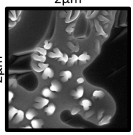
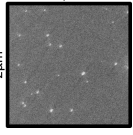
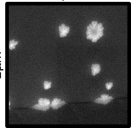
Table 23 : Experimental reaction recipes for four samples with increased silicon content, where the Si was dragged to the surface by different oxygen partial pressures and subsequently removed by a second high-pressure hydrogen treatment. (Experimental details: E. 66 + E. 67)

#	$T = 1050^{\circ}C$	Conditions	Sample c)	Sample d)
i)	Pretreatment	80 min, 1 mbar Ar, 10^{-5} mbar O_2	Yes	Yes
ii)	Hydrogen exposure	60 min, 300 mbar H_2	Yes	Yes
iii)	Re-oxidation	60 min, Ar/ O_2 atmosphere	$p(O_2) = 10^{-5}$ mbar → remove sample c1)	$p(O_2) = 10^{-3}$ mbar → remove sample d1)
iv)	Reduction	60 min, 300 mbar H_2	Yes → remove sample c2)	Yes → remove sample d2)

the ones in sample c1) and might be agglomerates of these smaller particles. None of these structures show a distinct Raman signature. XPS spectra of both samples (Fig. 82) show that the silicon quantity is significantly higher for sample d1) regardless of the agglomeration effect. Assuming thick silicon oxide particles, the quantification of the Si 2p signal with regard to the Cu 3p signal leads to a surface coverage of 7% (sample c1) and 22% (sample d2). The oxidation state of the silicon also changes for sample d1). With an increase in the oxygen dosing the amount of fully oxidized SiO_2 is the most abundant oxidation state of the silicon.

The differences between both samples show that the silicon surface content does not saturate after 60 min treatment in 10^{-5} mbar O_2 . As the complete silicon is assumed to accumulate in the copper bulk during the high-pressure H_2 treatment (which is equal for both samples), there must still be a significant amount of Si in the bulk of sample c1).

Table 24 : Summary of the results from characterizational methods of experiments c) and d) presented in Table 23 regarding the observation of Si impurities on the sample surface (Yes) or their absence (No).

#	Method	Si detected?	
		Sample c)	Sample d)
Samples 1) removed after the oxidation step iii	XPS	7% (Fig. 82)	22% (Fig. 82)
	SEM	Yes (Fig. 80)	Yes (Fig. 81)
			
	EDX	Yes (Tab. 25)	-
	Raman	No	No
Samples 2) removed after the subsequent reduction step iv	XPS	No (Fig. 85)	≤ 1% (Fig. 85)
	SEM	Yes (Fig. 83)	Yes (Fig. 84)
			
	EDX	No (Tab. 26)	-
	Raman	-	-

Sample c1)

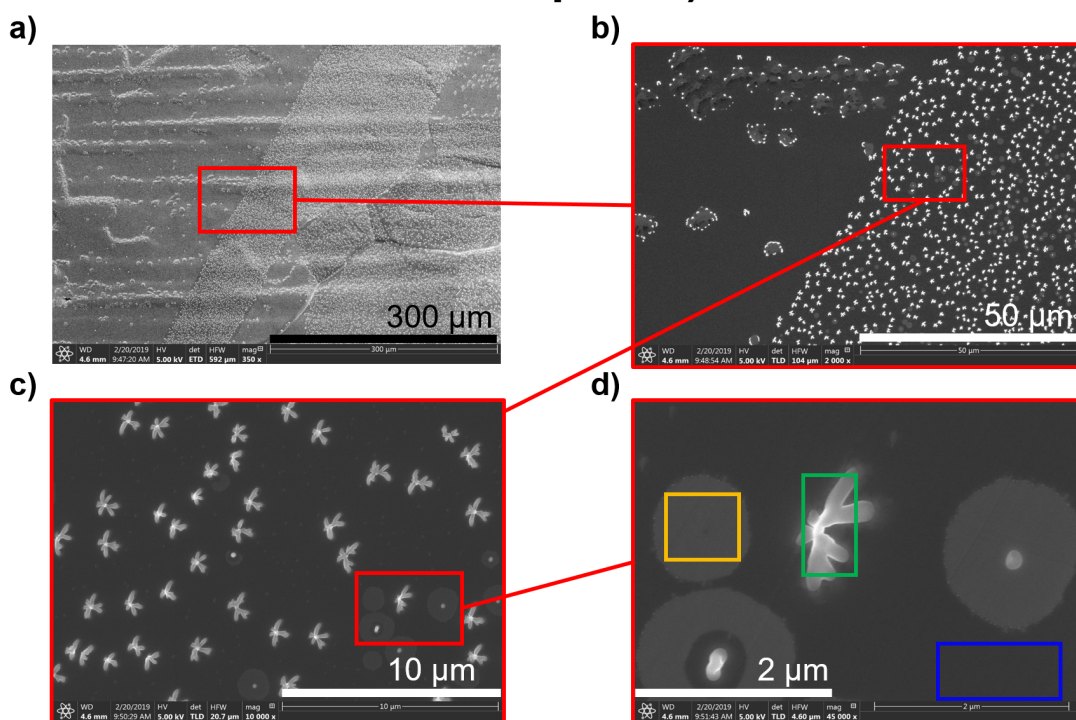


Figure 80 : SEM images of sample c1) exposed to a lower oxygen partial pressure in different magnifications. The colored squares in d) show the areas of EDX measurement for bare Cu (blue), silicon particles (green) and circular features (yellow).

Table 25 : EDX elemental analysis from the areas of sample c1) shown in Fig. 80. While the blue and green areas coincide with the expected pure Cu and silicon oxide contents, the feature found in the yellow area seems to originate from an increased carbon content in this area.

Sample c1)

Element	Area ■	Area ■	Area ■
C	23%	12%	13%
O	-	12%	-
Si	-	7%	-
Cu	77%	69%	87%

Sample d1)

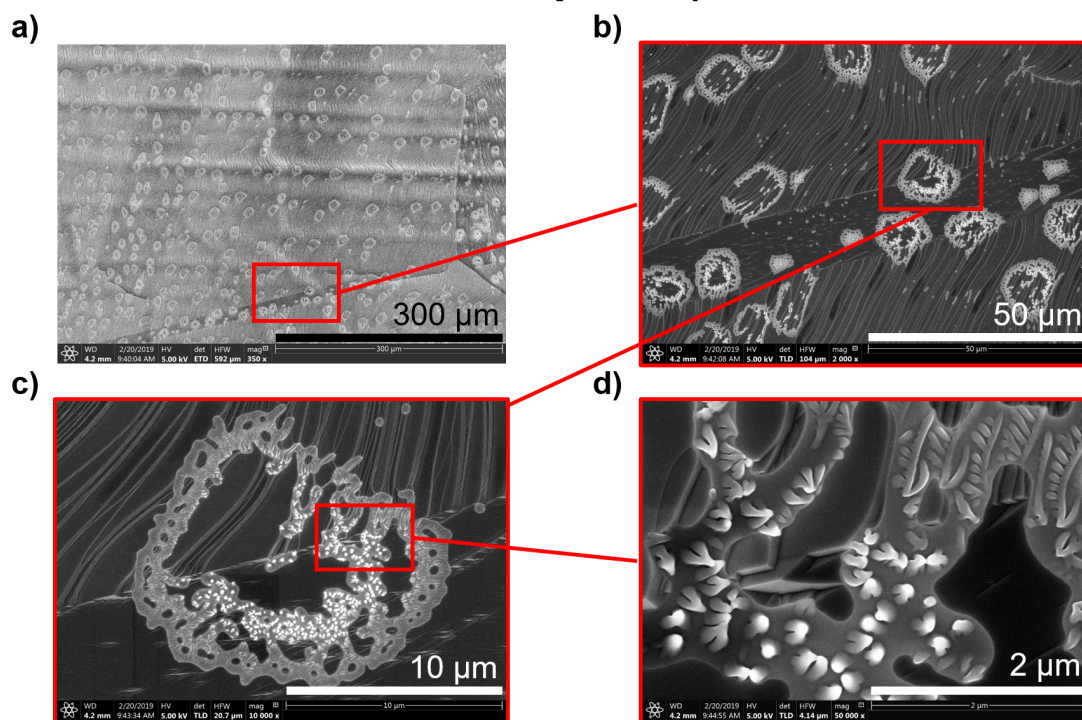


Figure 81 : SEM images of sample d1) exposed to a higher oxygen partial pressure in different magnifications.

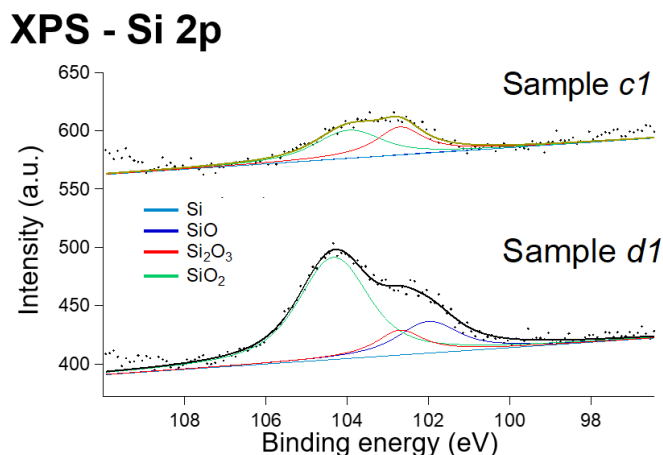


Figure 82 : Characterization of samples c1) and d1) by XPS. The observations regarding the quantity of silicon particles formed on the sample surface are in agreement with the acquired XPS data. A significantly larger amount of silicon oxide at higher binding energies is found on sample d1). The position of the highest signal even shows a slight charging of the micron-sized silicon particles (see SEM images in Fig. 81), as the peak is found above the maximum possible oxidation state of Si(IV).

Samples c2) and d2)

After subsequent exposure of the second half of these samples (*c2* and *d2*) to the reductive hydrogen atmosphere, the surface constitution shows strong modifications. In sample *c2*) the silicon oxide particles on the sample surface decay almost completely (Fig. 83). Very small particles of ≈ 50 nm diameter remain on the surface in a high abundance of $\approx 10^6$ particles per mm^2 . These cannot be characterized neither by EDX (Tab. 26) nor by XPS (Fig. 85).

Sample *d2*) also shows a significant reduction in the amount of silicon found on the sample surface. The former Si particles of up to 20 μm diameter transform into a higher number ($\approx 10^6$ $1/\text{mm}^2$) of small particles with diameters of up to 200 nm (Fig. 84). The XPS signal is strongly decreased (Fig. 85), but does not vanish completely as in sample *c*).

Both samples show a strong reduction of the silicon content upon exposure to hydrogen conditions. As it was shown that these conditions accumulate silicon in the Cu bulk, the silicon must dissolve in the Cu foil during this reductive treatment. Nevertheless, a certain fraction of the particles remains on the surface in both cases. The outlasting of these particles must be caused by one or more of the following processes:

- Silicon oxide particles decompose very slowly by reduction through the reaction with adsorbed hydrogen H_{ad} . Even the high H_2 pressure treatment for one hour is not enough to completely reduce these particles.

- Crystallized silicon dioxide particles with stable crystal structure may not be affected by adsorbed hydrogen on the Cu surface and therefore remain as stable residues of the former particles mainly composed of a silicon suboxide SiO_x
- Silicon oxide particles might nucleate at impurities composed of other elements that stabilize the SiO_x particles, inhibiting the H_2 induced decomposition and dissolution. In such a case potential impurities are below the EDX detection limit.

The experiments described above allow observing the precise reaction of the silicon species in the sample with different gases commonly used for the synthesis of graphene by CVD. This reaction of the silicon contamination (sketched in Fig. 86) on the exposure to oxidative atmospheres (dragging to the surface as SiO_x with $x = 1 - 2$) and reducing atmospheres (accumulation of SiO from the reactor walls, dissolution of surface oxides in the Cu bulk as SiO_y with $0 \geq y < x$) greatly allows to increase the control over this contamination during the growth reaction of graphene. The following conclusions can be drawn:

- I A reducing hydrogen atmosphere at high temperatures $\geq 1050^\circ C$ leads to the accumulation of silicon in the Cu substrate bulk. This also applies for CVD conditions of graphene growth in a $CH_4 + H_2$ atmosphere.
- II The silicon species dissolved in the substrate bulk are dragged to the sample surface upon exposure to an oxidative atmosphere.
- III Oxidative treatment at the beginning of the reaction process according to the reaction recipe presented in section 3.2 has only a small impact regarding the silicon impurity, as no high-temperature hydrogen treatment is performed beforehand.

As soon as the two conditions I and II are executed in this order during synthesis, the formation of silicon oxide particles on the copper surface is expected. If single layer graphene with the highest amount of purity is the aim of the reaction, it is crucial to omit an oxidative treatment after high-temperature hydrogen conditions. On the other hand, it is possible to specifically introduce impurity particles onto the growth substrate, which can lead to defined growth of multilayer graphene, as repeatedly stated in literature.^{335,288,308}

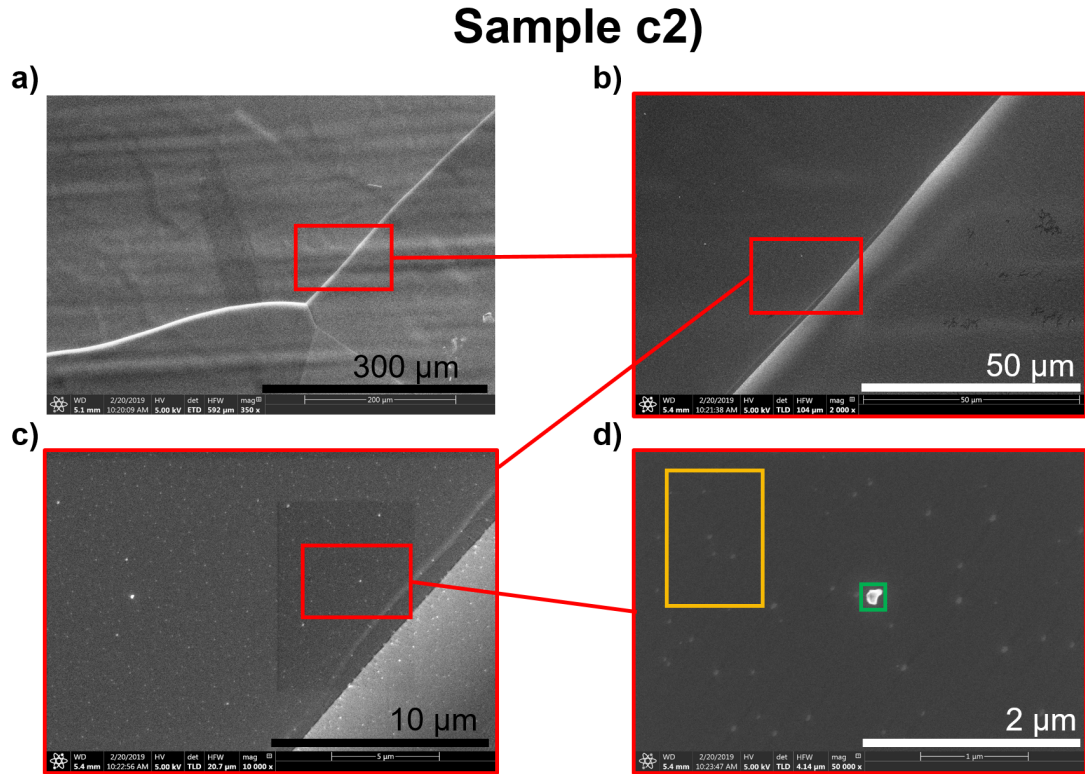


Figure 83 : SEM images of sample c2) exposed to a lower oxygen partial pressure and subsequently reduced in a high-pressure hydrogen atmosphere. While low-magnification images suggest a uniform Cu surface, higher magnification allows the identification of small particles in the size regime of few tens of *nm* up to ≈ 100 *nm*. EDX spectra are acquired at the larger particle in d) (green square) and over a larger surface region (yellow rectangle).

Table 26 : EDX elemental ratios of the areas shown in Fig. 83. No silicon content can be identified, only an increased carbon signal is found between the larger and smaller particle areas. Due to the large difference in measured area, the carbon content may also be caused by different impurity deposition during measurement.

Sample c2)

Element	Area ■	Area ■
C	11%	24%
O	-	-
Si	-	-
Cu	89%	76%

Sample d2)

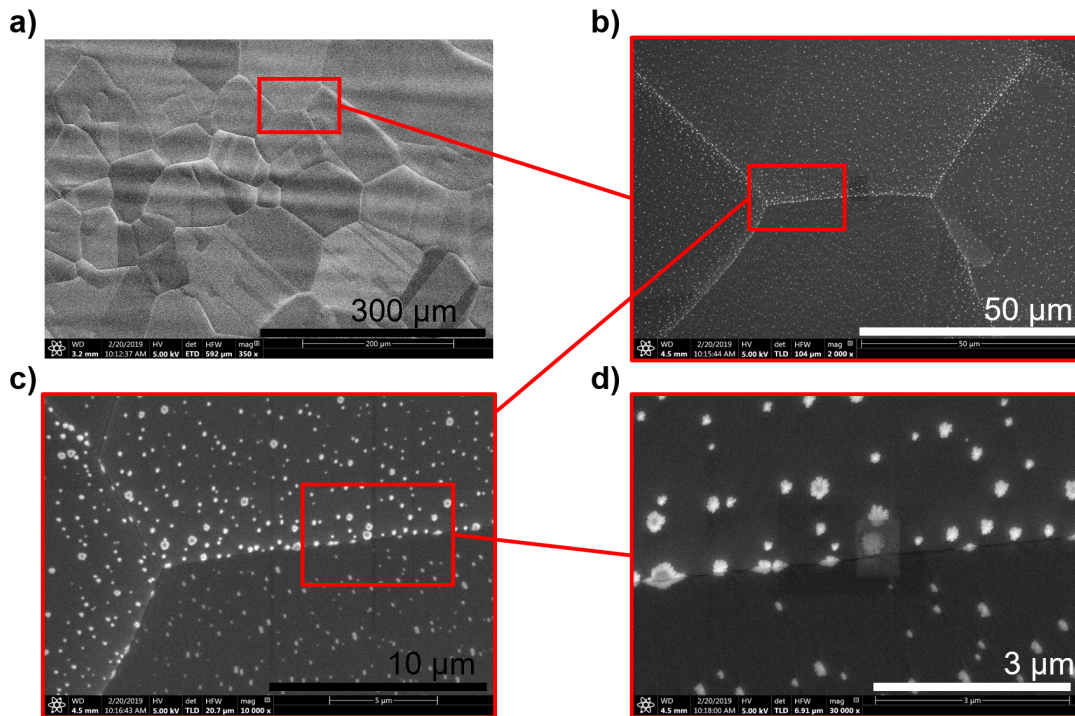


Figure 84 : SEM images of sample d2) exposed to a higher oxygen partial pressure and subsequently reduced in an high-pressure hydrogen atmosphere. Contrary to sample c2), here the remaining particles are significantly larger up to some 100 nm in size and still show the particular shape observed for silicon oxide particles.

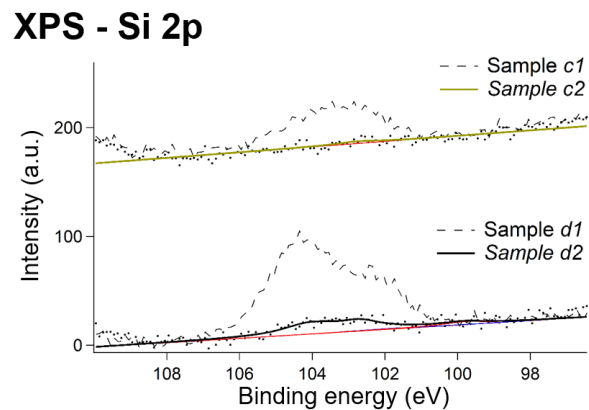


Figure 85 : Characterization of samples c2) and d2) by XPS after high-pressure hydrogen treatment. XPS spectra before hydrogen treatment (c1 and d1) are inserted as dashed lines. While in sample c2) the silicon is below the detection limit, a small residual signal in sample d2) shows the incomplete removal of silicon from the surface.

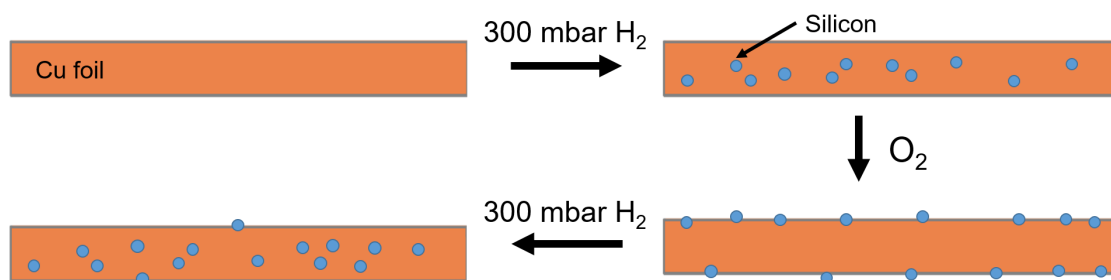


Figure 86 : Modification of the silicon impurities accumulated in the Cu foil upon exposure to reductive hydrogen atmosphere and oxidative oxygen atmosphere at 1045 °C. Hydrogen accumulates Silicon in the Cu bulk, oxygen drags this silicon to the surface forming silicon oxide particles. Repeating the hydrogen treatment again dissolves most of the SiO_x in the bulk, while the total amount of accumulated Si in the Cu bulk increases.

In chapter 8, the decomposition reaction of graphene by the addition of oxygen to the gas phase is described (Figs. 72 and 75). The decomposition of the graphene layer is observed to originate from specific impurity particles formed on the Cu surface, showing exactly the same characteristics as the particles observed in this chapter. After the full decomposition of graphene flakes (Fig. 72d), an imprint on the Cu surface remains, marking the former position of the graphene flake, which is also composed of the inhomogeneously formed silicon oxide particles during the etching process. In all these cases, the silicon was introduced into the Cu foil during graphene growth and subsequently the formation of silicon particles was enabled by introducing oxygen into the reactive system.

Similarly, an analysis of CVD literature studies reporting the formation of silicon oxide particles shows that all studies providing sufficient information on their growth procedure list the successive exposure of the sample to a hydrogen atmosphere and subsequently the (unintentional in most cases) exposure to oxygen impurities. These are mostly expected to be introduced as contaminations in the used Ar carrier gas, which in most cases is used at a high flow rate. The effect of oxygen contaminations increases during the cooling process of the sample. Due to the much lower activation energy of the dissociative sticking of oxygen ($E_{ads} = 0.1 - 0.2 \text{ eV}$) compared to hydrogen ($E_{ads} = 0.6 \text{ eV}$) O_{ad} accumulates on the surface when cooling down the sample because hydrogen does not dissociatively stick on the Cu foil anymore to react off the oxygen impurity. Table 27 lists the literature references and my interpretation to what might have caused the formation of silicon oxide particles on the respective sample surface.

Table 27 : Literature references where the formation of silicon particles was described and/or observed in the published data. All samples were in the course of the described experiments exposed to H_2 atmosphere. The addition of O_2 after/during synthesis is often not stated directly but can be assumed from the used reaction conditions, as noted in the third table column.

Source	Si particles observed?	Previous H_2 atmosphere?	O_2 added after synthesis?
Han 2011 ²⁸¹	Yes	Yes	1000 sccm Ar during sample growth and cooling
Vlassioug 2011 ¹¹⁶	Yes	Yes	500 sccm Ar during sample growth and cooling
Kim 2013 ³³⁷	Yes	Yes	Growth and cooling in only 0.2-0.4 mbar H_2 increases effect of reactor leak
Ruiz 2014 ³³⁴	Yes	Yes	No information
Suzuki 2014 ²⁸⁸	Yes	Yes	500 and 1000 sccm Ar during sample growth and cooling
Kasap 2015 ³³⁵	Yes	Yes	200 sccm Ar without H_2 during sample cooling
Chaitoglu 2016 ³⁰⁵	Yes	Yes	Cooling in vacuum without H_2
Geng 2016 ³³⁸	Yes	Yes	Intentional formation in 1500 sccm Ar
Gomez-Martinet 2016 ³⁴⁰	Yes	Yes	Intentional formation in 600 sccm Ar
Li 2016 ³⁰⁸	Yes	Yes	180 sccm Ar during sample growth and cooling
Yasunishi 2016 ³⁵⁴	Yes	Yes	145 sccm Ar during sample growth and cooling
Zhang 2016 ²⁴⁵	Yes	Yes	1000 sccm Ar during sample growth and cooling
Lisi 2017 ³³⁹	Yes	Yes	750 sccm Ar during sample cooling
Ge 2018 ³³⁶	Yes	Yes	1000 sccm Ar during sample growth and cooling

9.1.3. Interaction of silicon contaminations with graphene

In order to test the influence of the silicon oxide particles on the graphene flakes, graphene was grown on Si contaminated samples and, vice versa, Si contaminations were tried to segregate to the surface of graphene covered samples.

Graphene growth on samples with silicon oxide particles

Graphene was grown on the sample on a Cu substrate after the accumulation of Si contaminations in the Cu foil and their dragging to the surface by exposure to oxygen gas, as described in Table 22 (Sample a). After growth of a complete graphene film, the sample was removed from the reactor and characterized by Raman microscopy, SEM and EDX. Raman and SEM data are shown in Fig. 87.

The sample still shows a large number of Si particles after graphene growth. Observable are agglomerated particles merged to a large compound, as shown in Fig. 87a) and single distributed particles as shown in Fig. 87c). The larger Si compounds show an intense Raman signal which can be attributed to cristoballite (see Fig. 87b). A small D-band can be identified, which is not present in the graphene spectrum acquired slightly beside the particles, i. e. the graphene film contains defects only in their closest vicinity. EDX measurements also confirm the SiO_x composition of the particles. The scanning electron microscopy images and the Raman spectra locally acquired around the particles show that these SiO_x particles are found in the center of multilayer graphene islands. This indicates that the particles most likely act as nucleation centers for few-layer islands in the graphene film. The respective fits of the Raman spectra are shown in Fig. 87f), where at least four-layer graphene can be identified. The presence of Si particles prior to graphene growth significantly increases the multilayer fraction on the sample. At these growth conditions ($w = 1000, p(H_2) = 20 \text{ mbar}$) typically less than 5% of the surface are covered with multilayer graphene. The presence of Si particles increases this value to roughly 40%.

Graphene growth on Cu surface with Si particles

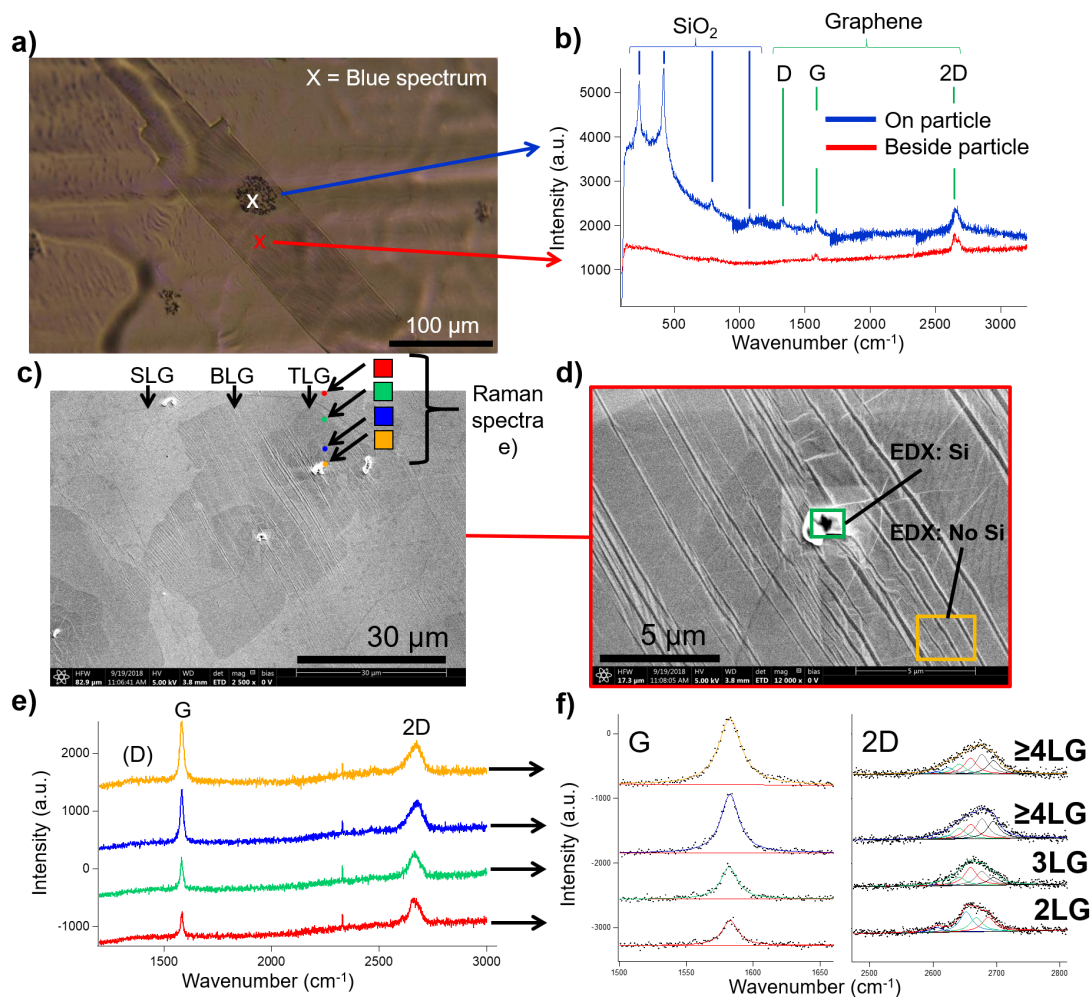


Figure 87 : Graphene growth on silicon-rich sample surfaces. a) Optical image of a graphene covered Cu surface with an agglomeration of silicon oxide particles. Crosses mark the positions of Raman-spectra measurements shown in b). While beside the particle only the characteristic graphene signals can be identified, additional signals at low wavenumbers appear on the particles. These signals belong to cristobalite, a high-temperature modification of silicon dioxide.³⁴⁶ The D-band is detected on the silicon oxide particle but not in its vicinity, indicating defects in the graphene film exclusively in the closest vicinity to the SiO_x -particles. c-d) SEM images of the same sample identifying silicon oxide particles in the center of graphene flakes as nucleation seeds. EDX measurement performed at the colored rectangles in d) approves the silicon oxide nature of the bright particle. Raman spectra acquired in the vicinity of the nucleation seed at positions of changing contrast are shown in e) and f). Fits to these spectra approve the increasing layer number around the silicon oxide particle, indicating that the nucleation of multilayers is facilitated at these specific nucleation points. (Raman spectra measured at a wavelength of 633 nm) (Experimental details: E. 59)

Dragging of silicon to the sample surface after graphene growth

Graphene can also be grown on a Si filled Cu foil before dragging the Si contamination to the surface by the following treatment:

- i High pressure hydrogen treatment (Si accumulation in Cu bulk)
- ii $H_2 + CH_4$ treatment (graphene growth)
- iii $Ar + O_2$ treatment (Si pulling to the surface)

In this case, the silicon particles are not formed prior to the graphene growth but are dragged to the sample surface after growth of graphene upon exposure to O_2 . The silicon on the surface may change the characteristics of the graphene layer, as will be shown in the following.

Note that the O_2 exposure might also attack the graphene itself, as was already described in chapter 8.1.1. As was concluded in chapter 8.1.1, oxygen exposure at 1045 °C removes the graphene layer from the sample. Therefore, the subsequent oxygen treatment step was also done at lower temperatures, to determine whether at some temperature the silicon in the bulk is still mobile while the oxygen does not react with the grown graphene.

The growth conditions for four samples grown at 1045 °C and subsequently exposed to oxygen traces at 750 °C are listed in Table 28. Sample I was grown without the accumulation of Si prior to the reaction, Samples II and III were grown to an incomplete coverage (flakes) to preserve bare Cu areas on the sample during the O_2 treatment and in Sample IV a complete graphene film was grown without any uncovered Cu areas in between. All samples were characterized by photoelectron spectroscopy to survey the amount of Si on the sample surface.

The XPS Si 2p spectra are shown in Fig. 88a). Sample I (Graphene flakes, no Si accumulation by high pressure H_2 treatment) shows no Si signal, as expected because no Si accumulation step was performed. Optical microscopy images (Fig. 88d) indicate that oxygen does not etch the graphene flakes at this temperature. Samples II and III (Graphene flakes, Si accumulation by high pressure H_2 treatment) show an increased Si 2p photoelectron signal after O_2 exposure at 750 °C. The acquired Si 2p signal from sample III (30% graphene, 70% bare Cu) exceeds the one of sample II (90% graphene, 10% bare Cu) by a factor of about 6, which scales well with the area of the Cu foil which is not covered by graphene. The scaling of the Si accumulation with the uncovered Cu foil area is also in agreement with the SEM images displayed in Fig. 88 b+c, where thick particles almost completely cover the graphene-free Cu surface, while these are not detectable on the neighboring graphene covered Cu foil. A fully covered graphene film does not lead to a measurable Si intensity after oxygen exposure, as shown in the data of sample IV.

Table 28 : Reaction protocol for four samples grown under different conditions regarding the silicon accumulation in the substrate volume through high-pressure hydrogen treatment and the graphene covered area after sample growth. All samples were treated with O_2 at 750 °C after the graphene growth reaction.

Exp	Before g growth			After g growth		Si detectable by XPS?
	Si accumulation 300 mbar H_2 , 60 min at 1045 °C	Graphene growth at 1045 °C	Gr. Coverage of the Cu foil	O_2 (4×10^{-5} mbar) in 20 mbar Ar at 750 °C		
E. 68	Sample I	No	Flakes	$\leq 30\%$	60 min	No
E. 69	Sample II	Yes	Flakes	$\geq 90\%$	10 min	Yes (low amount)
E. 70	Sample III	Yes	Flakes	$\leq 30\%$	60 min	Yes (high amount)
E. 71	Sample IV	Yes	Complete Film	100%	60 min	No

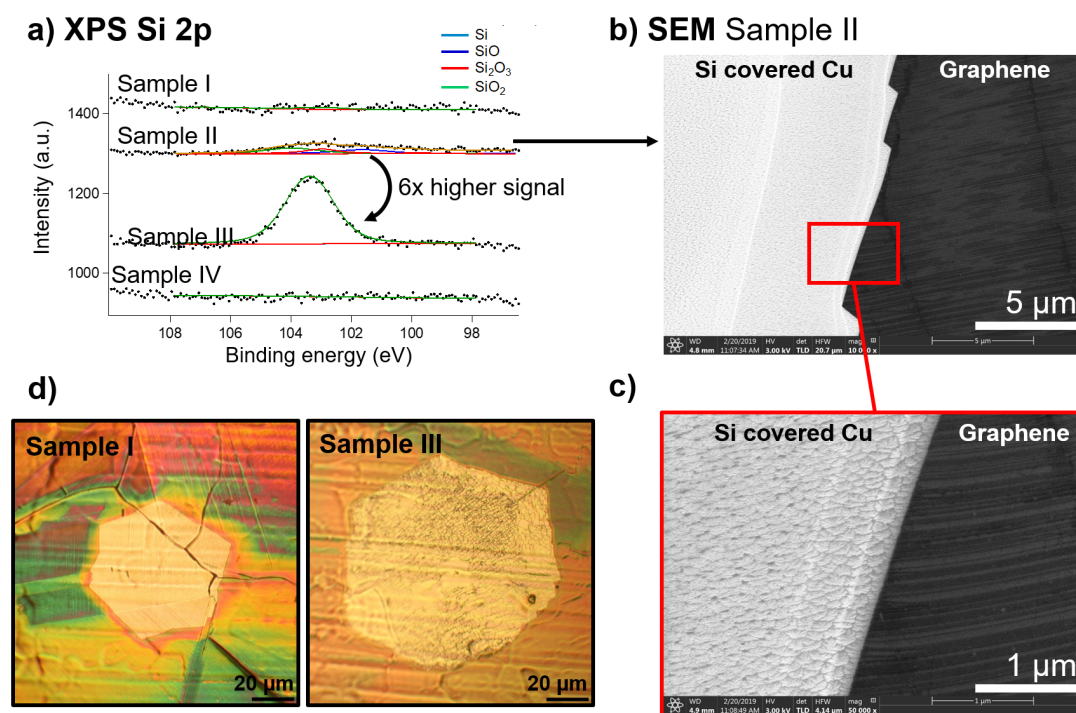


Figure 88 : Experimental results of the samples I-IV as described in Table 28. a) Si 2p XPS spectra of the samples. While sample I without Si accumulation shows no Si signal, samples II and III show intense Si 2p peaks. For sample IV with a complete graphene coverage, no measurable Si 2p signal is detected. b) SEM images of sample II showing that Si is greatly accumulated on the graphene free Cu areas, which accounts for the bright contrast (see text). The Si 2p intensity scales with the bare, graphene free Cu foil area. d) Optical images of samples I and III show no defects in the graphene flakes. Lines and contrasts on the graphene flakes originate from the *ex situ* heating procedure to make the flakes visible.

Characterization of a complete graphene film (sample IV) with local techniques:

The Si 2p resolution limit of the XPS experiment amounts to the photoemission intensity from a Cu surface covered by $\approx 1\%$ Si. To detect the effect of lower amounts of segregated silicon, local characterization techniques were additionally used. Sample IV already described in Table 28 was also characterized by rastering a graphene covered surface section and acquiring Raman spectra at each spot. An optical image with increased contrast of the analyzed area is shown in Fig. 89a) with two multilayer areas appearing darker on the upper left and lower right side of the image. The array of red dots in the image shows the positions where Raman spectra were measured.

For simplicity, only an excerpt of spectra is displayed in Fig. 89b)-e) that were acquired along line I and II. The respective fits are compiled in Fig. 89b+c) (Line I) and Fig. 89d)+e) (Line II). Both lines show spectra taken along the steps of the multilayer regions. The spectra from Line I can be fitted according to single-, bi- and trilayer graphene measured by 633 nm laser wavelength as done by Ferrari³³ which was already used for the fits displayed in Fig. 87. The 2D signal of the single graphene layer can be fitted by a single Lorentzian curve, while several Lorentzians are required for the multilayers. In contrast to the data acquired along Line I, the Raman data acquired along the second multilayer island (Line II) show a splitting of both graphene peaks, without the presence of a defect-mediated D-band. The three spectra recorded on bilayer graphene can be fitted by two Lorentzian curves for the G- as well as the 2D-band. The signal intensity ratio of both species ranges between 2:1 and 3:1.

While the spectra from Line I follow the reference spectra also found in literature,³³ the spectra along Line II show an unknown peak splitting. The spectra appear as two independent SLG graphene layers (fits with one single Lorentzian) shifted in their peak positions. The G-band position can be plotted against the 2D-band position to achieve information on the influence of strain and doping on the graphene. Fig. 89 shows the fitted peak positions in a grid of isotropic strain and isotropic doping lines according to values published by Ding *et al.*³⁵⁵ The plotting of the G- and 2D-band positions allows to determine strain and doping of the graphene layers. The plotted data shows that the two peaks are almost identical in the electronic doping while strongly differing in the mechanical strain of the graphene layers.

The absolute values for strain and doping induced peak shifts derived by Ding *et al* cannot be used for the performed experiment because of the different laser wavelengths used (532 nm by Ding and 633 nm in this experiment). However, the qualitative trends of the recorded spectra are well transferrable. In the plots of Fig. 89e)+f) the Raman signal with the higher intensities belong to the red markers in the bottom right of plot f), while the low intensity features belong to the blue markers. According to the coordinate system introduced by Ding, the low intensity features belong to graphene with low compressive strain.

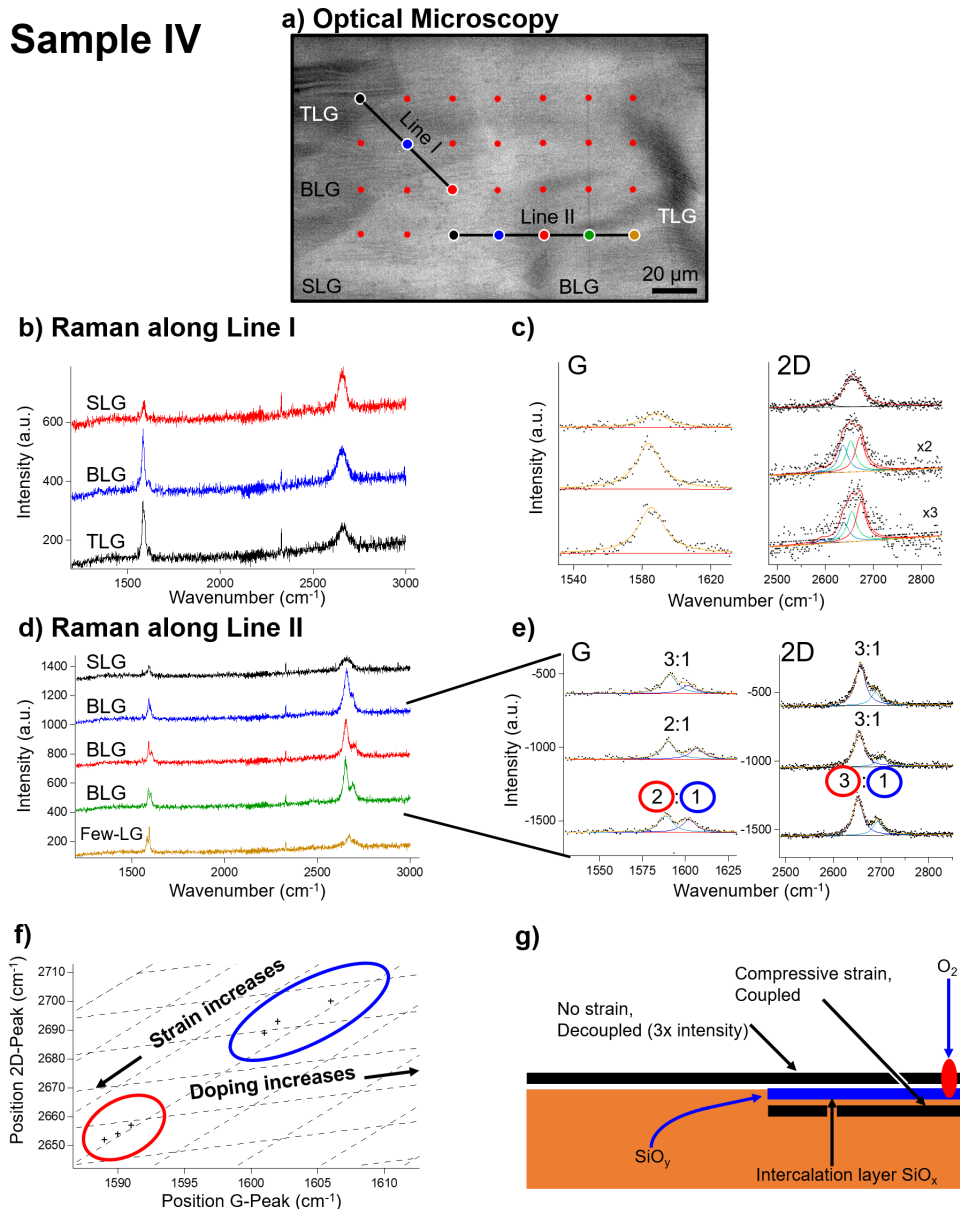


Figure 89 : Raman mapping experiment conducted on sample IV synthesized as described in Table 28 with Si accumulation, graphene growth and additional O_2 treatment at $750^\circ C$ after growth. a) Positions of Raman spectra acquisition are marked by a red raster. All spectra displayed in the following graphs are marked with thicker circles. The optical image shows two multilayer islands with up to three graphene layers thickness. b-c) Raman spectra measured along Line I shown in a). The stepwise increase from 1-3 layers is confirmed by the Raman fits in c), in agreement with the known Raman spectra for Bernal-stacked graphene. d-e) Raman spectra acquired along Line II shown in a). Bilayer graphene positions show a splitting of both G and 2D Raman signals in two peaks with an intensity ratio of approximately 3:1. Individual fitting of each component allows the classification of each peak according to the strain-doping diagram as shown in f). While the G and 2D peak positions indicate the same electronic doping, they significantly differ in their strain induced peak shift. The Raman signals with lower intensity show a higher amount of strain. g) Proposed scenario explaining the observed results: Intercalation of silicon impurities between the graphene layers decouples the upper graphene layer from the lower one. This decoupling results in an increase of the overall Raman signal intensity for the upper layer and a reduction of the formed strain on the graphene during cooling, which is usually caused by the interaction between the cooling Cu surface and the covering graphene sheet. The lower graphene sheet on the other side remains in atomic contact with the Cu support, leading to a low signal intensity and a peak shift caused by high compressive strain.

The observations can be explained by a model with two stacked graphene layers (as expected optically from Fig. 89a)) which are decoupled by an intermediate intercalated layer of a different material. In this case, the decoupled upper layer shows a stronger intensity of about three times the intensity of the SLG signal. This is equal to the case of decoupled multilayer graphene layers described in previous chapters, e.g. in Fig. 87. It is known that graphene on the growth Cu substrate mostly shows a compressive strain,¹⁹⁹ while the decoupled graphene layers are typically strain-free, which can be distinguished in the peak-position-plot of Fig. 89f). A possible scenario leading to the observed data is sketched in g): The intercalation layer results from silicon from the Cu bulk. The oxygen from the gas phase, could in this case penetrate the graphene through the nucleation center of the multilayer island, which in many cases is a larger particle allowing adsorbates to penetrate the graphene layer. The O_{ad} would in this case meet the silicon diffusing from the bulk in between both graphene layers, creating the resulting silicon oxide intercalation layer. As shown in the dataset taken from the first multilayer island along Line I, this intercalation does not take place in absence of defects. As a result, traces of silicon oxides are not expected to be observable by lab-based XPS as long as the graphene film contains a low amount of defects and nucleation sites that allow the diffusion of oxygen below the graphene layer.

9.2. Carbon contaminations

The second main contamination playing a major role in the defined synthesis of high quality graphene are carbon-based impurities. As has been made clear in the previous chapters, the control over the carbon content on the sample surface is crucial to accomplish a defined nucleation process, growth velocity and layer thickness. When trying to control the carbon surface concentration one also has to control the carbon content of the Cu bulk. The influence of the overall carbon content in the Cu bulk on the nucleation behavior and a method to detect residual carbon traces in the Cu bulk by XPS have been extensively discussed by Kraus *et al.*^{183,126,174} Summarizing this work, an oxidative pre-treatment is used to remove the present carbon contaminations from the substrate prior to graphene growth. By using the right cooling rate after the reaction, it is possible to diffuse carbon from the substrate bulk to the surface and subsequently detect the segregated carbon by XPS.

The solubility of atomic carbon in Cu at common graphene growth temperatures is very low. According to López and Mittemeijer³⁵⁶ Cu can dissolve ≈ 7 ppm of C at 1020 °C, which would amount to a single atomic layer of carbon dissolved in the $\approx 10^5$ atomic layers of Cu contained in a 25 μm thick substrate foil. In the copper substrate foils used for

graphene growth, carbon contaminations are present in a much higher concentration, as could be detected by several groups^{357,358,359,112} using secondary ion mass spectroscopy (SIMS), in which the defined stripping of atomic layers enables to form an elemental depth profile of the sample. Several of the mentioned studies prove that these carbon impurities are not equally distributed in the foil, but increase towards the sample surface and are laterally enriched in lines of quite regular distance.³⁵⁸ The stronger impurity content along these lines is caused by the rolling process of the foil, during which most probably long-chained oil residues are inserted into the foil. The connection of these impurities to the nucleation behavior is straightforward and is reported in a large number of publications.^{126,358,357,360,141} After the nucleation process, carbon diffusion from the substrate bulk to the surface feeds the growth of multilayer islands. Several groups have proposed the coating of the substrate backside with materials that react with arriving carbon, therefore depleting the Cu bulk and lowering the amount of carbon atoms that may lead to multilayer formation. This material could for example be a tungsten layer³⁶¹ or a nickel foam.³⁵⁷

Most literature studies dealing with the topic of carbon contaminations and substrate pretreatments ultimately reveal a method to react the carbon from the sample prior to growth.^{183,358} What is less discussed in these works is the reaction pathway from the large agglomeration of impurities to the atomic carbon species able to react with arriving oxygen. This is particularly relevant for the oxidative pretreatment method presented by Kraus *et al*¹⁸³ and also used in this work (see chapter 3.2), where a low oxygen addition is used to exclusively form surface O_{ad} species. Thus, a certain mobility of the carbon impurities is necessary to reach the surface and react with the O_{ad} species. As the configuration of the carbon impurities is unknown, their mobility cannot be estimated. Literature studies indicate that the carbon from the impurities becomes more mobile and distributes in the sample upon exposure to hydrogen gas.^{359,362,363} The influence of the carbon impurities depending on the growth protocol is analyzed in the following.

The impact of the carbon impurity consistency becomes apparent when comparing sam-

Table 29 : Experimental protocol for two samples synthesis routes A and B with strongly differing results. The main difference in the reaction recipe consists in a different gas phase composition during the heating ramp of the reactor. Samples -1 were grown for few minutes at low total pressure in CVD conditions, leading to graphene flakes, while samples -2 were grown for extended time at high pressures, leading to a continuous graphene film.

Experiment		Heating ramp	Pretreatment	CVD Graphene growth
E. 48	Sample A-1	$Ar + O_2$	$Ar + O_2$	Nucleation: 5 min, $w = 1300$, $p(H_2) = 20$ mbar
E. 72	Sample A-2	$Ar + O_2$	$Ar + O_2$	90 min, $w = 300$, $p(H_2) = 100$ mbar
E. 4	Sample B-1	$H_2 (+ O_2)_{traces}$	$Ar + O_2$	Nucleation: 5 min, $w = 1300$, $p(H_2) = 20$ mbar
E. 73	Sample B-2	$H_2 (+ O_2)_{traces}$	$Ar + O_2$	90 min, $w = 300$, $p(H_2) = 85$ mbar

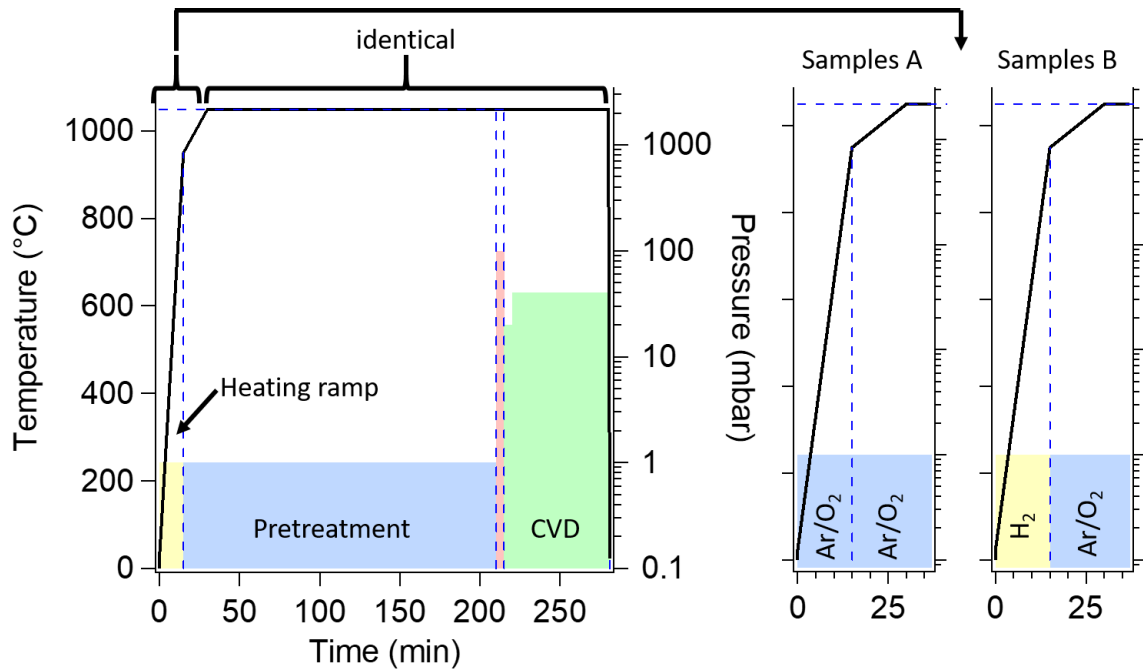


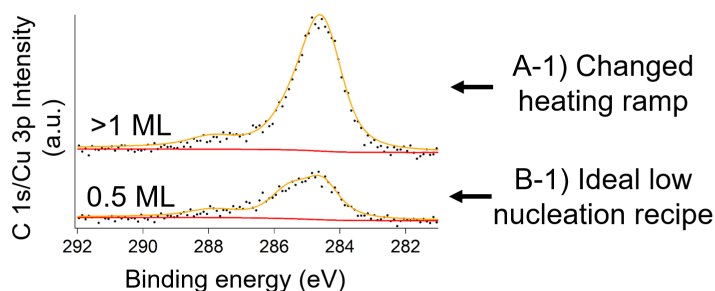
Figure 90 : Diagrams showing the typical reaction protocols for CVD graphene growth (reference samples B in Table 29) and the modified pretreatment experiments performed in samples A described in Table 29.

ples after slightly modified pretreatment protocols. Samples A-1 and A-2 described in Table 29 were grown after heating and pretreatment in an oxidative $Ar + O_2$ atmosphere, while the common reaction protocol (samples B-1 and B-2) used throughout this thesis consists of a heating ramp in 1 mbar hydrogen atmosphere (oxygen contamination $\approx 10^{-4}$ mbar) prior to the treatment in the $Ar + O_2$ atmosphere. The graphical sketch of both protocols is displayed in Fig. 90.

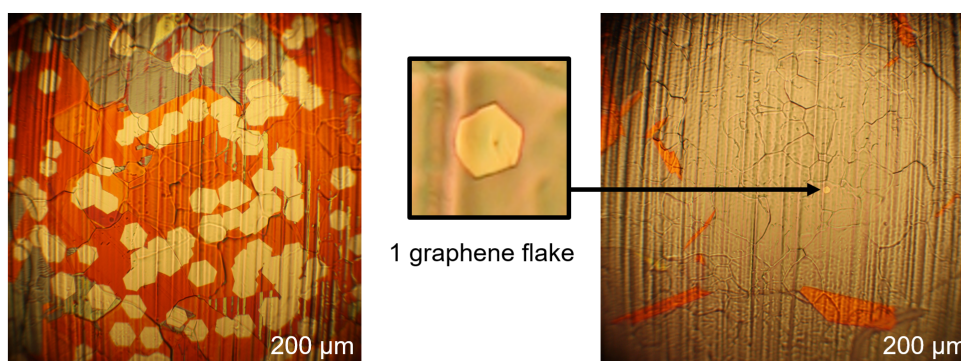
After pretreatment, one Cu foil from samples A-1 and B-1 was removed from the reactor and analyzed by *ex situ* XPS. The carbon C 1s (Fig. 91) content in sample A-1 is significantly higher than in the respective reference sample B-1, indicating that the sample still contains a higher amount of carbon impurities before graphene growth. After CVD growth of graphene flakes, the difference in carbon content of the samples becomes apparent in the nucleation density η_{Nuc} displayed in Fig. 91b). The nucleation density on sample A-1 is more than one order of magnitude higher than the one of reference sample B-1, preventing the growth of single, isolated graphene flakes. Thus, the higher amount of remaining (carbon) impurity particles in the Cu foil can explain the increased nucleation of graphene flakes.

These experiments indicate that the heating in hydrogen atmosphere is important to mobilize the carbon impurities, which subsequently can react on the sample surface with O_{ad} during the oxidative pretreatment.

a) C 1s signal after oxidative pretreatment



b) Nucleation after CVD growth



A-1) Changed heating ramp
 $\eta_{\text{nuc}} \approx 30 \text{ flakes/mm}^2$

B-1) Ideal low nucleation recipe
 $\eta_{\text{nuc}} \approx 0.5 \text{ flakes/mm}^2$

Figure 91 : Comparison of two graphene samples grown at equal conditions with a differing gas phase composition during the heating of the reactor before the oxidative pretreatment. While sample B-1 was heated in reductive hydrogen atmosphere (with traces of oxygen), referred to as “ideal low nucleation recipe”, sample A-1 was already heated in the oxidative $Ar + O_2$ atmosphere subsequently used for the oxidative pretreatment. Two samples removed from the reactor after the pretreatment step show a significantly larger C1s signal in XPS for sample A-1 compared to sample B-1. The difference in carbon content leads to a much higher nucleation density for sample A-1, as evidenced by optical microscopy in panel b).

Samples A-2 and B-2 were grown using the same pretreatment sequence as in A-1 and B-1, respectively, combined with CVD growth of a complete graphene film at a high total pressure, as listed in Table 29. Shown in Fig. 92 are optical and SEM images of the sample surface. Sample A-2 heated in air for contrast enhancement shows strong damage of the graphene along the milling marks of the Cu foil, whereas sample B-2 shows no contrast change compared to the non-oxidized sample, indicating an intact graphene layer protecting the Cu from oxidation.

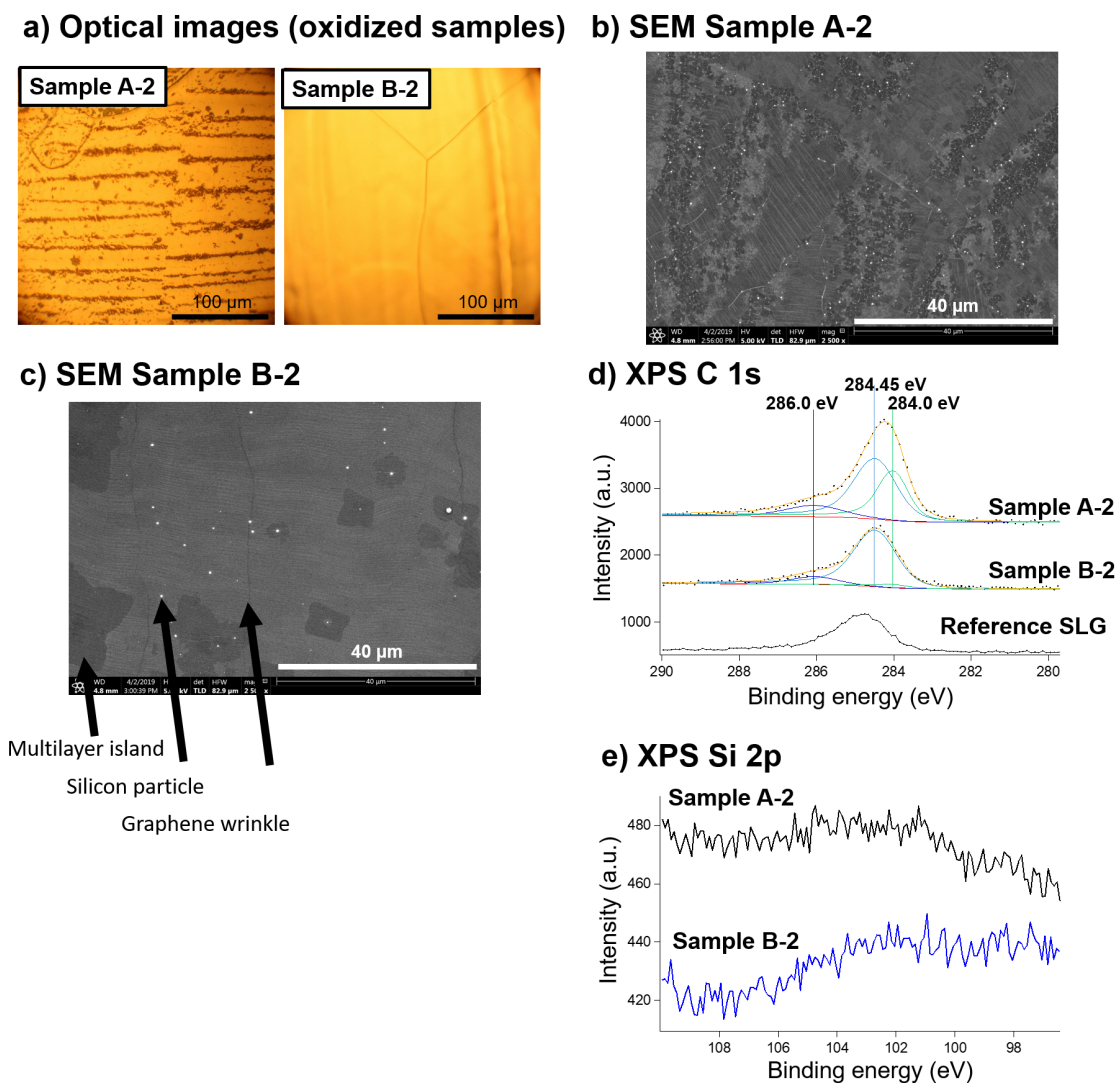


Figure 92 : Characterization of samples A-2 and B-2 described in Table 29 with similar growth conditions but a modified gas mixture during the heating ramp. a) Optical images showing an accumulation of defect sites and impurities in Sample A along parallel lines of the milling marks in the Cu substrate. b-c) SEM images of both samples showing a large amount of different contrast areas in Sample A-2. Instead, sample B-2 shows a homogeneous grey level of the grown graphene film with a certain amount of well-defined multilayer islands. Both samples show bright spots assigned to silicon impurities. d) C 1s XPS spectra of both samples. While both samples show similar amounts of the carbon species at $E_B = 284.45 \text{ eV}$ assigned to graphene, sample A-2 shows an additional carbon species at lower binding energies. The graphene signal comparison to a reference SLG spectrum indicates the existence of multilayer areas. Due to the presence of additional species of unknown nature, no normalization of the spectra was performed. e) Si 2p signals of samples A-2 and B-2, confirming the presence of silicon on both samples close to the detection limit.

The SEM images of the (non-oxidized) samples support this impression. In sample A-2 (Fig. 92b), no assignment of the different contrast areas to SLG, multilayer graphene, or amorphous carbon can be made. Strong variation of the contrast on an $\approx 10 \mu\text{m}$ length scale indicates the coalescence of many small graphene flakes, aggregated towards a low quality graphene film. Reference sample B-2 (Fig. 92c) allows a clear differentiation of SLG and Multi-LG (darker, flower shaped islands), additionally bright spots indicate the presence of silicon impurities and dark lines indicate graphene wrinkles. The homogeneous contrast of sample B-2 indicates the much higher graphene quality of defined thickness.

XPS spectra of both samples are shown in Fig. 92d) (C 1s) and e) (Si 2p). The C 1s peak indicates the presence of more than a monolayer of graphene ($E_B = 284.45 \text{ eV}^{364, 105}$) on both samples. However, an additional unassigned carbon species with considerable intensity ($>1\text{ML}$) is observed on sample A-2 at a binding energy of 284.0 eV. This species could be assigned to amorphous carbon with a significant amount of sp^3 hybridization, as the signal lies between the expected values of graphite and diamond.³⁶⁵ The tiny component at $\approx 286 \text{ eV}$ appears on both samples and is assigned to carbonate adsorption from the gas phase which is not relevant for the crystalline quality assessment of the grown graphene.

The Si 2p spectrum in Figure 92e) shows signal at the detection limit for both samples, verifying the presence of silicon contaminations on the sample surface, most probably in form of the bright particles that can be resolved by SEM.

Summing up the results obtained by OM, SEM and XPS, the samples show a similar amount of multilayered graphene, there is a large amount of an additional carbon species present in Sample A. This component is not homogeneously distributed, but present mainly along the substrate milling marks. Optical microscopy images show that the graphene at these positions is of minor quality. Additional information about the nature of the non- sp^2 -hybridized carbon impurity in sample A is acquired by Raman spectroscopy which is discussed in the following section.

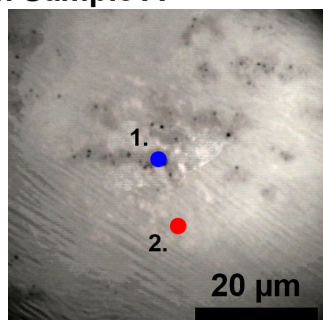
9.2.1. Analysis of Sample A by Raman spectroscopy of freestanding graphene

Additional information about the non- sp^2 -carbon species inside the CVD grown graphene on Cu is gained by Raman spectroscopy, especially when removing the graphene film from the Cu substrate. Fig. 93 compiles optical microscopy together with Raman data acquired from sample A-2 in its supported and freestanding state.

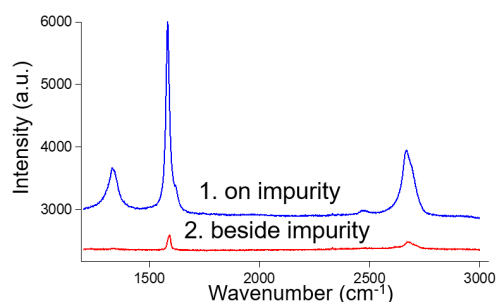
Graphene on Cu: Fig. 93a-b) shows Raman spectra acquired from the fresh, untreated graphene sample. The blue spectrum measured on an agglomeration of the amorphous carbon species, shows a strong defect band at an increased signal intensity. The red spectrum is obtained in between two areas of amorphous carbon, showing no defect band and a significantly lower overall intensity.

Raman Spectra – Sample A

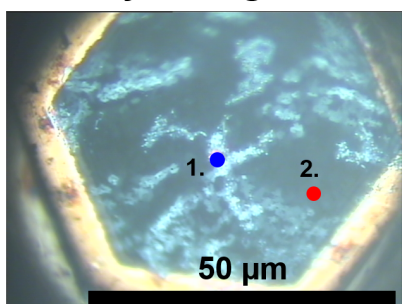
a) Fresh Sample A



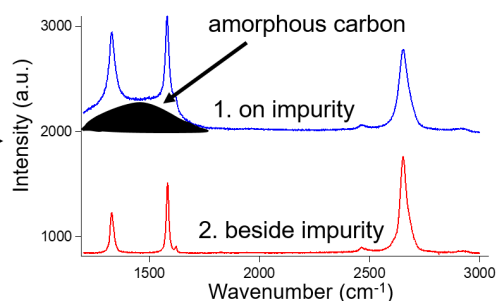
b)



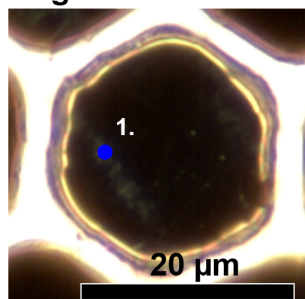
c) Transfer by etching



d)



e) Bubbling Transfer



f)

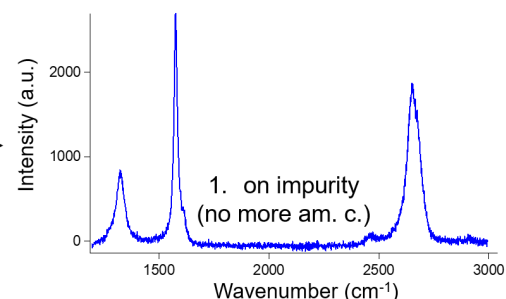


Figure 93 : Raman spectra of Sample A-2 after different sample treatments. a-b) Raman spectra acquired on the fresh sample directly on the observed impurity particles (blue) showing a strong Raman signal indicating decoupling from the Cu substrate and a large defect-mediated D-band. The red spectrum acquired beside these impurities shows almost defect-free graphene. c-d) Raman spectra acquired after graphene transfer by etching of the Cu substrate in etching solution. The impurities detected in a) remain on the graphene membrane and show a 3-dimensional structure by optical microscopy. The blue Raman spectrum acquired at the particles shows additionally to the spectrum in b) a broad peak around 1500 cm^{-1} assigned to amorphous carbon. This signal is missing at the red spectrum acquired beside the impurity particles. e-f) Graphene mechanically detached from the Cu foil by the bubbling transfer technique. The Raman spectrum shows no broad amorphous carbon signal.

The graphene layer was transferred to obtain freestanding graphene membranes using two different transfer methods:

Freestanding graphene: The sample shown in Fig. 93c-d) was transferred by chemical etching of the Cu substrate from below the graphene layer. This sample shows optically very abundant contaminations, which are also visible in the blue Raman spectrum in part d), showing in the very broad peak between $1300 - 1600\text{ cm}^{-1}$ superimposed by the graphene D and G bands. This broad signal (hatched dark) belongs to amorphous carbon³²⁰ and is not present at the reference position beside the impurity particles (red spectrum).

The second transfer method (bubbling transfer), separates the graphene mechanically from the Cu substrate by formation of hydrogen gas between both layers and successively lifting the graphene layer up (see chapter 3.4.3). The respective optical image is shown in Fig. 93e), where the areas affected by the amorphous carbon are visible in optical microscopy because it leads to multilayer areas in this region. The Raman spectrum taken at such a multilayer region is shown in panel f. The absence of the broad band between $1300 - 1600\text{ cm}^{-1}$ indicates that after bubbling transfer no amorphous carbon but solely (defective) multilayer graphene is present in the freestanding graphene membrane. The fact that the broad background Raman signal indicating amorphous carbon is not present for the fresh sample on Cu nor the freestanding graphene obtained by bubbling transfer, but only in case of wet chemical etching transfer, can be explained by the different transfer methods illustrated in Fig. 94.

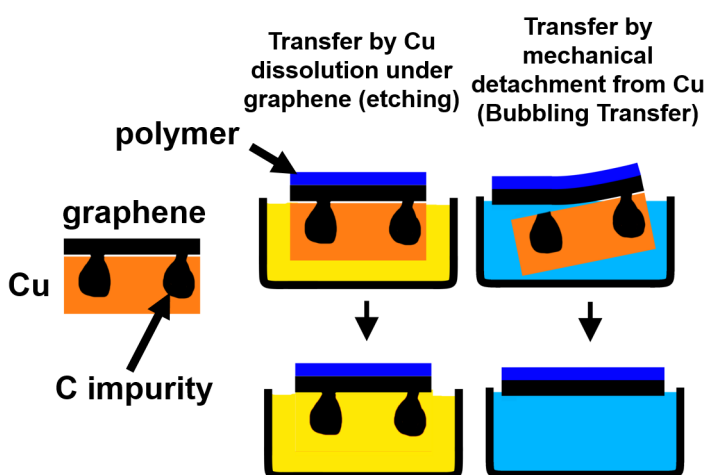


Figure 94 : Sketch of the proposed mechanism leading to different results after the graphene transfer by chemical etching and bubbling transfer. While impurity particles present in the Cu substrate volume remain attached to the membrane in the first case, the mechanical separation between both layers without decomposition inhibits the accumulation of contaminations on the graphene membrane.

In the etching approach everything which dissolves in (or after reaction with) the etching solution (in this case $Fe(NO_3)_3$) will be removed from the sample, but everything else will remain in the solid state and connected to the graphene film. This is well observable in the optical image of Fig. 93c), where the impurity particles seem to be extended below the graphene membrane. In contrast to this, the bubbling transfer approach mechanically detaches the graphene sheet from the Cu surface, and everything connected more strongly to the Cu substrate will remain on this substrate.

All in all, it can be concluded that large particles of amorphous carbon are embedded in the Cu bulk along the milling marks and remain interconnected with the grown graphene film after CVD growth at high pressures, causing a high amount of defects.

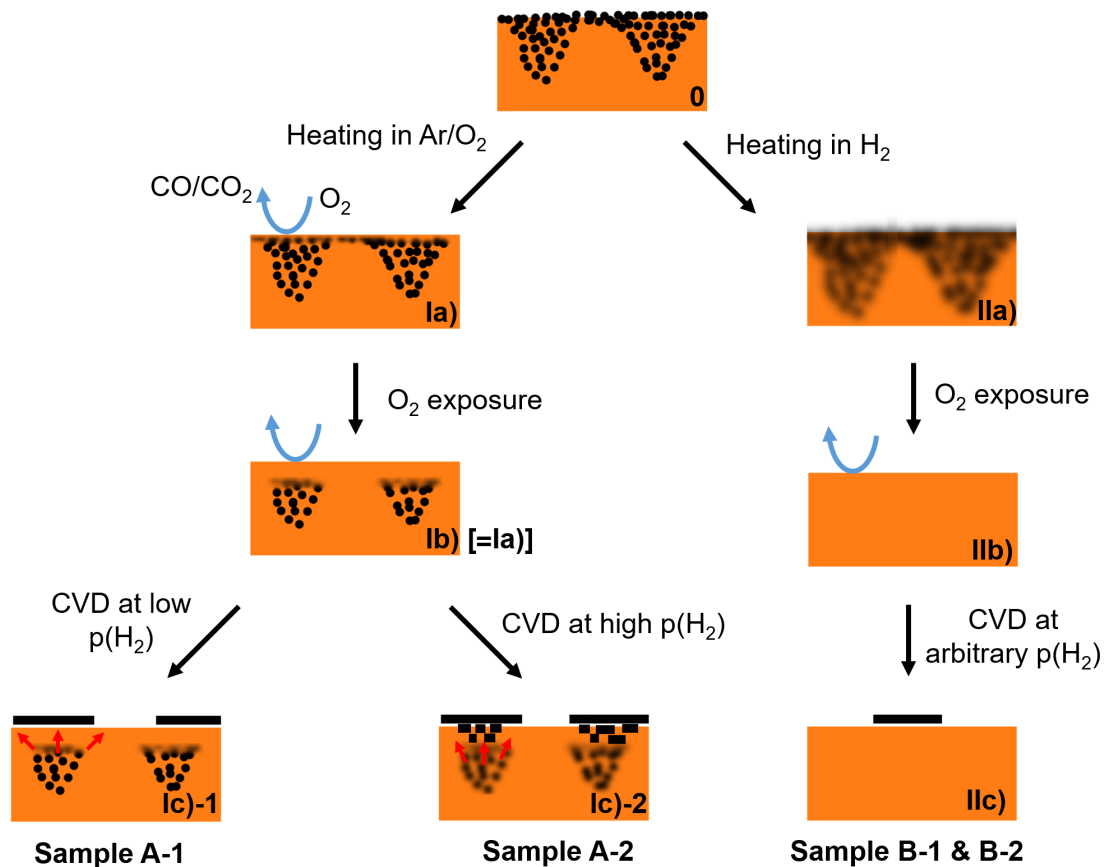


Figure 95 : Condensed model of a literature search and experimental results from this work compiled in Table 30 on the effect of carbon impurities in the Cu foil on the CVD growth of graphene. While the hydrogen treatment of a sample enables the decomposition of dense carbon impurity particles and their distribution over the sample volume, oxidative treatment removes atomic carbon dissolved in the Cu volume and diffusing to the surface. However, the exclusive exposure to oxygen does not fully remove compact carbon based particles from the Cu volume (see text).

A model summarizing the effect of carbon contaminations on the outcome of CVD graphene growth is sketched in Fig. 95. The discussion of findings reported in literature regarding this model are summed up in Table 30. The model contains two key points:

- Treatment of the sample with hydrogen turns the carbon impurities in the sample bulk into a mobile species.
- Treatment of the sample with oxygen removes the mobile fraction of the impurities, mainly from the sample surface.

Table 30 : Experimental evidence for the individual steps described in the model presented in Fig. 95 and respective literature citations and comments to these sources.

Step	Evidence for the model		
	Source	Method	Comment
0	Braeuninger-Weimer ³⁵⁸	TOF-SIMS	A 3D concentration profile of the Cu foil shows inhomogeneous distribution of carbon impurities, clustering at high concentrations along Cu rolling marks. H_2 exposure was shown to lead to a homogeneous carbon redistribution in the sample.
	Kraus ¹⁷⁴	XPS	The surface of the untreated Cu foil is covered by carbon contaminants.
Ia)&Ib)	This work - Sample A-1	XPS	The Cu foil shows no depletion of the carbon content even after long oxidative pretreatment if it was not heated in hydrogen gas.
Ic)-1	This work - Sample A-1	Nucleation analysis	Exposing the Cu foil without complete carbon depletion to CVD conditions leads to a strongly increased nucleation density compared to a carbon depleted Cu foil.
Ic)-2	This work - Sample A-2	XPS, Raman, SEM, OM	Inhomogeneously distributed, amorphous carbon is detected after high-pressure CVD growth on the Cu foil without full carbon depletion.
	Ge, ³⁶³ Khaksaran, ¹¹² Kraus ¹⁷⁴	Growth analysis	Cu foil exposed to high pressure hydrogen leads to the formation of (bad quality) graphene islands and amorphous surface carbon without an external carbon precursor.
IIa)	Khaksaran, ^{366,112} Kraus ¹⁷⁴	Raman	Same as step Ic)-2 above, mobilization of carbon in the Cu volume upon high-pressure hydrogen treatment.
IIb)	Kraus, ^{183,126} Ge, ³⁶³ Khaksaran ¹¹²	XPS, Nucleation analysis	The Cu foil shows no more carbon content after the succession of hydrogen treatment followed by oxidative treatment.
IIc)	Kraus, ¹⁸³ This work - Sample B-1	Nucleation analysis, Growth analysis	Using the correct succession of pretreatment steps it is possible to grow graphene with a very low amount of nucleation seeds on the sample.

10. Graphene transfer methods

The formation of high-quality freestanding graphene membranes requires the synthesis of defect-free graphene, the stress-free removal of the graphene film from the Cu substrate and a gentle transport to a new, holey substrate. While the previous chapters focused on graphene growth experiments, this chapter describes the transfer process. All of the known graphene synthesis and transfer methods^{367,73,368} allow a wide range of differing production pathways. The used sample parameters are listed in the following and examined regarding whether or not the freestanding graphene can serve as a gas-tight but electron transparent membrane for low energy photoelectrons ($E_{kin} < 1000 \text{ eV}$):

- **The graphene layer number:** The most prominent feature of graphene membranes is that they can be synthesized as a single atomic layer. Nevertheless, samples may also be composed of few graphene layers and still fulfill the experimental requirements of a leak-tight and electron transparent membrane. The transparency regarding low energy electrons decays exponentially with the layer thickness, but 2-4 graphene layers still show sufficient electron transparency in many cases,⁵⁹ which greatly simplifies the synthesis strategy.
- **The mechanical stability:** Pristine graphene has shown to have ultra-high mechanical stability and estimations for the possible pressure difference acting on a graphene layer have been presented in several references.^{174,369,370,86} These refer to Hencky's solution for the calculation of the deformation of circular membranes under uniformly distributed stress. The resulting formula to estimate the stress resistance of a round graphene membrane is shown in eq. 10.1:

$$\Delta p = 3.09 \frac{E * t * \delta^3}{a^4} \quad (10.1)$$

Here, Δp is the resisting pressure difference, $E = 1 \text{ TPa}$ the elasticity module of graphene, t the layer thickness ($n * 3.35 \times 10^{-10} \text{ m}$ for n-layer graphene), δ is the bulging of the membrane and a is the radius of the membrane hole. Assuming roughly that the graphene membrane bursts if the bulging expansion of the membrane is one tenth of the cavity radius ($\delta = 0.1 * a$), which is backed up by experimental data,⁸⁵ the formula can be rewritten as:

$$\Delta p = 3.09 \frac{E * t}{1000 * a} \quad (10.2)$$

An ideal SLG membrane with a diameter of 200 μm would then resist a pressure difference of up to 100 mbar.

- **The total membrane area:** The required membrane area used as electron-transparent membrane should match the field-of-view (FOV) of the respective instrument in which the graphene sample should serve as sealing membrane. The required area may range from several mm² of sample area (e.g. lab-based XPS), to areas of 200x50 μm (e.g. synchrotron beam irradiation) or illumination areas of around 1x1 μm (Raman Laser spot size). Note that this membrane area must not necessarily be achieved by a single graphene membrane, but can rather be obtained by an array of several small membranes, which may also comply with the requirements set by the mechanical stability.
- **Transfer success rate and leak rate:** Graphene acting as a sealing membrane requires a defect-free film over the entire freestanding area, transfer methods must therefore minimize the acting stress on the transferred graphene.
- **Resistance to temperature change:** Depending on different post-synthesis treatment methods it may be required to heat the sample to a certain temperature. In this case, substrates and support structures need to resist such temperatures. Most importantly, different expansion coefficients in ultra-thin samples may lead to strong stress between membrane and support.

Sample goals: The transfer methods developed in this work mainly aim for the applicability in UHV-compatible, pressurized cells for the analysis in synchrotron facilities. In this case, a sample would require about 1-6 layer total thickness, a pressure resistance up to 100-1000 mbar (for bilayer graphene, following eq. 10.2, this would allow membrane diameters of 400 μm (at 100 mbar) or 40 μm (at 1 bar)). A total membrane area of 200x50 μm , complete leak tightness (UHV-side at pressures below $\approx 10^{-7}$ mbar) and the possibility to degas the sample in UHV to temperatures above at least 100 °C defines the requirement on the envisioned membrane material. Note that test samples described in the following often allow extracting more information when differing in single points from these strict requirements. Large hole arrays for example will not suit the needed sample area or leak tightness but allow a much larger transfer number giving insights about the statistics of the transfer success rate.

In section 10.1, new treatment steps for the transfer of graphene films are presented. To achieve UHV-compatible, leak-tight graphene membranes, the range of graphene layer numbers is exploited in section 10.2 by forming an artificial multilayer graphene stack. Exchanging one of the two merged graphene layers by a patterned material also allows the fabrication of reinforced ultra-thin graphene layers down to a single layer thickness, while allowing larger hole structures. The increasing complexity of the sample production allows a large number of modifications. In this way, it is possible to use thin metal grids as reinforcement (section 10.3.1), but also the reinforcement with patterned graphene is possible (section 10.3.2). The controversy between the in experimental prac-

tice commonly achieved graphene membranes (large connected membrane areas with <100% total coverage) and the - in our case - desired product (a single aperture with 100% coverage) is addressed in section 10.4 together with a proof-of-principle experiment showing a way to transfer single intact membranes from one target to another.

10.1. Enhanced treatment steps required for the transfer of graphene layers

10.1.1. Bottom-up preparation of an ultra-flat, clean Cu foil

Industrial Cu foils are not perfectly flat, they rather contain milling marks as inherent morphology from the metal cold rolling. They appear as regular, parallel stripes in optical microscopy, as shown in Fig. 96a). After graphene synthesis, the Cu grain volume restructuring also comes along with morphological changes on the sample surface. Grain boundaries with higher surface free energy lead to trenches in the Cu foil. Note that these morphological inhomogeneities may remain as imprints ($\approx 100 \mu m$ apart) even if the Cu grains subsequently grow larger ($mm - cm$ diameters). The foil milling process also leads to an increased amount of carbon-based impurities rolled into the foil, as discussed in the previous chapter. A way to prepare a fresh metal foil with an extremely flat surface (see Fig. 96b) and without an increased amount of impurities is described in the following and sketched in Fig. 96c). A Cu foil is heated in vacuum by a radiofrequency (RF)- coil, as described by J. Kraus.¹⁷⁴ The foil is heated to temperatures above $800 \text{ }^\circ\text{C}$, where an elevated vapor pressure leads to the evaporation of Cu to an arbitrary substrate, in this case a flat quartz-glass piece or an ultra-flat silicon wafer. The method allows the formation of a Cu layer of several 100 nm thickness, which is too thin to be mechanically removed from the substrate. It must therefore be thickened by electrochemical deposition of Cu on top of the respective thin layer (step ii in Fig. 96c). In this way, thicknesses in the μm regime can be obtained in the range of a few hours. The thickened Cu layer can then be removed mechanically from the substrate.

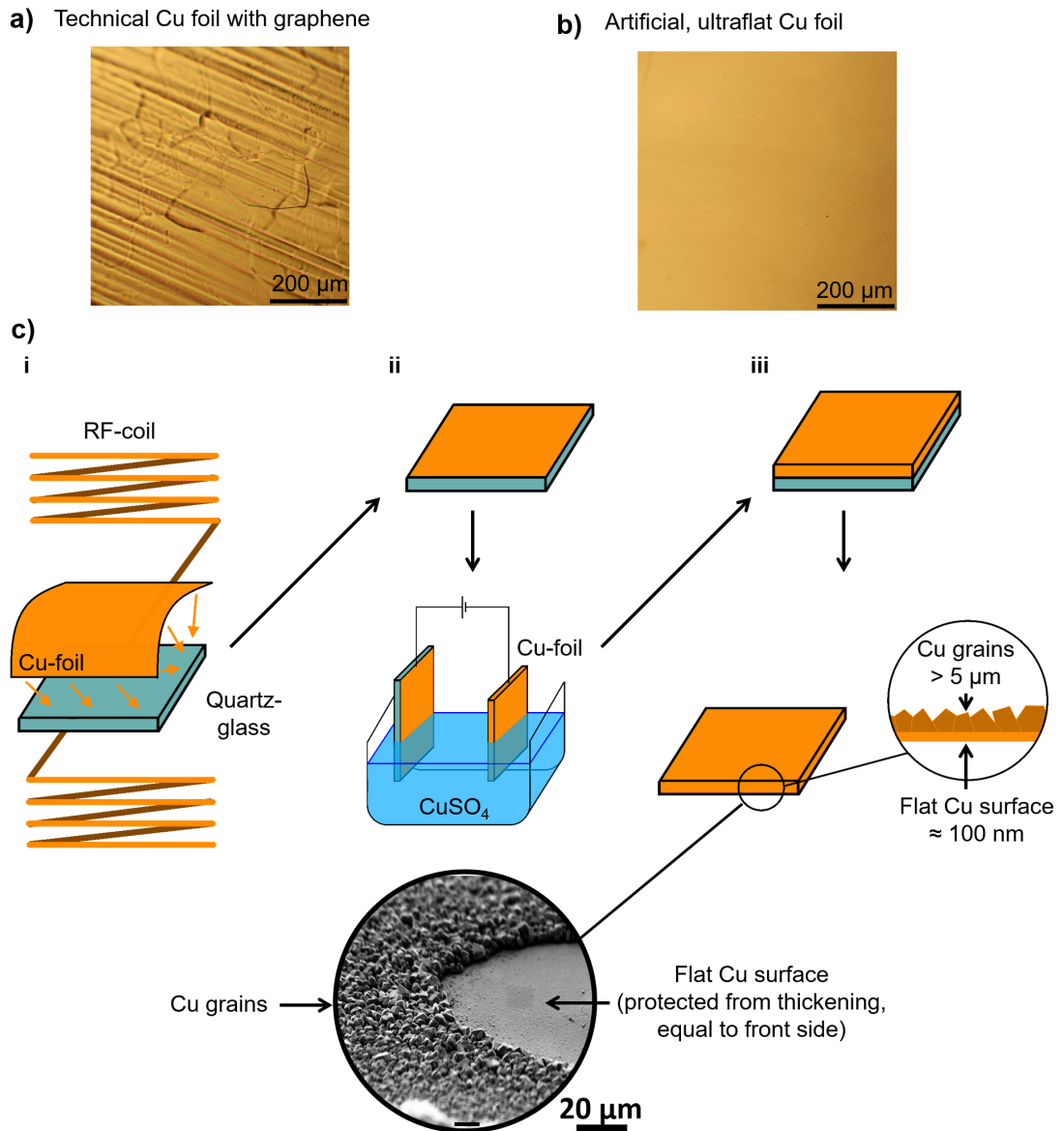


Figure 96 : Comparison of optical images of the technical Cu foil (a) after graphene growth, showing milling marks (parallel lines) and grain boundaries (linked lines), and *in situ* formed Cu foil (b) according to the procedure described in (c) without any morphological defects. c) Production of a flat Cu foil. In vacuum, a Cu foil is inductively heated via a radiofrequency (RF)-coil. At elevated temperatures, the increased vapor pressure of the Cu foil covers a quartz glass piece located below the foil. Cu layers of about 100 nm can be deposited in this way in the course of one hour on the quartz plate. The thin Cu layer can be thickened by subsequent electrochemical Cu deposition in an electrolyte with a Cu counter electrode. This creates small Cu crystals of approx. 5 μm diameter on one side of the Cu layer (see SEM image inset). The fortified amorphous Cu layer can then be removed from the quartz glass slide, providing a flat surface on one side of the Cu foil.

10.1.2. Formation of supporting, ultra-thin metal grids

Freestanding graphene membranes must be stabilized by some sort of holey structure. The interaction between the two materials is a key point for the successful production of membranes with enhanced mechanical stability. Here, a way is presented to prepare such a stabilizing metal film with a thickness below ≈ 50 nm on top of any substrate or graphene surface. The synthesis protocol is sketched in Fig. 97. A patterned metal foil (e.g. a Cu TEM grid, typically used in this study) is covered on one side with a thin evaporated metal layer using an equivalent procedure as the Cu evaporation described before. For the outlined protocol, it is important to use a more noble metal than the Cu-TEM grid. In the current study, Ag was evaporated and afterwards the Cu substrate was removed electrochemically from below the silver layer. The remaining thin Ag film was floating on the electrolyte/etching solution, which was then exchanged by water. The generated metal grid can be laid on top of the graphene layer in a final preparation step and after cleaning it can act as a support structure for freestanding graphene (see Fig. 97).

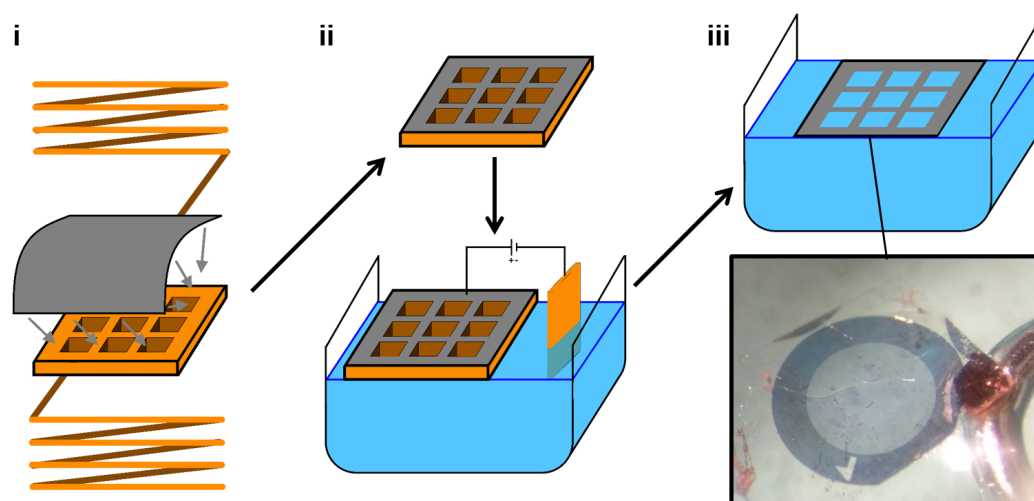


Figure 97 : Procedure for the formation of thin metal supporting grids. i) In vacuum, a more noble metal (e.g. Ag) is deposited on a patterned metal grid (e.g. Cu). With this evaporation technique, layers of 50-100 nm can be evaporated. The coated grid can then be placed on an electrolyte solution, in which the less noble grid metal is dissolved. Remaining is then only the thin metal layer on the solution, as also shown in the optical inset image. Note: The optical image shows a thin Ag grid already positioned below a graphene/PMMA stack, which is also visible in the image. To the right side of the image a silver rod can be seen which connects the grid to the electric circuit.

10.1.3. Structuring of graphene with a photoresist

Similar to the formation of metal supporting grids, it is also possible to produce 2-dimensional, patterned graphene structures. These patterns can be imprinted into a continuous graphene layer using a photoresist, as shown in Fig. 98. A graphene film (image i) is coated with a photoresist (ii), illuminated with UV-light (iii) and developed, leading to the patterned photoresist shown in image (iv). The exposed graphene is removed by Ar-ion-sputtering (v) and the photoresist is removed by washing in acetone, leading to the patterned graphene film (vi). The patterning of graphene is known in literature³⁷¹ and frequently used to create electronic devices or heterostructures.^{70,372,373,374} However, it has not been used so far for the fabrication of freestanding graphene membranes.

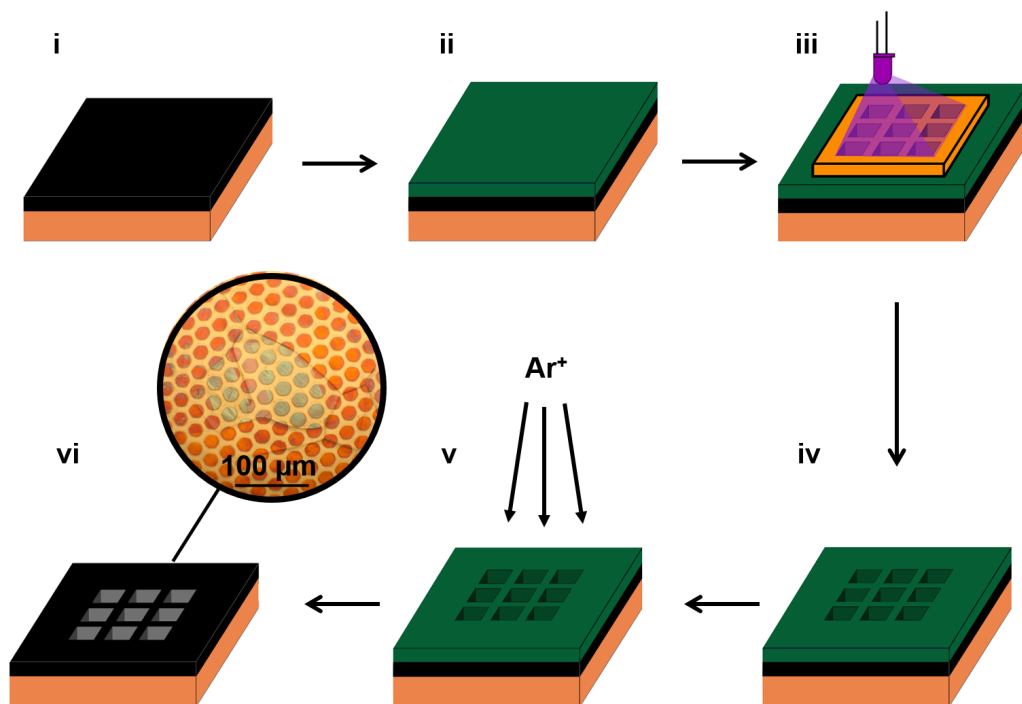


Figure 98 : Patterning of graphene using a photoresist. Graphene is coated with a photoresist layer and subsequently illuminated through a mask with the desired hole structure. Using a positive photoresist, the illuminated holes are removed after developing of the photoresist and Ar-ion sputtering of the sample leads to selective graphene etching in these places. After removal of the photoresist in acetone solvent, the patterned graphene remains. The optical image shows an oxidized, patterned graphene layer with a 20 μm hole structure.

10.1.4. Selective removal of graphene from the Cu backside

After CVD growth, both front- and backside of the used Cu foil are covered with graphene. For several treatment methods, such as the chemical etching of the Cu substrate, it is necessary to remove the graphene film from the sample backside. Several ways to do this are reported in literature, such as the etching in plasma²⁵⁶ or the removal by bombardment with high-energy ions.⁵⁹ Here, I mention an additional, fast way to remove the graphene from the sample backside. After coating of both the front and backside of the sample with PMMA, the bubbling transfer procedure is applied to the sample, with the difference that the sample is not inserted vertically but horizontally into the solution (shown in Fig. 99). While the frontside remains dry, the backside graphene/PMMA stack is released as known for the bubbling transfer.

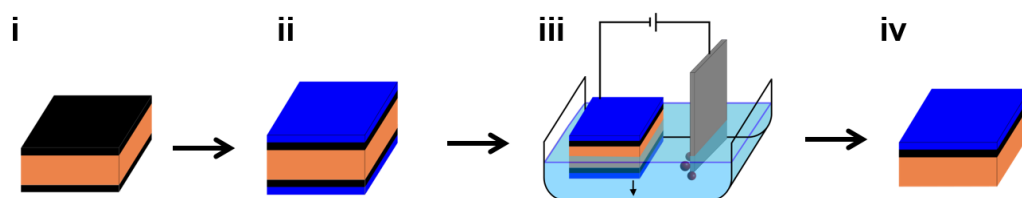


Figure 99 : Selective removal of graphene from one side of the Cu foil. Graphene can be coated with PMMA polymer from both sides. After drying, the sample is horizontally placed in the electrolyte solution and the bubbling transfer is started, leading to the selective removal of the backside PMMA/graphene stack which is immersed in the solution. The procedure can be applied if a Cu sample with graphene on one side of the sample is needed.

10.2. Formation of artificial stacks of multiple graphene membranes

The experimental results of several groups working on the synthesis of graphene on Cu have shown that while the formation of almost exclusive SLG is possible, the formation of a homogeneous graphene film with a constant layer number larger than one is rather difficult. Growth conditions favoring the synthesis of thicker graphene layers mostly lead to the formation of pyramid-like flake-stacks of several different thicknesses (with the pyramid facing into the Cu substrate, "inverted wedding cake"-morphology³⁷⁵). While the targeted synthesis of bi- and trilayer graphene seems possible using a combination of different growth conditions (see chapter 7 and ref.²⁴⁶), further development steps are required to achieve this goal. Currently, the easiest way to produce defined multilayer graphene stacks is therefore to grow single layer graphene and transfer one layer on top of a second one. This has been done by several groups with a high success rate, showing that the artificial combination of single layer graphene to a bilayer graphene stack is possible and effective.^{269,376,377,72} Moreover, laying two graphene layers with randomly

distributed point and line defects on top of each other compensates local imperfections and leads to a mechanically stable membrane.

Nevertheless, the joining of two graphene layers in a mostly liquid environment also leads to the encapsulation of impurities and solvent residues, which may increase the effective thickness of the graphene membrane. These encapsulated liquid cells can even be characterized in UHV.^{378,379} Additionally, any impurities attached to the graphene layers will also be encapsulated in the artificial multilayer stack. It has been shown that the graphene transfer by etching of the growth substrate leads to more contaminations than the alternative bubbling transfer method (see chapter 7 and ref.²⁴⁶). In the following, I present a synthesis route for clean multilayer graphene membranes, as sketched in Fig. 100.

After graphene growth, the graphene layer is protected with PMMA and transferred by bubbling transfer to a super-flat Cu film (see Fig. 96). After drying, the PMMA layer can be removed by heating the sample to 400 °C in a H_2 atmosphere. This also removes all liquid impurities from the sample and Cu surface. A second, identical transfer on top of the first layer and subsequent drying plus heating creates the artificial graphene multilayer. The heating of the sample to 400 °C prevents the formation of large liquid bubbles between both graphene layers. When using SLG as initial graphene films artificial bilayer graphene can be transferred to the final sample substrate, e.g. by chemically etching the Cu film. Note that the graphene layers were only mechanically transferred on top of the ultra-flat Cu film and are therefore not connected to any impurity particles present in the Cu, as is the case in samples described in section 9.2. As a result, the chemical etching of the Cu film should not significantly increase the amount of impurities on the membrane. Figure 101 displays a sample produced by the treatment described above, which is also described in reference ¹⁹. The optical images show a single hole with 100 μm diameter, covered by the graphene membrane. Enhancing the contrast of the optical image and recording the image with illumination from the backside (Fig. 101b) allows the identification of few, still existing impurity particles as dark/bright areas on the membrane. At such positions, one may expect that the membrane will rupture when exposing it to mechanical stress. As during the synthesis of the artificial bilayer two graphene layers were positioned on top of each other, liquid droplets will be trapped between both layers. If such droplets are entirely enclosed by the two graphene films, heating the sample stack to 400 °C to remove the PMMA layer will also induce an enormous pressure on the graphene membrane. However, as soon as one of the graphene membranes breaks, the liquid should be released so that the second graphene layer remains intact. An UHV leak test, performed on this sample by T. Kratky and described in reference ¹⁹ verifies that this ideal case is almost met in reality. Applying a pressure of 10 mbar on one side of the membrane increases the pressure in an UHV setup by less than 1×10^{-9} mbar on the opposite side of the membrane which is pumped by a 75 L s^{-1} turbo molecular pump.

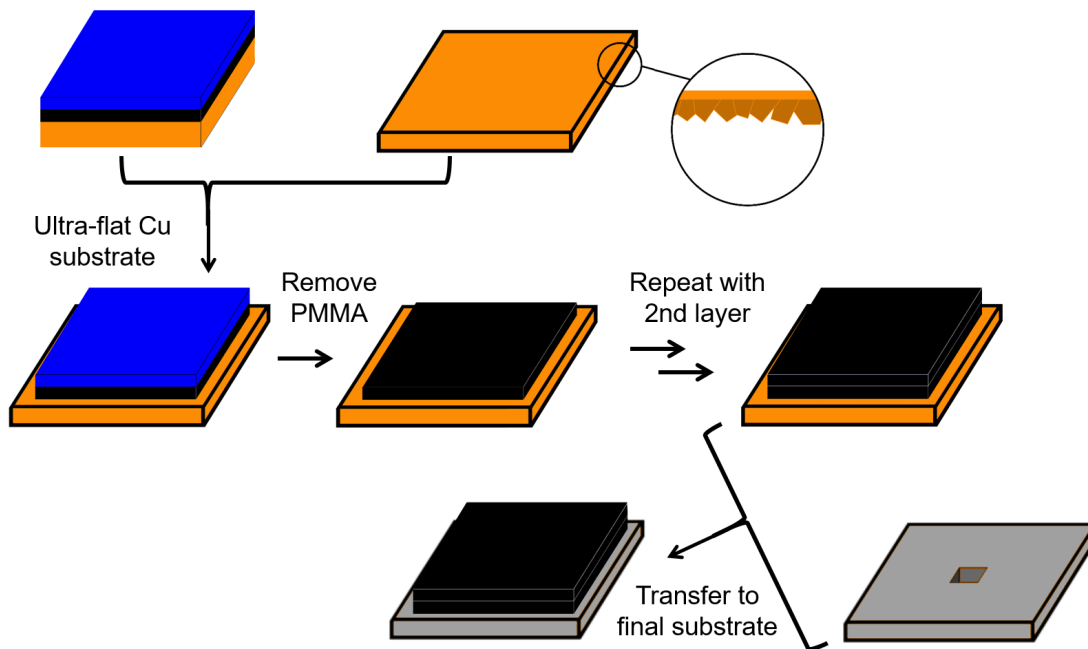
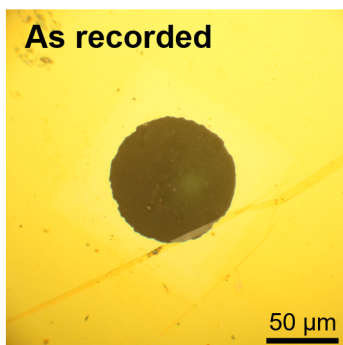
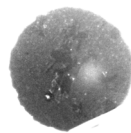


Figure 100 : Synthesis route for the production of freestanding artificial bilayer graphene membranes. The first graphene layer is transferred by bubbling transfer on a flat Cu surface produced as described in Fig. 96. After removal of the PMMA layer, a second graphene layer can be placed on top of the first, also transferred by bubbling transfer. Final removal of the PMMA layer by heating in low pressure hydrogen to 400 °C leads to the collapse of trapped liquid droplets between both graphene layers. The resulting super-flat, artificial bilayer graphene can then be transferred to the final patterned substrate structure. The sketch displays the transfer onto a single-hole aperture.

a) Frontlight image



Contrast enhanced



b) Backlight image

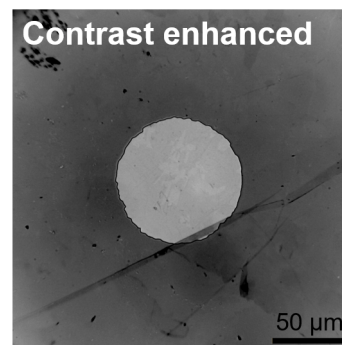


Figure 101 : 100 μm hole covered by artificial multilayer graphene. The optical image is shown also with an enhanced contrast, where impurities and defects in one of both graphene layers can be detected. These are also visible with the illumination from the back of the sample in b). The properties of the sealing membrane are discussed in the text and also in reference ¹⁹.

The measured pressure of 1×10^{-9} mbar relates to a nominal leakage rate of less than 2.75×10^{-8} mbar $L s^{-1}$, which would correspond to a hole in the membrane with ≈ 130 nm diameter on the 100 μ m-diameter membrane area.¹⁹ This sample proves that also large single membranes can be produced in a leak-tight manner and withstand considerable pressure differences.

The overlaying of two continuous graphene layers is a useful method to eliminate potential defects in a single membrane and to reliably synthesize completely sealed membrane samples. Nevertheless, the combination of two graphene layers with possible capturing of (solid) impurities in between increases the membrane thickness which then reduces the electron transparency of the membrane. To overcome this drawback, the synthesis route has been expanded by an additional step presented in the following section.

10.3. Combination of patterned materials with a continuous graphene layer

Instead of overlaying of two continuous layers of ultra-thin material, it is possible to pattern one of both layers in order to act as a reinforcement frame for the second, ultra-thin, continuous layer. The approach has been realized using a metal support grid and also using a patterned graphene layer as supporting structure. Both strategies are discussed in the following. The benefits of an inherently fortified membrane show up in several properties during transfer and in the final state of the sample, as sketched in Fig. 102. A classic freestanding membrane sample needs a support structure with a close-meshed hole structure, because freestanding graphene membranes are weak when being suspended over holes with large diameters (see eq. 10.2). This is changed with an inherently supported membrane, as the alternation of thicker and thinner membrane areas already acts as support. The 3-dimensional support structure can therefore contain larger holes.

The flexibility regarding the choice of support structure allows the adaptation to applications of the final sample. In this way the sample geometry can for example be optimized to increase the measurement interaction area. Fig. 102a) shows the classical and optimized sample-geometries for an XPS measurement (photon in, photoelectron out) of a membrane sealed, pressurized gas cell. Most of the gas cell can be illuminated with X-ray photons, as these also penetrate the supporting grid, strongly reducing the shadow cast on the gas. The large reinforced hole structures are also less frail regarding capillary forces that appear during drying of the membrane structure, as imaged in Fig. 102b). This situation occurs for example after the protecting polymer layer has been dissolved in acetone and the sample is dried in air. The role of the polymer is also relevant for the provided contact area between graphene and reinforced substrate. While thicker polymer layers provide more support to the graphene below (see Fig. 102c), it also leads to a stiffening

of the graphene/polymer stack. If the graphene/polymer stack and the support structure are not absolutely flat and coplanar, which is generally the case, the stiffening reduces the contact area between graphene and the desired support grid. As a result, delamination of graphene while removing the polymer layer is often observed. For reinforced samples, the thickened areas are already integrated in the graphene layer before the final transfer. Thus, the bare SLG areas are exposed to the solvent only in the holes of the reinforcement structure. Lastly, if the material of continuous and supporting layer are equal, the influence of the thermal expansion during annealing is greatly lowered compared to the classical sample setup, as shown in Fig. 102d).

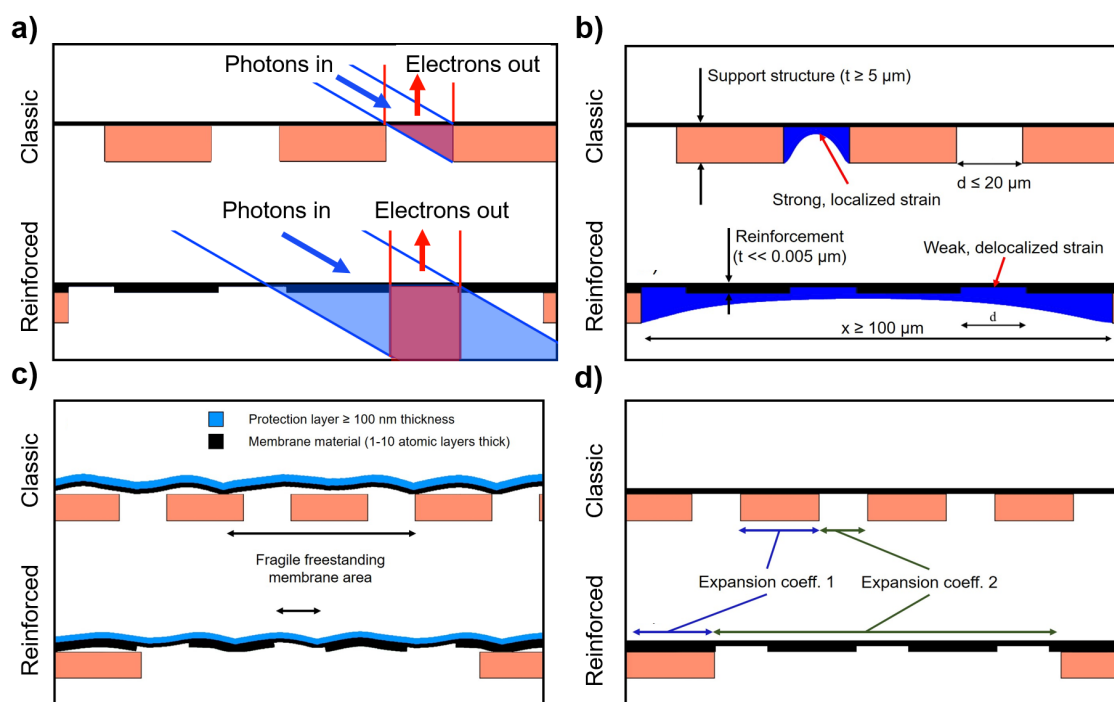


Figure 102 : Differences between the classical freestanding graphene sample and the reinforced graphene layer approach. a) The flexibility in the sample geometry allows to increase the illuminated sample region and hence, also increases the obtained measurement signal. b) The omitting of small capillary holes reduces the strain acting on the graphene membranes when a solvent is drying around the membrane. c) The polymer-protected graphene layer is commonly not ideally flat and therefore not in perfect contact with the substrate grid. While in the classical sample setup this may lead to large SLG areas exposed to the solvent without contact to the support, the graphene film is in close contact with a thin reinforcement layer. d) A membrane in direct contact to a mesh-support consisting of a 3-dimensional grid is exposed to large volume variations upon heating and cooling if the substrate material has a significant thermal expansion coefficient. The thermally induced stress is greatly reduced if both continuous and patterned support layer are made of the same ultrathin material.

10.3.1. Graphene + Metal

As already shown in Fig. 97, it is possible to create very thin metal grids of noble metals without the use of a photoresist or other possible contaminants. The protocol for the synthesis of a Ag grid as reinforcement for a graphene layer is shown in Fig. 103. PMMA coated graphene is removed from the growth substrate by bubbling transfer, picked up with the Ag coated Cu grid and dried in air. Then, the Cu is electrochemically removed from the grid and the remaining Ag/graphene/PMMA stack is fished with a final substrate. As the last step, the PMMA protection layer is removed, leading to the freestanding, reinforced graphene membrane. Optical images of some graphene/silver sample stacks are shown in Fig. 104, where the interplay between the large, thick support structure and the thin Ag supporting grid becomes apparent. If synthesized in the way described in Fig. 103, the Raman signature indicates clean suspended graphene layers, as shown in Fig. 104b).

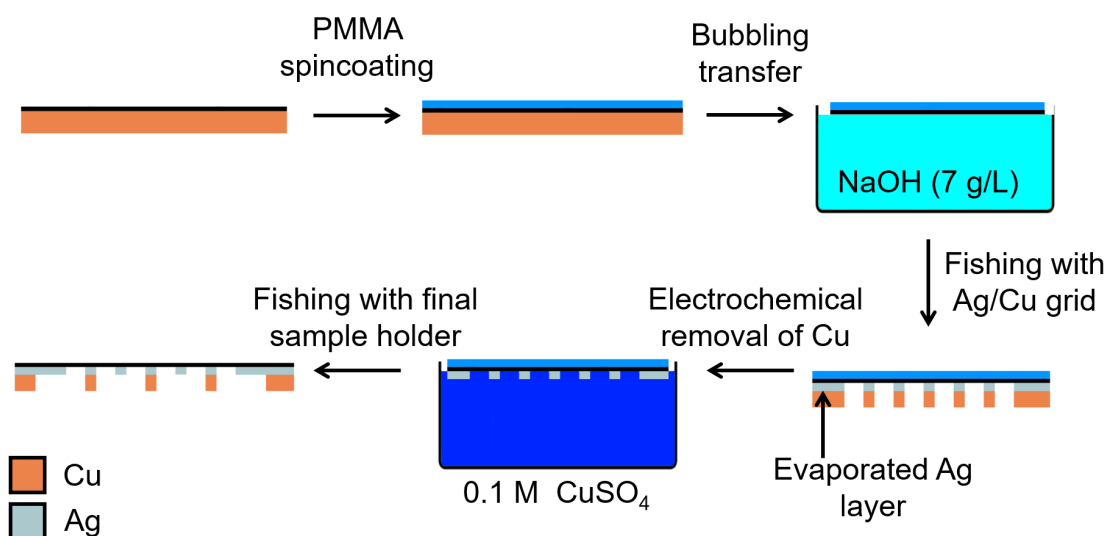


Figure 103 : Synthesis route for freestanding graphene layers supported by a thin, patterned metal grid. The protected graphene layer is released from the growth substrate by bubbling transfer and then "fished" from the solution with a silver-coated copper grid. The Cu layer can then be removed as described in Fig. 97, leading to the thin Ag layer attached to the graphene/PMMA stack. Fishing the stack with the final sample substrate leads to the Ag-supported graphene membranes after the removal of the PMMA layer.

The transfer of graphene assisted by a thin supporting layer in close contact to the graphene was presented by Lin *et al* in literature.³⁸⁰ They present a way to evaporate a patterned Au layer on top of the graphene film and subsequently create freestanding membranes out of this graphene/gold stack. Although this procedure leads to the same structural results, published Raman data show that the direct application of photoresist to the graphene layer and the direct evaporation of Au onto the graphene leads to significant

defects in the graphene film. This is omitted in the procedure described here, in which no photoresist is used and the continuous graphene layer is not present during metal evaporation. The actual support of the metal layer provided under applied stress on the membrane must be further examined, as freestanding metal films (thickness 10-100 nm) may rupture at strains as low as 1 – 2%, while supported metal films resist strains of up to $\approx 20\%$.³⁸¹ Other thin materials which are often used for the support of graphene films are silicon nitride and glassy carbon.^{382,383} So far, it has only been reported that graphene was transferred onto such reinforcement substrates. The stabilization of the transfer process itself by one of these materials as discussed here was not reported before.

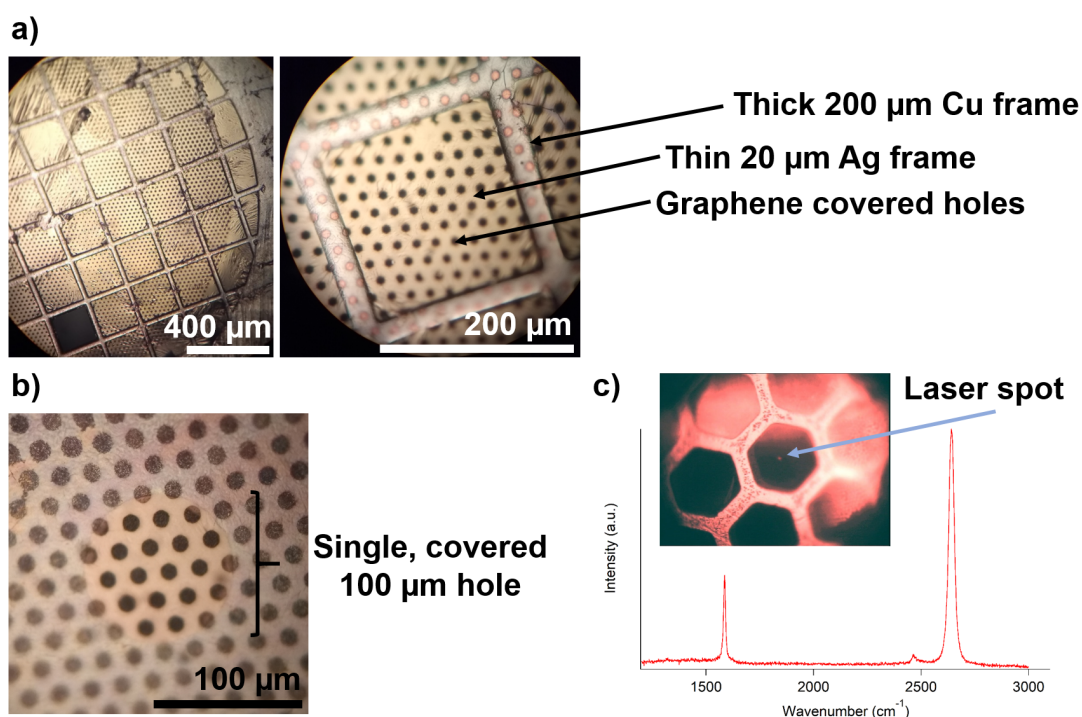


Figure 104 : Different samples showing freestanding graphene membranes fortified by a regular silver grid. a) Covered 200x200 μm patterned Cu grid covered with a patterned Ag layer with 20 μm diameter holes and a continuous graphene layer. b) Single hole aperture of 100 μm diameter covered by a 10 μm Ag layer and a continuous graphene membrane. c) Raman spectrum recorded on a sample transferred according to the procedure described in Fig. 103, showing no signs of the defect-induced D-band. The optical image is contrast-enhanced and shows the reflection of the laser spot on the area from which the Raman spectrum was recorded (see arrow).

However, one difficulty of this sample arrangement is the superposition of thin material layers with different thermal expansion coefficients. The stack composed of closely contacted Ag (high thermal expansion coefficient) and graphene (negative thermal expansion coefficient) does not withstand thermal annealing. Since thermal cleaning procedures are mandatory in order to use freestanding graphene under UHV conditions, an alternative reinforcement protocol was developed, which is presented in the next paragraph.

10.3.2. Graphene + Graphene

Similar to the metal supporting grid, an ultrathin graphene layer can be patterned to also form a supporting grid for a second, continuous graphene layer. There exist several ways to achieve the combination of both graphene layers, which may differ in the acquired sample strength and the remaining impurities on the membrane. Fig. 105 shows a very simple way to produce an artificial, patterned graphene stack from the front- and backside of a Cu foil where graphene was grown. After patterning the graphene film lithographically and dissolving the Cu foil by chemical etching, the patterned backside merges with the continuous graphene film on the frontside. The results of the synthesis protocol are presented in Fig. 106. Fig. 106a) shows the patterned backside of the graphene layer on Cu. Figure 106b) displays the optical image of the final reinforced graphene membrane after successful transfer onto a 200 μm hole array on silicon nitride. The high transfer success rate can be seen in the large optical image, while the cleanness of the samples can be observed at higher magnification. Finally, optical microscopy combined with Raman spectroscopy data is shown in Fig. 106c). Here, arrows point to the laser spot on the freestanding graphene membrane from which Raman data were taken. The acquired Raman spectra show almost perfect graphene, although a tiny D-band close to spectral resolution still indicates the presence of a certain amount of defects in the membrane.

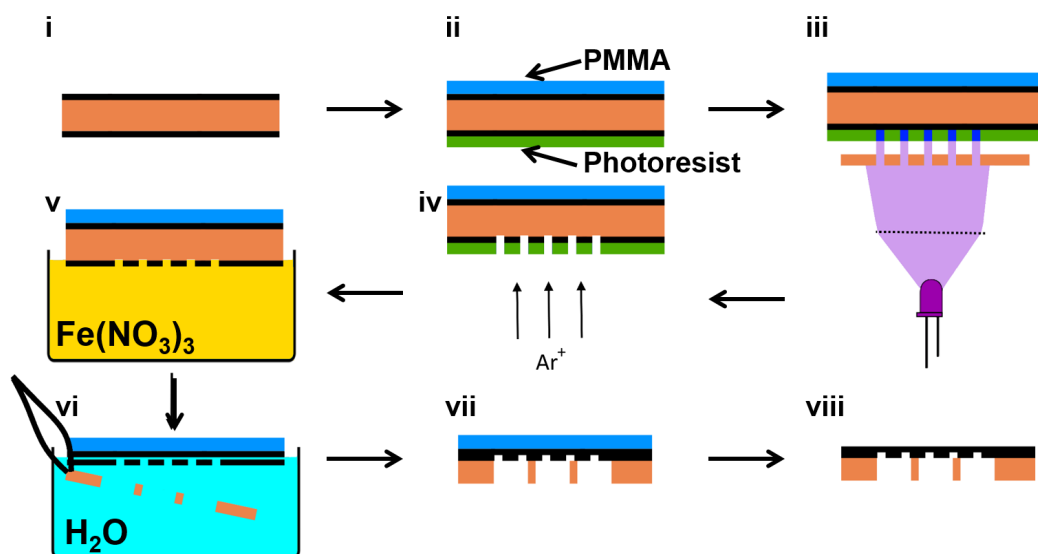


Figure 105 : Complete transfer procedure leading to a patterned artificial bilayer graphene sample. A Cu foil covered with graphene films on front- and backside is protected with PMMA on one side and covered with a photoresist on the backside. The backside is illuminated, developed and sputtered as described in Fig. 98. Subsequently, the Cu in between both graphene layers is removed by chemical etching, leading to the merging of both graphene films. After cleaning in several solutions the sample stack can be removed from the final water surface, transferred to the final target support and dried. Finally, the protecting PMMA layer on the continuous graphene layer is dissolved in hot acetone.

In contrast to the graphene+metal support structure, the pure graphene sandwich membrane has a single thermal expansion coefficient. Only by choosing the correct substrate material (e.g. silicon nitride with the low thermal expansion coefficient of $\alpha \approx 1.5 \text{ ppm K}^{-1}$),³⁸⁴ the degassing of samples in UHV is not hindered due to the thermal stress during annealing any more.

This newly created sandwich membrane material can be seen as both laterally and vertically patterned heterostructure. While heterostructures are already the topic of several research reports,^{70,5} the inherently fortified heterostructure with thicker and thinner segments for the formation of stabilized membrane materials has not been discussed so far. Combining both, the stability of thicker graphene with the ideal, atomically thin segments greatly reduces the gap between the required sample properties, e.g. for pressurized, vacuum-compatible cells analyzed by *in operando* photoelectron spectroscopy.

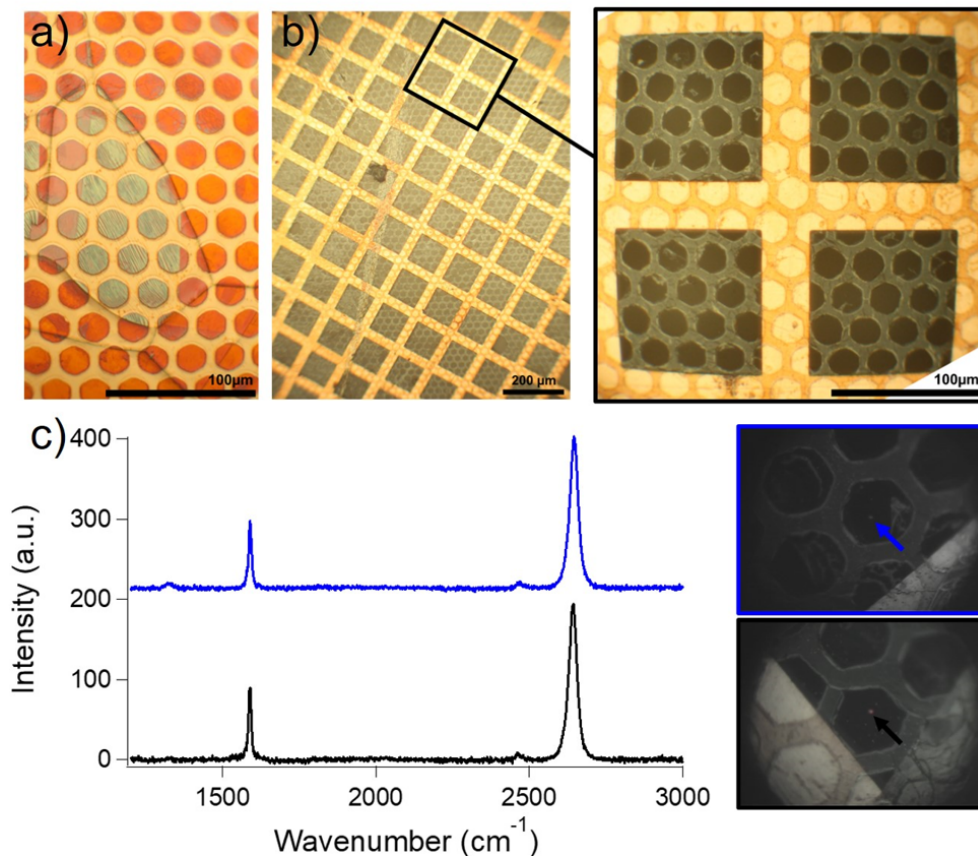


Figure 106 : Sample synthesized according to the procedure described in Fig. 105. a) Optical image of the oxidized sample showing the structure of the backside graphene film. b) Optical images of the final reinforced graphene layer (20 μm holes) on a 200x200 μm silicon nitride support grid. c) Local Raman spectra recorded on the freestanding part of the synthesized membrane (see blue and red arrows). The graphene layer can be identified by Raman spectroscopy. While the reinforced segments show an optical contrast, this is almost not visible for the single graphene areas where arrows point to the reflection of the laser spot. The respective Raman spectra show the signature of perfect SLG with a tiny defect-induced D-band close to the spectral resolution of the instrument.

10.4. Selective transfer of ideal sample areas to single hole apertures

As shown in the sections above, there are two main substrate geometries used for the transfer of graphene: A regular array of holes or a single hole aperture. Transfer onto an array of holes leads to good information about the transfer statistics and a higher chance of a particularly well covered segment. Nevertheless, such samples cannot be used to create a leak tight, UHV compatible cell, as the amount of defects on a large membrane will increase. Reducing the number of holes to a single isolated aperture increases the chance of successfully sealing the sample, but most of the transferred sample (typically at least $3 \times 3 \text{ mm}$ in size) is wasted on the unpatterned substrate surface. The ideal utilization of a graphene sample would be to transfer a large graphene layer onto an array of holes. From the results acquired after a graphene transfer, the best area of the suspended graphene membrane could be chosen in order to subsequently seal a second sample substrate with a single hole aperture. A method to achieve such type of transfer is shown in Fig. 107: If the chosen area of the hole array sample covered with graphene is exactly positioned above the single hole aperture, a single droplet of solvent can be used to create a liquid layer between both substrates, which assures intense contact of both surfaces. After the evaporation of the droplet, the adhesion between both samples will allow the smaller (single hole aperture) substrate to connect to the graphene layer.

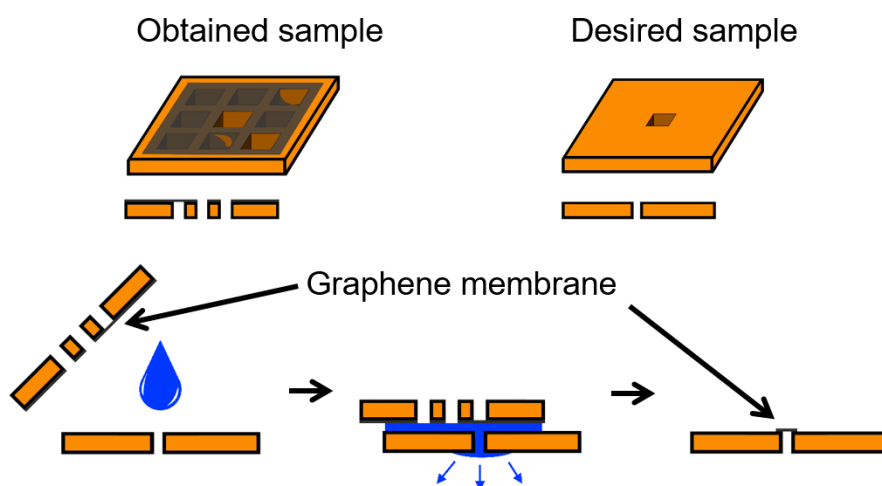


Figure 107 : Method for the selective transfer of membranes from one substrate to another. To increase the chance of producing a pristine graphene membrane, transfer procedures are often performed onto hole array structures. It is possible to transfer a selected hole from a grid substrate to a single hole aperture by placing both samples on top of each other and introducing a single droplet of acetone between both samples. The evaporating solvent will create a strong contact between both samples, leading to the sticking of the graphene membrane to the one with the smaller hole size. If the single hole aperture is smaller than a single hole in the grid structure, this transfer procedure can be applied.

A successful proof of principle experiment is imaged by optical microscopy as shown in Fig. 108: a) The Ag-grid type supported graphene membrane shows 4 ideally graphene covered, $200 \times 200 \mu\text{m}$ sized holes on the main grid. One of these membranes is placed on top of a single, $100 \mu\text{m}$ diameter aperture, as shown in Fig. 108b). The exact position is fixed with a tweezer pressed against the substrates. After applying a small acetone droplet between both samples and evaporation of the liquid, the graphene/silver membrane is attached to the single hole aperture. The resulting sealing membrane is imaged in Fig. 108c).

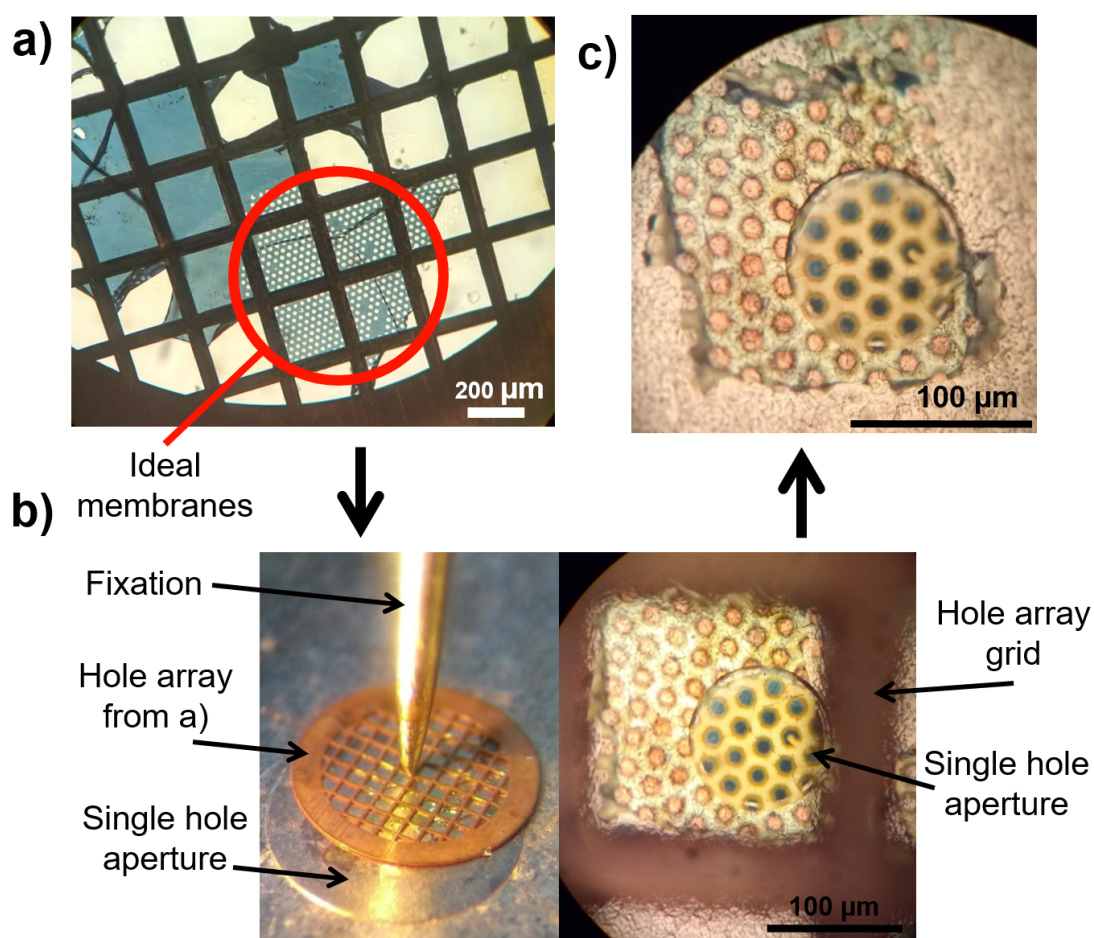


Figure 108 : Optical images of a Ag-grid type reinforced graphene membrane transferred onto a local hole. a) The covered grid substrate shows four well-covered holes of $200 \times 200 \mu\text{m}$ size. b) One of these holes is placed on a $100 \mu\text{m}$ diameter single hole aperture. The grid is positioned using a fixed tweezer. c) After application and evaporation of an acetone droplet, the Ag-fortified graphene layer is attached to the single hole of the target substrate.

The procedure will greatly facilitate the synthesis of ideally closed, single hole aperture samples. Moreover, the sample substrate is only in the final transfer step exposed to an acetone droplet and does not get in contact with polymers or contaminating solvents. In

principle, the transfer step may be done in vacuum, but a method would be required to increase the contact area between both sample substrates, which replaces the effect of the acetone droplet. A sample substrate could then be prepared in UHV and covered with graphene without exposure to air, which would allow to synthesize new surface structures in UHV which are then sealed with graphene.

11. Summary and Conclusions

CVD growth of graphene was analyzed regarding nucleation density, growth rate, multi-layer formation, contamination influence and finally the transfer success rate of the resulting freestanding graphene membranes. By separate analysis of the topics it was possible to individually develop parameter-dependencies of these characteristics and pinpoint key steps of the synthesis routes.

When approaching the **thermodynamic reaction equilibrium conditions** K_{eq} of the CVD graphene formation reaction from methane, the flake growth rate converges towards zero. To reliably distinguish graphene growth and decay at vanishing growth speeds, the flake shape was identified as reliable criterion, which changes from a hexagonal shape during flake growth towards a rounded shape during graphene island decay. Using this shape change as criterion for graphene growth or decay the equilibrium constant K_{eq} value at 1045 °C was pinpointed. Subsequently, the temperature dependence of K_{eq} was determined, allowing the determination of the reaction enthalpy of $\Delta_R H^\circ = 91.8 \pm 2.4 \text{ kJ mol}^{-1}$ and reaction entropy $\Delta_R S^\circ = 108.0 \pm 1.8 \text{ J mol}^{-1} \text{ K}^{-1}$.

Using this information, a **kinetic growth model** was developed that describes the flake growth fed by a pre-equilibrated C_{ad} lattice gas. The growth model contains two unknown parameters, the detachment energy E_{det} of carbon atoms detaching from the graphene flake and the entropy $\Delta_{dec} S^\circ$ of the methane decomposition reaction. Using a large dataset of experimentally determined graphene growth velocities v these two fit parameters are determined to be $E_{det} = 451 \pm 26 \text{ kJ mol}^{-1} = 4.7 \pm 0.3 \text{ eV}$ and $\Delta_{dec} S^\circ = 260 \pm 20 \text{ J mol}^{-1} \text{ K}^{-1}$. The complete parameter set allows to predict the flake growth velocity for any chosen CVD growth condition, which is displayed in a 3-dimensional plot with the mass action constant Q_{exp} and temperature T as axis. For a better overview, a plot at one temperature can be used as shown in Fig. 109, where the equilibrium lines of graphene and graphite formation, as well as several predicted growth velocities can be directly related to the set parameters $p(H_2)$ and w of the CVD synthesis.

The fit value of $\Delta_{dec} S^\circ$ allows estimating the entropy of the adsorbed carbon atoms S_{Cad} on the Cu surface, which is related to the coverage $[C_{ad}]$ according to the effect of the configurational entropy of the C_{ad} phase. The C_{ad} coverage is calculated to range between $10^{-10} - 10^{-8} \text{ ML}$ under reaction conditions. The experimental growth rates from 59 literature references were compared to the predictions of the growth model, with the conclusion that the model correctly predicts the growth velocity v up to a certain distance to K_{eq} , with velocities v up to 1 mm h^{-1} . Further away from equilibrium, the provided carbon from the gas phase seems to be the limiting factor, reducing the observed growth rate. A systematic study of experiments under $p(CH_4)$ -limiting conditions indicates a proportionality between the CH_4 partial pressure and the growth rate.

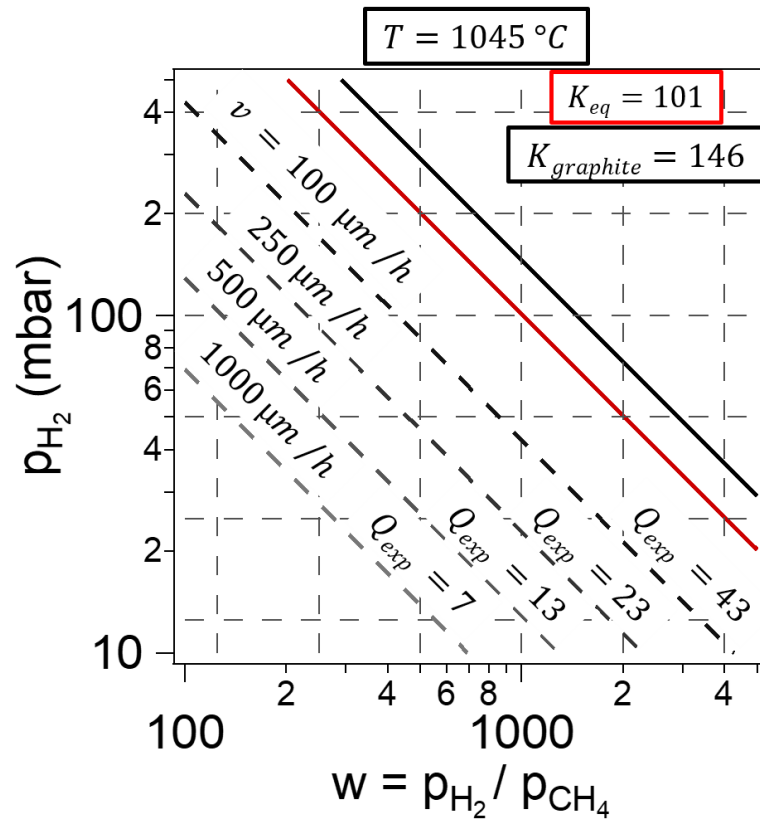


Figure 109 : $p(H_2) - w$ -diagram for graphene growth at 1045 °C, including the thermodynamic equilibrium conditions for graphene (K_{eq}) and graphite ($K_{graphite}$), as well as several kinetic growth velocities v predicted by the established growth model.

This empirically determined correlation is approved by the literature references which could not be explained solely by the kinetic growth model. The proposed growth process leading to a direct $p(CH_4)$ -limitation indicates that each grown graphene flake develops a capture zone on the surrounding Cu surface, inside which all adsorbing methane from the gas phase provides the required carbon material for flake growth.

The **nucleation** of new graphene flakes depends on the impurities present on the sample surface and the chosen reaction conditions. The study of nucleation rates under different growth conditions on pre-cleaned Cu substrates allows to determine several critical C_{ad} concentration levels on the surface. It could be shown that graphene flakes form upon heterogeneous nucleation. The effect of two different C_{ad} concentrations could be identified:

- $[C_{ad}] > c_{nuc}$: Nucleation at stationary impurity particles sets in. When slightly lowering $[C_{ad}]$ afterwards, graphene can be grown without nucleation of new islands during flake growth.
- $[C_{ad}] > c_{continuous} > c_{nuc}$: Continuous nucleation over the course of the complete CVD growth reaction is observed on the sample.

Making use of the above finding, the introduction of an artificial nucleation step allows disentangling the flake nucleation and flake growth. It then becomes possible to grow graphene at conditions where due to the absence of nucleation events commonly no graphene flakes are observed.

The evaluation of the thermodynamic properties of graphene on Cu indicates that the formation of single layer graphene (SLG) is less exergonic than the one of graphite and, hence, also as **multilayer graphene**. This is visible in the shifted equilibrium lines in the $Q_{exp} - T$ chart of Fig. 109. The shift indicates that a parameter regime between both equilibrium lines exists, at which SLG becomes unstable while multilayer graphene should remain stable. I was able to verify this hypothesis using several experimental approaches, leading to the targeted growth of multilayer graphene flakes with a minimum SLG share.

The influence of oxygen impurities on the graphene decay process was analyzed to ensure the negligible influence under common growth conditions. Oxygen contaminations can be reliably identified by observing the formation of hexagonal holes in the graphene flakes, while the graphene rim remains straight. This can reliably be distinguished from thermodynamically induced graphene decay, during which the graphene decay sets in from the island rim, also leading to a flake shape change.

Silicon and carbon impurities have been identified as highly relevant for the understanding of graphene growth on industrial Cu foils in quartz glass reactors. The silicon contamination originating from the quartz tube wall was shown to be accumulated in the Cu foil by high-temperature, high-pressure hydrogen treatment. This dissolved Si contamination can be segregated and pinned on the foil surface upon oxygen exposure. This process can be very reliably observed on pure Cu as well as on Cu partially covered with graphene flakes. On Cu entirely covered by graphene, oxygen induced Si surface enrichment could be identified only at defects in the graphene film. When growing graphene on a Si enriched Cu surface, graphene is observed to nucleate at such silicon oxide particles. However, the intercalation of larger amounts of silicon between grown graphene and the Cu substrate is not possible. Carbon contaminations present as impurities in the Cu foil can severely diminish the graphene quality and influence the formed layer number. In addition to the already known oxidative pretreatment, the foregoing treatment in hydrogen was identified to be necessary to increase the cleaning effect of the oxygen treatment regarding carbon contaminations in the Cu foil.

The **transfer of grown graphene films** was optimized with the aim to produce a leak-tight gas cell for the separation of a high-pressure sample from an ultra-high vacuum environment. This is possible using an artificially prepared stack of two graphene films, spanning holes in the 100 μm diameter regime. Here, leak tight membranes were achieved that relate to a single defect hole of $\approx 130 \text{ nm}$ diameter on the 100x100 μm sized membrane. I. e., a membrane with the defective area fraction of $1 : 10^8$ was achieved. To increase

the transparency of sealing membranes, a continuous graphene layer was combined with a patterned metal and also with a patterned graphene layer, leading to an intrinsically reinforced, ultrathin membrane material. The efficiency of the graphene membrane formation can be enhanced by a proposed second transfer mechanism, which allows the transfer of a single membrane from a mesh to a second substrate with a single hole.

The gained insights into the graphene growth and transfer processes described in this thesis can be used to develop growth recipes for custom-tailored graphene samples. Using the data obtained from thermodynamic and kinetic experiments, it is possible to design a complete reaction sequence before starting the growth process. Key demands for the control of multilayer areas and contaminants were mapped out, and also the strengths and weaknesses of known transfer techniques were described. Depending on the research topic or application device, this work offers a large amount of information on how to improve the synthesis pathway. Fundamental values of graphene on Cu were derived from the experimental data, enhancing the data available also for theoretical calculations in the future.

Using the presented data as a reference, it is facilitated to transfer the gained knowledge onto graphene growth on different substrates, by different precursor molecules, at different growth conditions or even the growth of other 2D materials by chemical vapor deposition.

12. Appendix

12.1. Calibration of the XPS signal ratio C/Cu for SLG

12.1.1. Theoretically predicted photoemission ratio ratio between C and Cu

The theoretically expected values for the signal intensity ratio between the C 1s peak and several Cu signals is determined according to case c) of a layered sample system presented in the XPS methods section. The used values are listed in Table 31. The ratio of molar volumes between graphene/graphite and copper is 1.34 : 1, and the thickness of a single graphene layer is set to 3.35 Å.

Table 31 : Ionization cross section σ of $Al_{K\alpha}$ radiation in Megabarn (Mb) with regard to the noted atomic orbitals of C and Cu,³⁸⁵ as well as the inelastic mean free path of the emitted photoelectrons λ_X through the respective materials.⁸⁸

	$\sigma(Mb)$	E_B	λ_C	λ_{Cu}
C 1s	0.013	284 eV	21.0 Å	18.6 Å
Cu 3p	0.033	76 eV	23.9 Å	21 Å
Cu 3s	0.013	122 eV	23.2 Å	20.5 Å
Cu 2p	0.3438	932 eV	11.7 Å	10.8 Å

According to eq. 3.7 in section 3.3.4, the ratio between the C 1s signal intensity for SLG/BLG and the respective signal from the copper substrate is determined and listed in Table 32. The low kinetic photoelectron energy leads to higher surface sensitivity of the Cu 2p-photoelectrons compared to the ones originating from the Cu 3s and Cu 3p core levels. As a result the Cu 2p is the signal most sensitive to changes between single and double layered graphene.

Table 32 : Calculated signal intensity ratios for single- and double layer graphene between the C 1s and several Cu signals excited by $Al_{K\alpha}$ radiation and detected at normal emission.

	C 1s/Cu 3p	C 1s/Cu 3s	C 1s/Cu 2p
SLG	0.100	0.255	0.011
BLG	0.214	0.547	0.0277

12.1.2. Experimentally determined ratio

A single layer graphene sample was grown at 945 °C according to the experimental recipe E. 74 and a photoelectron spectrum of the sample was recorded immediately after growth. The areal intensity ratios of the fitted C 1s and Cu(2p, 3s, 3p) signals are listed in Table 31, showing a nominal amount which exceeds the theoretically predicted value by a factor $\approx 2.3x$. It is largely unknown how the carbon dissolves in the Cu bulk during graphene growth and whether or not it accumulates during cooling of the Cu foil after CVD growth. Kraus *et al*¹⁸³ have characterized bare Cu samples after heating to reaction conditions and observed that carbon dissolved in the bulk can segregate to the substrate surface during cooling. The process seems to depend on the cooling rate and, as a result, the expected C 1s/Cu 2p intensity ratio of a covering graphene layer on graphene covered Cu surface remains unknown. It may be possible that non-graphene carbon segregates from the Cu bulk and contributes to the measured carbon signal intensity in addition to the covering graphene layer. Note that the normalization with SLG/BLG used here assumes all carbon to be above the Cu atoms. A carbon species distributed in the Cu volume would be underestimated by the referencing to single- and bilayer graphene. Also, transport through air may cause adsorption of impurities and increase the amount of carbon based species, although this would be expected to result in the increase of carbonaceous or other organic species at ≥ 286 eV.

In order to eliminate or decompose the potential contaminants, the sample was heated in UHV to 450 °C at a maximum background pressure of 8×10^{-8} mbar and subsequently again photoelectron spectra were recorded after sample cooling in UHV. *Ex situ* Raman spectroscopy showed that the complete graphene film remained intact and no defects were introduced by this heating procedure, as can be seen in Fig. 110b). The C 1s spectra before and after heating are shown in Fig. 110a), their respective fitted integral intensities are listed in Table 33. The C 1s intensity has dropped by about one third after the heating process, the overall peak has slightly shifted towards higher binding energies, from a maximum of ≈ 284.65 eV before to ≈ 284.75 eV after heating.

The unchanged Raman spectra before and after heating show that the carbon in the graphene layer is not affected by the heating process in UHV. Thus, there must be carbon of a different species present, which does not contribute to the Raman signal. The nominal quantity of this graphene species is in the order of up to 1 ML graphene (2 atomic Cu layers), which coincides with the observations made by Kraus *et al*.¹⁸³ They observe that Cu samples cooled from reaction conditions (950 °C, H_2 gas phase) without any grown graphene islands show a C 1s signal amounting to ≈ 2 ML of carbon on the surface. As all Cu signals before heating are damped almost equally according to the normalized peak areas shown in Table 33, it seems that this carbon species is not purely on the surface, but rather homogeneously distributed over the probed Cu layers (see Table 33). Otherwise, stronger damping of the Cu 2p signal would have been expected compared to the less

surface sensitive Cu 3p and Cu 3s species. After heating, the amount of carbon detected is still too high by about 20-40%. As atomic or amorphous carbon on the sample surface would not desorb from the surface by itself during heating to these temperatures in UHV, other processes cause the C 1s signal reduction upon annealing. The agglomeration of this carbon species on the surface may be possible, or the diffusion into the substrate bulk. The reaction of carbon with adsorbed oxygen and subsequent desorption cannot explain the strong decrease in C 1s intensity, as the detected oxygen signal on the sample is very low (see Fig. 110c).

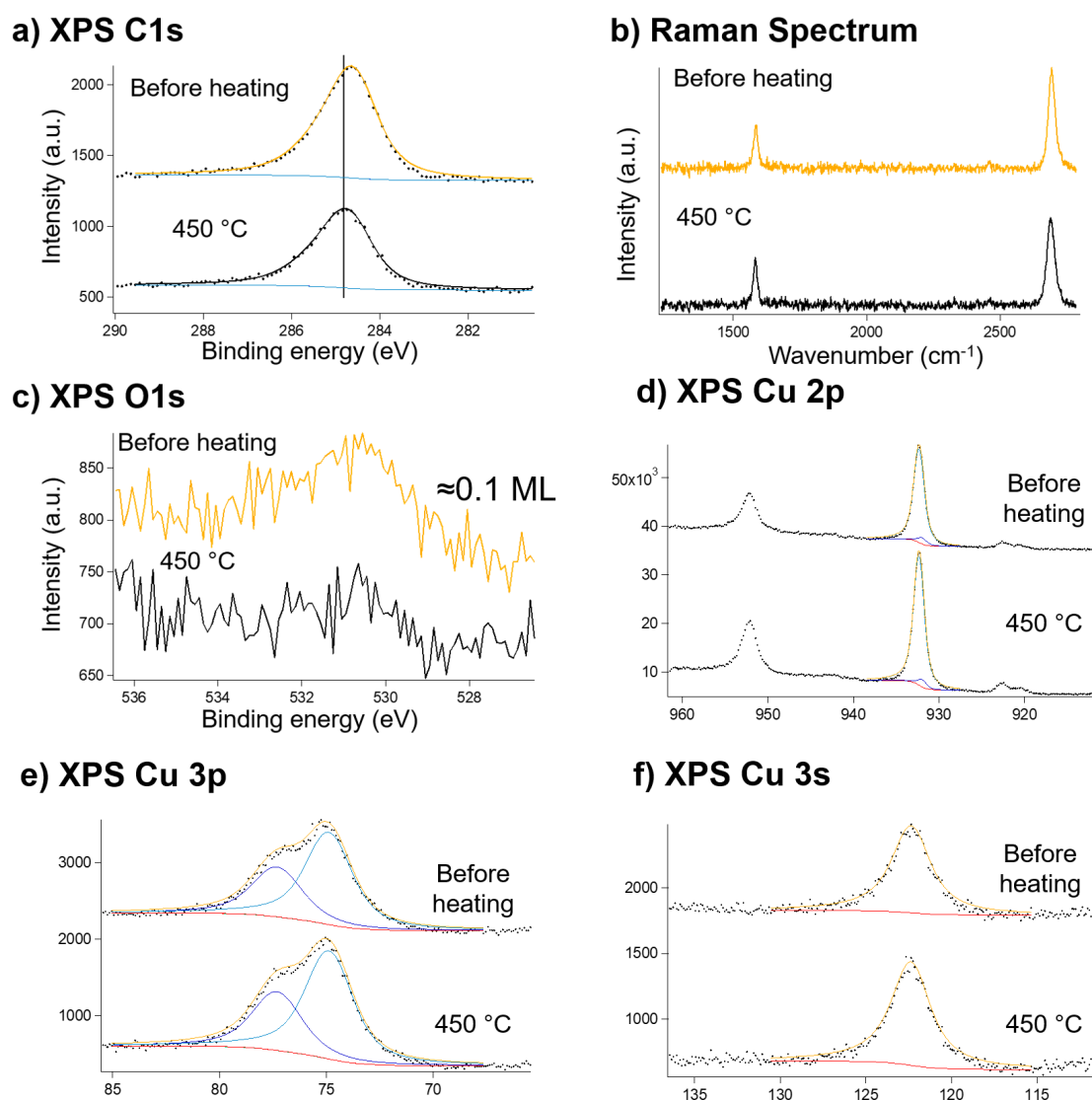


Figure 110 : Calibration SLG sample used to determine the minimum C 1s signal of a continuous graphene layer. a) XPS C 1s spectra as-synthesized and after heating in UHV to 450 °C, showing a significant reduction in absolute C 1s intensity. b) Raman spectra show the same spectral signature of the graphene film before and after the UHV-annealing. c) O 1s XPS spectrum showing the removal of oxygen species on the sample during heating. d-f) Cu core level XPS spectra before and after annealing in UHV.

Table 33 : Experimentally determined C 1s intensities of the sample shown in Fig. 110 and the relative amount compared to the expected ratio for SLG. While the carbon content before heating is too high by a factor of around 2.4x, this is reduced to a factor of 1.4x after the sample heating in UHV.

	C 1s/Cu 3p	C 1s/Cu 3s	C 1s/Cu 2p
Reference SLG	0.100	0.255	0.011
Reference BLG	0.214	0.547	0.0277
CVD growth at 945 °C before heating in UHV to 450 °C	0.23	0.61	0.025
Normalized to theoretical prediction (tab. 32)	2.3	2.4	2.3
CVD growth at 945 °C after heating in UHV to 450 °C	0.14	0.36	0.013
Normalized to theoretical prediction (tab. 32)	1.4	1.4	1.2

According to Blume *et al.*,³⁶⁴ the C 1s signal from the carbon in the graphene layer may shift towards higher binding energies after heating in UHV due to the coupling to the Cu substrate, caused by the detachment of intercalated oxygen species. The shift in the peak position of the C 1s signal may therefore be related to the graphene and not to the non-graphene carbon contaminant.

12.1.3. Dependence of the C 1s/Cu signal ratio on the CVD growth temperature

If the second carbon species present in the grown graphene samples was caused by the segregation of dissolved carbon during the sample cooling from CVD growth conditions, a correlation between the carbon signal and the growth temperature would be expected. A series of SLG samples was grown at different temperatures to test this hypothesis. XPS spectra of each sample were measured directly after synthesis and after heating in UHV to 450 °C. The fitted peak intensities are listed in Table 34. It can be seen that at all temperatures, the carbon signal before heating in UHV is significantly larger than expected for SLG. The ratio drops after the heating process. As for the analyzed samples the amount of formed multilayer areas varied, the multilayer ratio was estimated by optical microscopy after the oxidation of the sample. The C 1s intensity was then normalized by eq. 12.1:

$$I_{Norm} = \frac{I_{measured}}{\chi_{SLG} * I_{SLG} + \chi_{BLG} * I_{BLG}} \quad (12.1)$$

Table 34 : Results of the XPS characterization of several continuous graphene samples grown at different temperatures. All samples show a strongly increased C 1s content before heating in UHV. After heating, the C 1s/Cu ratio drops significantly to a factor of 1.2-1.7 after multilayer ratio correction (see text).

Normalized signal to theoretical prediction		C 1s/Cu 3p	C 1s/Cu 3s	C 1s/Cu 2p
Exp. E. 74	before heating	2.3	2.4	2.3
(945 °C, 0% BLG)	after heating	1.4	1.4	1.2
Exp. E. 75	before heating	2.9	2.9	3.0
(970°C, 0% BLG)	after heating	1.7	1.7	1.5
Exp. E. 76	before heating	2.5	2.5	2.4
(1045°C, 16% BLG)	after heating	1.5	1.5	1.3
Multilayer corrected:	after heating	1.3	1.3	1.1
Exp. E. 77	before heating	2.9	2.9	2.7
(1060°C, 26% BLG)	after heating	1.9	1.9	1.7
Multilayer corrected:	after heating	1.5	1.5	1.3

In this equation, χ refers to the determined ratio of SLG and BLG, and I_X refers to the predicted C 1s/Cu (2p, 3s, 3p) ratios as listed in Table 32. These multilayer-corrected values are also inserted in Table 34. For the normalization, all multilayer areas were assumed to be bilayer graphene areas.

No clear trend can be observed for the temperature dependence of the signal for the additional carbon species. The first carbon signal is approximately 1 ML higher than expected in each sample and drops after the heating procedure. After multilayer-correction, all samples show approximately the same C 1s/Cu signal ratio within the experimental precision. As all grown graphene samples lead to the same carbon to copper ratios of approximately 1.4 times the theoretically expected value for SLG, this value is used as reference for CVD grown single layer (UHV heated) graphene in this work. This means that the ratios used as SLG-graphene calibration are: $C\ 1s/Cu\ 2p = 0.013$, $C\ 1s/Cu\ 3s = 0.36$, $C\ 1s/Cu\ 3p = 0.14$.

12.1.4. Calibration by removing the graphene layer

A second, destructive measurement method can be used to control the results acquired above. In this case, the measured sample SLG/Cu can be sputtered with Ar^+ ions to remove the graphene layer. A subsequent XPS measurement delivers the values of the

undamped Cu signals for this sample. This procedure was already applied by Kraus *et al* and is in detail explained in reference ⁵⁹. By performing this type of measurement with $Al_{K\alpha}$ and $Mg_{K\alpha}$ radiation, the damping of the Cu signals (Cu 2p, Cu 3s, Cu 3p) can be determined for 6 different electron kinetic energies. The ratio values obtained for an unheated and heated graphene sample are plotted in Fig. 111 together with the predicted electron damping by Tanuma *et al.*⁸⁸ It is very well visible that the values for the heated graphene sample show damping as predicted by calculations for SLG, while the unheated samples show damping according to BLG. The usage of the above-mentioned C/Cu ratios for SLG by the described, undestructive XPS procedure is approved by this second quantification method. The presence of a significant surplus of carbon of about one additional monolayer is also seen for the unheated samples using this method.

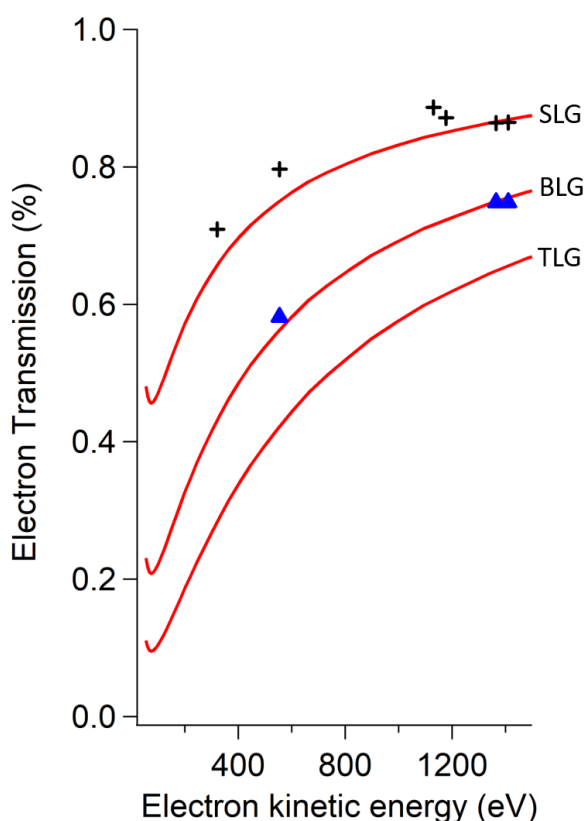


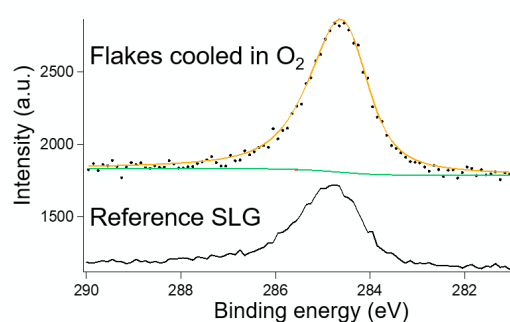
Figure 111 : Electron transmission of graphene samples before (blue) and after (black) heating of the sample in UHV to 450 °C. The reference of the electron transmission is obtained by sputtering the sample for 20 min with Ar^+ ions (Acceleration voltage: $E_{ion} = 1$ kV, Ion flux: $I_{ion} \approx 6 \mu A$) and measuring the graphene free Cu surface afterwards. The red lines mark the calculated values for a single atomic graphite layer (SLG), two graphite layers (BLG) and TLG, all at 0° emission angle.⁸⁸

12.1.5. Origin of the additional C 1s signal

After the experiments described above, the question remained unanswered, whether the additional carbon signal in the XPS spectra originated from the reactor growth and cool-

ing process, or from the exposure of the sample to air. To clarify this uncertainty, two experiments were conducted. First, a sample of graphene flakes (coverage <50% ML) was grown in reaction gas and subsequently cooled to 750 °C in the reaction gas mixture. At this temperature, the $CH_4 + H_2$ mixture was replaced by an Ar gas flow (20 sccm, 20 mbar), which contains traces of oxygen impurities. These are enough to react with the carbon on the sample (see also chapter 8.1.1). This treatment was kept for 60 min to deplete the carbon from the sample. After this time, the sample was removed from the hot reactor zone and analyzed by XPS, which is shown in Fig. 112a). The C 1s spectrum is normalized to the intensity of the Cu 3p signal to be able to compare the intensities to the signal of the heated SLG sample shown as a reference. The C 1s signal, regardless of the heating procedure in O_2 , still shows a C 1s coverage of approximately 2 ML compared to a graphene flake coverage relating to $\approx 50\%$.

a) XPS C1s



b) XPS C1s/Cu3p ratio

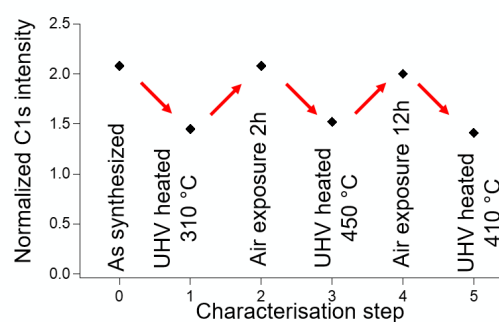


Figure 112 : Characterization of specially treated graphene samples to identify the origin of the unknown carbon signal detected by XPS for freshly grown graphene samples. a) XPS C 1s spectrum of a flake-covered graphene sample (coverage < 50%). Instead of direct cooling in reaction gas, the sample was cooled to 750 °C in reaction gas, treated in an Ar/O_2 atmosphere for 60 min and subsequently cooled in this same atmosphere to room temperature. Comparison to the reference SLG spectrum shows a significantly higher C 1s signal for the flake-covered sample, indicating that the additional carbon content does not originate from the reactor cooling process. b) Normalized XPS C 1s/Cu 3p intensity ratio of a completely covered (multilayer) graphene sample. The sample was repeatedly heated in UHV and subsequently exposed to laboratory air, showing that the C 1s content is accordingly reduced after UHV-heating and recovers after ventilation of the sample. The stability of the graphene layers over several heating/ventilation cycles was tested by Raman-spectroscopy. (Experimental details: a: E. 68 , b: E. 77)

In a second experiment, the multilayer sample also described in Table 34 was alternately heated in UHV and then exposed to air. The intensity of the C 1s/Cu 3p XPS spectra measured after each step are plotted in Fig. 112, the respective spectra are shown in Fig. 113. It shows that, while the C 1s signal lowers after the heating procedure in UHV, it returns to the original value after the exposure of the sample to air. This process can be repeated several times with the same result.

The two experiments described above show that the origin of the additional C 1s signal intensity observed for untreated samples in UHV does not purely originate from the cooling process in the reactor after the graphene synthesis procedure. For the sample cooled in an $Ar(O_2)$ atmosphere, the treatment for 60 min at 750 °C should be enough to remove surface carbon from the sample.

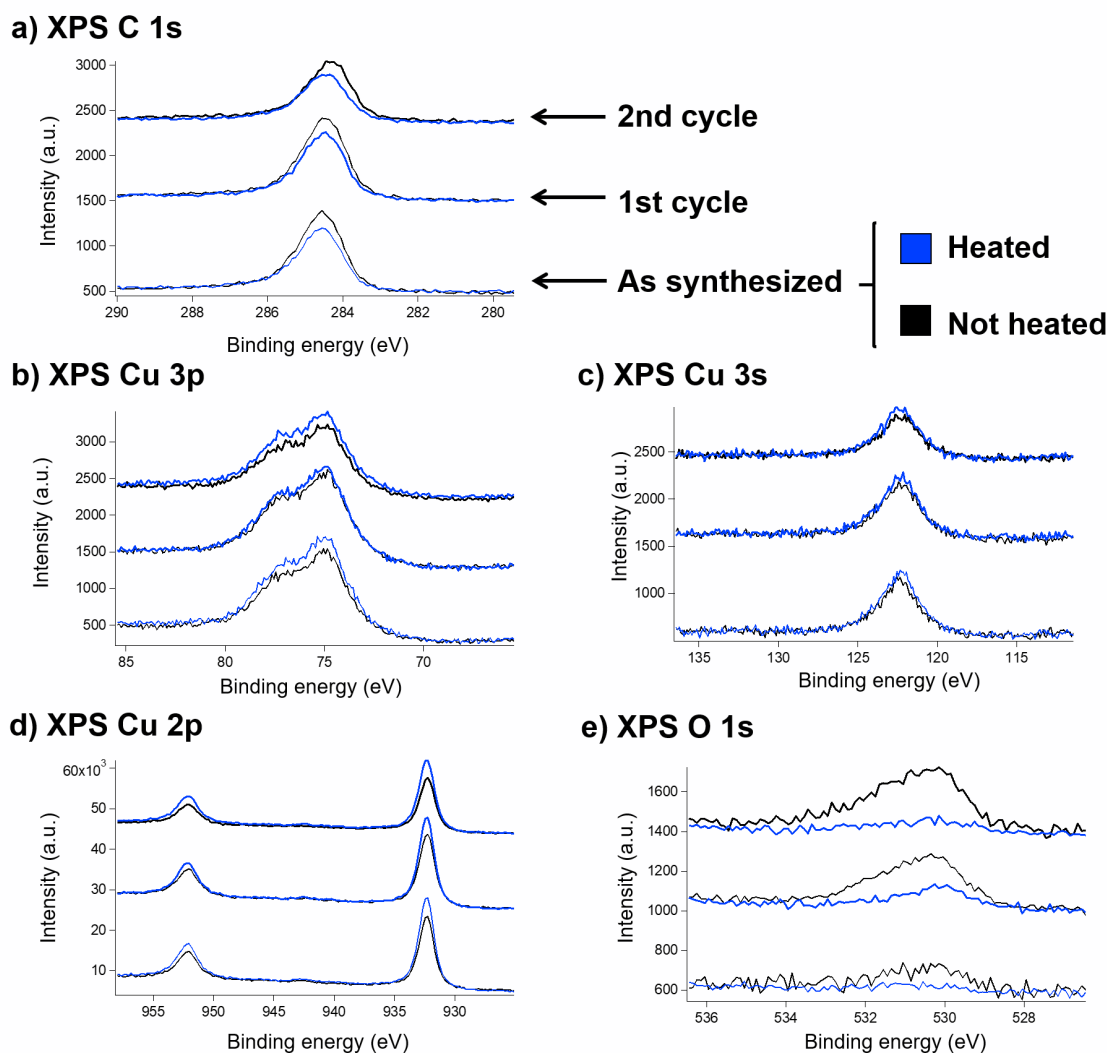


Figure 113 : Respective XPS spectra of the samples shown in Fig. 112. One sample is measured by XPS after synthesis (black curve "as synthesized") and subsequently after annealing in UHV (blue curve "as synthesized"). The same procedure is repeated twice after exposing the sample to air and re-inserting it into UHV.

With a graphene coverage lower than 50%, the blocking effect of the graphene towards gas adsorption cannot explain this retained C 1s signal. As for the sample repeatedly heated in UHV, the return of the C 1s signal only allows two possible scenarios. Either an external carbon source replenishes the carbon adsorption sites on the surface or the present carbon is dissolved into the substrate bulk (XPS signal vanishes) and again

dragged to the surface (XPS signal returns). For the first possibility, the sample completely covered with graphene would only allow direct adsorption on top of the graphene layer. A diffusion process below the closed graphene layer would be expected to take much longer than the air exposure time of 2 h. For the second possibility, the diffusion of carbon from the bulk to the sample surface in air at room temperature should not be possible. While the exact nature of the carbon content in the Cu sample cannot be identified, the described experiments help to improve the handling of the samples and the correct interpretation of obtained data. Generally, carbon XPS spectra of graphene samples without an additional UHV treatment should be interpreted in a very restrained manner.

12.2. Derivation of the correlation between the carbon coverage and the configurational entropy S_{config}

12.2.1. Configurational entropy of a fixed number of adsorbates on a fixed number of adsorbate sites

When distributing N carbon particles on M copper adsorption sites, this creates a total of Ω possible distributions:

$$\Omega = \frac{M!}{(M-N)! - N!} \quad (12.2)$$

This leads to a configurational entropy resulting from this number of microstates of:

$$S_{config} = k_B \ln(\Omega) = k_B \ln \left\{ \frac{M!}{(M-N)! - N!} \right\} \quad (12.3)$$

The factorials can be resolved using Stirlings relation, according to which $\vartheta! \approx \vartheta \ln(\vartheta) - \vartheta$:

$$S_{config} = k_B \{ [M \ln(M) - M] - [(M-N) \ln(M-N) - (M-N)] - [N \ln(N) - N] \} \quad (12.4)$$

Neglecting the comparably small contributions from the linear terms and introducing the ratio of carbon coverage relative to the total number of copper atoms $\vartheta = N/M$, the equation can be converted in the following steps:

$$S_{config} = N k_B \left\{ \left[\frac{1}{\vartheta} \ln\left(\frac{M}{N}\right) \right] - \left(\frac{1}{\vartheta} - 1\right) \ln(M-N) - \ln(N) \right\} \quad (12.5a)$$

$$S_{config} = N k_B \left\{ \frac{1}{\vartheta} \left[\ln\left(\frac{1}{\vartheta}\right) + \ln(N) \right] - \left(\frac{1}{\vartheta} - 1\right) \left[\ln\left(\frac{1}{\vartheta} - 1\right) + \ln(N) \right] - \ln(N) \right\} \quad (12.5b)$$

$$S_{config} = N k_B \left\{ \frac{1}{\vartheta} \ln\left(\frac{1}{\vartheta}\right) - \left(\frac{1}{\vartheta} - 1\right) \left[\ln\left(\frac{1}{\vartheta} - 1\right) \right] + \frac{1}{\vartheta} \ln(N) - \left(\frac{1}{\vartheta} - 1\right) \ln(N) + \ln(N) \right\} \quad (12.5c)$$

$$S_{config} = N k_B \left\{ \frac{1}{\vartheta} \ln\left(\frac{1}{\vartheta}\right) - \left(\frac{1}{\vartheta} - 1\right) \ln\left(\frac{1}{\vartheta} - 1\right) \right\} \quad (12.5d)$$

$$S_{config} = N k_B \frac{1}{\vartheta} \left\{ \ln\left(\frac{1}{\vartheta}\right) - (1 - \vartheta) \ln\left(\frac{1}{\vartheta} - 1\right) \right\} \quad (12.5e)$$

$$S_{config} = N k_B \frac{1}{\vartheta} \left\{ \ln\left(\frac{1}{\vartheta}\right) - \ln\left(\frac{1 - \vartheta}{\vartheta}\right) + \vartheta \ln\left(\frac{1 - \vartheta}{\vartheta}\right) \right\} \quad (12.5f)$$

$$S_{config} = N k_B \frac{1}{\vartheta} \left\{ \ln\left(\frac{1}{1-\vartheta}\right) + \vartheta \ln\left(\frac{1-\vartheta}{\vartheta}\right) \right\} \quad (12.5g)$$

Calculating the entropy for 1 *mol* of carbon atoms, the product of carbon atoms and the Boltzmann constant is the gas constant R , leading to:

$$S_{config} = R \left\{ \ln\left(\frac{1-\vartheta}{\vartheta}\right) + \frac{1}{\vartheta} \ln\left(\frac{1}{1-\vartheta}\right) \right\} \quad (12.5h)$$

12.2.2. Configurational entropy of an equilibrated graphene system with a fixed total number of atoms on a fixed number of adsorbate sites

To estimate the configurational entropy of the adsorbed carbon atoms, C_{ad} , in thermodynamic equilibrium, we describe the system as sketched in Fig. 114. The total number of carbon atoms on the substrate is assumed to be constant, composed by the amount of carbon atoms in the graphene crystals and all C_{ad} atoms. The amount of adsorbing and desorbing carbon species from the gas phase is constant and does not modify the equilibrium entropy. The total number of adsorption sites on the Cu substrate M_{tot} is split up into the substrate sites blocked by the graphene island (M_{gr}) and the ones available for carbon adsorption (M_{ad}). Carbon atoms are assumed to adsorb on one particular site per substrate Cu atom, while the lattice constant of the graphene flake is different from that of the Cu lattice by a factor ρ , as given in eq. 12.6.

$$N_{gr} = M_{gr} * \rho \quad (\rho_{Cu} = 2.15) \quad (12.6)$$

If a carbon atom is detached from the graphene island, the respective N_{ad} value is increased by one, following eq. 12.6. Accordingly, per detached atom a fraction of adsorption site is created, increasing M_{ad} by this amount.

$$dN_{ad} = -dN_{gr} \quad (12.7)$$

In equilibrium, the Helmholtz free energy A_{ges} of the system is minimized. A_{ges} is the Legendre-transformation of the inner energy U regarding the entropy S , which leads to:

$$A = U - TS \quad (12.8)$$

Inserting the values for both the graphene island and C_{ad} , this leads to:

$$A_{ges} = A_{ad} + A_{gr} = U_{ad} + U_{gr} - T(S_{ad} + S_{gr}) \quad (12.9)$$

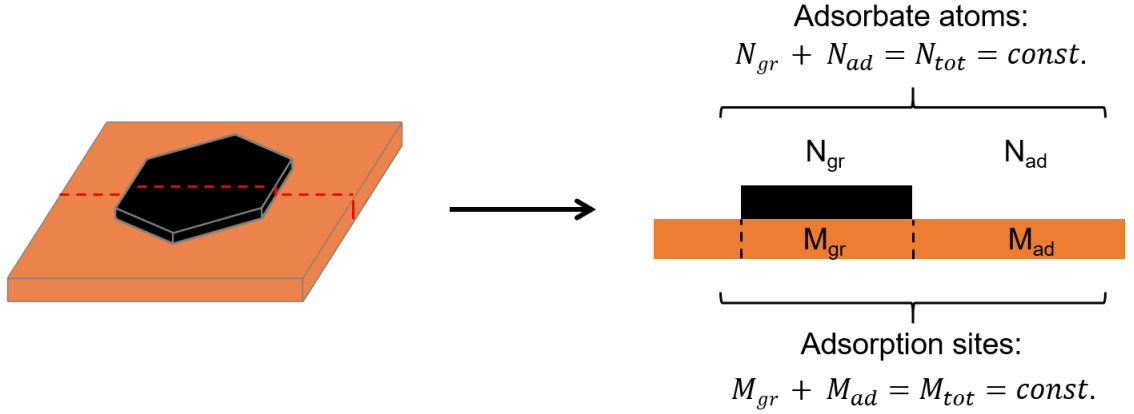


Figure 114 : Sketch illustrating the used parameters and conversion factors for the estimation of the configurational entropy. While the total amount of adsorbed carbon atoms on the sample and the total amount of surface Cu sites remains constant, the different lattice constant of graphene with regard to Cu(111) as described by eq. 12.6 leads to shifts in the values of N_{ad} and M_{ad} .

As A_{ges} is in its global minimum state in equilibrium, the derivation regarding the amount of adsorbed atoms, must be zero.

$$\frac{dA_{ges}}{dn_{ad}} \stackrel{!}{=} 0 \quad (\text{in equilibrium}) \quad (12.10)$$

Here, the molar quantity n_{ad} is replacing the atomic value $N_{ad} = n_{ad} * N_A$. This leads to the formulation:

$$U_{(m, ad)} - U_{(m, gr)} = T \left(\frac{S_{ad}}{n_{ad}} - S_{(m, gr)} \right) = T \left(\frac{N_A * S_{ad}}{N_{ad}} - S_{(m, gr)} \right) \quad (12.11)$$

As stated in the beginning, the total number of carbon atoms, N_{ges} is assumed to be constant, and of course the total number of available Cu surface sites, M_{tot} , is also constant. The entropy of the adsorbed carbon atoms distributed over M_{ad} adsorption sites is given by eq. 12.12, as also presented in eq. 12.2.

$$S_{ad} = k_B * \ln(\Omega) \quad (12.12)$$

with Ω being the sum over all possible microstates expressed as:

$$\Omega = \frac{M_{ad}!}{(M_{ad} - N_{ad})! * N_{ad}!} \quad (12.13)$$

If the number of adsorbed C-atoms is increased by one, this must be removed from the graphene crystal, creating the respective amount of adsorption sites M_{ad} :

$$\frac{\partial M_{ad}}{\partial N_{ad}} = \frac{1}{\rho} \quad (12.14)$$

Using Stirling's relation, as in eq. 12.4, the derivative of S_{ad} with regard to the number of adsorbed atoms, N_{ad} , leads to:

$$\frac{\partial S_{ad}}{\partial N_{ad}} = \frac{k_B \partial \{M_{ad} \ln(M_{ad}) - (M_{ad} - N_{ad}) \ln(M_{ad} - N_{ad}) - (M_{ad} - N_{ad}) - N_{ad} \ln(N_{ad})\}}{\partial N_{ad}} \quad (12.15a)$$

$$\frac{\partial S_{ad}}{\partial N_{ad}} = k_B \left\{ \frac{1}{\rho} M_{ad} + M_{ad} \frac{1}{M_{ad}} \frac{1}{\rho} - \left(\frac{1}{\rho} - 1\right) \ln(M_{ad} - N_{ad}) - (M_{ad} - N_{ad}) \frac{1}{M_{ad} - N_{ad}} \left(\frac{1}{\rho} - 1\right) - \ln(N_{ad}) - N_{ad} \frac{1}{N_{ad}} \right\} \quad (12.15b)$$

$$\frac{\partial S_{ad}}{\partial N_{ad}} = k_B \left\{ \frac{1}{\rho} \ln\left(\frac{M_{ad}}{M_{ad} - N_{ad}}\right) + \ln\left(\frac{M_{ad} - N_{ad}}{N_{ad}}\right) \right\} \quad (12.15c)$$

Introducing the ratio of carbon coverage relative to the total number of copper atoms $\vartheta = N_{ad}/M_{ad}$, the relation converts to:

$$\frac{\partial S_{ad}}{\partial N_{ad}} = k_B \left\{ \frac{1}{\rho} \ln\left(\frac{1}{1 - \vartheta}\right) + \ln\left(\frac{1 - \vartheta}{\vartheta}\right) \right\} \quad (12.16)$$

Comparing the relation from eq. 12.16 to the one obtained without the exchange between C_{ad} and graphene, eq. 12.5g, we see that while the first term is constant in both cases, the second one only becomes relevant in the current model, as $\rho^{-1} \gg \vartheta^{-1} \approx 0$. Inserting eq. 12.16 into eq. 12.11 and solving the equation regarding $\partial S_{ad}/\partial n_{ad}$, we receive the relation:

$$\frac{U_{(m, ad)} - U_{(m, gr)}}{T} + S_{(m, gr)} = \frac{\partial S_{ad}}{\partial n_{ad}} = R \left\{ \frac{1}{\rho} \ln\left(\frac{1}{1 - \vartheta}\right) + \ln\left(\frac{1 - \vartheta}{\vartheta}\right) \right\} \quad (12.17)$$

Using this relation, it is possible to correctly predict the coverages of adsorbed carbon for graphene in equilibrium with a bare Ru(0001) surface, as presented in reference¹²⁸ using data published by Loginova *et al.*^{271,274}

12.3. Correlation between the oxygen sticking and the etching rate of a hexagonal hole

The etching of graphene in a hexagonal hole by oxygen depends on the rate of oxygen adsorption on the surface. For a hexagonal hole in the graphene island with an impurity particle in the center, the oxygen input on the surface can either scale according to the sticking on the impurity particle (case a in Fig. 115) or according to the sticking on the bare Cu surface (case b).

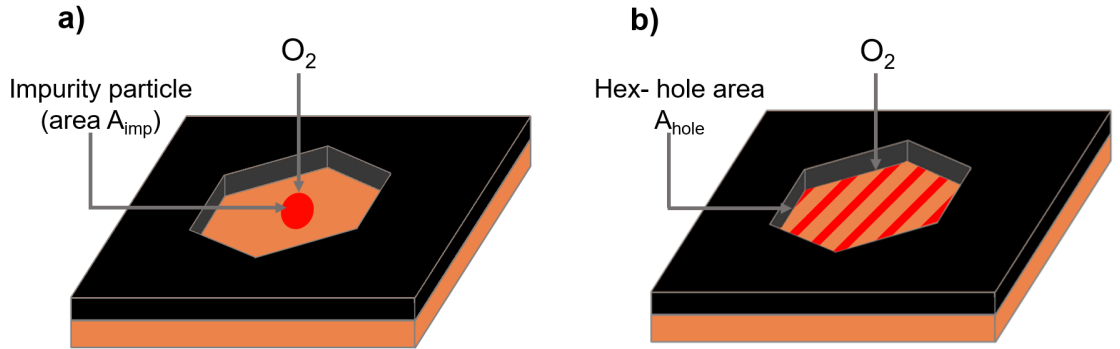


Figure 115 : Scenarios of the possible oxygen adsorption sites in a hexagonal graphene hole. Either the oxygen mainly dissociatively adsorbs on the central impurity particle (case a) or on the complete bare Cu surface (case b).

Case a: The oxygen input in the hexagonal hole is constant. If every oxygen atom reacts with one carbon atom from the graphene sheet, the etched carbon atoms are constant in time (eq. 12.18a). This leads to a scaling of $r \propto \sqrt{t}$, as calculated in eq. 12.18b-12.18e.

$$\frac{dN}{dt} = k \quad (12.18a)$$

$$\frac{dN}{dt} = \frac{A_g}{2} \frac{dA}{dt} = \frac{A_g}{2} \frac{dA}{dr} \frac{dr}{dt} = \frac{A_g}{2} L \frac{dr}{dt} \quad (12.18b)$$

$$\Rightarrow \frac{A_g}{2} L \frac{dr}{dt} = k \quad (12.18c)$$

$$\Rightarrow \int \frac{A_g}{2} L dr = \int k dt \quad (12.18d)$$

$$\int \frac{A_g}{2} 4\sqrt{3}r dr = A_g \sqrt{3}r^2 = \int k dt = k * t \quad (12.18e)$$

$$\Rightarrow r \propto \sqrt{t} \quad (12.18f)$$

Case b: The oxygen input and the carbon etching scale with the area A of the hole (eq. 12.19a). This leads to a scaling of $r \propto e^{0.5t}$ (eq. 12.19b-12.19e).

$$\frac{dN}{dt} = A * k \quad (12.19a)$$

$$\frac{dN}{dt} = \frac{A_g}{2} \frac{dA}{dt} \quad (12.19b)$$

$$\frac{A_g}{2} \frac{dA}{dt} = A * k \quad (12.19c)$$

$$\Rightarrow \int \frac{dA}{A} \propto \int dt \quad (12.19d)$$

$$\Rightarrow \ln(A) = \ln(2\sqrt{3}r^2) = \propto t \quad (12.19e)$$

$$\Rightarrow r \propto e^{0.5t} \quad (12.19f)$$

12.4. Estimation of the Area of Capture from the limiting growth velocity and the adsorbed methane

To estimate the radius r_{AoC} of the Area of Capture around a graphene flake, the methane molecules $\dot{N}_{Provided}$ arriving inside the Area of Capture are compared to the carbon atoms incorporated in the graphene crystal $\dot{N}_{Consumed}$ at $p(CH_4)$ limited conditions. The conditions used for the calculation are $T = 1045\text{ }^\circ\text{C}$, $p(CH_4) = 10^{-2}\text{ mbar}$ and $v = 480\text{ }\mu\text{m h}^{-1}$. At this temperature the sticking coefficient of methane is $S_{CH_4} = 3 \times 10^{-6}$. To facilitate the calculation, a graphene rim segment of $1\text{ }\mu\text{m}$ length is used for the calculation, as also sketched in Fig. 116.

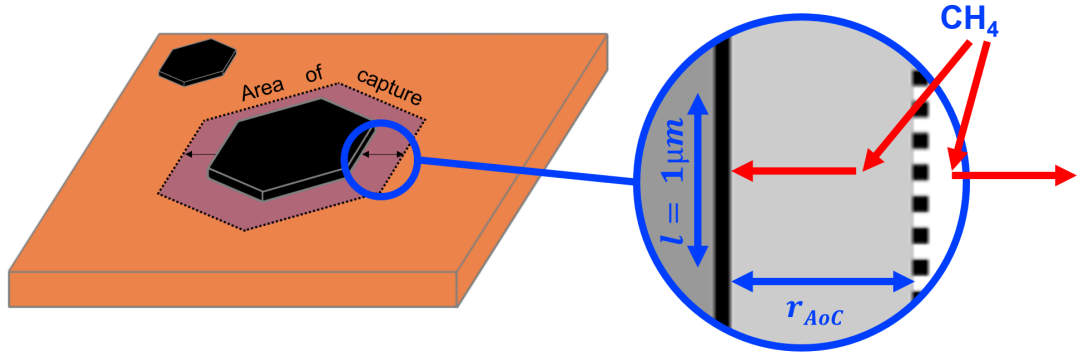


Figure 116 : Sketch of the proposed Area of Capture leading to the observed graphene growth behavior under limiting methane intake. The methane adsorbed inside the Area of Capture is assumed to arrive at the graphene flake, while every methane arriving outside is not relevant for the growth of this flake. The calculation of the Area of Capture is performed exemplarily on a rim section of $1\text{ }\mu\text{m}$ length.

By knowing the growth velocity v , the area increase of the graphene flake and the C_{ad} atoms incorporated in the flake can be calculated according to eqs. 12.20b-12.21a. The adsorbing methane molecules on the bare Cu surface are calculated according to eq. 12.21b. An area $A_{AoC} = l * r_{AoC}$ is needed to adsorb enough methane molecules for the observed growth velocity v . Using eqs. 12.21b+12.21c, this leads to an Area of Capture radius of approximately $100\text{ }\mu\text{m}$.

$$v = 480\text{ }\mu\text{m h}^{-1} = 0.13\text{ }\mu\text{m s}^{-1} \quad (12.20a)$$

$$\dot{A} = v * l = 0.13\text{ }\mu\text{m s}^{-1} * 1\text{ }\mu\text{m} = 1.3 \times 10^{-13}\text{ m}^2\text{ s}^{-1} \quad (12.20b)$$

$$\dot{N}_{Consumed} = \frac{\dot{A}}{0.5 * A_g} = \frac{1.3 \times 10^{-13}\text{ m}^2\text{ s}^{-1}}{0.5 * 5.24 \times 10^{-20}\text{ m}^2} = 5 \times 10^6\text{ atoms s}^{-1} \quad (12.20c)$$

$$\dot{N}_{Provided} = p(CH_4) \sqrt{\frac{1}{m_{CH_4} * 2\pi * k_B * T}} * S_{CH_4} = 5 \times 10^{16} atoms m^{-2} s^{-1} \quad (12.21a)$$

$$\dot{N}_{Consumed} = \dot{N}_{Provided} * A_{AoC} = \dot{N}_{Provided} * l * r_{AoC} \quad (12.21b)$$

$$r_{AoC} = \frac{\dot{N}_{Consumed}}{\dot{N}_{Provided}} * l = 95 \mu m \quad (12.21c)$$

13. List of Experiments

All graphene growth experiments used in this thesis are shortly summarized in the following pages. The experiments are sorted by order of appearance in the text, where they are referenced with the respective numbering.

The indicated reaction steps indicate the main reaction process occurring during this step. The used abbreviations are:

- **Pre-A:** Pretreatment method A refers to the reaction steps: 1. Reactor heating, 2. Oxygen pretreatment and 3. Gas setup, as shown in the diagram of Fig. 117. If these were conducted using the standard pretreatment procedure described in chapter 3.2 and shortly summarized in the following, then no additional comments are inserted in the description of this text.
 1. Reactor heating: The reactor is heated from room temperature to 950 °C with a gas flow of 20 sccm H_2 at a total pressure of ≈ 1 mbar. Added to the hydrogen atmosphere is a low flux of oxygen at a ratio of around $H_2 : O_2 \approx 50000 : 1$. After reaching the temperature of 950 °C and keeping the gas phase for further 15 min follows step 2.
 2. Oxidative pretreatment: The hydrogen is turned off and at the same time the Ar valve is opened at 20 sccm while retaining the oxygen leak flow. The reactor temperature is set to the desired pretreatment temperature (commonly 1045 °C, noted in the table of experiments) and kept at this temperature for the time stated in the table of experiments.
 3. Gas setup: After the oxidative pretreatment, the oxygen leak flow is closed and after a short time the Ar valve is closed while the hydrogen valve is opened again. The reactor is shortly purged with hydrogen and then filled up to 100 mbar with hydrogen. In the meantime, the desired gas ratio for the graphene growth is set via the reactor bypass.
- **Nuc:** The nucleation phase is commonly the first insertion of a methane-hydrogen mixture at conditions allowing graphene flake nucleation, as described in chapter 6. The used reaction conditions (w-ratio, total pressure, Q_{exp} , reaction time, temperature) are listed in the table of experiments.
- **G:** The growth step follows the nucleation phase and defines the development of the formed graphene islands. There may be several growth steps at different conditions, or the nucleation and growth step may be combined at equal conditions in experiments.

- **C-fill:** Experimental conditions set after pretreatment, at which no graphene islands are expected to form, are referred to as carbon-filling steps to indicate that the Cu foil bulk is filled by carbon from the gas phase until the equilibrium concentration is reached.
- **Etch:** After graphene formation, the addition of oxygen or the lowering of the methane partial pressure may lead to the decay of graphene islands, referred to as etching steps in the table.
- **Si-fill:** High-pressure hydrogen treatment of the cleaned Cu foil inserts Si into the foil volume, as described in chapter 9.1. This treatment is therefore abbreviated at silicon-filling of the Cu foil.
- **O2-pull:** Insertion of oxygen at lower temperatures may lead to the formation of silicon oxides on the sample surface without affecting the graphene quality, which is described in chapter 9.1 and referred to as oxygen-pulling of the silicon.

Comments on the correct reading of the reaction conditions:

- If no temperature is noted in a particular reaction step, then the temperature is not changed regarding the step before.
- The table column "Samples" refers to the point, at which samples were removed from the hot reactor zone. Up to three samples may be present in a single reactor run.

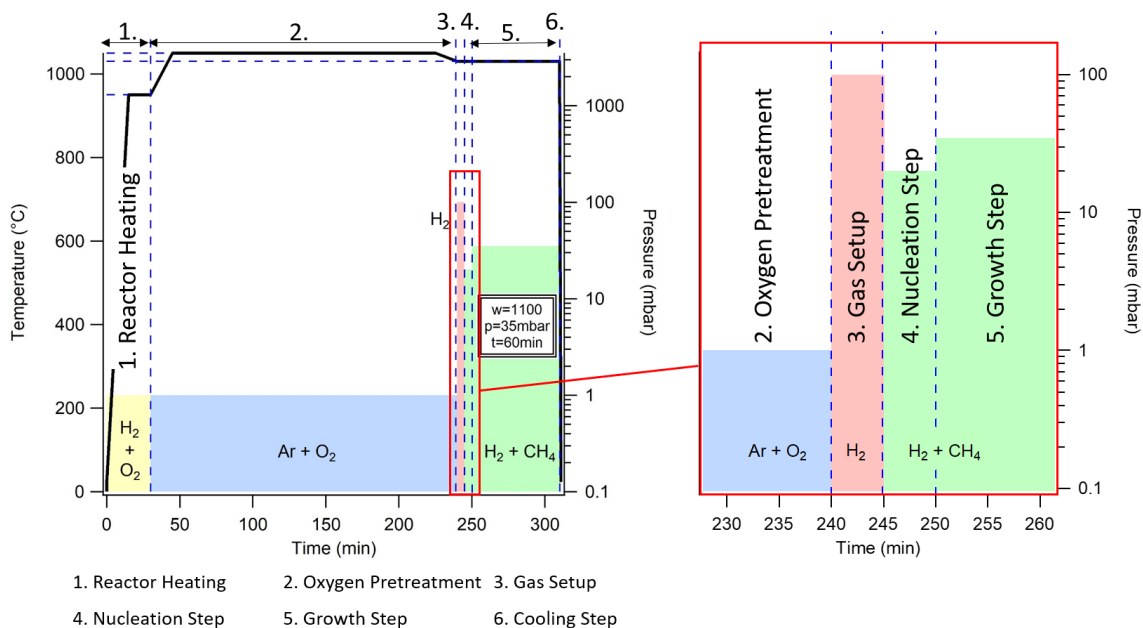


Figure 117 : Example for a used reactor recipe. The common reactor run consists of six consecutive reaction steps, where the main part of the reaction time is used to ensure that the used substrates are reproducibly cleaned and before the synthesis. Step 3 consists of a defined succession of steps to exchange the oxidative pretreatment gases by the reaction gases. While these gases are set and purged through the reactor bypass, the samples are exposed to high hydrogen pressure of 100 mbar to prevent the accumulation of impurities from the gas phase and allow a defined transition to growth conditions. The following nucleation step described in chapter 6 is relevant for the formation of graphene nucleation seeds. The subsequent growth step defines the size of the produced graphene islands and in the final cooling step the samples are cooled to room temperature. Reprinted with permission from¹²⁸. Copyright 2021 American Chemical Society.

Experiment #	Step	w-ratio	pressure (mbar)	Q_exp	Time t (min)	Temperature (°C)	Samples	Annotation
1	2002_10							
	Pre-A				180	1045		
	Nuc	375	200.0	75.0	5	1075		
	G-1		400.0		60			
	G-2		375.0		60		i	
2	1903_10							
	Pre-A				100	1045		
	G-1	1127	20	22.5	110			
	G-3	1000	70.0	70.0	5		ii	
	G-4				25		iii	
3	1903_11							
	Pre-A				120	1045		
	H2		100.0		5		ii	
	G-1							
	G-2							
4	2105_01							
	Pre-A				120	1045		
	Nuc	1266	20.1	25.5	5		i	
	G-1	1266	36.1	45.7	5		ii	
	G-2				5.0		iii	
5	1907_13							
	Pre-A				120			
	Nuc	1181	20.0	23.6	2	1045		
	G-1	1837	47.6	87.4	120		ii	
	G-2	1837	49.1	90.2	60		iii	
6	1907_10							
	Pre-A				120			
	Nuc	1252	19.9	24.9	2	1045		
	G-1	1878	54.5	102.4	120		ii	
	G-2							
7	1907_14							
	Pre-A				120			
	Nuc	1236	20.0	24.7	2	1045		
	G-1	2465	37.4	92.2	60		ii	
	G-2	2465	39.0	96.1	32		iii	
8	1908_02							
	Pre-A				180			
	Nuc	1233	20.0	24.7	2	1045		
	G-1	3385	28.7	97.1	90			
	G-2	3385	30.1	101.9	5		ii+iii	
9	1910_08							
	Pre-A				180			
	Nuc	1261	20.0	25.2	3	1045		
	G-1	2258	42.9	96.9	45		ii	
	G-2	2258	44.5	100.5	30		iii	
10	1910_09							
	Pre-A				180			
	Nuc	1248	19.6	24.5	3	1045		
	G-1	2921	33.6	98.2	60		i	
	G-2	2921	34.6	101.1	60		ii	
11	1908_03							
	Pre-A				180			
	Nuc	1262	20.0	25.2	2	1045		
	G-1	631	123.0	77.6	120		ii	
	G-2	631	125	78.9	60.0		iii	
12	1912_03							
	Pre-A							
	Nuc	1253	20.4	25.5	5		i	
	G-1	650	127.8	83.0	34		ii	
	G-2	650	140.1	91.0	32		iii	
13	1911_06							
	Pre-A				360	1045		
	Nuc	1257	19.9	25.0	3		i	O2 off
	G-1	2748	35.2	96.7	15		ii	1.1 10-4 sccm O2 added
	G-2	2748	35.2	96.7	15		iii	O2 off
14	2105_03							
	Pre-A				120	1045		
	Nuc	1289	20.0	25.8	5		i	
	G-1	1289	36.9	47.6	20		ii	
	G-2				10		iii	
15	1910_04							
	Pre-A				240			
	Nuc	1467	20.1	29.5	60	1045		
	G-1	1178	36.3	42.8	30		ii	
	G-2				30		iii	
16	1910_01							
	Pre-A				300			
	Nuc	1253	20.0		3	1045		
	G-1	1253	36.3		60		ii	
	G-2	1253	36.3		60		iii	
17	2002_07							
	Pre-A				180	1045		
	Nuc	1254	20.9	26.2	4		i	
	G-1	747	61.0	45.5	30		ii	
	G-2	498	91.0	45.3	30		iii	
18	1911_10							
	Pre-A				180	1045		
	Nuc	1244	20.2	25.1	3	1075		
	G-1	1239	55.6	68.9	30		ii	
	G-2	1239	36.6	45.3	11		iii	
19	1911_13							
	Pre-A				180	1045		
	Nuc	1240	20.0	24.7	3	1960		
	G-1	1240	45.8	56.7	31		ii	
	G-2	1240	36.6	45.3	10		iii	

Experiment #	Step	w-ratio	pressure (mbar)	Q_exp	Time t (min)	Temperature (°C)	Samples	Annotation
20	1911_08							
	Pre-A				180	1045		
	Nuc	1007	20.1	20.2	10		i	
	G-1	1996	36.4	72.6	62		ii	
21	1907_12							
	Pre-A				120			
	Nuc	1245	20.1	25.0	2	1045	i	
	G-1	2458	35.6	87.5	120		ii	
22	1907_09							
	Pre-A				120			
	Nuc	939	18.8	17.7	2	1045	i	
	G-1	1878	35.0	65.7	120		ii	
23	1912_01							
	Pre-A				180	1045		
	Nuc	1239	20.0	24.8	3	1020	i	
	G-1	1239	36.3	45.0	35		ii	
24	1911_15							
	Pre-A				180	1045		
	Nuc	1246	20.0	24.9	3	1015	i	
	G-1	1241	36.3	45.0	30		ii	
25	1911_09							
	Pre-A				180	1045		
	Nuc	1245	19.8	25	3	1000	i	
	G-1	1240	15.9	20	30		ii	
26	1912_02							
	Pre-A				180	1045		
	Nuc	1239	20.1	24.9	5	975	i	
	G-1	1239	36.3	45.0	30		ii	
27	1911_11							
	Pre-A				180	1045		
	Nuc	620	9.5	5.9	15	950	i	
	G-1	1240	36.5	45.3	60		ii	
28	1911_12							
	Pre-A				180	1045		
	Nuc	623	9.5	5.9	15	950	i	
	G-1	40	34.2	1.4	32	900	ii	
29	1910_10							
	Pre-A				360	1045		
	Nuc	1257	19.6	24.6	3	1070		
	G-1	2475	46.2	114.3	30		i	
30	1910_03							
	Pre-A				240	1045		
	Nuc	1247	20.3	25.3	60	1020	i	
	G-1	2494	32.1	80.1	20		ii	
31	1911_02							
	Pre-A				120	1045		
	Nuc	1260	19.8	25.0	3	1010		
	G-1	2002	40.1	80.2	10		i	
32	1909_07							
	Pre-A				180	1045		
	Nuc	1246	20.0	24.9	60	995	i	
	G-1	1246	54.3	67.7	30		ii	
33	1910_02							
	Pre-A				240	1045		
	Nuc	1247	20.0	24.9	61	970	i	
	G-1	1247	43.3	54.0	63		ii	
34	2105_05							
	Pre-A				180	1045		
	Nuc	1042	10.0	10.4	5		i	
	G-1				11		ii	
35	2105_06							
	Pre-A				180	1045		
	Nuc	716	7.1	5.1	5		i	
	G-1				5		ii	
36	2105_07							
	Pre-A				180	1045		
	Nuc	504	4.9	2.5	5		i	
	G-1				5		ii	
37	2105_08							
	Pre-A				180	1045		
	Nuc	2271	5.0	11.4	5		i	
	G-1				5		ii	
38	2105_09							
	Pre-A				180	1045		
	Nuc	571	19.8	11.3	5		i	
	G-1				5		ii	
	G-2				5		iii	

Experiment #	Step	w-ratio	pressure (mbar)	Q_exp	Time t (min)	Temperature (°C)	Samples	Annotation
39	2105_10				180	1045		
	Pre-A				3.25		i	
	Nuc	356	14.4	5.1	1.75		ii	
	G-1				5		iii	
40	2105_11				180	1045		
	Pre-A				3		i	
	Nuc	251	10.3	2.6	2		ii	
	G-1				5		iii	
41	2105_12				180	1045		
	Pre-A				3.25		i	
	Nuc	398	7.0	2.8	2		ii	
	G-1				5		iii	
42	2105_13				180	1045		
	Pre-A				3		i	
	Nuc	293	8.7	2.6	2		ii	
	G-1				2		iii	
43	2105_14				180	1045		
	Pre-A				5	1005	i	
	Nuc	500	4.9	2.4	5		ii	
	G-1				5		iii	
44	2105_15				180	1045		
	Pre-A				5	1025	i	
	Nuc	507	5.0	2.5	5		ii	
	G-1				5		iii	
45	2105_16				180	1045		
	Pre-A				3		i	
	Nuc	496	5	2.5	2		ii	
	G-1				2		iii	
46	2001_02				300	1045		
	Pre-A				10		i	
	Nuc	330	300.0	99.0	30		ii	
	G-1	1268	36.3	46.0	31		iii	
47	1903_07				150			
	Pre-A				10	1045	i	
	Nuc	2254	10.0	22.5	90		ii	
	G-1							
48	2105_04				180	1045		
	Pre-A				5		i	
	Nuc	1284	20.3	26.1	23		ii	
	G-1	1284	36.5	46.9	7		iii	
	G-2				15			
49	2011_01				300	1045		
	Pre-A				40		i	
	Nuc	2997	40.3	120.8	3		ii	
	G-1	1239	20.5	25.4	16		iii	
50	2001_06				180	1045		Cu samples on glass
	Pre-A				10	1086	i	
	Nuc	1258	36.1	45.3				
51	2001_01				240	1045		
	Pre-A				100		i	
	Nuc	300	147.0	44.1				
52	1911_01				180	1045		
	Pre-A				3	1078		
	Nuc	1361	20.0	27.2	10		i	
	G-1	3380	36.0	121.7	10		ii	
	G-2	3380	36.4	122.9	10		iii	
53	2007_03				300	1045		
	Pre-A				3	1075		
	Nuc	323	200.0	64.5	60		i	
	G-1	323	350.0	112.9	14.5h		ii	
	G-2	360	425.0	152.8	120		iii	
54	2001_04				180	1045		
	Pre-A				30		i	
	Nuc	300	151.0	45.3	30		ii	
	G-1	900	151.0	135.9	30		iii	
	G-2	500	151.0	75.5				
55	2002_09				135	1045		
	Pre-A				5	1075	i	
	Nuc	375	150.0	56.3	60			
	G-1		400.0		5		ii	
	G-2		200.0		30		iii	
	G-3		400.0		60			
56	1906_03				220			
	Pre-A				20	1045	i	
	Nuc	1127	20.0	22.5	40		ii	

Experiment #	Step	w-ratio	pressure (mbar)	Q_exp	Time t (min)	Temperature (°C)	Samples	Annotation
57	1906_05							
	Pre-A				220			
	Nuc	1127	20.0	22.5	20	1045		
	Etch-1				2		i	Etch in 30 sccm/20 mbar Ar
	Etch-2				3		ii	Etch in 30 sccm/20 mbar Ar
58	1906_04							
	Pre-A				220			
	Nuc	1127	20.0	22.5	20	1045		
	Etch-1				20		i	Etch in 30 sccm/20 mbar Ar
	Etch-2				20		ii	Etch in 30 sccm/20 mbar Ar
59	1809_03							
	Pre-A				210	1045		
	G-1	2000	20.0	40.0	180		i	Cool sample in Ar gas
60	1907_08							
	Pre-A				120			
	Nuc	626	19.4	12.1	2	1045	i	
	G-1	1878	30.1	56.5	120		ii	
61	1907_06							
	Pre-A				150			
	Si-Fill	H2	300.0		60	1045		
	O2-Pull	Ar/O2	30.0		10			
	G-2	1127	20.0	22.5	10			
	G-3	1127	30.0	34.0	20		i	Addition of 10-3 mbar O2
	G-4				20		ii	
62	1907_07							
	Pre-A				150			
	Si-Fill	H2	300.0		60	1045		
	O2-Pull	Ar/O2	30.0		10			
	G-2	1127	20.0	22.5	10			
	Etch-1	1127	30.0	34.0	20		i	
	Etch-2				20		ii	
63	1907_11							
	Pre-A				120			
	Nuc	1225	19.7	24.1	5	1045	i	
	G-1	1838	44.3	81.4	120		ii	
	Etch-1				10		iii	Etch in pure H2
64	1808_05							
	Pre-A				210	1045	i	
65	1808_06							
	Pre-A				200	1045		
	H2		300.0		120			Si accumulation
	Ox		2.0		90		i	Si dragging to surface
66	1901_04							
	Pre-A				80			
	Si-Fill	H2	300.0		60	1045	i	
	O2-Pull	Ar/O2	20.0		60		ii	10-5 mbar O2
	Si-Fill	H2	300.0		60		iii	
67	1902_01							
	Pre-A				80			
	Si-Fill	H2	300.0		90	1045	i	
	O2-Pull	Ar/O2	20.0		60		ii	10-3 mbar O2
	Si-Fill	H2	300.0		60		iii	
68	2011_08							
	Pre-A				210	1045		
	Nuc	660	10.0	6.6	90		i	
	O2-Pull		20.4		60	750	ii	Oxygen added by 20sscm Ar
69	1902_07							
	Pre-A				120			
	Si-Fill	H2	300.0		60	1045		
	G-1	1127	20.0	22.5	120		i	
	O2-Pull	Ar	20.0		10	750	ii	
70	2011_07							
	Pre-A				270	1045		
	Si-Fill	H2	300.0		60			
	G-1	1090	19.8	21.6	120		i	
	O2-Pull		20.4		60	750	ii	Oxygen added by 20sscm Ar
71	2011_09							
	Pre-A				300	1045		
	Si-Fill	H2	300.0		60			
	G-1	281	10.0	2.8	90		i	
	O2-Pull		21.0		60	750	ii	Oxygen added by 20sscm Ar
72	1903_01							
	Pre-A				120			
	Nuc	338	100.0	33.8	5	1045	i	
	G-1				150		ii	
73	1903_04							
	Pre-A				120			
	Nuc	338	85.0	28.7	90	1045	i	
74	2010_04							
	Pre-A				210	1045		
	Nuc	25	1.4	0.035	60	945	i	
75	2009_01							
	Pre-A				300	1045	i	
	Nuc	1519	35.3	53.6	60	970		
	G-1	25	60.0	1.5	60		ii	

Experiment #	Step	w-ratio	pressure (mbar)	Q_exp	Time t (min)	Temperature (°C)	Samples	Annotation
76	2010_05							
	Pre-A				180	1045		
	Nuc	1239	20.0	24.8	10			
	G-1	1239	30.3	37.5	120			
	G-2	1239	20.1	24.9	60		i	
77	2009_03							
	Pre-A				360	1045		
	Nuc	406	40.5	16.4	5	1058		i
	G-1				55			ii

Danksagung

Diese Arbeit wäre natürlich nicht ohne das Mitwirken vieler Personen entstanden, denen ich an dieser Stelle herzlich danken möchte:

Prof. Sebastian Günther, der durch das Angebot der Promotion in seiner Gruppe den Weg für diese Arbeit bereitet hat und mir währenddessen genug Freiraum für die Entfaltung eigener Ideen ließ, aber auch zur rechten Zeit für die notwendige Unterstützung sorgte und mit allerlei Geistesblitzen, Motivationsschüben und Kaffees für die nötige Energie sorgte.

Prof. Joost Wintterlin nicht nur dafür, dass er mir ein Labor und einen Arbeitsplatz zur Verfügung stellte, sondern auch für unzählige Tipps, Denkanstöße, die Organisation der Gruppenretreats in Blaustein und die Übernahme der Zweitkorrektur dieser Arbeit.

Der gesamten Heizgruppe für die Integration unserer kleinen Gruppe in verschiedenste Festivitäten, Verwaltungsaufgaben und natürlich in die Group Meetings, insbesondere gilt mein Dank

Prof. Barbara Lechner für die Rolle der Prüferin dieser Dissertation.

Daniela Reicheneder, Rita Römling-Engl, Regina Huber und **Uta LeGuay** für die gruppen- und universitätsübergreifende Übernahme verschiedenster bürokratischer Angelegenheiten.

Dr. Steffen Schmidt für die Übernahme der SEM-Messungen, **Prof. Thomas Bein** für die Möglichkeit der Mitbenutzung verschiedener Gerätschaften.

Meinen aktuellen und ehemaligen Kollegen **Dr. Bernhard Böller, Katharina Golder, Dr. Ann-Kathrin Henß, Hannah Illner, Tim Kratky, Dr. Jürgen Kraus, Dr. Laerte Patera, Dr. Regina Wyrwich** und **Dr. Patrick Zeller** für alle gemeinsamen Momente, sei es in der Mittagspause, beim Kaffeetrinken, im Festzelt oder bei der Weihnachtsfeier. Nur durch die gegenseitige Unterstützung und die immerwiederkehrende Belehrung, manche Sachen mit Humor zu nehmen, konnte die Arbeit in dieser Form entstehen. Danke auch für das Vorleben, dass man Doktorarbeiten auch wirklich abschließen kann.

Durch verschiedene Praktika und Abschlussarbeiten haben Dennis Meier, Varena März, Katharina Nisi, Muhammad Zulfadhli Bin Abdul Manaf, Franziska Hnyk, Anne Oppelt, Markus Heindl, Laura Fuchs und Mirza Grebo für genügend Abwechslung gesorgt und mich bei verschiedensten Forschungsangelegenheiten kräftig unterstützt.

Bei **Sebastian, Tim** und **Laerte** außerdem für das Ermöglichen verschiedenster Forschungsreisen und die hervorragende Zusammenarbeit während dieser. Sie hielten die Stimmung immer hoch, auch wenn der Tank sich mal leerte.

Den Wissenschaftlern, die mir durch verschiedene Kooperationen unter anderem an der **Nanospectroscopy** und **Bach-Beamline**, sowie der **Nano fabrication facility** in Trieste den Einblick in neue Methoden und den Arbeitsalltag am Synchrotron ermöglichten.

Meiner **Familie** und meinen **Freunden**, die mir immer den Rücken gestärkt haben und die wir gemeinsam durch die verschiedenen Phasen einer jeden Promotion gingen.

Tack till lilla björnen!

Bibliography

- [1] K. S. Novoselov, A. K. Geim, S. V. Morozov, D. Jiang, Y. Zhang, S. V. Dubonos, I. V. Grigorieva, and A. A. Firsov. Electric field effect in atomically thin carbon films. *Science*, 306(5696):666–9, 2004.
- [2] Junfeng Gao, Ziwei Xu, Shuai Chen, Madurai S. Bharathi, and Yong-Wei Zhang. Computational understanding of the growth of 2d materials. *Advanced Theory and Simulations*, 1(11), 2018.
- [3] G. Cheon, K. N. Duerloo, A. D. Sendek, C. Porter, Y. Chen, and E. J. Reed. Data mining for new two- and one-dimensional weakly bonded solids and lattice-commensurate heterostructures. *Nano Lett*, 17(3):1915–1923, 2017.
- [4] N. Mounet, M. Gibertini, P. Schwaller, D. Campi, A. Merkys, A. Marrazzo, T. Sohier, I. E. Castelli, A. Cepellotti, G. Pizzi, and N. Marzari. Two-dimensional materials from high-throughput computational exfoliation of experimentally known compounds. *Nat Nanotechnol*, 13(3):246–252, 2018.
- [5] K. S. Novoselov, A. Mishchenko, A. Carvalho, and A. H. Castro Neto. 2d materials and van der waals heterostructures. *Science*, 353(6298):aac9439, 2016.
- [6] F. Pulizzi, O. Bubnova, S. Milana, D. Schilter, D. Abergel, and A. Moscatelli. Graphene in the making. *Nat Nanotechnol*, 14(10):914–918, 2019.
- [7] D. Li, M. B. Muller, S. Gilje, R. B. Kaner, and G. G. Wallace. Processable aqueous dispersions of graphene nanosheets. *Nat Nanotechnol*, 3(2):101–5, 2008.
- [8] Sasha Stankovich, Dmitriy A. Dikin, Richard D. Piner, Kevin A. Kohlhaas, Alfred Kleinhammes, Yuanyuan Jia, Yue Wu, SonBinh T. Nguyen, and Rodney S. Ruoff. Synthesis of graphene-based nanosheets via chemical reduction of exfoliated graphite oxide. *Carbon*, 45(7):1558–1565, 2007.
- [9] Claire Berger, Zhimin Song, Tianbo Li, Xuebin Li, Asmerom Y. Ogbazghi, Rui Feng, Zhenting Dai, Alexei N. Marchenkov, Edward H. Conrad, Phillip N. First, and Walt A. de Heer. Ultrathin epitaxial graphite: 2d electron gas properties and a route toward graphene-based nanoelectronics. *The Journal of Physical Chemistry B*, 108(52):19912–19916, 2004.
- [10] S. Marchini, S. Günther, and J. Wintterlin. Scanning tunneling microscopy of graphene on ru(0001). *Physical Review B*, 76(7):075429, 2007.
- [11] Peter W. Sutter, Jan-Ingo Flege, and Eli A. Sutter. Epitaxial graphene on ruthenium. *Nat Mater*, 7(5):406–411, 2008.

- [12] Patrick Zeller, Florian Speck, Michael Weinl, Markus Ostler, Matthias Schreck, Thomas Seyller, and Joost Wintterlin. Healing of graphene on single crystalline ni(111) films. *Applied Physics Letters*, 105(19), 2014.
- [13] Xuesong Li, Weiwei Cai, Jinho An, Seyoung Kim, Junghyo Nah, Dongxing Yang, Richard Piner, Aruna Velamakanni, Inhwa Jung, Emanuel Tutuc, Sanjay K. Banerjee, Luigi Colombo, and Rodney S. Ruoff. Large-area synthesis of high-quality and uniform graphene films on copper foils. *Science*, 324(5932):1312–1314, 2009.
- [14] N. C. Bartelt and K. F. McCarty. Graphene growth on metal surfaces. *MRS Bulletin*, 37(12):1158–1165, 2012.
- [15] J. Wintterlin and M. L. Bocquet. Graphene on metal surfaces. *Surface Science*, 603(10-12):1841–1852, 2009.
- [16] A. Dahal and M. Batzill. Graphene-nickel interfaces: a review. *Nanoscale*, 6(5):2548–62, 2014.
- [17] Xuesong Li, Weiwei Cai, Luigi Colombo, and Rodney S. Ruoff. Evolution of graphene growth on ni and cu by carbon isotope labeling. *Nano Letters*, 9(12):4268–4272, 2009.
- [18] Cecilia Mattevi, Hokwon Kim, and Manish Chhowalla. A review of chemical vapour deposition of graphene on copper. *Journal of Materials Chemistry*, 21(10):3324–3334, 2011.
- [19] Paul Leidinger, Jürgen Kraus, Tim Kratky, Patrick Zeller, Tevfik Onur Mente, Francesca Genuzio, Andrea Locatelli, and Sebastian Günther. Toward the perfect membrane material for environmental x-ray photoelectron spectroscopy. *Journal of Physics D: Applied Physics*, 54(23), 2021.
- [20] W. Guo, B. Wu, S. Wang, and Y. Liu. Controlling fundamental fluctuations for reproducible growth of large single-crystal graphene. *ACS Nano*, 12(2):1778–1784, 2018.
- [21] Yufeng Hao, M. S. Bharathi, Lei Wang, Yuanyue Liu, Hua Chen, Shu Nie, Xiaohan Wang, Harry Chou, Cheng Tan, Babak Fallahazad, H. Ramanarayan, Carl W. Magnuson, Emanuel Tutuc, Boris I. Yakobson, Kevin F. McCarty, Yong-Wei Zhang, Philip Kim, James Hone, Luigi Colombo, and Rodney S. Ruoff. The role of surface oxygen in the growth of large single-crystal graphene on copper. *Science*, 342(6159):720–723, 2013.
- [22] Hoang Danh Phan, Jaehyuck Jung, Youngchan Kim, Van Ngoc Huynh, and Changgu Lee. Large-area single-crystal graphene grown on a recrystallized cu(111) surface by using a hole-pocket method. *Nanoscale*, 8(28):13781–13789, 2016.
- [23] Hailong Zhou, Woo Jong Yu, Lixin Liu, Rui Cheng, Yu Chen, Xiaoqing Huang, Yuan Liu, Yang Wang, Yu Huang, and Xiangfeng Duan. Chemical vapour deposition growth of large single crystals of monolayer and bilayer graphene. *Nat Commun*, 4, 2013.

- [24] Zheng Yan, Yuanyue Liu, Long Ju, Zhiwei Peng, Jian Lin, Gunuk Wang, Haiqing Zhou, Changsheng Xiang, E. L. G. Samuel, Carter Kittrell, Vasilii I. Artyukhov, Feng Wang, Boris I. Yakobson, and James M. Tour. Large hexagonal bi- and trilayer graphene single crystals with varied interlayer rotations. *Angewandte Chemie International Edition*, 53(6):1565–1569, 2014.
- [25] Li Lin, Luzhao Sun, Jincan Zhang, Jingyu Sun, Ai Leen Koh, Hailin Peng, and Zhongfan Liu. Rapid growth of large single-crystalline graphene via second passivation and multi-stage carbon supply. *Advanced Materials*, 28(23):4671–4677, 2016.
- [26] Xiaozhi Xu, Zhihong Zhang, Jichen Dong, Ding Yi, Jingjing Niu, Muhong Wu, Li Lin, Rongkang Yin, Mingqiang Li, Jingyuan Zhou, Shaoxin Wang, Junliang Sun, Xiaojie Duan, Peng Gao, Ying Jiang, Xiaosong Wu, Hailin Peng, Rodney S. Ruoff, Zhongfan Liu, Dapeng Yu, Enge Wang, Feng Ding, and Kaihui Liu. Ultrafast epitaxial growth of metre-sized single-crystal graphene on industrial cu foil. *Science Bulletin*, 62(15):1074–1080, 2017.
- [27] Xiaozhi Xu, Zhihong Zhang, Lu Qiu, Jianing Zhuang, Liang Zhang, Huan Wang, Chongnan Liao, Huading Song, Ruixi Qiao, Peng Gao, Zonghai Hu, Lei Liao, Zhimin Liao, Dapeng Yu, Enge Wang, Feng Ding, Hailin Peng, and Kaihui Liu. Ultrafast growth of single-crystal graphene assisted by a continuous oxygen supply. *Nat Nano*, 11(11):930–935, 2016.
- [28] Z. Zhang, X. Xu, L. Qiu, S. Wang, T. Wu, F. Ding, H. Peng, and K. Liu. The way towards ultrafast growth of single-crystal graphene on copper. *Adv Sci (Weinh)*, 4(9):1700087, 2017.
- [29] D. Hou, S. Zhang, X. Chen, R. Song, D. Zhang, A. Yao, J. Sun, W. Wang, L. Sun, B. Chen, Z. Liu, and L. Wang. Decimeter-scale atomically thin graphene membranes for gas-liquid separation. *ACS Appl Mater Interfaces*, 13(8):10328–10335, 2021.
- [30] E. S. Polsen, D. Q. McNerny, B. Viswanath, S. W. Pattinson, and A. John Hart. High-speed roll-to-roll manufacturing of graphene using a concentric tube cvd reactor. *Sci Rep*, 5:10257, 2015.
- [31] Nicolas Reckinger, Xiaohui Tang, Frederic Joucken, Luc Lajaunie, Raul Arenal, Emmanuel Dubois, Benoit Hackens, Luc Henrard, and Jean-Francois Colomer. Oxidation-assisted graphene heteroepitaxy on copper foil. *Nanoscale*, 8(44):18751–18759, 2016.
- [32] H. Wang, X. Xu, J. Li, L. Lin, L. Sun, X. Sun, S. Zhao, C. Tan, C. Chen, W. Dang, H. Ren, J. Zhang, B. Deng, A. L. Koh, L. Liao, N. Kang, Y. Chen, H. Xu, F. Ding, K. Liu, H. Peng, and Z. Liu. Surface monocrystallization of copper foil for fast growth of large single-crystal graphene under free molecular flow. *Adv Mater*, 28(40):8968–8974, 2016.

- [33] Andrea C. Ferrari. Raman spectroscopy of graphene and graphite: Disorder, electron-phonon coupling, doping and nonadiabatic effects. *Solid State Communications*, 143(12):47–57, 2007.
- [34] L. M. Malard, M. A. Pimenta, G. Dresselhaus, and M. S. Dresselhaus. Raman spectroscopy in graphene. *Physics Reports*, 473(56):51–87, 2009.
- [35] Jaesung Lee, Xuqian Zheng, Robert C. Roberts, and Philip X. L. Feng. Scanning electron microscopy characterization of structural features in suspended and non-suspended graphene by customized cvd growth. *Diamond and Related Materials*, 54:64–73, 2015.
- [36] Zhu-Jun Wang, Gisela Weinberg, Qiang Zhang, Thomas Lunkenbein, Achim Klein-Hoffmann, Michalina Kurnatowska, Milivoj Plodinec, Qing Li, Lifeng Chi, R. Schloegl, and Marc-Georg Willinger. Direct observation of graphene growth and associated copper substrate dynamics by in situ scanning electron microscopy. *ACS Nano*, 9(2):1506–1519, 2015.
- [37] Chuancheng Jia, Jiaolong Jiang, Lin Gan, and Xuefeng Guo. Direct optical characterization of graphene growth and domains on growth substrates. *Sci. Rep.*, 2, 2012.
- [38] L. Banszerus, M. Schmitz, S. Engels, J. Dauber, M. Oellers, F. Haupt, K. Watanabe, T. Taniguchi, B. Beschoten, and C. Stampfer. Ultrahigh-mobility graphene devices from chemical vapor deposition on reusable copper. *Sci Adv*, 1(6):e1500222, 2015.
- [39] K. I. Bolotin, K. J. Sikes, Z. Jiang, M. Klima, G. Fudenberg, J. Hone, P. Kim, and H. L. Stormer. Ultrahigh electron mobility in suspended graphene. *Solid State Communications*, 146(9-10):351–355, 2008.
- [40] Otakar Frank, Jana Vejpravova, Vaclav Holy, Ladislav Kavan, and Martin Kalbac. Interaction between graphene and copper substrate: The role of lattice orientation. *Carbon*, 68(0):440–451, 2014.
- [41] W. X. Wang, S. H. Liang, T. Yu, D. H. Li, Y. B. Li, and X. F. Han. The study of interaction between graphene and metals by raman spectroscopy. *Journal of Applied Physics*, 109(7), 2011.
- [42] Jiang-Bin Wu, Huan Wang, Xiao-Li Li, Hailin Peng, and Ping-Heng Tan. Raman spectroscopic characterization of stacking configuration and interlayer coupling of twisted multi-layer graphene grown by chemical vapor deposition. *Carbon*, 110:225–231, 2016.
- [43] Dongfei Li, Da Zhan, Jiayu Yan, Chenglin Sun, Zuowei Li, Zhenhua Ni, Lei Liu, and Zexiang Shen. Thickness and stacking geometry effects on high frequency overtone and combination raman modes of graphene. *Journal of Raman Spectroscopy*, 44(1):86–91, 2013.
- [44] Sinisa Coh, Liang Z. Tan, Steven G. Louie, and Marvin L. Cohen. Theory of the raman spectrum of rotated double-layer graphene. *Physical Review B*, 88(16):165431, 2013.

- [45] Pedro Venezuela, Michele Lazzeri, and Francesco Mauri. Theory of double-resonant raman spectra in graphene: Intensity and line shape of defect-induced and two-phonon bands. *Physical Review B*, 84(3), 2011.
- [46] R. Beams, L. Gustavo Cancado, and L. Novotny. Raman characterization of defects and dopants in graphene. *J Phys Condens Matter*, 27(8):083002, 2015.
- [47] L. G. Cancado, A. Jorio, E. H. Ferreira, F. Stavale, C. A. Achete, R. B. Capaz, M. V. Moutinho, A. Lombardo, T. S. Kulmala, and A. C. Ferrari. Quantifying defects in graphene via raman spectroscopy at different excitation energies. *Nano Lett*, 11(8):3190–6, 2011.
- [48] Jakob Zabel, Rahul R. Nair, Anna Ott, Thanasis Georgiou, Andre K. Geim, Kostya S. Novoselov, and Cinzia Casiraghi. Raman spectroscopy of graphene and bilayer under biaxial strain: Bubbles and balloons. *Nano Letters*, 12(2):617–621, 2012.
- [49] J. E. Lee, G. Ahn, J. Shim, Y. S. Lee, and S. Ryu. Optical separation of mechanical strain from charge doping in graphene. *Nat Commun*, 3:1024, 2012.
- [50] Ruizhe Wu, Lin Gan, Xuewu Ou, Qicheng Zhang, and Zhengtang Luo. Detaching graphene from copper substrate by oxidation-assisted water intercalation. *Carbon*, 98:138–143, 2016.
- [51] L. G. Cancado, M. A. Pimenta, B. R. Neves, M. S. Dantas, and A. Jorio. Influence of the atomic structure on the raman spectra of graphite edges. *Phys Rev Lett*, 93(24):247401, 2004.
- [52] Benjamin Krauss, Peter Nemes-Incze, Viera Skakalova, Laszlo P. Biro, Klaus von Klitzing, and Jurgen H. Smet. Raman scattering at pure graphene zigzag edges. *Nano Letters*, 10(11):4544–4548, 2010.
- [53] U. Lee, Y. Han, S. Lee, J. S. Kim, Y. H. Lee, U. J. Kim, and H. Son. Time evolution studies on strain and doping of graphene grown on a copper substrate using raman spectroscopy. *ACS Nano*, 14(1):919–926, 2020.
- [54] T. Ohta, A. Bostwick, T. Seyller, K. Horn, and E. Rotenberg. Controlling the electronic structure of bilayer graphene. *Science*, 313(5789):951–4, 2006.
- [55] M. D. Stoller, S. Park, Y. Zhu, J. An, and R. S. Ruoff. Graphene-based ultracapacitors. *Nano Lett*, 8(10):3498–502, 2008.
- [56] F. Xia, T. Mueller, Y. M. Lin, A. Valdes-Garcia, and P. Avouris. Ultrafast graphene photodetector. *Nat Nanotechnol*, 4(12):839–43, 2009.
- [57] Y. Cao, V. Fatemi, S. Fang, K. Watanabe, T. Taniguchi, E. Kaxiras, and P. Jarillo-Herrero. Unconventional superconductivity in magic-angle graphene superlattices. *Nature*, 556(7699):43–50, 2018.

- [58] F. Withers, O. Del Pozo-Zamudio, A. Mishchenko, A. P. Rooney, A. Gholinia, K. Watanabe, T. Taniguchi, S. J. Haigh, A. K. Geim, A. I. Tartakovskii, and K. S. Novoselov. Light-emitting diodes by band-structure engineering in van der waals heterostructures. *Nat Mater*, 14(3):301–6, 2015.
- [59] Juergen Kraus, Robert Reichelt, Sebastian Guenther, Luca Gregoratti, Matteo Amati, Maya Kiskinova, Alexander Yulaev, Ivan Vlassiouk, and Andrei Kolmakov. Photoelectron spectroscopy of wet and gaseous samples through graphene membranes. *Nanoscale*, 6(23):14394–14403, 2014.
- [60] A. Yulaev, H. Guo, E. Strelcov, L. Chen, I. Vlassiouk, and A. Kolmakov. Graphene microcapsule arrays for combinatorial electron microscopy and spectroscopy in liquids. *ACS Appl Mater Interfaces*, 9(31):26492–26502, 2017.
- [61] Albert Boretti, Sarim Al-Zubaidy, Miroslava Vaclavikova, Mohammed Al-Abri, Stefania Castelletto, and Sergey Mikhailovsky. Outlook for graphene-based desalination membranes. *npj Clean Water*, 1(1):5, 2018.
- [62] David Cohen-Tanugi and Jeffrey C. Grossman. Water desalination across nanoporous graphene. *Nano Letters*, 12(7):3602–3608, 2012.
- [63] S. Hu, M. Lozada-Hidalgo, F. C. Wang, A. Mishchenko, F. Schedin, R. R. Nair, E. W. Hill, D. W. Boukhvalov, M. I. Katsnelson, R. A. Dryfe, I. V. Grigorieva, H. A. Wu, and A. K. Geim. Proton transport through one-atom-thick crystals. *Nature*, 516(7530):227–30, 2014.
- [64] S. M. Fatemi, S. J. Fatemi, and Z. Abbasi. Gas separation using graphene nanosheet: insights from theory and simulation. *J Mol Model*, 26(11):322, 2020.
- [65] K. Ji, J. Han, A. Hirata, T. Fujita, Y. Shen, S. Ning, P. Liu, H. Kashani, Y. Tian, Y. Ito, J. I. Fujita, and Y. Oyama. Lithium intercalation into bilayer graphene. *Nat Commun*, 10(1):275, 2019.
- [66] Keun Soo Kim, Yue Zhao, Houk Jang, Sang Yoon Lee, Jong Min Kim, Kwang S. Kim, Jong-Hyun Ahn, Philip Kim, Jae-Young Choi, and Byung Hee Hong. Large-scale pattern growth of graphene films for stretchable transparent electrodes. *Nature*, 457(7230):706–710, 2009.
- [67] Bruno Dlubak, Marie-Blandine Martin, Robert S. Weatherup, Heejun Yang, Cyrille Deranlot, Raoul Blume, Robert Schloegl, Albert Fert, Abdelmadjid Anane, Stephan Hofmann, Pierre Seneor, and John Robertson. Graphene-passivated nickel as an oxidation-resistant electrode for spintronics. *ACS Nano*, 6(12):10930–10934, 2012.
- [68] Vikas Berry. Impermeability of graphene and its applications. *Carbon*, 62(0):1–10, 2013.
- [69] Ji Won Suk, Alexander Kitt, Carl W. Magnuson, Yufeng Hao, Samir Ahmed, Jinho An, Anna K. Swan, Bennett B. Goldberg, and Rodney S. Ruoff. Transfer of cvd-grown monolayer graphene onto arbitrary substrates. *ACS Nano*, 5(9):6916–6924, 2011.

- [70] A. K. Geim and I. V. Grigorieva. Van der waals heterostructures. *Nature*, 499(7459):419–25, 2013.
- [71] S. Afyouni Akbari, V. Ghafarinia, T. Larsen, M. M. Parmar, and L. G. Villanueva. Large suspended monolayer and bilayer graphene membranes with diameter up to 750 microm. *Sci Rep*, 10(1):6426, 2020.
- [72] Y. M. Chen, S. M. He, C. H. Huang, C. C. Huang, W. P. Shih, C. L. Chu, J. Kong, J. Li, and C. Y. Su. Ultra-large suspended graphene as a highly elastic membrane for capacitive pressure sensors. *Nanoscale*, 8(6):3555–64, 2016.
- [73] LaiPeng Ma, Wencai Ren, and HuiMing Cheng. Transfer methods of graphene from metal substrates: A review. *Small Methods*, 3(7), 2019.
- [74] Mingguang Chen, Robert C. Haddon, Ruoxue Yan, and Elena Bekyarova. Advances in transferring chemical vapour deposition graphene: a review. *Materials Horizons*, 4(6):1054–1063, 2017.
- [75] K. S. Novoselov, A. K. Geim, S. V. Morozov, D. Jiang, M. I. Katsnelson, I. V. Grigorieva, S. V. Dubonos, and A. A. Firsov. Two-dimensional gas of massless dirac fermions in graphene. *Nature*, 438(7065):197–200, 2005.
- [76] L. M. Malard, J. Nilsson, D. C. Elias, J. C. Brant, F. Plentz, E. S. Alves, A. H. Castro Neto, and M. A. Pimenta. Probing the electronic structure of bilayer graphene by raman scattering. *Physical Review B*, 76(20), 2007.
- [77] Y. Zhang, T. T. Tang, C. Girit, Z. Hao, M. C. Martin, A. Zettl, M. F. Crommie, Y. R. Shen, and F. Wang. Direct observation of a widely tunable bandgap in bilayer graphene. *Nature*, 459(7248):820–3, 2009.
- [78] Keun Su Kim, Andrew L. Walter, Luca Moreschini, Thomas Seyller, Karsten Horn, Eli Rotenberg, and Aaron Bostwick. Coexisting massive and massless dirac fermions in symmetry-broken bilayer graphene. *Nat Mater*, 12(10):887–892, 2013.
- [79] A. K. Geim and K. S. Novoselov. The rise of graphene. *Nat Mater*, 6(3):183–191, 2007.
- [80] A. A. Balandin, S. Ghosh, W. Bao, I. Calizo, D. Teweldebrhan, F. Miao, and C. N. Lau. Superior thermal conductivity of single-layer graphene. *Nano Lett*, 8(3):902–7, 2008.
- [81] Jia-An Yan, W. Y. Ruan, and M. Y. Chou. Phonon dispersions and vibrational properties of monolayer, bilayer, and trilayer graphene: Density-functional perturbation theory. *Physical Review B*, 77(12), 2008.
- [82] C. Lee, X. Wei, J. W. Kysar, and J. Hone. Measurement of the elastic properties and intrinsic strength of monolayer graphene. *Science*, 321(5887):385–8, 2008.

- [83] Carlos S. Ruiz-Vargas, Houlong L. Zhuang, Pinshane Y. Huang, Arend M. van der Zande, Shivank Garg, Paul L. McEuen, David A. Muller, Richard G. Hennig, and Jiwoong Park. Softened elastic response and unzipping in chemical vapor deposition graphene membranes. *Nano Letters*, 11(6):2259–2263, 2011.
- [84] G. Zamborlini, M. Imam, L. L. Patera, T. O. Mentes, N. Stojic, C. Africh, A. Sala, N. Binggeli, G. Comelli, and A. Locatelli. Nanobubbles at gpa pressure under graphene. *Nano Lett*, 15(9):6162–9, 2015.
- [85] J. S. Bunch, S. S. Verbridge, J. S. Alden, A. M. van der Zande, J. M. Parpia, H. G. Craighead, and P. L. McEuen. Impermeable atomic membranes from graphene sheets. *Nano Lett*, 8(8):2458–62, 2008.
- [86] Steven P. Koenig, Narasimha G. Boddeti, Martin L. Dunn, and J. Scott Bunch. Ultrastrong adhesion of graphene membranes. *Nat Nano*, 6(9):543–546, 2011.
- [87] R. S. Weatherup, B. Eren, Y. Hao, H. Bluhm, and M. B. Salmeron. Graphene membranes for atmospheric pressure photoelectron spectroscopy. *J Phys Chem Lett*, 7(9):1622–7, 2016.
- [88] S. Tanuma, C. J. Powell, and D. R. Penn. Calculations of electron inelastic mean free paths. ix. data for 41 elemental solids over the 50 ev to 30 kev range. *Surface and Interface Analysis*, 43(3):689–713, 2011.
- [89] R. R. Nair, P. Blake, A. N. Grigorenko, K. S. Novoselov, T. J. Booth, T. Stauber, N. M. Peres, and A. K. Geim. Fine structure constant defines visual transparency of graphene. *Science*, 320(5881):1308, 2008.
- [90] B. Segall. Calculated shape of the fermi surface of copper. *Physical Review Letters*, 7(5):154–155, 1961.
- [91] Glenn A. Burdick. Energy band structure of copper. *Physical Review*, 129(1):138–150, 1963.
- [92] A. Spitzer and H. Lüth. The adsorption of oxygen on copper surfaces. *Surface Science*, 118(1-2):136–144, 1982.
- [93] Kenji Toyoda, Katsuya Nozawa, Nozomu Matsukawa, and Shigeo Yoshii. Density functional theoretical study of graphene on transition-metal surfaces: The role of metal d-band in the potential-energy surface. *The Journal of Physical Chemistry C*, 117(16):8156–8160, 2013.
- [94] S. J. Bennett. The thermal expansion of copper between 300 and 700k. *Journal of Physics D: Applied Physics*, 11(5):777–780, 1978.
- [95] D. Yoon, Y. W. Son, and H. Cheong. Negative thermal expansion coefficient of graphene measured by raman spectroscopy. *Nano Lett*, 11(8):3227–31, 2011.

- [96] Jin-Wu Jiang, Jian-Sheng Wang, and Baowen Li. Thermal expansion in single-walled carbon nanotubes and graphene: Nonequilibrium greens function approach. *Physical Review B*, 80(20), 2009.
- [97] K. V. Zakharchenko, M. I. Katsnelson, and A. Fasolino. Finite temperature lattice properties of graphene beyond the quasiharmonic approximation. *Phys Rev Lett*, 102(4):046808, 2009.
- [98] Patrick Zeller, Xinzhou Ma, and Sebastian Günther. Indexing moiré patterns of metal-supported graphene and related systems: strategies and pitfalls. *New Journal of Physics*, 19(1):013015, 2017.
- [99] Y. H. Zhang, B. Wang, H. R. Zhang, Z. Y. Chen, Y. Q. Zhang, B. Wang, Y. P. Sui, X. L. Li, X. M. Xie, G. H. Yu, Z. Jin, and X. Y. Liu. The distribution of wrinkles and their effects on the oxidation resistance of chemical vapor deposition graphene. *Carbon*, 70:81–86, 2014.
- [100] H. Hattab, A. T. N’Diaye, D. Wall, C. Klein, G. Jnawali, J. Coraux, C. Busse, R. van Gastel, B. Poelsema, T. Michely, F. J. zu Heringdorf, and M. Horn-von Hoegen. Interplay of wrinkles, strain, and lattice parameter in graphene on iridium. *Nano Lett*, 12(2):678–82, 2012.
- [101] Paul Leidinger. Master’s thesis. *Technical University of Munich (TUM)*, 2016.
- [102] J. J. De Yoreo. Principles of crystal nucleation and growth. *Reviews in Mineralogy and Geochemistry*, 54(1):57–93, 2003.
- [103] K. Celebi, M. T. Cole, K. B. K. Teo, and H. G. Park. Observations of early stage graphene growth on copper. *Electrochemical and Solid-State Letters*, 15(1), 2012.
- [104] N. Srivastava, Qin Gao, M. Widom, R. M. Feenstra, Shu Nie, K. F. McCarty, and I. V. Vlassiuk. Low-energy electron reflectivity of graphene on copper and other substrates. *Physical Review B*, 87(24):245414, 2013.
- [105] Piran R. Kidambi, Bernhard C. Bayer, Raoul Blume, Zhu-Jun Wang, Carsten Baecht, Robert S. Weatherup, Marc-Georg Willinger, Robert Schloegl, and Stephan Hofmann. Observing graphene grow: Catalyst-graphene interactions during scalable graphene growth on polycrystalline copper. *Nano Letters*, 13(10):4769–4778, 2013.
- [106] Niclas S. Mueller, Anthony J. Morfa, Daniel Abou-Ras, Valerio Oddone, Tymoteusz Ciuk, and Michael Giersig. Growing graphene on polycrystalline copper foils by ultra-high vacuum chemical vapor deposition. *Carbon*, 78:347–355, 2014.
- [107] Tianru Wu, Guqiao Ding, Honglie Shen, Haomin Wang, Lei Sun, Da Jiang, Xiaoming Xie, and Mianheng Jiang. Triggering the continuous growth of graphene toward millimeter-sized grains. *Advanced Functional Materials*, 23(2):198–203, 2013.

- [108] Remi Papon, Subash Sharma, Sachin M. Shinde, Amutha Thangaraja, Golap Kalita, and Masaki Tanemura. Formation of graphene nanoribbons and y-junctions by hydrogen induced anisotropic etching. *RSC Advances*, 5(44):35297–35301, 2015.
- [109] Thais Chagas, Thiago H. R. Cunha, Matheus J. S. Matos, Diogo D. dos Reis, Karolline A. S. Araujo, Angelo Malachias, Mario S. C. Mazzoni, Andre S. Ferlauto, and Rogerio Magalhaes-Paniago. Room temperature observation of the correlation between atomic and electronic structure of graphene on cu(110). *RSC Advances*, 6(100):98001–98009, 2016.
- [110] Remi Papon, Golap Kalita, Subash Sharma, Sachin M. Shinde, Riteshkumar Vishwakarma, and Masaki Tanemura. Controlling single and few-layer graphene crystals growth in a solid carbon source based chemical vapor deposition. *Applied Physics Letters*, 105(13), 2014.
- [111] Fangzhu Qing, Ruitao Jia, Bao-Wen Li, Chunlin Liu, Congzhou Li, Bo Peng, Longjiang Deng, Wanli Zhang, Yanrong Li, Rodney S. Ruoff, and Xuesong Li. Graphene growth with 'no' feedstock. *2D Materials*, 4(2):025089, 2017.
- [112] M. Hadi Khaksaran and Ismet I. Kaya. Spontaneous nucleation and growth of graphene flakes on copper foil in the absence of external carbon precursor in chemical vapor deposition. *ACS Omega*, 3(10):12575–12583, 2018.
- [113] Xuesong Li, Carl W. Magnuson, Archana Venugopal, Jinho An, Ji Won Suk, Boyang Han, Mark Borysiak, Weiwei Cai, Aruna Velamakanni, Yanwu Zhu, Lianfeng Fu, Eric M. Vogel, Edgar Voelkl, Luigi Colombo, and Rodney S. Ruoff. Graphene films with large domain size by a two-step chemical vapor deposition process. *Nano Letters*, 10(11):4328–4334, 2010.
- [114] Seunghyun Lee, Kyunghoon Lee, and Zhaohui Zhong. Wafer scale homogeneous bilayer graphene films by chemical vapor deposition. *Nano Letters*, 10(11):4702–4707, 2010.
- [115] Xuesong Li, Carl W. Magnuson, Archana Venugopal, Rudolf M. Tromp, James B. Hannon, Eric M. Vogel, Luigi Colombo, and Rodney S. Ruoff. Large-area graphene single crystals grown by low-pressure chemical vapor deposition of methane on copper. *Journal of the American Chemical Society*, 133(9):2816–2819, 2011.
- [116] Ivan Vlassiouk, Murari Regmi, Pasquale Fulvio, Sheng Dai, Panos Datskos, Gyula Eres, and Sergei Smirnov. Role of hydrogen in chemical vapor deposition growth of large single-crystal graphene. *ACS Nano*, 5(7):6069–6076, 2011.
- [117] Birong Luo, Patrick R. Whelan, Abhay Shivayogimath, David M. A. Mackenzie, Peter Bøggild, and Timothy J. Booth. Copper oxidation through nucleation sites of chemical vapor deposited graphene. *Chemistry of Materials*, 28(11):3789–3795, 2016.
- [118] Shuting Zheng, Mengqi Zeng, Hui Cao, Tao Zhang, Xiaowen Gao, Yao Xiao, and Lei Fu. Insight into the rapid growth of graphene single crystals on liquid metal via chemical vapor deposition. *Science China Materials*, 62(8):1087–1095, 2019.

- [119] T. Liang, G. He, G. Huang, Y. Kong, W. Fu, H. Chen, Q. Wang, H. Iwai, D. Fujita, Y. Liu, and M. Xu. Graphene nucleation preferentially at oxygen-rich cu sites rather than on pure cu surface. *Adv Mater*, 27(41):6404–10, 2015.
- [120] Baoshan Hu, Hiroki Ago, Yoshito Ito, Kenji Kawahara, Masaharu Tsuji, Eisuke Magome, Kazushi Sumitani, Noriaki Mizuta, Ken-ichi Ikeda, and Seigi Mizuno. Epitaxial growth of large-area single-layer graphene over cu(111)/sapphire by atmospheric pressure cvd. *Carbon*, 50(1):57–65, 2012.
- [121] Libo Gao, Wencai Ren, Jinping Zhao, Lai-Peng Ma, Zongping Chen, and Hui-Ming Cheng. Efficient growth of high-quality graphene films on cu foils by ambient pressure chemical vapor deposition. *Applied Physics Letters*, 97(18):183109, 2010.
- [122] L. Liu, H. Zhou, R. Cheng, W. J. Yu, Y. Liu, Y. Chen, J. Shaw, X. Zhong, Y. Huang, and X. Duan. High-yield chemical vapor deposition growth of high-quality large-area ab-stacked bilayer graphene. *ACS Nano*, 6(9):8241–9, 2012.
- [123] Hong Wang, Guanzhong Wang, Pengfei Bao, Shaolin Yang, Wei Zhu, Xing Xie, and Wen-Jun Zhang. Controllable synthesis of submillimeter single-crystal monolayer graphene domains on copper foils by suppressing nucleation. *Journal of the American Chemical Society*, 134(8):3627–3630, 2012.
- [124] K. Kumar and E. H. Yang. On the growth mode of two-lobed curvilinear graphene domains at atmospheric pressure. *Sci Rep*, 3:2571, 2013.
- [125] J. Kwak, Y. Jo, S. D. Park, N. Y. Kim, S. Y. Kim, H. J. Shin, Z. Lee, S. Y. Kim, and S. Y. Kwon. Oxidation behavior of graphene-coated copper at intrinsic graphene defects of different origins. *Nat Commun*, 8(1):1549, 2017.
- [126] Jürgen Kraus, Lena Böbel, Gregor Zwaschka, and Sebastian Günther. Understanding the reaction kinetics to optimize graphene growth on cu by chemical vapor deposition. *Annalen der Physik*, 529(11):1700029, 2017.
- [127] Gyula Eres, Murari Regmi, Christopher M. Rouleau, Jihua Chen, Iliia N. Ivanov, Alexander A. Puretzky, and David B. Geohegan. Cooperative island growth of large-area single-crystal graphene on copper using chemical vapor deposition. *ACS Nano*, 8(6):5657–5669, 2014.
- [128] P. Leidinger, J. Kraus, and S. Günther. Predicting graphene growth on cu: Universal kinetic growth model and its experimental verification. *ACS Nano*, 2021.
- [129] National Institute of Standards and U.S. Department of Commerce Technology (NIST). Nist chemistry webbook, 2021.
- [130] Grzegorz Gajewski and Chun-Wei Pao. Ab initio calculations of the reaction pathways for methane decomposition over the cu (111) surface. *The Journal of Chemical Physics*, 135(6):064707, 2011.

- [131] Pai Li, Zhenyu Li, and Jinlong Yang. Dominant kinetic pathways of graphene growth in chemical vapor deposition: The role of hydrogen. *The Journal of Physical Chemistry C*, 121(46):25949–25955, 2017.
- [132] Wenhua Zhang, Ping Wu, Zhenyu Li, and Jinlong Yang. First-principles thermodynamics of graphene growth on cu surfaces. *The Journal of Physical Chemistry C*, 115(36):17782–17787, 2011.
- [133] N. Galea, D. Knapp, and T. Ziegler. Density functional theory studies of methane dissociation on anode catalysts in solid-oxide fuel cells: Suggestions for coke reduction. *Journal of Catalysis*, 247(1):20–33, 2007.
- [134] Hongyan Liu, Riguang Zhang, Ruixia Yan, Jingrui Li, Baojun Wang, and Kechang Xie. Insight into ch₄ dissociation on nicu catalyst: A first-principles study. *Applied Surface Science*, 258(20):8177–8184, 2012.
- [135] X. Wang, Q. Yuan, J. Li, and F. Ding. The transition metal surface dependent methane decomposition in graphene chemical vapor deposition growth. *Nanoscale*, 9(32):11584–11589, 2017.
- [136] Kai Li, Chaozheng He, Menggai Jiao, Ying Wang, and Zhijian Wu. A first-principles study on the role of hydrogen in early stage of graphene growth during the ch₄ dissociation on cu(111) and ni(111) surfaces. *Carbon*, 74:255–265, 2014.
- [137] Chak-Tong Au, Meng-Sheng Liao, and Ching-Fai Ng. A detailed theoretical treatment of the partial oxidation of methane to syngas on transition and coinage metal (m) catalysts (m = ni, pd, pt, cu). *The Journal of Physical Chemistry A*, 102(22):3959–3969, 1998.
- [138] Nobuo Tajima, Tomoaki Kaneko, Jun Nara, and Takahisa Ohno. A first principles study on the cvd graphene growth on copper surfaces: A carbon atom incorporation to graphene edges. *Surface Science*, 653:123–129, 2016.
- [139] Xi Mi, Vincent Meunier, Nikhil Koratkar, and Yunfeng Shi. Facet-insensitive graphene growth on copper. *Physical Review B*, 85(15), 2012.
- [140] Z. Qiu, P. Li, Z. Li, and J. Yang. Atomistic simulations of graphene growth: From kinetics to mechanism. *Acc Chem Res*, 51(3):728–735, 2018.
- [141] HoKwon Kim, Cecilia Mattevi, M. Reyes Calvo, Jenny C. Oberg, Luca Artiglia, Stefano Agnoli, Cyrus F. Hirjibehedin, Manish Chhowalla, and Eduardo Saiz. Activation energy paths for graphene nucleation and growth on cu. *ACS Nano*, 6(4):3614–3623, 2012.
- [142] H. Chen, W. Zhu, and Z. Zhang. Contrasting behavior of carbon nucleation in the initial stages of graphene epitaxial growth on stepped metal surfaces. *Phys Rev Lett*, 104(18):186101, 2010.
- [143] Charles Kittel. *Introduction to Solid State Physics*. John Wiley & Sons, 2018.

- [144] Ping Wu, Wenhua Zhang, Zhenyu Li, Jinlong Yang, and Jian Guo Hou. Communication: Coalescence of carbon atoms on cu (111) surface: Emergence of a stable bridging-metal structure motif. *The Journal of Chemical Physics*, 133(7):–, 2010.
- [145] H. Shu, X. M. Tao, and F. Ding. What are the active carbon species during graphene chemical vapor deposition growth? *Nanoscale*, 7(5):1627–34, 2015.
- [146] Yingfeng Li, Meicheng Li, TianSheng Gu, Fan Bai, Yue Yu, Trevor Mwenya, and Yangxin Yu. The over-step coalescence of carbon atoms on copper surface in the cvd growth of graphene: density functional calculations. *AIP Advances*, 3(5), 2013.
- [147] S. Riikonen, A. V. Krasheninnikov, L. Halonen, and R. M. Nieminen. The role of stable and mobile carbon adspecies in copper-promoted graphene growth. *The Journal of Physical Chemistry C*, 116(9):5802–5809, 2012.
- [148] Z. X. Chen, K. M. Neyman, K. H. Lim, and N. Rosch. Ch₃o decomposition on pdzn(111), pd(111), and cu(111). a theoretical study. *Langmuir*, 20(19):8068–77, 2004.
- [149] M. Vanin, J. J. Mortensen, A. K. Kelkkanen, J. M. Garcia-Lastra, K. S. Thygesen, and K. W. Jacobsen. Graphene on metals: A van der waals density functional study. *Physical Review B*, 81(8), 2010.
- [150] Cheng Gong, Geunsik Lee, Bin Shan, Eric M. Vogel, Robert M. Wallace, and Kyeong-jae Cho. First-principles study of metalgraphene interfaces. *Journal of Applied Physics*, 108(12), 2010.
- [151] Zhiping Xu and Markus J. Buehler. Interface structure and mechanics between graphene and metal substrates: a first-principles study. *Journal of Physics: Condensed Matter*, 22(48), 2010.
- [152] M. Xia, C. Liang, Z. Cheng, R. Hu, and S. Liu. The adhesion energy measured by a stress accumulation-peeling mechanism in the exfoliation of graphite. *Phys Chem Chem Phys*, 21(3):1217–1223, 2019.
- [153] L. A. Girifalco and R. A. Lad. Energy of cohesion, compressibility, and the potential energy functions of the graphite system. *J. Chem. Phys.*, 25(4):693–697, 1956.
- [154] J. Weippert, J. Hauns, J. Bachmann, A. Bottcher, X. Yao, B. Yang, A. Narita, K. Mullen, and M. M. Kappes. A tpd-based determination of the graphite interlayer cohesion energy. *J Chem Phys*, 149(19):194701, 2018.
- [155] D. H. Jung, C. Kang, J. E. Nam, H. Jeong, and J. S. Lee. Surface diffusion directed growth of anisotropic graphene domains on different copper lattices. *Sci Rep*, 6:21136, 2016.
- [156] O. V. Yazyev and A. Pasquarello. Effect of metal elements in catalytic growth of carbon nanotubes. *Phys Rev Lett*, 100(15):156102, 2008.

- [157] Qiang Wang, Li Wei, Michael Sullivan, Shuo-Wang Yang, and Yuan Chen. Graphene layers on cu and ni (111) surfaces in layer controlled graphene growth. *RSC Advances*, 3(9), 2013.
- [158] Ikutaro Hamada and Minoru Otani. Comparative van der waals density-functional study of graphene on metal surfaces. *Physical Review B*, 82(15), 2010.
- [159] Haibo Shu, Xiaoshuang Chen, and Feng Ding. The edge termination controlled kinetics in graphene chemical vapor deposition growth. *Chem. Sci.*, 5(12):4639–4645, 2014.
- [160] Chao Ming Chiang, Tim H. Wentzlaff, and Brian E. Bent. Iodomethane decomposition on copper(110): surface reactions of c1 fragments. *The Journal of Physical Chemistry*, 96(4):1836–1848, 1992.
- [161] Yin-Zhong Lin, Jie Sun, Jun Yi, Jing-Dong Lin, Hong-Bo Chen, and Dai-Wei Liao. Energetics of chemisorption and conversion of methane on transition metal surfaces. *Journal of Molecular Structure: THEOCHEM*, 587(1-3):63–71, 2002.
- [162] A. Kokalj, N. Bonini, S. de Gironcoli, C. Sbraccia, G. Fratesi, and S. Baroni. Methane dehydrogenation on rh@cu(111): a first-principles study of a model catalyst. *J Am Chem Soc*, 128(38):12448–54, 2006.
- [163] I. Alstrup, I. Chorkendorff, and S. Ullmann. The interaction of ch₄ at high temperatures with clean and oxygen precovered cu(100). *Surface Science*, 264(12):95–102, 1992.
- [164] Q. Yu, L. A. Jauregui, W. Wu, R. Colby, J. Tian, Z. Su, H. Cao, Z. Liu, D. Pandey, D. Wei, T. F. Chung, P. Peng, N. P. Guisinger, E. A. Stach, J. Bao, S. S. Pei, and Y. P. Chen. Control and characterization of individual grains and grain boundaries in graphene grown by chemical vapour deposition. *Nat Mater*, 10(6):443–9, 2011.
- [165] H. Shu, X. Chen, X. Tao, and F. Ding. Edge structural stability and kinetics of graphene chemical vapor deposition growth. *ACS Nano*, 6(4):3243–50, 2012.
- [166] Xiuyun Zhang, Lu Wang, John Xin, Boris I. Yakobson, and Feng Ding. Role of hydrogen in graphene chemical vapor deposition growth on a copper surface. *Journal of the American Chemical Society*, 136(8):3040–3047, 2014.
- [167] Q. Yuan, B. I. Yakobson, and F. Ding. Edge-catalyst wetting and orientation control of graphene growth by chemical vapor deposition growth. *J Phys Chem Lett*, 5(18):3093–9, 2014.
- [168] Thomas Fauster, Lutz Hammer, Klaus Heinz, and M. Alexander Schneider. *Oberflächenphysik: Grundlagen und Methoden*. Oberflächenphysik: Grundlagen und Methoden. De Gruyter Oldenbourg, 2019.
- [169] J. M. Campbell and Charles T. Campbell. The dissociative adsorption of h₂ and d₂ on cu(110): activation barriers and dynamics. *Surface Science*, 259(12):1–17, 1991.

- [170] H. Wilmer, T. Genger, and O. Hinrichsen. The interaction of hydrogen with alumina-supported copper catalysts: a temperature-programmed adsorption/temperature-programmed desorption/isotopic exchange reaction study. *Journal of Catalysis*, 215(2):188–198, 2003.
- [171] T. Genger, O. Hinrichsen, and M. Muhler. The temperature-programmed desorption of hydrogen from copper surfaces. *Catalysis Letters*, 59(2/4):137–141, 1999.
- [172] G. Anger, A. Winkler, and K. D. Rendulic. Adsorption and desorption kinetics in the systems h₂/cu(111), h₂/cu(110) and h₂/cu(100). *Surface Science*, 220(1):1–17, 1989.
- [173] HoKwon Kim, Eduardo Saiz, Manish Chhowalla, and Cecilia Mattevi. Modeling of the self-limited growth in catalytic chemical vapor deposition of graphene. *New Journal of Physics*, 15(5):053012, 2013.
- [174] J. Kraus. *Erzeugung von graphenbasierten Filmen und elektronentransparenten Membranen sowie ihrer Bedeutung für katalytische Systeme*. Thesis, 2021.
- [175] K. Wong, S. J. Kang, C. W. Bielawski, R. S. Ruoff, and S. K. Kwak. First-principles study of the role of o₂ and h₂o in the decoupling of graphene on cu(111). *J Am Chem Soc*, 138(34):10986–94, 2016.
- [176] Ye Xu and Manos Mavrikakis. Adsorption and dissociation of o₂ on cu(): thermochemistry, reaction barrier and the effect of strain. *Surface Science*, 494(2):131–144, 2001.
- [177] F. H. P. M. Habraken, E. Ph Kieffer, and G. A. Bootsma. A study of the kinetics of the interactions of o₂ and n₂o with a cu(111) surface and of the reaction of co with adsorbed oxygen using aes, leed and ellipsometry. *Surface Science*, 83(1):45–59, 1979.
- [178] S. Lopez-Moreno and A. H. Romero. Atomic and molecular oxygen adsorbed on (111) transition metal surfaces: Cu and ni. *J Chem Phys*, 142(15):154702, 2015.
- [179] Denise C. Ford, Anand Udaykumar Nilekar, Ye Xu, and Manos Mavrikakis. Partial and complete reduction of o₂ by hydrogen on transition metal surfaces. *Surface Science*, 604(19-20):1565–1575, 2010.
- [180] Gui-Chang Wang and Junji Nakamura. Structure sensitivity for forward and reverse water-gas shift reactions on copper surfaces: A dft study. *The Journal of Physical Chemistry Letters*, 1(20):3053–3057, 2010.
- [181] Max Wutz, Hermann Adam, and Wilhelm Walcher. *Theorie und Praxis der Vakuumtechnik*. Springer, 1992.
- [182] Pfeiffer Vacuum GmbH. Commercial pump oil distributor, 2021.
- [183] Jürgen Kraus, Magdalene Böbel, and Sebastian Günther. Suppressing graphene nucleation during cvd on polycrystalline cu by controlling the carbon content of the support foils. *Carbon*, 96:153–165, 2016.

- [184] O. C. Bridgeman and E. W. Aldrich. Vapor pressure tables for water. *Journal of Heat Transfer*, 86(2):279–286, 1964.
- [185] J. P. Neumann, T. Zhong, and Y. A. Chang. The cu-o (copper-oxygen) system. *Bulletin of Alloy Phase Diagrams*, 5(2):136–140, 1984.
- [186] A. Righi, P. Venezuela, H. Chacham, S. D. Costa, C. Fantini, R. S. Ruoff, L. Colombo, W. S. Bacsa, and M. A. Pimenta. Resonance raman spectroscopy in twisted bilayer graphene. *Solid State Communications*, 175-176:13–17, 2013.
- [187] K. Sato, R. Saito, Y. Oyama, J. Jiang, L. G. Cançado, M. A. Pimenta, A. Jorio, Ge G. Samsonidze, G. Dresselhaus, and M. S. Dresselhaus. D-band raman intensity of graphitic materials as a function of laser energy and crystallite size. *Chemical Physics Letters*, 427(13):117–121, 2006.
- [188] Kwanpyo Kim, Sinisa Coh, Liang Z. Tan, William Regan, Jong Min Yuk, Eric Chatterjee, M. F. Crommie, Marvin L. Cohen, Steven G. Louie, and A. Zettl. Raman spectroscopy study of rotated double-layer graphene: Misorientation-angle dependence of electronic structure. *Physical Review Letters*, 108(24):246103, 2012.
- [189] R. W. Havener, H. Zhuang, L. Brown, R. G. Hennig, and J. Park. Angle-resolved raman imaging of interlayer rotations and interactions in twisted bilayer graphene. *Nano Lett*, 12(6):3162–7, 2012.
- [190] V. Carozo, C. M. Almeida, B. Fragneaud, P. M. Bedê, M. V. O. Moutinho, J. Ribeiro-Soares, N. F. Andrade, A. G. Souza Filho, M. J. S. Matos, B. Wang, M. Terrones, Rodrigo B. Capaz, A. Jorio, C. A. Achete, and L. G. Cançado. Resonance effects on the raman spectra of graphene superlattices. *Physical Review B*, 88(8), 2013.
- [191] Wenjing Fang, Allen L. Hsu, Roman Caudillo, Yi Song, A. Glen Birdwell, Eugene Zakar, Martin Kalbac, Madan Dubey, Tomás Palacios, Millie S. Dresselhaus, Paulo T. Araujo, and Jing Kong. Rapid identification of stacking orientation in isotopically labeled chemical-vapor grown bilayer graphene by raman spectroscopy. *Nano Letters*, 13(4):1541–1548, 2013.
- [192] D. M. Basko, S. Piscanec, and A. C. Ferrari. Electron-electron interactions and doping dependence of the two-phonon raman intensity in graphene. *Physical Review B*, 80(16), 2009.
- [193] Simone Pisana, Michele Lazzeri, Cinzia Casiraghi, Kostya S. Novoselov, A. K. Geim, Andrea C. Ferrari, and Francesco Mauri. Breakdown of the adiabatic born-oppenheimer approximation in graphene. *Nat Mater*, 6(3):198–201, 2007.
- [194] M. Lazzeri and F. Mauri. Nonadiabatic kohn anomaly in a doped graphene monolayer. *Phys Rev Lett*, 97(26):266407, 2006.

- [195] Zhen Hua Ni, Ting Yu, Yun Hao Lu, Ying Ying Wang, Yuan Ping Feng, and Ze Xiang Shen. Uniaxial strain on graphene: Raman spectroscopy study and band-gap opening. *ACS Nano*, 2(11):2301–2305, 2008.
- [196] T. M. G. Mohiuddin, A. Lombardo, R. R. Nair, A. Bonetti, G. Savini, R. Jalil, N. Bonini, D. M. Basko, C. Galiotis, N. Marzari, K. S. Novoselov, A. K. Geim, and A. C. Ferrari. Uniaxial strain in graphene by raman spectroscopy: gpeak splitting, grüneisen parameters, and sample orientation. *Physical Review B*, 79(20), 2009.
- [197] Mingyuan Huang, Huguen Yan, Tony F. Heinz, and James Hone. Probing strain-induced electronic structure change in graphene by raman spectroscopy. *Nano Letters*, 10(10):4074–4079, 2010.
- [198] Otakar Frank, Marcel Mohr, Janina Maultzsch, Christian Thomsen, Ibtisam Riaz, Rashid Jalil, Kostya S. Novoselov, Georgia Tsoukleri, John Parthenios, Konstantinos Papagelis, Ladislav Kavan, and Costas Galiotis. Raman 2d-band splitting in graphene: Theory and experiment. *ACS Nano*, 5(3):2231–2239, 2011.
- [199] Jin Hyoun Kang, Joonhee Moon, Dong Jin Kim, Yooseok Kim, Insu Jo, Cheolho Jeon, Jouhahn Lee, and Byung Hee Hong. Strain relaxation of graphene layers by cu surface roughening. *Nano Letters*, 16(10):5993–5998, 2016.
- [200] Yuyoung Shin, Marcelo Lozada-Hidalgo, Jose L. Sambricio, Irina V. Grigorieva, Andre K. Geim, and Cinzia Casiraghi. Raman spectroscopy of highly pressurized graphene membranes. *Applied Physics Letters*, 108(22):221907, 2016.
- [201] A. Ismach, C. Druzgalski, S. Penwell, A. Schwartzberg, M. Zheng, A. Javey, J. Bokor, and Y. Zhang. Direct chemical vapor deposition of graphene on dielectric surfaces. *Nano Lett*, 10(5):1542–8, 2010.
- [202] Z. Yan, Z. Peng, Z. Sun, J. Yao, Y. Zhu, Z. Liu, P. M. Ajayan, and J. M. Tour. Growth of bilayer graphene on insulating substrates. *ACS Nano*, 5(10):8187–92, 2011.
- [203] Ang-Yu Lu, Sung-Yen Wei, Chih-Yu Wu, Yenny Hernandez, Tzu-Yin Chen, Te-Huan Liu, Chun-Wei Pao, Fu-Rong Chen, Lain-Jong Li, and Zhen-Yu Juang. Decoupling of cvd graphene by controlled oxidation of recrystallized cu. *RSC Advances*, 2(7):3008–3013, 2012.
- [204] X. Wu, G. Zhong, L. D’Arsie, H. Sugime, S. Esconjauregui, A. W. Robertson, and J. Robertson. Growth of continuous monolayer graphene with millimeter-sized domains using industrially safe conditions. *Sci Rep*, 6:21152, 2016.
- [205] H. Seiler. Secondary electron emission in the scanning electron microscope. *Journal of Applied Physics*, 54(11):R1–R18, 1983.
- [206] O. Leenaerts, B. Partoens, F. M. Peeters, A. Volodin, and C. Van Haesendonck. The work function of few-layer graphene. *J Phys Condens Matter*, 29(3):035003, 2017.

- [207] Herbert B. Michaelson. The work function of the elements and its periodicity. *Journal of Applied Physics*, 48(11):4729–4733, 1977.
- [208] Ludwig Reimer. *Scanning Electron Microscopy*. Springer, 1998.
- [209] E. H. Darlington and V. E. Cosslett. Backscattering of 0.5-10 keV electrons from solid targets. *Journal of Physics D: Applied Physics*, 5(11):1969–1981, 1972.
- [210] Burkhard Beckhoff, Birgit Kanngießer, Norbert Langhoff, Reiner Wedell, and Helmut Wolff. *Handbook of Practical X-Ray Fluorescence Analysis*. Springer, 2006.
- [211] Gerald V. Troppe, Marc A. Gluba, Marco Kraft, Jörg Rappich, and Norbert H. Nickel. Strain relaxation in graphene grown by chemical vapor deposition. *Journal of Applied Physics*, 114(21), 2013.
- [212] S. Tanuma, C. J. Powell, and D. R. Penn. Calculations of electron inelastic mean free paths ii. data for 27 elements over the 50-2000 eV range. *Surface and Interface Analysis*, 17:26, 1991.
- [213] G. Ertl and J. Küppers. *Low energy electrons and surface chemistry*. VCH, 1985.
- [214] Robert F. Reilman, Alfred Msezane, and Steven T. Manson. Relative intensities in photoelectron spectroscopy of atoms and molecules. *Journal of Electron Spectroscopy and Related Phenomena*, 8(5):389–394, 1976.
- [215] B. L. Henke, E. M. Gullikson, and J. C. Davis. X-ray interactions: Photoabsorption, scattering, transmission, and reflection at $e = 50-30,000$ eV, $z = 1-92$. *Atomic Data and Nuclear Data Tables*, 54(2):181–342, 1993.
- [216] National Institute of Standards and U.S. Department of Commerce Technology (NIST). NIST x-ray photoelectron spectroscopy database, 2012.
- [217] T. Ma, W. Ren, Z. Liu, L. Huang, L. P. Ma, X. Ma, Z. Zhang, L. M. Peng, and H. M. Cheng. Repeated growth-etching-regrowth for large-area defect-free single-crystal graphene by chemical vapor deposition. *ACS Nano*, 8(12):12806–13, 2014.
- [218] L. Brown, E. B. Lochocki, J. Avila, C. J. Kim, Y. Ogawa, R. W. Havener, D. K. Kim, E. J. Monkman, D. E. Shai, H. I. Wei, M. P. Levendorf, M. Asensio, K. M. Shen, and J. Park. Polycrystalline graphene with single crystalline electronic structure. *Nano Lett*, 14(10):5706–11, 2014.
- [219] J. Hu, J. Xu, Y. Zhao, L. Shi, Q. Li, F. Liu, Z. Ullah, W. Li, Y. Guo, and L. Liu. Roles of oxygen and hydrogen in crystal orientation transition of copper foils for high-quality graphene growth. *Sci Rep*, 7:45358, 2017.

- [220] Kamal P. Sharma, Sachin M. Shinde, Mohamad Saufi Rosmi, Subash Sharma, Golap Kalita, and Masaki Tanemura. Effect of copper foil annealing process on large graphene domain growth by solid source-based chemical vapor deposition. *Journal of Materials Science*, 51(15):7220–7228, 2016.
- [221] Y. Li, L. Sun, Z. Chang, H. Liu, Y. Wang, Y. Liang, B. Chen, Q. Ding, Z. Zhao, R. Wang, Y. Wei, H. Peng, L. Lin, and Z. Liu. Large single-crystal cu foils with high-index facets by strain-engineered anomalous grain growth. *Adv Mater*, 32(29):e2002034, 2020.
- [222] Insu Jo, Subeom Park, Dongjin Kim, Jin San Moon, Won Bae Park, Tae Hyeong Kim, Jin Hyoun Kang, Wonbae Lee, Youngsoo Kim, Dong Nyung Lee, Sung-Pyo Cho, Hyunchul Choi, Inbyeong Kang, Jong Hyun Park, Jeong Soo Lee, and Byung Hee Hong. Tension-controlled single-crystallization of copper foils for roll-to-roll synthesis of high-quality graphene films. *2D Materials*, 5(2), 2018.
- [223] Niewczas Marek. Chapter 75 dislocations and twinning in face centred cubic crystals. *Dislocations in Solids*, 13:263–364, 2007.
- [224] R. D. Doherty, D. A. Hughes, F. J. Humphreys, J. J. Jonas, D. Juul Jensen, M. E. Kassner, W. E. King, T. R. McNelley, H. J. McQueen, and A. D. Rollett. Current issues in recrystallization: a review. *Materials Science and Engineering: A*, 238(2):219–274, 1997.
- [225] Yu Wang, Yi Zheng, Xiangfan Xu, Emilie Dubuisson, Qiaoliang Bao, Jiong Lu, and Kian Ping Loh. Electrochemical delamination of cvd-grown graphene film: Toward the recyclable use of copper catalyst. *ACS Nano*, 5(12):9927–9933, 2011.
- [226] L. Gao, W. Ren, H. Xu, L. Jin, Z. Wang, T. Ma, L. P. Ma, Z. Zhang, Q. Fu, L. M. Peng, X. Bao, and H. M. Cheng. Repeated growth and bubbling transfer of graphene with millimetre-size single-crystal grains using platinum. *Nat Commun*, 3:699, 2012.
- [227] Wei Liu, Hong Li, Chuan Xu, Yasin Khatami, and Kaustav Banerjee. Synthesis of high-quality monolayer and bilayer graphene on copper using chemical vapor deposition. *Carbon*, 49(13):4122–4130, 2011.
- [228] B. Aleman, W. Regan, S. Aloni, V. Altoe, N. Alem, C. Girit, B. Geng, L. Maserati, M. Crommie, F. Wang, and A. Zettl. Transfer-free batch fabrication of large-area suspended graphene membranes. *ACS Nano*, 4(8):4762–8, 2010.
- [229] Robert S. Weatherup. 2d material membranes for operando atmospheric pressure photoelectron spectroscopy. *Topics in Catalysis*, 61(20):2085–2102, 2018.
- [230] Alessia Matruglio, Silvia Nappini, Denys Naumenko, Elena Magnano, Federica Bondino, Marco Lazzarino, and Simone Dal Zilio. Contamination-free suspended graphene structures by a ti-based transfer method. *Carbon*, 103:305–310, 2016.

- [231] William Regan, Nasim Alem, Benjamín Alemán, Baisong Geng, Çalar Girit, Lorenzo Maserati, Feng Wang, Michael Crommie, and A. Zettl. A direct transfer of layer-area graphene. *Applied Physics Letters*, 96(11):113102, 2010.
- [232] Gabriela Borin Barin, Yi Song, Iara de Fátima Gimenez, Antonio Gomes Souza Filho, Ledjane Silva Barreto, and Jing Kong. Optimized graphene transfer: Influence of polymethylmethacrylate (pmma) layer concentration and baking time on graphene final performance. *Carbon*, 84:82–90, 2015.
- [233] Zehao Wu, Xuwei Zhang, Atanu Das, Jinglan Liu, Zhenxing Zou, Zilong Zhang, Yang Xia, Pei Zhao, and Hongtao Wang. Step-by-step monitoring of cvd-graphene during wet transfer by raman spectroscopy. *RSC Advances*, 9(71):41447–41452, 2019.
- [234] Gerardo Algara-Siller, Ossi Lehtinen, Andrey Turchanin, and Ute Kaiser. Dry-cleaning of graphene. *Applied Physics Letters*, 104(15):153115, 2014.
- [235] A. Yulaev, G. Cheng, A. R. Walker, I. V. Vlassiouk, A. Myers, M. S. Leite, and A. Kolmakov. Toward clean suspended cvd graphene. *RSC Adv*, 6(87):83954–83962, 2016.
- [236] Zhifa Shan, Qiongyu Li, Zhijuan Zhao, Zhenzhong Wang, Yanqing Wu, and Weiwei Cai. One-step transfer and doping of large area graphene by ultraviolet curing adhesive. *Carbon*, 84:9–13, 2015.
- [237] Guilhermino J. M. Fechine, Iñigo Martin-Fernandez, George Yiapanis, Ricardo Bentini, Eeshan Sandeep Kulkarni, Ricardo V. Bof de Oliveira, Xiao Hu, Irene Yarovsky, Antônio H. Castro Neto, and Barbaros Özyilmaz. Direct dry transfer of chemical vapor deposition graphene to polymeric substrates. *Carbon*, 83:224–231, 2015.
- [238] Viktoryia Shautsova, Adam M. Gilbertson, Nicola C. G. Black, Stefan A. Maier, and Lesley F. Cohen. Hexagonal boron nitride assisted transfer and encapsulation of large area cvd graphene. *Scientific Reports*, 6:30210, 2016.
- [239] B. Wang, M. Huang, L. Tao, S. H. Lee, A. R. Jang, B. W. Li, H. S. Shin, D. Akinwande, and R. S. Ruoff. Support-free transfer of ultrasmooth graphene films facilitated by self-assembled monolayers for electronic devices and patterns. *ACS Nano*, 10(1):1404–10, 2016.
- [240] Z. Wu, Y. Guo, Y. Guo, R. Huang, S. Xu, J. Song, H. Lu, Z. Lin, Y. Han, H. Li, T. Han, J. Lin, Y. Wu, G. Long, Y. Cai, C. Cheng, D. Su, J. Robertson, and N. Wang. A fast transfer-free synthesis of high-quality monolayer graphene on insulating substrates by a simple rapid thermal treatment. *Nanoscale*, 8(5):2594–600, 2016.
- [241] X. Chen, B. Wu, and Y. Liu. Direct preparation of high quality graphene on dielectric substrates. *Chem Soc Rev*, 45(8):2057–74, 2016.

- [242] Y. Y. Stehle, X. Sang, R. R. Unocic, D. Voylov, R. K. Jackson, S. Smirnov, and I. Vlassiouk. Anisotropic etching of hexagonal boron nitride and graphene: Question of edge terminations. *Nano Lett*, 17(12):7306–7314, 2017.
- [243] T. Ma, W. Ren, X. Zhang, Z. Liu, Y. Gao, L. C. Yin, X. L. Ma, F. Ding, and H. M. Cheng. Edge-controlled growth and kinetics of single-crystal graphene domains by chemical vapor deposition. *Proc Natl Acad Sci U S A*, 110(51):20386–91, 2013.
- [244] Bin Wang, Yanhui Zhang, Haoran Zhang, Zhiying Chen, Xiaoming Xie, Yanping Sui, Xiaoliang Li, Guanghui Yu, Lizhong Hu, Zhi Jin, and Xinyu Liu. Wrinkle-dependent hydrogen etching of chemical vapor deposition-grown graphene domains. *Carbon*, 70:75–80, 2014.
- [245] H. Zhang, Y. Zhang, Y. Zhang, Z. Chen, Y. Sui, X. Ge, G. Yu, Z. Jin, and X. Liu. Edge morphology evolution of graphene domains during chemical vapor deposition cooling revealed through hydrogen etching. *Nanoscale*, 8(7):4145–50, 2016.
- [246] Paul Leidinger and Sebastian Günther. Insight into the thermodynamics of graphene growth on copper. *The Journal of Physical Chemistry C*, 125(23):12663–12671, 2021.
- [247] Jr. Chase, M.W. *NIST-JANAF Thermochemical Tables*. NIST-JANAF. American Institute of Physics, New York, 1998.
- [248] A. M. Lewis, B. Derby, and I. A. Kinloch. Influence of gas phase equilibria on the chemical vapor deposition of graphene. *ACS Nano*, 7(4):3104–17, 2013.
- [249] Nathaniel S. Safron and Michael S. Arnold. Experimentally determined model of atmospheric pressure cvd of graphene on cu. *J. Mater. Chem. C*, 2(4):744–755, 2014.
- [250] Wenhua Zhang, Ping Wu, Zhenyu Li, and Jinlong Yang. First-principles thermodynamics of graphene growth on cu surfaces. *The Journal of Physical Chemistry C*, 115(36):17782–17787, 2011.
- [251] P. Zeller S. Günther. *Moiré Patterns of Graphene on Metals*, volume 4, pages 295–307. Elsevier, 2018.
- [252] Taeshik Yoon, Woo Cheol Shin, Taek Yong Kim, Jeong Hun Mun, Taek-Soo Kim, and Byung Jin Cho. Direct measurement of adhesion energy of monolayer graphene as-grown on copper and its application to renewable transfer process. *Nano Letters*, 12(3):1448–1452, 2012.
- [253] Matthias Batzill. The surface science of graphene: Metal interfaces, cvd synthesis, nanoribbons, chemical modifications, and defects. *Surface Science Reports*, 67:83–115, 2012.
- [254] A. Al Taleb and D. Farias. Phonon dynamics of graphene on metals. *J Phys Condens Matter*, 28(10):103005, 2016.

- [255] J. Wang, D. C. Sorescu, S. Jeon, A. Belianinov, S. V. Kalinin, A. P. Baddorf, and P. Maksymovych. Atomic intercalation to measure adhesion of graphene on graphite. *Nat Commun*, 7:13263, 2016.
- [256] Santanu Das, Debrupa Lahiri, Dong-Yoon Lee, Arvind Agarwal, and Wonbong Choi. Measurements of the adhesion energy of graphene to metallic substrates. *Carbon*, 59:121–129, 2013.
- [257] Xin Hao, Borduin Russell, Jiang Wei, M. Liechti Kenneth, and Li Wei. Adhesion energy of as-grown graphene on copper foil with a blister test. *Carbon*, 123:243–249, 2017.
- [258] Lorin X. Benedict, Nasreen G. Chopra, Marvin L. Cohen, A. Zettl, Steven G. Louie, and Vincent H. Crespi. Microscopic determination of the interlayer binding energy in graphite. *Chemical Physics Letters*, 286(5-6):490–496, 1998.
- [259] S. R. Na, J. W. Suk, L. Tao, D. Akinwande, R. S. Ruoff, R. Huang, and K. M. Liechti. Selective mechanical transfer of graphene from seed copper foil using rate effects. *ACS Nano*, 9(2):1325–35, 2015.
- [260] Ze Liu, Jefferson Zhe Liu, Yao Cheng, Zhihong Li, Li Wang, and Quanshui Zheng. Interlayer binding energy of graphite: A mesoscopic determination from deformation. *Physical Review B*, 85(20), 2012.
- [261] S. R. Na, S. Rahimi, L. Tao, H. Chou, S. K. Ameri, D. Akinwande, and K. M. Liechti. Clean graphene interfaces by selective dry transfer for large area silicon integration. *Nanoscale*, 8(14):7523–33, 2016.
- [262] Wen Wang, Shuyang Dai, Xide Li, Jiarui Yang, David J. Srolovitz, and Quanshui Zheng. Measurement of the cleavage energy of graphite. *Nature Communications*, 6:7853, 2015.
- [263] Z. Cao, P. Wang, W. Gao, L. Tao, J. W. Suk, R. S. Ruoff, D. Akinwande, R. Huang, and K. M. Liechti. A blister test for interfacial adhesion of large-scale transferred graphene. *Carbon*, 69:390–400, 2014.
- [264] Peng Li, Zheng You, and Tianhong Cui. Adhesion energy of few layer graphene characterized by atomic force microscope. *Sensors and Actuators A: Physical*, 217:56–61, 2014.
- [265] L. A. Girifalco and R. A. Lad. Energy of cohesion, compressibility, and the potential energy functions of the graphite system. *The Journal of Chemical Physics*, 25(4):693–697, 1956.
- [266] J. Weippert, J. Hauns, J. Bachmann, A. Bottcher, X. Yao, B. Yang, A. Narita, K. Mullen, and M. M. Kappes. A tpd-based determination of the graphite interlayer cohesion energy. *J Chem Phys*, 149(19):194701, 2018.

- [267] B. W. Li, D. Luo, L. Zhu, X. Zhang, S. Jin, M. Huang, F. Ding, and R. S. Ruoff. Orientation-dependent strain relaxation and chemical functionalization of graphene on a cu(111) foil. *Adv Mater*, 30(10), 2018.
- [268] Ali Mohsin, Lei Liu, Peizhi Liu, Wan Deng, Iliia N. Ivanov, Guoliang Li, Ondrej E. Dyck, Gerd Duscher, John R. Dunlap, Kai Xiao, and Gong Gu. Synthesis of millimeter-size hexagon-shaped graphene single crystals on resolidified copper. *ACS Nano*, 7(10):8924–8931, 2013.
- [269] V. L. Nguyen, D. J. Perello, S. Lee, C. T. Nai, B. G. Shin, J. G. Kim, H. Y. Park, H. Y. Jeong, J. Zhao, Q. A. Vu, S. H. Lee, K. P. Loh, S. Y. Jeong, and Y. H. Lee. Wafer-scale single-crystalline ab-stacked bilayer graphene. *Adv Mater*, 28(37):8177–8183, 2016.
- [270] B. Wang, M. L. Bocquet, S. Guenther, and J. Winterlin. Comment on "periodically rippled graphene: Growth and spatially resolved electronic structure". *Physical Review Letters*, 101(9), 2008.
- [271] Elena Loginova, Norman C. Bartelt, Peter J. Feibelman, and Kevin F. McCarty. Evidence for graphene growth by c cluster attachment. *New Journal of Physics*, 10(9), 2008.
- [272] Kemal Celebi, Matthew T. Cole, Jong Won Choi, Frederic Wyczisk, Pierre Legagneux, Nalin Rupesinghe, John Robertson, Kenneth B. K. Teo, and Hyung Gyu Park. Evolutionary kinetics of graphene formation on copper. *Nano Letters*, 13(3):967–974, 2013.
- [273] Yun-Hi Lee and Jong-Hee Lee. Scalable growth of free-standing graphene wafers with copper(cu) catalyst on sio₂/si substrate: Thermal conductivity of the wafers. *Applied Physics Letters*, 96(8), 2010.
- [274] E. Loginova, N. C. Bartelt, P. J. Feibelman, and K. F. McCarty. Factors influencing graphene growth on metal surfaces. *New Journal of Physics*, 11(6), 2009.
- [275] Hamid Mehdipour and Kostya Ostrikov. Kinetics of low-pressure, low-temperature graphene growth: Toward single-layer, single-crystalline structure. *ACS Nano*, 6(11):10276–10286, 2012.
- [276] Sirui Xing, Wei Wu, Yanan Wang, Jiming Bao, and Shin-Shem Pei. Kinetic study of graphene growth: Temperature perspective on growth rate and film thickness by chemical vapor deposition. *Chemical Physics Letters*, 580:62–66, 2013.
- [277] G. Zinsmeister. A contribution to frenkel's theory of condensation. *Vacuum*, 16(10):529–535, 1966.
- [278] A. Cabrero-Vilatela, R. S. Weatherup, P. Braeuninger-Weimer, S. Caneva, and S. Hofmann. Towards a general growth model for graphene cvd on transition metal catalysts. *Nanoscale*, 8(4):2149–58, 2016.

- [279] R. S. Weatherup, A. J. Shahani, Z. J. Wang, K. Mingard, A. J. Pollard, M. G. Willinger, R. Schloegl, P. W. Voorhees, and S. Hofmann. In situ graphene growth dynamics on polycrystalline catalyst foils. *Nano Lett*, 2016.
- [280] Y. Hao, L. Wang, Y. Liu, H. Chen, X. Wang, C. Tan, S. Nie, J. W. Suk, T. Jiang, T. Liang, J. Xiao, W. Ye, C. R. Dean, B. I. Yakobson, K. F. McCarty, P. Kim, J. Hone, L. Colombo, and R. S. Ruoff. Oxygen-activated growth and bandgap tunability of large single-crystal bilayer graphene. *Nat Nanotechnol*, 11(5):426–31, 2016.
- [281] G. H. Han, F. Gunes, J. J. Bae, E. S. Kim, S. J. Chae, H. J. Shin, J. Y. Choi, D. Pribat, and Y. H. Lee. Influence of copper morphology in forming nucleation seeds for graphene growth. *Nano Lett*, 11(10):4144–8, 2011.
- [282] A. W. Robertson and J. H. Warner. Hexagonal single crystal domains of few-layer graphene on copper foils. *Nano Lett*, 11(3):1182–9, 2011.
- [283] Yimin A. Wu, Alex W. Robertson, Franziska Schäffel, Susannah C. Speller, and Jamie H. Warner. Aligned rectangular few-layer graphene domains on copper surfaces. *Chemistry of Materials*, 23(20):4543–4547, 2011.
- [284] Shu Nie, Wei Wu, Shirui Xing, Qingkai Yu, Jiming Bao, Shin-shem Pei, and K. F. McCarty. Growth from below: bilayer graphene on copper by chemical vapor deposition. *New Journal of Physics*, 14(9):093028, 2012.
- [285] Ivan Vlassiouk, Sergei Smirnov, Murari Regmi, Sumedh P. Surwade, Nishtha Srivastava, Randall Feenstra, Gyula Eres, Chad Parish, Nick Lavrik, Panos Datskos, Sheng Dai, and Pasquale Fulvio. Graphene nucleation density on copper: Fundamental role of background pressure. *The Journal of Physical Chemistry C*, 117(37):18919–18926, 2013.
- [286] Bin Wu, Dechao Geng, Zhiping Xu, Yunlong Guo, Liping Huang, Yunzhou Xue, Jianyi Chen, Gui Yu, and Yunqi Liu. Self-organized graphene crystal patterns. *NPG Asia Mater*, 5:e36, 2013.
- [287] Yui Ogawa, Katsuyoshi Komatsu, Kenji Kawahara, Masaharu Tsuji, Kazuhito Tsukagoshi, and Hiroki Ago. Structure and transport properties of the interface between cvd-grown graphene domains. *Nanoscale*, 6(13):7288–7294, 2014.
- [288] Seiya Suzuki, Takashi Nagamori, Yuki Matsuoka, and Masamichi Yoshimura. Threefold atmospheric-pressure annealing for suppressing graphene nucleation on copper in chemical vapor deposition. *Japanese Journal of Applied Physics*, 53(9):095101, 2014.
- [289] Chaocheng Wang, Wei Chen, Cheng Han, Guang Wang, Binbing Tang, Changxin Tang, Yan Wang, Wennan Zou, Wei Chen, Xue-Ao Zhang, Shiqiao Qin, Shengli Chang, and Li Wang. Growth of millimeter-size single crystal graphene on cu foils by circumfluence chemical vapor deposition. *Sci. Rep.*, 4:4537, 2014.

- [290] V. L. Nguyen, B. G. Shin, D. L. Duong, S. T. Kim, D. Perello, Y. J. Lim, Q. H. Yuan, F. Ding, H. Y. Jeong, H. S. Shin, S. M. Lee, S. H. Chae, Q. A. Vu, S. H. Lee, and Y. H. Lee. Seamless stitching of graphene domains on polished copper (111) foil. *Adv Mater*, 27(8):1376–82, 2015.
- [291] haoran zhang, yanhui zhang, bin wang, zhiying chen, Yaqian Zhang, Ping Yan Sui, Guanghui Yu, Zhi Jin, and Xin-yu Liu. Stripe distributions of graphene-coated cu foils and their effects on the reduction of graphene wrinkles. *RSC Advances*, 2015.
- [292] D. Ding, P. Solis-Fernandez, H. Hibino, and H. Ago. Spatially controlled nucleation of single-crystal graphene on cu assisted by stacked ni. *ACS Nano*, 10(12):11196–11204, 2016.
- [293] H. Q. Ta, D. J. Perello, D. L. Duong, G. H. Han, S. Gorantla, V. L. Nguyen, A. Bachmatiuk, S. V. Rotkin, Y. H. Lee, and M. H. Rummeli. Stranski-krastanov and volmer-weber cvd growth regimes to control the stacking order in bilayer graphene. *Nano Lett*, 2016.
- [294] Shengnan Wang, Hiroki Hibino, Satoru Suzuki, and Hideki Yamamoto. Atmospheric pressure chemical vapor deposition growth of millimeter-scale single-crystalline graphene on the copper surface with a native oxide layer. *Chemistry of Materials*, 28(14):4893–4900, 2016.
- [295] Haoran Zhang, Yaqian Zhang, Yanhui Zhang, Zhiying Chen, Yanping Sui, Xiaoming Ge, Rongxuan Deng, Guanghui Yu, Zhi Jin, and Xinyu Liu. Realizing controllable graphene nucleation by regulating the competition of hydrogen and oxygen during chemical vapor deposition heating. *Physical Chemistry Chemical Physics*, 18(34):23638–23642, 2016.
- [296] Oliver J. Burton, Vitaliy Babenko, Vlad-Petru Veigang-Radulescu, Barry Brennan, Andrew J. Pollard, and Stephan Hofmann. The role and control of residual bulk oxygen in the catalytic growth of 2d materials. *The Journal of Physical Chemistry C*, 123(26):16257–16267, 2019.
- [297] Zheng Yan, Jian Lin, Zhiwei Peng, Zhengzong Sun, Yu Zhu, Lei Li, Changsheng Xiang, E. Loïc Samuel, Carter Kittrell, and James M. Tour. Toward the synthesis of wafer-scale single-crystal graphene on copper foils. *ACS Nano*, 6(10):9110–9117, 2012.
- [298] Yi Zhang, Luyao Zhang, Pyojae Kim, Mingyuan Ge, Zhen Li, and Chongwu Zhou. Vapor trapping growth of single-crystalline graphene flowers: Synthesis, morphology, and electronic properties. *Nano Letters*, 12(6):2810–2816, 2012.
- [299] Murari Regmi, Matthew F. Chisholm, and Gyula Eres. The effect of growth parameters on the intrinsic properties of large-area single layer graphene grown by chemical vapor deposition on cu. *Carbon*, 50(1):134–141, 2012.
- [300] Yaping Wu, Yufeng Hao, Hu Young Jeong, Zonghoon Lee, Shanshan Chen, Wei Jiang, Qingzhi Wu, Richard D. Piner, Junyong Kang, and Rodney S. Ruoff. Crystal structure

- evolution of individual graphene islands during cvd growth on copper foil. *Advanced Materials*, 25(46):6744–6751, 2013.
- [301] Zheng Han, Amina Kimouche, Dipankar Kalita, Adrien Allain, Hadi Arjmandi-Tash, Antoine Reserbat-Plantey, Laëtitia Marty, Sébastien Pairis, Valérie Reita, Nedjma Bendiab, Johann Coraux, and Vincent Bouchiat. Homogeneous optical and electronic properties of graphene due to the suppression of multilayer patches during cvd on copper foils. *Advanced Functional Materials*, 24(7):964–970, 2014.
- [302] Priyadarshini Ghosh, Shishir Kumar, Gopalakrishnan Ramalingam, Vidya Kochat, Madhavan Radhakrishnan, Sukanya Dhar, Satyam Suwas, Arindam Ghosh, N. Ravishankar, and Srinivasan Raghavan. Insights on defect-mediated heterogeneous nucleation of graphene on copper. *The Journal of Physical Chemistry C*, 119(5):2513–2522, 2015.
- [303] V. Miseikis, D. Convertino, N. Mishra, M. Gemmi, T. Mashoff, S. Heun, N. Haghighian, F. Bisio, M. Canepa, V. Piazza, and C. Coletti. Rapid cvd growth of millimetre-sized single crystal graphene using a cold-wall reactor. *2D Materials*, 2(1):014006, 2015.
- [304] Z. Zhao, Z. Shan, C. Zhang, Q. Li, B. Tian, Z. Huang, W. Lin, X. Chen, H. Ji, W. Zhang, and W. Cai. Study on the diffusion mechanism of graphene grown on copper pockets. *Small*, 11(12):1418–22, 2015.
- [305] S. Chaitoglou, E. Pascual, E. Bertran, and J. L. Andujar. Effect of a balanced concentration of hydrogen on graphene cvd growth. *Journal of Nanomaterials*, 2016:1–10, 2016.
- [306] Yu Cheng, Yenan Song, Dongchen Zhao, Xuwei Zhang, Shaoqian Yin, Peng Wang, Miao Wang, Yang Xia, Shigeo Maruyama, Pei Zhao, and Hongtao Wang. Direct identification of multilayer graphene stacks on copper by optical microscopy. *Chemistry of Materials*, 28(7):2165–2171, 2016.
- [307] Y. P. Hsieh, Y. H. Chu, H. G. Tsai, and M. Hofmann. Reducing the graphene grain density in three steps. *Nanotechnology*, 27(10):105602, 2016.
- [308] Jun Li, Jianing Zhuang, Chengmin Shen, Yuan Tian, Yande Que, Ruisong Ma, Jinbo Pan, Yanfang Zhang, Yeliang Wang, Shixuan Du, Feng Ding, and Hong-Jun Gao. Impurity-induced formation of bilayered graphene on copper by chemical vapor deposition. *Nano Research*, 9(9):2803–2810, 2016.
- [309] J. Yin, H. Wang, H. Peng, Z. Tan, L. Liao, L. Lin, X. Sun, A. L. Koh, Y. Chen, H. Peng, and Z. Liu. Selectively enhanced photocurrent generation in twisted bilayer graphene with van hove singularity. *Nat Commun*, 7:10699, 2016.
- [310] Kumar Varoon Agrawal, Jesse D. Benck, Zhe Yuan, Rahul Prasanna Misra, Ananth Govind Rajan, Yannick Eatmon, Suneet Kale, Ximo S. Chu, Duo O. Li, Chuncheng Gong,

- Jamie Warner, Qing Hua Wang, Daniel Blankschtein, and Michael S. Strano. Fabrication, pressure testing, and nanopore formation of single-layer graphene membranes. *The Journal of Physical Chemistry C*, 121(26):14312–14321, 2017.
- [311] S. Das and J. Drucker. Nucleation and growth of single layer graphene on electrodeposited cu by cold wall chemical vapor deposition. *Nanotechnology*, 28(10):105601, 2017.
- [312] Benjamin Huet and Jean-Pierre Raskin. Pressure-controlled chemical vapor deposition of single-layer graphene with millimeter-size domains on thin copper film. *Chemistry of Materials*, 29(8):3431–3440, 2017.
- [313] Da Luo, Xueqiu You, Bao-Wen Li, Xianjue Chen, Hyo Ju Park, Minbok Jung, Taeg Yeoung Ko, Kester Wong, Masood Yousaf, Xiong Chen, Ming Huang, Sun Hwa Lee, Zonghoon Lee, Hyung-Joon Shin, Sunmin Ryu, Sang Kyu Kwak, Noejung Park, Revathi R. Bacsá, Wolfgang Bacsá, and Rodney S. Ruoff. Role of graphene in water-assisted oxidation of copper in relation to dry transfer of graphene. *Chemistry of Materials*, 29(10):4546–4556, 2017.
- [314] Zhikai Qi, Haohao Shi, Mingxing Zhao, Hongchang Jin, Song Jin, Xianghua Kong, Rodney S. Ruoff, Shengyong Qin, Jiamin Xue, and Hengxing Ji. Chemical vapor deposition growth of bernal-stacked bilayer graphene by edge-selective etching with h₂o. *Chemistry of Materials*, 30(21):7852–7859, 2018.
- [315] Robert G. Van Wesep, Hua Chen, Wenguang Zhu, and Zhenyu Zhang. Communication: Stable carbon nanoarches in the initial stages of epitaxial growth of graphene on cu(111). *The Journal of Chemical Physics*, 134(17):–, 2011.
- [316] Qinghong Yuan, Junfeng Gao, Haibo Shu, Jijun Zhao, Xiaoshuang Chen, and Feng Ding. Magic carbon clusters in the chemical vapor deposition growth of graphene. *Journal of the American Chemical Society*, 134(6):2970–2975, 2011.
- [317] J. Gao, J. Yip, J. Zhao, B. I. Yakobson, and F. Ding. Graphene nucleation on transition metal surface: structure transformation and role of the metal step edge. *J Am Chem Soc*, 133(13):5009–15, 2011.
- [318] T. Wu, G. Ding, H. Shen, H. Wang, L. Sun, Y. Zhu, D. Jiang, and X. Xie. Continuous graphene films synthesized at low temperatures by introducing coronene as nucleation seeds. *Nanoscale*, 5(12):5456–61, 2013.
- [319] W. Wu, L. A. Jauregui, Z. Su, Z. Liu, J. Bao, Y. P. Chen, and Q. Yu. Growth of single crystal graphene arrays by locally controlling nucleation on polycrystalline cu using chemical vapor deposition. *Adv Mater*, 23(42):4898–903, 2011.
- [320] J. A. Lenz, C. A. Perottoni, N. M. Balzaretta, and J. A. H. da Jornada. Processing of amorphous carbon films by ultrafast temperature treatment in a confined geometry. *Journal of Applied Physics*, 89(12):8284–8290, 2001.

- [321] M. R. Habib, T. Liang, X. Yu, X. Pi, Y. Liu, and M. Xu. A review of theoretical study of graphene chemical vapor deposition synthesis on metals: nucleation, growth, and the role of hydrogen and oxygen. *Rep Prog Phys*, 81(3):036501, 2018.
- [322] Shijie Xu, Zhongbi Hou, Xiaoyu Chuai, and Yanfei Wang. Overview of secondary nucleation: From fundamentals to application. *Industrial & Engineering Chemistry Research*, 59(41):18335–18356, 2020.
- [323] Takayuki Iwasaki, Alexei A. Zakharov, Thomas Eelbo, Marta Waniowska, Roland Wiesendanger, Jurgen H. Smet, and Ulrich Starke. Formation and structural analysis of twisted bilayer graphene on ni(111) thin films. *Surface Science*, 625:44–49, 2014.
- [324] Birong Luo, Bingyan Chen, Anle Wang, Dechao Geng, Jie Xu, Huaping Wang, Zhiyong Zhang, Lianmao Peng, Zhiping Xu, and Gui Yu. Chemical vapor deposition of bilayer graphene with layer-resolved growth through dynamic pressure control. *Journal of Materials Chemistry C*, 4(31):7464–7471, 2016.
- [325] A. V. Rozhkov, A. O. Sboychakov, A. L. Rakhmanov, and Franco Nori. Electronic properties of graphene-based bilayer systems. *Physics Reports*, 648:1–104, 2016.
- [326] A. O. Sboychakov, A. L. Rakhmanov, A. V. Rozhkov, and Franco Nori. Electronic spectrum of twisted bilayer graphene. *Physical Review B*, 92(7), 2015.
- [327] I. V. Vlassiouk, Y. Stehle, P. R. Pudasaini, R. R. Unocic, P. D. Rack, A. P. Baddorf, I. N. Ivanov, N. V. Lavrik, F. List, N. Gupta, K. V. Bets, B. I. Yakobson, and S. N. Smirnov. Evolutionary selection growth of two-dimensional materials on polycrystalline substrates. *Nat Mater*, 17(4):318–322, 2018.
- [328] W. Guo, B. Wu, Y. Li, L. Wang, J. Chen, B. Chen, Z. Zhang, L. Peng, S. Wang, and Y. Liu. Governing rule for dynamic formation of grain boundaries in grown graphene. *ACS Nano*, 9(6):5792–8, 2015.
- [329] Saman Choubak, Maxime Biron, Pierre L. Levesque, Richard Martel, and Patrick Desjardins. No graphene etching in purified hydrogen. *The Journal of Physical Chemistry Letters*, 4(7):1100–1103, 2013.
- [330] Yi Zhang, Zhen Li, Pyojae Kim, Luyao Zhang, and Chongwu Zhou. Anisotropic hydrogen etching of chemical vapor deposited graphene. *ACS Nano*, 6(1):126–132, 2011.
- [331] Kamal P. Sharma, Rakesh D. Mahyavanshi, Golap Kalita, and Masaki Tanemura. Influence of copper foil polycrystalline structure on graphene anisotropic etching. *Applied Surface Science*, 393:428–433, 2017.
- [332] J. Liu, Y. Xu, H. Cai, C. Zuo, Z. Huang, L. Lin, X. Guo, Z. Chen, and F. Lai. Double hexagonal graphene ring synthesized using a growth-etching method. *Nanoscale*, 8(29):14178–83, 2016.

- [333] Liang Ma, Xiao Cheng Zeng, and Jinlan Wang. Oxygen intercalation of graphene on transition metal substrate: An edge-limited mechanism. *The Journal of Physical Chemistry Letters*, 6(20):4099–4105, 2015.
- [334] Isaac Ruiz, Wei Wang, Aaron George, Cengiz S. Ozkan, and Mihrimah Ozkan. Silicon oxide contamination of graphene sheets synthesized on copper substrates via chemical vapor deposition. *Advanced Science, Engineering and Medicine*, 6(10):1070–1075, 2014.
- [335] S. Kasap, H. Khaksaran, S. Celik, H. Ozkaya, C. Yanik, and II Kaya. Controlled growth of large area multilayer graphene on copper by chemical vapour deposition. *Phys Chem Chem Phys*, 17(35):23081–7, 2015.
- [336] Xiaoming Ge, Yanhui Zhang, Lingxiu Chen, Yonghui Zheng, Zhiying Chen, Yijian Liang, Shike Hu, Jing Li, Yanping Sui, Guanghui Yu, Zhi Jin, and Xinyu Liu. Mechanism of siox particles formation during cvd graphene growth on cu substrates. *Carbon*, 139:989–998, 2018.
- [337] S. M. Kim, A. Hsu, Y. H. Lee, M. Dresselhaus, T. Palacios, K. K. Kim, and J. Kong. The effect of copper pre-cleaning on graphene synthesis. *Nanotechnology*, 24(36):365602, 2013.
- [338] Dechao Geng, Huaping Wang, Jie Yang, and Gui Yu. Controlled assembly of siox nanoparticles in graphene. *Materials Horizons*, 3(6):568–574, 2016.
- [339] N. Lisi, T. Dikonimos, F. Buonocore, M. Pittori, R. Mazzaro, R. Rizzoli, S. Marras, and A. Capasso. Contamination-free graphene by chemical vapor deposition in quartz furnaces. *Sci Rep*, 7(1):9927, 2017.
- [340] A. Gomez-Martinez, F. Márquez, and C. Morant. A new approach of the synthesis of sio2 nanowires by using bulk copper foils as catalyst. *Applied Surface Science*, 387:1072–1079, 2016.
- [341] Stephen T. Iso and Joseph A. Pask. Reaction of silicate glasses and mullite with hydrogen gas. *Journal of the American Ceramic Society*, 65(8):383–387, 1982.
- [342] Stephen T. Tso and Joseph A. Pask. Reaction of fused silica with hydrogen gas. *Journal of the American Ceramic Society*, 65(9):457–460, 1982.
- [343] Frank T. Ferguson and Joseph A. Nuth. Vapor pressure and evaporation coefficient of silicon monoxide over a mixture of silicon and silica. *Journal of Chemical & Engineering Data*, 57(3):721–728, 2012.
- [344] Stanley G. Davis, Donald F. Anthrop, and Alan W. Searcy. Vapor pressure of silicon and the dissociation pressure of silicon carbide. *The Journal of Chemical Physics*, 34(2):659–664, 1961.

- [345] Robert F. Davis, Ilhan A. Aksay, and Joseph A. Pask. Decomposition of mullite. *Journal of the American Ceramic Society*, 55(2):98–101, 1972.
- [346] John B. Bates. Raman spectra of and cristobalite. *The Journal of Chemical Physics*, 57(9):4042–4047, 1972.
- [347] T. P. Nguyen and S. Lefrant. Raman spectra of silicon monoxide. *Solid State Communications*, 57(4):235–236, 1986.
- [348] T. P. Nguyen and S. Lefrant. Xps study of sio thin films and sio-metal interfaces. *Journal of Physics: Condensed Matter*, 1(31):5197–5204, 1989.
- [349] M. Anwar, C. A. Hogarth, and R. Bulpett. An xps study of amorphous moo₃/sio films deposited by co-evaporation. *Journal of Materials Science*, 25(3):1784–1788, 1990.
- [350] R. Alfonsetti, L. Lozzi, M. Passacantando, P. Picozzi, and S. Santucci. Xps studies on siox thin films. *Applied Surface Science*, 70-71:222–225, 1993.
- [351] R. Alfonsetti, G. De Simone, L. Lozzi, M. Passacantando, P. Picozzi, and S. Santucci. Siox surface stoichiometry by xps: A comparison of various methods. *Surface and Interface Analysis*, 22(1-12):89–92, 1994.
- [352] Hiroyuki Yamamoto, Yuji Baba, and Teikichi A. Sasaki. Electronic structures of n₂⁺ and o₂⁺ ion-implanted si(100). *Surface and Interface Analysis*, 23(6):381–385, 1995.
- [353] F. J. Grunthaner, P. J. Grunthaner, R. P. Vasquez, B. F. Lewis, J. Maserjian, and A. Madhukar. High-resolution x-ray photoelectron spectroscopy as a probe of local atomic structure: Application to amorphous sio₂ and the si-sio₂ interface. *Physical Review Letters*, 43(22):1683–1686, 1979.
- [354] Tomohiro Yasunishi, Yuya Takabayashi, Shigeru Kishimoto, Ryo Kitaura, Hisanori Shinohara, and Yutaka Ohno. Origin of residual particles on transferred graphene grown by cvd. *Japanese Journal of Applied Physics*, 55(8):080305, 2016.
- [355] Fei Ding, Hengxing Ji, Yonghai Chen, Andreas Herklotz, Kathrin Dörr, Yongfeng Mei, Armando Rastelli, and Oliver G. Schmidt. Stretchable graphene: A close look at fundamental parameters through biaxial straining. *Nano Letters*, 10(9):3453–3458, 2010.
- [356] G. A. López and E. J. Mittemeijer. The solubility of c in solid cu. *Scripta Materialia*, 51(1):1–5, 2004.
- [357] Irfan H. Abidi, Yuanyue Liu, Jie Pan, Abhishek Tyagi, Minghao Zhuang, Qicheng Zhang, Aldrine A. Cagang, LuTao Weng, Ping Sheng, William A. Goddard, and Zhengtang Luo. Regulating topsurface multilayer/singlecrystal graphene growth by gettering carbon diffusion at backside of the copper foil. *Advanced Functional Materials*, 27(23), 2017.

- [358] P. Braeuninger-Weimer, B. Brennan, A. J. Pollard, and S. Hofmann. Understanding and controlling cu-catalyzed graphene nucleation: The role of impurities, roughness, and oxygen scavenging. *Chem Mater*, 28(24):8905–8915, 2016.
- [359] D. Luo, M. Wang, Y. Li, C. Kim, K. M. Yu, Y. Kim, H. Han, M. Biswal, M. Huang, Y. Kwon, M. Goo, D. C. Camacho-Mojica, H. Shi, W. J. Yoo, M. S. Altman, H. J. Shin, and R. S. Ruoff. Adlayer-free large-area single crystal graphene grown on a cu(111) foil. *Adv Mater*, 31(35):e1903615, 2019.
- [360] N. Li, R. J. Zhang, Z. Zhen, Z. H. Xu, R. D. Mu, and L. M. He. The effect of catalytic copper pretreatments on cvd graphene growth at different stages. *Nanotechnology*, 32(9):095607, 2021.
- [361] N. Reckinger, M. Casa, J. E. Scheerder, W. Keijers, M. Paillet, J. R. Huntzinger, E. Haye, A. Felten, J. Van de Vondel, M. Sarno, L. Henrard, and J. F. Colomer. Restoring self-limited growth of single-layer graphene on copper foil via backside coating. *Nanoscale*, 11(11):5094–5101, 2019.
- [362] M. H. Khaksaran and II Kaya. On the dynamics of intrinsic carbon in copper during the annealing phase of chemical vapor deposition growth of graphene. *ACS Omega*, 4(6):9629–9635, 2019.
- [363] X. Ge, Y. Zhang, Z. Chen, Y. Liang, S. Hu, Y. Sui, G. Yu, S. Peng, Z. Jin, and X. Liu. Effects of carbon-based impurities on graphene growth. *Phys Chem Chem Phys*, 20(22):15419–15423, 2018.
- [364] R. Blume, P. R. Kidambi, B. C. Bayer, R. S. Weatherup, Z. J. Wang, G. Weinberg, M. G. Willinger, M. Greiner, S. Hofmann, A. Knop-Gericke, and R. Schlogl. The influence of intercalated oxygen on the properties of graphene on polycrystalline cu under various environmental conditions. *Phys Chem Chem Phys*, 16(47):25989–6003, 2014.
- [365] W. M. Lau, L. J. Huang, I. Bello, Y. M. Yiu, and S. T Lee. Modification of surface band bending of diamond by low energy argon and carbon ion bombardment. *Journal of Applied Physics*, 75(7):3385–3391, 1994.
- [366] Mohammad Hadi Khaksaran. *Role Of Intrinsic Carbon In Copper And Its Hydrogen-Assisted Depletion During Growth Of Graphene By Chemical Vapor Deposition*. Thesis, 2019.
- [367] H. Cheun Lee, Wei-Wen Liu, Siang-Piao Chai, Abdul Rahman Mohamed, Azizan Aziz, Cheng-Seong Khe, N. äM S. Hidayah, and U. Hashim. Review of the synthesis, transfer, characterization and growth mechanisms of single and multilayer graphene. *RSC Adv.*, 7(26):15644–15693, 2017.
- [368] Yanjing Gao, Jieli Chen, Guorui Chen, Chunhai Fan, and Xiaoguo Liu. Recent progress in the transfer of graphene films and nanostructures. *Small Methods*, 2021.

- [369] H. Hencky. Über den spannungszustand in kreisrunden platten mit verschwindender biegungssteifigkeit. *Zeitschrift für Mathematik und Physik*, 63:311–317, 1915.
- [370] Jun-yi Sun, Yong-sheng Lian, Ying-min Li, Xiao-ting He, and Zhou-lian Zheng. Closed-form solution of elastic circular membrane with initial stress under uniformly-distributed loads: Extended hencky solution. *ZAMM - Journal of Applied Mathematics and Mechanics / Zeitschrift für Angewandte Mathematik und Mechanik*, 95(11):1335–1341, 2015.
- [371] Y. Wu, H. Tao, S. Su, H. Yue, H. Li, Z. Zhang, Z. Ni, and X. Chen. Patterning graphene film by magnetic-assisted uv ozonation. *Sci Rep*, 7:46583, 2017.
- [372] P. Solis-Fernandez, M. Bissett, and H. Ago. Synthesis, structure and applications of graphene-based 2d heterostructures. *Chem Soc Rev*, 46(15):4572–4613, 2017.
- [373] Shiyu Zhang, Jidong Li, Hongrong Wu, Xuemei Li, and Wanlin Guo. Direct synthesizing in-plane heterostructures of graphene and hexagonal boron nitride in designed pattern. *Advanced Materials Interfaces*, 5(12), 2018.
- [374] Andreas Winter, Antony George, Christof Neumann, Zian Tang, Michael J. Mohn, Johannes Biskupek, Nirul Masurkar, Arava Leela Mohana Reddy, Thomas Weimann, Uwe Hübner, Ute Kaiser, and Andrey Turchanin. Lateral heterostructures of two-dimensional materials by electron-beam induced stitching. *Carbon*, 128:106–116, 2018.
- [375] Nie Shu, Wu Wei, Xing Shirui, Yu Qingkai, Bao Jiming, Pei Shin-shem, and F. McCarty Kevin. Growth from below: bilayer graphene on copper by chemical vapor deposition. *New Journal of Physics*, 14(9):093028, 2012.
- [376] X. D. Chen, W. Xin, W. S. Jiang, Z. B. Liu, Y. Chen, and J. G. Tian. High-precision twist-controlled bilayer and trilayer graphene. *Adv Mater*, 28(13):2563–70, 2016.
- [377] Z. Tan, J. Yin, C. Chen, H. Wang, L. Lin, L. Sun, J. Wu, X. Sun, H. Yang, Y. Chen, H. Peng, and Z. Liu. Building large-domain twisted bilayer graphene with van hove singularity. *ACS Nano*, 10(7):6725–30, 2016.
- [378] J. Zhang, L. Lin, L. Sun, Y. Huang, A. L. Koh, W. Dang, J. Yin, M. Wang, C. Tan, T. Li, Z. Tan, Z. Liu, and H. Peng. Clean transfer of large graphene single crystals for high-intactness suspended membranes and liquid cells. *Adv Mater*, 29(26), 2017.
- [379] Silvia Nappini, Alessia Matruglio, Denys Naumenko, Simone Dal Zilio, Marco Lazzarino, Frank M. F. De Groot, Coskun Kocabas, Osman Balci, and Elena Magnano. Graphene nanoreactors: Photoreduction of prussian blue in aqueous solution. *The Journal of Physical Chemistry C*, 121(40):22225–22233, 2017.
- [380] Y. C. Lin, C. Jin, J. C. Lee, S. F. Jen, K. Suenaga, and P. W. Chiu. Clean transfer of graphene for isolation and suspension. *ACS Nano*, 5(3):2362–8, 2011.

- [381] Teng Li, Zhenyu Huang, Z. Suo, Stéphanie P. Lacour, and Sigurd Wagner. Stretchability of thin metal films on elastomer substrates. *Applied Physics Letters*, 85(16):3435–3437, 2004.
- [382] J. R. Dwyer and M. Harb. Through a window, brightly: A review of selected nanofabricated thin-film platforms for spectroscopy, imaging, and detection. *Appl Spectrosc*, 71(9):2051–2075, 2017.
- [383] Eugen Ermantraut, Klaus Wohlfart, and Willem Tichelaar. Perforated support foils with pre-defined hole size, shape and arrangement. *Ultramicroscopy*, 74(1-2):75–81, 1998.
- [384] T. F. Retajczyk and A. K. Sinha. Elastic stiffness and thermal expansion coefficients of various refractory silicides and silicon nitride films. *Thin Solid Films*, 70(2):241–247, 1980.
- [385] J. J. Yeh and I. Lindau. Atomic subshell photoionization cross sections and asymmetry parameters: $1 \leq z \leq 103$. *Atomic Data and Nuclear Data Tables*, 32(1):1–155, 1985.